



HAL
open science

Field locked to Fock state by quantum feedback with single photon corrections

Xingxing Zhou

► **To cite this version:**

Xingxing Zhou. Field locked to Fock state by quantum feedback with single photon corrections. Quantum Physics [quant-ph]. Université Pierre et Marie Curie - Paris VI, 2012. English. NNT : . tel-00737657

HAL Id: tel-00737657

<https://theses.hal.science/tel-00737657>

Submitted on 2 Oct 2012

HAL is a multi-disciplinary open access archive for the deposit and dissemination of scientific research documents, whether they are published or not. The documents may come from teaching and research institutions in France or abroad, or from public or private research centers.

L'archive ouverte pluridisciplinaire **HAL**, est destinée au dépôt et à la diffusion de documents scientifiques de niveau recherche, publiés ou non, émanant des établissements d'enseignement et de recherche français ou étrangers, des laboratoires publics ou privés.

DÉPARTEMENT DE PHYSIQUE
DE L'ÉCOLE NORMALE SUPÉRIEURE
LABORATOIRE KASTLER BROSSSEL



THÈSE DE DOCTORAT DE L'UNIVERSITÉ PARIS VI

Spécialité : **PHYSIQUE QUANTIQUE**

présentée par

Xingxing ZHOU

pour obtenir le grade de

Docteur de l'Université Paris VI

Sujet :

*Champ asservi sur un état de Fock par
rétroaction quantique utilisant des corrections à
photon unique*

Soutenue le 11/05/2012 devant le jury composé de :

| | |
|-------------------------|--------------------|
| Dr. OLIVIER BUISSON | Rapporteur |
| Pr. JEAN-MICHEL RAIMOND | Directeur de thèse |
| Dr. MAZYAR MIRRAHIMI | Examineur |
| Pr. AGNÈS MAÎTRE | Président |
| Dr. PASCAL DEGIOVANNI | Rapporteur |

Champ asservi sur un état de Fock par rétroaction quantique utilisant des corrections à photon unique

Résumé La rétroaction quantique est un outil prometteur pour la préparation et la protection d'un état quantique. Elle entraîne un système quantique vers un état cible par l'action répétée d'une boucle de sonde-contrôleur-actionneur. Néanmoins, sa réalisation expérimentale est très difficile, car elle doit surmonter une difficulté fondamentale: le processus de mesure modifie inévitablement et de façon aléatoire par une action en retour le système à contrôler. Nous avons réalisé un protocole de rétroaction quantique continue dans le cadre de l'électrodynamique quantique en cavité. Le système à contrôler est un mode de champ électromagnétique piégé dans une cavité Fabry-Pérot micro-onde de très haute finesse. Des atomes de Rydberg circulaires interagissant avec le champ dispersivement servent de sondes. Ils effectuent des mesures quantiques non destructives du nombre de photons. Étant donnés les résultats de ces mesures, et connaissant toutes les imperfections expérimentales, un ordinateur de contrôle estime en temps réel l'état du champ. Il commande ensuite la préparation des atomes de Rydberg circulaires à résonance pour absorber ou émettre des photons dans le but de stabiliser le champ autour de l'états de Fock cible. De cette façon, nous avons réussi à préparer à la demande et à protéger des états de Fock contenant 1 à 7 photons.

Mots-clés CQED, rétroaction quantique, atomes de Rydberg, états de Fock, décohérence, actionneur atomique

Field locked to Fock state by quantum feedback with single photon corrections

Abstract Quantum feedback is a promising tool for preparing and protecting a quantum state. It drives a quantum system towards a target state by the repeated action of a sensor-controller-actuator loop. Nevertheless its experimental implementation is very challenging, as it must overcome a fundamental difficulty: the sensor measurement causes a random back-action on the system. We have implemented a continuous quantum feedback protocol in the context of cavity quantum electrodynamics. The system to be controlled is a mode of the electromagnetic field confined in a very high finesse microwave cavity in the Fabry-Pérot configuration. Circular Rydberg atoms interacting dispersively with the field serve as sensors. They perform quantum non-demolition measurements of the photon number. Knowing the results of these measurements, and knowing all the experimental imperfections, a classical computer estimates in real time the field state. It then commands the preparation of resonant circular Rydberg atoms to absorb or to emit photons in order to stabilize the field around target Fock state. In this way, we have been able to prepare on demand and protect Fock states containing 1 to 7 photons.

Keywords CQED, quantum feedback, Rydberg atoms, Fock states, decoherence, atomic actuator

Table of contents

| | |
|---|-----------|
| Introduction | 1 |
| I Atoms and photons in cavity | 13 |
| I.1 Two-level atoms | 15 |
| I.1.1 Circular Rydberg atoms | 15 |
| I.1.1.a Properties | 15 |
| I.1.1.b Preparation | 18 |
| I.1.1.c Detection | 22 |
| I.1.2 Theory of two-level systems | 23 |
| I.1.2.a Atomic pseudo spin and Bloch sphere | 23 |
| I.1.2.b Manipulation of atomic states | 24 |
| I.1.2.c Ramsey interferometer | 26 |
| I.2 Photons in cavity | 27 |
| I.2.1 The high finesse Fabry-Pérot cavity | 27 |
| I.2.2 Theoretical description | 30 |
| I.2.2.a A quantized field | 30 |
| I.2.2.b Coupling to the environment | 31 |
| I.3 Coupling the two systems | 33 |
| I.3.1 Resonant regime | 35 |
| I.3.2 Dispersive regime | 36 |
| I.3.3 Rapid adiabatic passage | 38 |
| I.4 Measurement of field state | 38 |
| I.4.1 General measurement theory | 39 |
| I.4.2 Quantum nondemolition measurement of photon numbers | 41 |
| I.4.2.a Measurement principle | 41 |
| I.4.2.b Modification of photon number distribution | 42 |
| I.4.2.c Reconstruction of photon number distributions | 45 |
| I.4.2.d Phase shifts in photon number states | 47 |
| II Quantum feedback: state estimation | 51 |
| II.1 General principle | 51 |
| II.1.1 From classical to quantum feedback | 51 |
| II.1.2 Principle of the quantum feedback experiment | 52 |
| II.2 Sensor samples | 53 |
| II.3 Actuator samples | 59 |
| II.3.1 Sample with 1 atom | 59 |
| II.3.1.a Ideal resonant interaction | 59 |

| | | |
|------------|--|------------|
| II.3.1.b | Imperfect Rabi oscillations | 62 |
| II.3.1.c | Rabi oscillations in the Fock states | 68 |
| II.3.1.d | Mixing of the Kraus operators | 72 |
| II.3.2 | Sample with 2 atoms | 74 |
| II.3.2.a | Ideal resonant interaction | 74 |
| II.3.2.b | Vacuum Rabi oscillations of two atoms | 76 |
| II.3.3 | Quantum maps | 77 |
| II.4 | State estimation | 79 |
| III | Quantum feedback: algorithms and optimizations | 81 |
| III.1 | Complete timing of the feedback experiment | 81 |
| III.2 | Quantum state estimator | 84 |
| III.3 | Controller | 85 |
| III.3.1 | Measure of distance | 85 |
| III.3.2 | Decision making | 86 |
| III.4 | Simulations and optimization of parameters | 87 |
| III.4.1 | Parameters for the simulations | 87 |
| III.4.2 | Results of the simulations | 89 |
| III.4.3 | Optimizations | 91 |
| III.4.3.a | The partition of samples | 92 |
| III.4.3.b | Distance functions | 93 |
| III.4.3.c | The interaction time for actuators | 94 |
| IV | Experimental implementation | 97 |
| IV.1 | Control systems | 97 |
| IV.1.1 | Organization of the control systems | 97 |
| IV.1.2 | Main components of the Active system | 99 |
| IV.2 | Sequence | 100 |
| IV.2.1 | Experimental events for one sample | 101 |
| IV.2.2 | The feedback sequence | 101 |
| IV.2.3 | The measurement sequence | 102 |
| IV.3 | Results | 104 |
| IV.3.1 | Individual trajectories | 104 |
| IV.3.2 | Photon number distributions | 113 |
| IV.3.2.a | Stationary regime | 113 |
| IV.3.2.b | Termination by a threshold on fidelity | 116 |
| IV.3.3 | Behavior of the controller | 119 |
| IV.3.3.a | Sample types in the stationary regime | 119 |
| IV.3.3.b | Sample types dependent on the mean photon number | 121 |
| | Conclusion | 123 |
| | A Two-atom Rabi oscillations | 127 |
| | B Simulation procedure | 129 |
| | Bibliography | 133 |

List of Figures

| | | |
|------|--|----|
| 1 | Scheme of the «coherent actuator» quantum feedback experiment | 4 |
| 2 | Scheme of the «atomic actuator» quantum feedback experiment | 5 |
| I.1 | The experimental setup | 14 |
| I.2 | Two energy levels of circular Rydberg atoms | 15 |
| I.3 | Energy levels in the presence of an external electric field | 17 |
| I.4 | Preparation of circular Rydberg states | 19 |
| I.5 | Velocity selection using Doppler effect | 20 |
| I.6 | Velocity distributions of atoms | 21 |
| I.7 | State resolved detection of atoms | 22 |
| I.8 | Bloch sphere representation | 24 |
| I.9 | Manipulation of atomic states | 25 |
| I.10 | Scheme of a Ramsey interferometer | 26 |
| I.11 | Geometrical parameters of the cavity and mirrors | 28 |
| I.12 | Spectrum of the cavity mode | 30 |
| I.13 | Mounts of PZT tubes and adjustment of cavity frequency | 30 |
| I.14 | Energies of dressed states | 34 |
| I.15 | Quantum Rabi oscillations | 35 |
| I.16 | Evolution of the Bloch vector due to dispersive interaction | 37 |
| I.17 | Rapid adiabatic passage | 38 |
| I.18 | Modification of $P(n)$ by one atomic detection | 44 |
| I.19 | Decimation process illustrated in the Bloch sphere representation | 45 |
| I.20 | Progressive decimation of photon number distribution | 46 |
| I.21 | Phase shifts in photon number states | 49 |
| II.1 | Classical and quantum feedback loops | 52 |
| II.2 | Scheme of the feedback experiment | 53 |
| II.3 | Typical experimental Ramsey fringes | 55 |
| II.4 | Calibration of detector efficiency | 57 |
| II.5 | Modification of the photon number distribution by a resonant atom in $ e\rangle$ | 61 |
| II.6 | Modification of the photon number distribution by a resonant atom in $ g\rangle$ | 63 |
| II.7 | Vacuum Rabi oscillations | 64 |

| | | |
|--------|--|-----|
| II.8 | Fit of vacuum Rabi oscillations | 68 |
| II.9 | Rabi oscillations with atoms prepared in e^p | 70 |
| II.10 | Rabi oscillations with atoms prepared in g^p | 71 |
| II.11 | Frequencies and damping rates of quantum Rabi oscillations | 72 |
| II.12 | From a prepared state to detection outcomes | 73 |
| II.13 | Two-atom vacuum Rabi oscillations | 76 |
| III.1 | Spatial configurations of the atomic samples | 82 |
| III.2 | Implementation of different sample types | 83 |
| III.3 | Choosing Ramsey phases | 88 |
| III.4 | Simulated individual quantum trajectory with $n_t = 3$ | 89 |
| III.5 | Evolution of average photon number distribution in a simulation | 90 |
| III.6 | Steady state photon number distribution | 91 |
| III.7 | Convergence speed in simulations | 91 |
| III.8 | Comparison of different sensor-control partitions | 92 |
| III.9 | Comparison of different distance functions | 93 |
| III.10 | Comparison of different interaction times | 94 |
| III.11 | Probability for emitting or absorbing one photon | 95 |
| IV.1 | Organization of control systems | 98 |
| IV.2 | Front panel view of the Active system | 100 |
| IV.3 | Space-time diagram of one atomic sample | 101 |
| IV.4 | Space-time diagram of the feedback sequence | 103 |
| IV.5 | Individual quantum trajectory with $n_t = 1$ | 105 |
| IV.6 | Individual quantum trajectory with $n_t = 2$ | 106 |
| IV.7 | Individual quantum trajectory with $n_t = 3$ | 107 |
| IV.8 | Individual quantum trajectory with $n_t = 4$ | 108 |
| IV.9 | Individual quantum trajectory with $n_t = 5$ | 109 |
| IV.10 | Individual quantum trajectory with $n_t = 6$ | 110 |
| IV.11 | Individual quantum trajectory with $n_t = 7$ | 111 |
| IV.12 | Individual quantum trajectory of a sequential preparation | 112 |
| IV.13 | Photon number distributions in the stationary regime | 114 |
| IV.14 | Photon number distributions of the converged trajectories | 117 |
| IV.15 | Speed of convergence | 118 |
| IV.16 | Evolution of the average photon number distribution with $n_t = 3$ | 119 |
| IV.17 | Probabilities of commanding specific types for the control samples | 120 |
| IV.18 | Probabilities of control sample types dependent on n_t | 120 |
| IV.19 | Probabilities of the sample types as functions of mean photon number | 121 |

Introduction en français

La mécanique quantique, développée au début du XX^e siècle, révèle un monde contre-intuitif dans lequel les notions d'onde et particules sont intimement mélangées. D'une part, la lumière se comporte à la fois comme une onde continue et en comme un ensemble de photons, excitations élémentaires du champ électromagnétique quantifié. D'autre part, les objets perçus comme particules bien localisées, tels que des électrons, présentent également des comportements d'onde. Par exemple, dans une expérience d'interférences à deux fentes réalisée par Tonomura *et al.* [1], une série d'électrons individuels forment progressivement des figures d'interférence similaires aux figures d'interférence optiques observées dans l'expérience originale de Young.

La physique quantique permet également des phénomènes contre-intuitifs comme les états chat de Schrödinger et la non-localité quantique. Les premiers furent observés dans une expérience [2] au cours de laquelle une superposition mésoscopique d'états quantiques évolue progressivement vers un mélange statistique du fait de la décohérence. La seconde s'est avérée être une caractéristique spécifique de théorie quantique, qui ne peut pas être expliquée par des modèles classiques utilisant des «variables cachées» [3, 4, 5].

Dans la théorie quantique, la description de la mesure est également assez différente de son équivalent classique. Un principe bien connu de la physique quantique dit que la mesure modifie en général l'état du système mesuré. Comme postulé par la mécanique quantique, la mesure de l'observable \hat{O} sur un système quantique est soumise aux règles suivantes :

- Les résultats ne peuvent être que des valeurs propres de \hat{O} ;
- Après avoir obtenu une certaine valeur propre, le système est projeté dans l'état propre correspondant.

Une telle mesure est dite projective ou de von Neumann [6]. Les *mesures quantiques non destructives* (QND) [7, 8, 9, 10], dans lequel l'observable \hat{O} commute avec le hamiltonien H du système, assurant la répétabilité de la mesure, en constituent un cas particulier.

Le fait qu'un système quantique soit modifié après avoir été mesuré est exploité pour des applications pratiques. Par exemple, un protocole sécurisé de *distribution de clés quantiques* (QKD) fut proposé par Bennett et Brassard en 1984 [11]. Dans ce schéma, la sécurité du QKD repose sur les postulats de la mesure de la théorie quantique. Un espion extrayant des informations à partir du canal quantique partagé par deux communicants est démasqué, puisque sa mesure modifie le système mesuré.

Une autre application possible de la théorie quantique exploite la non-localité quantique et *l'intrication*. Initialement proposé par Bennett *et al.* en 1993 [12], un protocole de *téléportation quantique* fut réalisé expérimentalement par D. Bouwmeester *et al.* en 1997 [13]. Dans cette expérience, l'expéditeur, «Alice», et le récepteur, «Bob», partagent une paire de photons intriqués. Alice fait une mesure commune sur son photon et un état quantique inconnu, puis

envoi à Bob le résultat classique de sa mesure. Connaissant ce résultat, Bob peut convertir l'état de son photon en une réplique exacte de l'état inconnu détruit par Alice.

L'application la plus ambitieuse de la théorie quantique est probablement son appariement avec l'informatique [14], donnant ainsi naissance à *l'ordinateur quantique*. Un ordinateur quantique opère sur des données codées sur des *qubits* (bits quantiques) et effectue des calculs basés entièrement sur les propriétés quantiques des données et des opérations. Cela est nécessaire car si les bits sont aussi petits qu'un atome, leur nature quantique peut changer profondément le calcul lui-même. Un tel ordinateur peut fonctionner plus efficacement que son équivalent classique pour certains problèmes, comme celui de la factorisation des grands nombres [15]. Des expériences de principe ont été menées dans lequel des opérations de calcul quantique ont été exécutées sur un petit nombre de qubits [16, 17].

Les applications de la théorie quantique reposent sur la capacité à manipuler les systèmes composés d'objets quantiques. On pourrait citer les paires de photons intriqués, les ions piégés, les atomes froids, les boîtes quantiques dans les semi-conducteurs, les qubits supraconducteurs, les résonateurs micro-ondes ou opto-mécaniques, etc. Parmi ces systèmes, certains sont plus adaptés à des fonctions spécifiques. Par exemple, les paires de photons intriqués sont des candidats idéaux pour la communication quantique, alors que les atomes froids sont plus adaptés pour une mémoire quantique. Cependant, les applications réelles pourront impliquer à l'avenir plus généralement un *réseau quantique* [18], dans lequel plusieurs systèmes de différente nature entrent en jeu.

Dans le cadre de la manipulation des systèmes quantiques, préserver la cohérence de leurs états s'avère être difficile. Le couplage inévitable des systèmes quantiques à leur environnement conduit à une fuite d'information et donc à la *décohérence* des systèmes. Dans le cadre du *traitement quantique de l'information*, la décohérence des qubits peut induire des erreurs dans le calcul quantique. Afin de lutter contre les erreurs, de nombreuses méthodes ont été proposées, comme les *codes correcteurs d'erreurs*, qui utilisent des qubits auxiliaires [19], ou le codage de l'information quantique dans des sous-espaces sans décohérence [20]. Une autre méthode basée sur des boucles de rétroaction a également été proposée [21]. Dans cette méthode, le système à contrôler est amené à interagir avec une sonde qui est ensuite détectée. Le signal détecté est ensuite traité et réinjecté dans le système par quelque actionneur. Un état prédéfini peut donc être préparé et préservé.

Plusieurs expériences ont été faites, réalisant certains aspects du protocole de rétroaction. Smith *et al.* [22] démontra la possibilité de geler et de libérer l'évolution d'un état non-classique d'un ensemble d'atomes couplé au mode d'une cavité, en exploitant la rétroaction quantique. Le mode de cavité est faiblement pompé par une source laser. Initialement, le système atome-cavité est dans un état stable. Un photon s'échappant du système le projette dans un nouvel état dans lequel le système atome-champ subit des oscillations de Rabi. Après un intervalle de temps bien choisi après la détection de ce photon, l'intensité du laser de contrôle est modifiée, de telle sorte que le système s'installe dans un nouvel état d'équilibre : les oscillations de Rabi sont supprimées. Une fois l'intensité de pompe initiale restaurée, les oscillations de Rabi redémarrent avec la même amplitude et la même phase.

Cook *et al.* [23] accomplirent une discrimination optimale entre deux états cohérents optiques en utilisant la rétroaction quantique en temps réel. Puisque les états cohérents ne sont pas orthogonaux, la mécanique quantique interdit toute mesure qui peut distinguer parfaitement deux tels états. Une mesure optimale, dite mesure «par état chat», nécessite la préparation d'un état chat de Schrödinger, mais sa réalisation expérimentale est délicate. Dans l'expérience de Cook *et al.*, le champ cohérent à discriminer est détecté par comptage de

photons et manipulé par des déplacements optiques de contrôle. La longueur de l'impulsion correspondant au champ cohérent optique fixe la durée de la mesure. À chaque instant, la discrimination des états est réalisée en sélectionnant celui des deux états qui maximise la probabilité des résultats de comptage de photons, compte tenu de toute l'histoire des déplacements optiques qui ont déjà été appliqués. Le déplacement optique qui minimise la probabilité d'erreurs de discrimination pour le temps de mesure restant est alors fait. De cette façon, ils ont pu distinguer deux états cohérents avec une probabilité d'erreurs inférieure au bruit de grenaille et même proche de la limite quantique.

Gillett *et al.* [24] réalisèrent une expérience dans laquelle des mesures faibles et des corrections par rétroaction furent combinées pour corriger des «phase flips» d'un qubit photonique. Le qubit préparé dans l'un de deux états non orthogonaux est transmis à travers un canal quantique bruité qui peut induire des «phase flips». La mesure faible sur le qubit transmis fournit un résultat, qui est utilisé pour déterminer la rotation optimale pour le qubit, afin de ramener le qubit aussi proche que possible de son état initial.

Geremia *et al.* [25] essayèrent d'utiliser un processus de rétroaction quantique continu pour préparer des états comprimés de spin atomique dans un gaz d'atomes froids. Néanmoins, l'article fut rétracté par la suite, ce qui reflète la difficulté de réaliser une rétroaction quantique continue.

Dans ce qui suit, nous nous intéressons aux expériences de rétroaction quantique continu réalisées dans le cadre de électrodynamique quantique en cavité (CQED). La CQED est particulièrement adaptée à l'étude de l'interaction entre photons et atomes. Un champ électromagnétique piégé dans une cavité de haute finesse est quasi-isolée de son environnement. Le champ quantifié et l'atome individuel qui interagit avec lui constituent un système idéal pour réaliser des expériences de test illustrant les principes fondamentaux de la mécanique quantique. Par exemple, nous pouvons citer l'observation de l'émission spontanée d'un seul atome exaltée par la cavité [26], un effet prédit par Purcell il y a des décennies [27], l'observation des oscillations de Rabi quantiques révélant la nature de quantification du champ de rayonnement [28] et la détection non destructive d'un seul photon [29].

Au cours des dernières années, grâce à l'amélioration de la durée de vie de mode de la cavité, notre groupe a été capable de réaliser des mesures QND répétées sur des champs de photons. Pour cette mesure, le champ micro-ondes piégé dans la cavité et les atomes à deux niveaux interagissent en régime dispersif, de telle sorte que l'échange d'énergie soit évitée. L'interaction induit des *déplacements lumineux* sur les états atomiques, qui dépendent du nombre de photons. La lecture de ces déplacements en utilisant un interféromètre de Ramsey correspond à une mesure QND du nombre de photons. Le groupe a ainsi observé des sauts quantiques de la lumière [30] et enregistré la projection progressive d'un champ cohérent dans les états nombre de photons [31]. Le groupe a également reconstruit plusieurs états non classiques des photons, comme des états de Fock et des états chat de Schrödinger [32]. En prenant des clichés de ces états à des instants successifs, nous avons enregistré le processus de décohérence en cours, illustration parfaite de la transition entre états quantiques et classiques d'un système microscopique couplé à son environnement. Lorsque cette dernière expérience a été réalisée, j'effectuais un stage dans le groupe avant de commencer officiellement ma thèse, et j'ai donc eu l'occasion de participer à la mesure.

Les états du champ non-classiques sont des outils indispensables pour explorer la frontière quantique-classique. En outre, leur préparation est également un aspect important pour des applications à la science de l'information. Par exemple, les états comprimés sont utilisés dans la métrologie et de la communication quantique; les états chat de Schrödinger sont exploitées

pour l'étude de la décohérence; les états de nombre de photons trouvèrent des applications dans l'information quantique. De nombreuses méthodes ont été utilisées pour préparer les états de nombre de photons. en 2000, Varcoe *et al.* prépara les états $|1\rangle$ et $|2\rangle$ en exploitant les «*trapping states*» [33]. Dans cette expérience, l'atome préparé dans son état excité fut à résonance avec le champ dans la cavité et a subi une impulsion de Rabi de 2π dans l'état cible, de telle sorte que le champ fut pris au piège dans cet état. Dans [31], nous utilisâmes les mesures QND répétées pour projeter un champ cohérent dans les états de nombre de photons. En 2009, Hofheinz *et al.* démontrèrent la préparation des états de photons arbitraires dans une expérience de «circuit QED». Le qubit de phase supraconductrice, agissant comme une atome artificielle à deux niveaux, fut à résonance avec le résonateur coplanaire et pompa des photons dans le résonateur cohérentement.

Néanmoins, les états de Fock préparés subissent à la décohérence et peuvent perdre leur non-classicisme rapidement [34, 35]. Ainsi les protéger est une tâche exigeante. La procédure déterministe qui alimente quanta un à la fois dans le champ du résonateur, utilisé par Hofheinz *et al.*, ne peut pas lutter contre la décohérence, car elle ne fournit pas d'informations en temps réel sur l'état du champ actuel. La préparation des états de Fock en utilisant la mesure QND ne peut pas préparer un état de Fock *sur demande*, parce que les différents états de Fock sortent au hasard avec des probabilités données par la distribution du nombre de photons du champ initial. Néanmoins, cette méthode fournit des informations en temps réel sur l'état du champ. Cette information peut être utilisée pour une direction déterministe du champ vers un état de Fock cible, ainsi que pour la détection et la correction ultérieure des sauts quantiques induits par la décohérence. Ainsi, en combinant la mesure QND et un processus de rétroaction peut nous permettre non seulement de préparer des états de Fock sur demande, mais aussi pour les protéger de la décohérence.

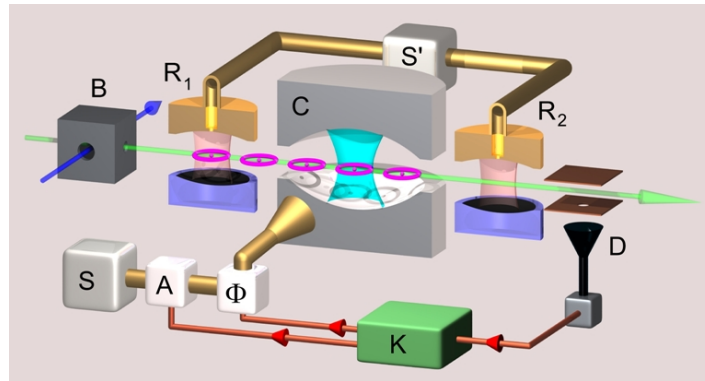


Figure 1. Schéma de l'expérience de rétroaction quantique de «actionneur cohérent». La cavité C de haute finesse est pris en sandwich par les deux zones de Ramsey R_1 et R_2 , qui forment un interféromètre de Ramsey. L'atome de Rydberg circulaires est préparés dans la boîte B et détectée dans D. Le résultat de détection est introduit dans l'ordinateur K (Adwin Pro-II), qui estime l'état du champ et commande une injection petite de champ micro-ondes. L'injection est réalisée par la source S, avec l'amplitude A et le phase Φ contrôlé par K.

Inspiré par la proposition de Geremia [36], nous avons conçu un protocole de rétroaction quantique continue [37] et a réalisé l'expérience qui prépare et stabilise les états nombre de photons sur demande [38]. Le dispositif expérimental est affiché dans la figure 1. Les actions des actionneurs sont des injections de champ micro-onde cohérente. Donc, nous appelons cette expérience un expérience rétroaction quantique de «actionneur cohérent».

Dans cette expérience, si nous préparons et protégeons l'état cible $|n_t\rangle$, un champ cohérent avec l'amplitude réelle $\sqrt{n_t}$ est d'abord injecté dans la cavité par la source S. Le champ est alors mesuré par des atomes de sonde effectuant des mesures QND. La détection de chaque atome dans D fournit des informations partielles sur le nombre de photons dans C. Basée du le résultat de la détection, l'ordinateur K estime l'état du champ en prenant en compte toutes ses connaissances disponibles, telles que l'état du champ initial, le résultat de la détection et de tous les imperfections expérimentales (amortissement du champ, l'efficacité du détecteur, des erreurs de détection, etc.). Il calcule ensuite l'amplitude d'une injection de micro-ondes, visant à apporter l'état du champ proche de l'état cible. Cette injection est ensuite réalisée par la source S, avec l'amplitude A et le phase Φ tous les deux contrôlés par l'ordinateur K.

En utilisant ce schéma, nous avons réussi à préparer et stabiliser des états de Fock avec un maximum de 4 photons. Néanmoins, la performance de ce régime est limité par l'incapacité de l'actionneur classique pour inverser un saut quantique en une seule étape. La disparité entre le classicisme de la source micro-ondes et le quantumness de l'état cible et de ses sauts quantiques limite la vitesse de la correction de ces sauts, et limite ainsi la procédure à nombre de photons faible. La participation à cette expérience constitue une partie importante de ma thèse. Je n'en discute pas ici plus loin. Au lieu de cela, je présente une expérience conduisant à une meilleure performance de rétroaction.

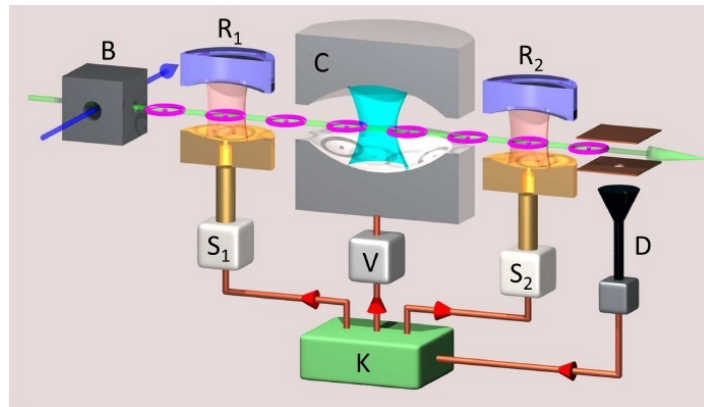


Figure 2. Schéma de l'expérience de rétroaction quantique de «actionneur atomique». La cavité C de haute finesse est pris en sandwich par les deux zones de Ramsey R_1 et R_2 , qui forment un interféromètre de Ramsey. L'atome de Rydberg circulaires est préparés dans la boîte B et détectée dans D. Le résultat de détection est introduit dans l'ordinateur K (Adwin Pro-II), qui estime l'état du champ et applique des rétroactions aux atomes d'actionneur en contrôlant le potentiel (V) sur l'un des miroirs de la cavité et les impulsions micro-ondes dans R_1 (S_1) et R_2 (S_2).

Afin d'améliorer la performance de la procédure de rétroaction, nous remplaçons le source micro-ondes classique S par des objets quantiques: atomes de Rydberg circulaires à résonance, qui échangent des photons avec le champ dans la cavité et agissent comme des *émetteurs* ou *absorbeurs* de photon. Le schéma montrant le principe de cette expérience est donné dans la figure 2. Puisque dans cette expérience, les actionneurs sont des atomes de Rydberg circulaires, il est donc désigné comme l'expérience de rétroaction de «actionneur atomique».

Les algorithmes d'estimation de l'état du champ et du choix des rétroaction différent de l'expérience précédente. Après l'obtention de l'état estimé, l'ordinateur K choisit une rétroaction afin d'apporter l'état actuel près de la cible. L'action peut être mise en l'atome

d'actionneur comme un émetteur ou un absorbeur. qui est réalisé à travers la maîtrise du potentiel V sur l'un des miroirs de la cavité et les impulsions micro-ondes dans R_1 (à travers S_1) et R_2 (à travers S_2). Le potentiel V change les régimes d'interaction entre le champ et les atomes: soit dispersif soit à résonance. L'impulsion micro-ondes dans R_1 prépare un bon état atomique initial. L'impulsion dans R_2 est utilisé pour former un interféromètre de Ramsey. En utilisant ce schéma, nous avons préparé et stabilisé les états de nombre de photons avec un maximum de 7 photons.

Ce manuscrit décrit l'expérience et présente les résultats, et il est organisé comme suit. Dans le chapitre I, nous d'abord donnons un aperçu de la dispositif expérimentale, puis présentons les outils fondamentaux de nos expériences: des atomes et des photons, sur les aspects techniques et théoriques. L'interaction des deux systèmes dans le régime dispersif est ensuite discuté et le principe de la mesure QND de nombre de photons est présenté.

Chapitre II est consacrée à l'estimation d'état dans le protocole de rétroaction. Les interactions des atomes avec le champ dans la cavité et leur détection ultérieure transforment l'état du champ, avec les transformations décrites par des cartes quantiques. Dans ces interactions, les imperfections expérimentales entrent en jeu, qui sont évalués et intégrés dans les cartes quantiques associés à les interactions dispersif et à résonance. A la fin, on obtient une estimation de l'état adapté à la situation expérimentale.

Dans le chapitre III, nous présentons les algorithmes réalistes pour l'estimateur d'état quantique et le contrôleur. Avec ces algorithmes, nous effectuons des simulations numériques, ce qui nous guident dans l'optimisation de certains paramètres du processus de rétroaction.

La réalisation expérimentale du processus de rétroaction est présentée dans le chapitre IV. Nous expliquons d'abord les systèmes de contrôle expérimentales et de la structure d'une séquence expérimentale. Ensuite, nous montrons plusieurs trajectoires quantiques individuelles et les distributions moyennes de nombre de photons obtenus en faisant la moyenne sur plusieurs milliers de telles trajectoires. A la fin, nous discutons de la façon dont le contrôleur fonctionne.

Introduction in English

Quantum mechanics, developed at the beginning of the 20th century, unveils a counter-intuitive world in which the notions of wave and particle are intimately mixed. On the one hand, light appears at the same time as a continuous wave and as an ensemble of photons, which are elementary excitations of the quantized electromagnetic field. On the other hand, the objects perceived as well-localized particles, such as electrons, also exhibit wave behaviors. For instance, in a double-slit interference experiment done by Tonomura *et al.* [1], a series of incoming single electrons gradually formed interference patterns similar to the optical interference patterns observed in the original Young's experiment.

Quantum physics also allows such counter-intuitive phenomena as Schrödinger's cat states and quantum nonlocality. The former was observed in an experiment [2], in which a mesoscopic superposition of quantum states gradually evolved into a statistical mixture due to decoherence. The latter was also demonstrated to be a specific feature associated to quantum theory, which cannot be explained by classical models involving "hidden variables" [3, 4, 5].

In quantum theory, the description of measurement is also quite different from its classical counterpart. A well-known tenet of quantum physics says that measurement in general modifies the state of the measured system. As postulated in quantum mechanics, the measurement with observable \hat{O} on a quantum system satisfies the following rules:

- The measurement outcomes can only be the eigenvalues of \hat{O} .
- After obtaining a certain eigenvalue, the system is projected to the corresponding eigenstate.

Such a measurement is called a projective or von Neumann measurement [6]. A special type of such measurement is the *quantum nondemolition measurement* (QND) [7, 8, 9, 10], in which the observable \hat{O} commutes with the Hamiltonian H of the system, ensuring the repeatability of the measurement.

The fact that measuring a quantum system in general modifies it is also exploited for practical applications. For example, a secure *quantum key distribution* (QKD) scheme was proposed by Bennett and Brassard in 1984 [11]. In this scheme, the security of the QKD traces back to the measurement postulates of quantum theory. An eavesdropper extracting information from the quantum channel shared by two communicators discloses himself, since his measurement modifies the measured system.

Another possible application of quantum theory exploits quantum nonlocality and *entanglement*. Initially proposed by Bennett *et al.* in 1993 [12], a *quantum teleportation* protocol was first demonstrated experimentally by D. Bouwmeester *et al.* in 1997 [13]. In this experiment, the sender, "Alice", and the receiver, "Bob", share an entangled pair of photons. Alice makes a joint measurement on her photon and an unknown quantum state, then sends Bob

the classical result of her measurement. Knowing this result, Bob can convert the state of his photon into an exact replica of the unknown state destroyed by Alice.

The most ambitious application of quantum theory may be its combination with computer science [14], which leads to the concept of a *quantum computer*. A quantum computer operates on data represented by *qubits* (quantum bits) and carries out computations based completely on the quantum properties of data and operations. This is necessary because if the bits of computation scale down to the size of individual atoms, the quantum nature of these bits may change profoundly computation itself. Such a computer can work more efficiently than its classical counterpart for some computation problem, e.g. the factorization of a large number [15]. Proof-of-principle experiments have been carried out in which quantum computational operations were executed on a small number of qubits [16, 17].

The applications of quantum theory rely on the ability to manipulate systems made of quantum objects. These systems include, to name a few, entangled photon pairs, trapped ions, cold atoms, semiconductor quantum dots, superconducting qubits, microwave oscillators, opto-mechanical oscillators, etc. Among these systems, certain are more suitable for specific functions. For instance, entangled photon pairs are ideal candidates for quantum communication, whereas cold atoms are suitable for acting as a quantum memory. However, the real applications in future may involve a more general *quantum network* [18], in which several different systems come into play.

While manipulating quantum systems, a challenging task is to preserve the coherence of their states. The inevitable coupling of the quantum systems to their environments leads to leakage of information and thus *decoherence* of the systems. In the context of *quantum information processing*, decoherence of the qubits may induce errors in the quantum computation. In order to fight against the errors, many methods have been proposed, such as the *error correcting codes* by exploiting auxiliary qubits [19], or the coding of quantum information in decoherence-free subspaces [20]. Another method based on feedback loops was also proposed [21]. In this method, the system to be controlled is brought to interact with a probe which is subsequently detected. The detected signal is then processed and fed back to the system through some actuator. A predefined state can thus be prepared and preserved.

Several experiments have been performed, which achieve some aspects of the feedback protocol. Smith *et al.* [22] demonstrated the ability to freeze and release the evolution of a non-classical coupled state of a cavity mode and an atom ensemble, by exploiting quantum feedback. The cavity mode was weakly driven by a laser source. Initially the coupled atom-cavity system was in a steady state. A photon escaping from the system projected the state into a new one in which the atom ensemble and the cavity mode underwent Rabi oscillations. After a properly chosen time interval following the detection of the escaping photon, the intensity of the driving laser was modified, such that the system settled down to a new steady state and the Rabi oscillations were suppressed. Once the initial driving intensity was reinstated, the Rabi oscillations returned with the same amplitude and phase.

Cook *et al.* [23] accomplished an optimized discrimination between two optical coherent states using real-time quantum feedback. Since coherent states are not orthogonal to each other, quantum mechanics precludes any measurement that can discriminate perfectly two such states. An optimal measurement, the so-called "cat-state" measurement, requires the preparation of a Schrödinger's cat state, and is considered very difficult for experimental implementation. In the experiment of Cook *et al.*, the coherent field to be discriminated was detected by photon counting and manipulated by feedback-mediated optical displacements. The optical pulse length of the coherent field set the duration of the measurement. At each

moment within the measurement, field discrimination was performed by selecting one of the two states that maximized the likelihood of the photon counting results, given the whole history of already-applied optical displacements. A new optical displacement was chosen to minimize the probability of discrimination errors over the remainder of the measurement duration. In this way, they could discriminate two coherent fields with probability of errors lower than shot noise and even approaching the quantum limit.

Gillett *et al.* [24] performed an experiment in which weak measurements and feedback control were combined to correct phase flip errors of a photonic qubit. The qubit prepared in one of two nonorthogonal states was transmitted through a noisy quantum channel that could induce a phase flip error. The weak measurement on the transmitted qubit provided a result, which was used for determining an optimal rotation to the qubit, aiming at recovering the qubit as close as possible to its noiseless initial state.

Geremia *et al.* [25] tried using a continuous quantum feedback process to prepare atomic spin-squeezing states in an ensemble of cold atoms. Nevertheless, the paper was later retracted, reflecting the difficulty of implementing a continuous quantum feedback.

In the following, we discuss continuous quantum feedback experiments implemented in the context of cavity quantum electrodynamics (CQED). CQED is particularly adapted to studying the interaction between photons and atoms. An electromagnetic field confined in a high finesse cavity is quasi-isolated from its environment. The quantized field and the individual atom interacting with it constitute an ideal system for performing test experiments illustrating the fundamental principles of quantum mechanics. For example, let us mention the observation of cavity-enhanced single-atom spontaneous emission [26], an effect predicted by Purcell decades ago [27]; the observation of quantum Rabi oscillations revealing the quantization nature of the radiation field [28]; and the non destructive detection of a single photon [29].

In recent years, thanks to the improvement of the lifetime of cavity mode, our group has been able to perform repeated QND measurement on photon fields. In this measurement, the microwave field confined in the cavity and the two-level atoms interact in the dispersive regime, such that no energy exchange occurs. The interaction induces *light shifts* on the atomic states, which depend on the photon number. Reading out these shifts using a Ramsey interferometer amounts to a QND measurement of the photon number. The group thus observed the quantum jumps of a light field [30] and monitored the progressive projection of a coherent field into photon number states [31]. The group also reconstructed several non classical photon states, such as the Fock states and the Schrödinger's cat states [32]. By taking snapshots of these states at successive times, we monitored decoherence process in progress, which clearly illustrated the transition from quantum to classical states of a microscopic system coupled to its environment. When the last experiment was performed, I was taking an internship in the group before officially starting my Ph.D. work, and thus had the opportunity to participate in the measurement.

Non-classical field states are indispensable tools for exploring the quantum-classical boundary. Moreover, their preparation is also an important aspect of the applications to information science. For example, squeezed states are used in metrology and quantum communication; Schrödinger's cat states are exploited for studying decoherence; and photon number states find applications in quantum information processes. Many methods have been used to prepare photon number states. In 2000, Varcoe *et al.* prepared the states $|1\rangle$ and $|2\rangle$ by exploiting the *trapping states* [33]. In this experiment, the atom prepared in its excited state interacted resonantly with the cavity field and underwent a Rabi 2π pulse in the target state, such that the field was trapped in this state. In [31], we used repeated QND measurement to collapse

a coherent field into individual photon number states. In 2009, Hofheinz *et al.* demonstrated the preparation of arbitrary photon states in a circuit-QED experiment. The superconducting phase qubit, acting as an artificial two-level atom, interacted resonantly with the coplanar resonator and phase-coherently pumped photons into the resonator.

Nevertheless, the prepared Fock states undergo decoherence and can lose their non-classicality rapidly [34, 35]. Thus protecting them is a demanding task. The deterministic procedure which feeds quanta one at a time into the resonator field, used by Hofheinz *et al.*, cannot counteract decoherence because it does not provide real time information on the actual field state. The preparation of the Fock states using the QND measurement cannot prepare a Fock state *on demand*, because different Fock states come out randomly with probabilities given by the photon number distribution of the initial field. Nevertheless, this method provides real time information about the field state. This information can be used for a deterministic steering of the field towards a target Fock state, as well as for detection and subsequent correction of decoherence-induced quantum jumps. Thus, combining the QND measurement and a feedback process can enable us not only to prepare Fock states on demand but also to protect them from decoherence.

Inspired by the proposal of Geremia [36], we have designed a protocol for continuous quantum feedback [37] and performed the experiment which prepares and stabilizes photon number states on demand [38]. The experimental scheme is displayed in Fig. 3. The actions of the actuators are injections of coherent microwave field. So we call this experiment a “coherent actuator” quantum feedback experiment.

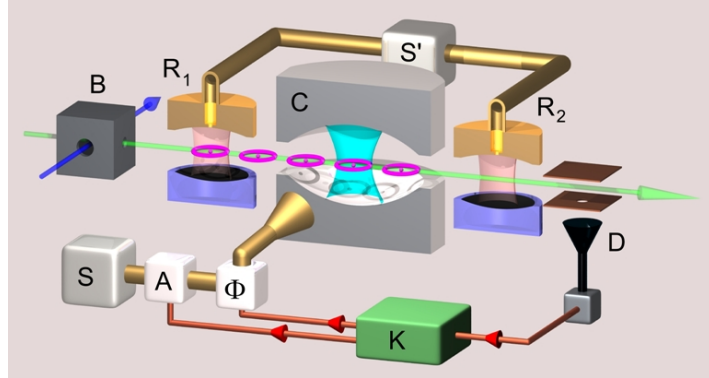


Figure 3. Scheme of the “coherent actuator” quantum feedback experiment. The high finesse cavity C is sandwiched by the two Ramsey zones R_1 and R_2 , which form a Ramsey interferometer. The circular Rydberg atom is prepared in box B and detected in D. The detection result is fed into the computer K (ADwin Pro-II), which estimates the field state and commands a small injection of microwave field. The injection is performed by the source S, with the amplitude A and phase Φ controlled by K.

In this experiment, if we prepare and protect the target Fock state $|n_t\rangle$, a coherent field with the real amplitude $\sqrt{n_t}$ is first fed into the cavity by the source S. The field is then probed by sensor atoms performing QND measurements. The detection of each atom in D provides partial information about the photon number in C. Based on the detection result, the computer K estimates the field state by taking into account all available knowledge, such as the initial field state, the detection result and all experimental imperfections (cavity decay, detector efficiency, detection errors, etc.). It then computes the amplitude of a microwave injection, aiming at bringing the field state closer to the target Fock state. This injection is

then carried out by the source S , with the amplitude A and phase Φ both controlled by the computer K .

Using this scheme, we succeeded in preparing and stabilizing the Fock states with up to 4 photons. Nevertheless, the performance of this scheme is limited by the inability of the classical actuator to reverse a quantum jump in a single step. The mismatch between the classicality of the microwave source and the quantumness of the target state and of its quantum jumps limits the speed of correcting these jumps, and thus limits the procedure to low photon number states. The participation in this experiment constitutes an important part of my Ph.D. work. I do not discuss it here any further. Instead, I present an experiment leading to better feedback performance.

In order to improve the performance of the feedback procedure, we substitute the classical microwave source S by quantum objects: resonant circular Rydberg atoms, which exchange photons with the cavity field and act as photon *emitters* or *absorbers*. The scheme showing the principle of this experiment is given in Fig. 4. Since in this experiment, the actuators are the circular Rydberg atoms, it is thus referred to as the ‘‘atomic actuator’’ feedback experiment.

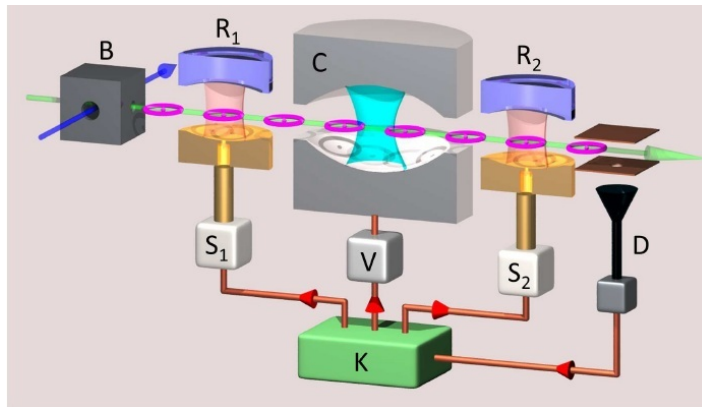


Figure 4. Scheme of the ‘‘atomic actuator’’ quantum feedback experiment. The high finesse cavity C is sandwiched by the two Ramsey zones R_1 and R_2 , which form a Ramsey interferometer. The circular Rydberg atom is prepared in box B and detected in D . The detection result is fed into the computer K (ADwin Pro-II), which estimates the field state and applies feedback actions to the actuator atoms by controlling the potential V on one of the cavity mirrors and the microwave pulses in R_1 (S_1) and R_2 (S_2).

The algorithms for estimating the field state and choosing feedback actions differ from the former experiment. After obtaining the estimated state, the computer K chooses a feedback action in order to bring the current state closer to the target. The action can be setting the actuator atom as a photon emitter or absorber, which is implemented through controlling the potential V on one of the cavity mirrors and the microwave pulses in R_1 (through S_1) and R_2 (through S_2). The potential V switches the interaction regimes between the cavity field and atoms: either dispersive or resonant. The microwave pulse in R_1 prepares a proper initial atomic state. The pulse in R_2 is used for forming a Ramsey interferometer. Using this scheme, we have prepared and stabilized photon number states with up to 7 photons.

This manuscript explains the experiment and presents the results, and it is organized as follows. In chapter I, we first give an overview of the experimental setup, then present the fundamental tools of our experiments: atoms and photons, on both technical and theoretical aspects. The interaction of the two systems in the dispersive regime is then discussed and the

principle of the QND measurement of photon numbers is presented.

Chapter II is devoted to state estimation in the feedback protocol. The interactions of atoms with the cavity field and their subsequent detection transform the field state, with transformations described by quantum maps. In these interactions, experimental imperfections come into play, which are measured and incorporated into the quantum maps associated to both the dispersive and resonant interactions. At the end, we obtain a state estimation adapted to the experimental situation.

In chapter III, we present the realistic algorithms for the quantum state estimator and controller. Based on these algorithms, we perform numerical simulations, which guide us in optimizing certain parameters of the feedback process.

The experimental implementation of the feedback process is presented in chapter IV. We first explain the experimental control systems and the structure of an experimental sequence. Then we show several individual quantum trajectories and the average photon number distributions obtained by averaging over thousands of such trajectories. At the end, we discuss how the controller operates.

Chapter I

Atoms and photons in cavity

We investigate the interaction between two-level atoms and few photons confined in a very high Q cavity. The current setup we use was completed during the thesis of Sébastien Gleyzes [39]. The long lifetime of the field confined in the cavity during which we can measure the field about 800 times enables us to perform a feedback experiment. This chapter is devoted to the introduction of the experimental tools. We first show the experimental scheme, then present the two-level atoms, the high Q cavity, the theories describing their interactions and measurement of the field state.

In section I.1, we present the circular Rydberg states of Rubidium atoms, including their special properties as two-level systems, the preparation and detection methods. Besides these technical aspects, we also explain the theoretical description of these two-level systems. At the end, we discuss the principle of a Ramsey interferometer. In section I.2, we introduce the high Q cavity and the description of the photon field. The coupling of the field to its environment is also discussed. In section I.3, we present the theory describing the interaction between the atoms and photons. Depending on their relative frequencies, the two systems may interact dispersively or resonantly. In section I.4, we discuss the quantum nondemolition (QND) measurement of photon numbers. We start by recalling the postulates on measurement in quantum mechanics, then explain the principle of the QND measurement. Afterwards, we explain the methods for field state reconstruction and measurement of phase shift per photon.

Experimental setup

The experimental scheme is displayed in Fig. I.1. Let us follow the long blue arrow showing the direction of the atomic beam to briefly present the main components of the setup.

Oven

Rubidium atoms are stored in the oven. They are heated up, then diffuse out of it through a small hole. After the velocity selection process, only the atoms with a selected velocity participate in experiments.

Circularization box

The atoms are excited to the circular Rydberg states in **B**. This process involves several lasers, microwave and RF fields, etc. The small entrance hole on this box and the exit hole of the oven define the quasi unidimensional atomic beam.

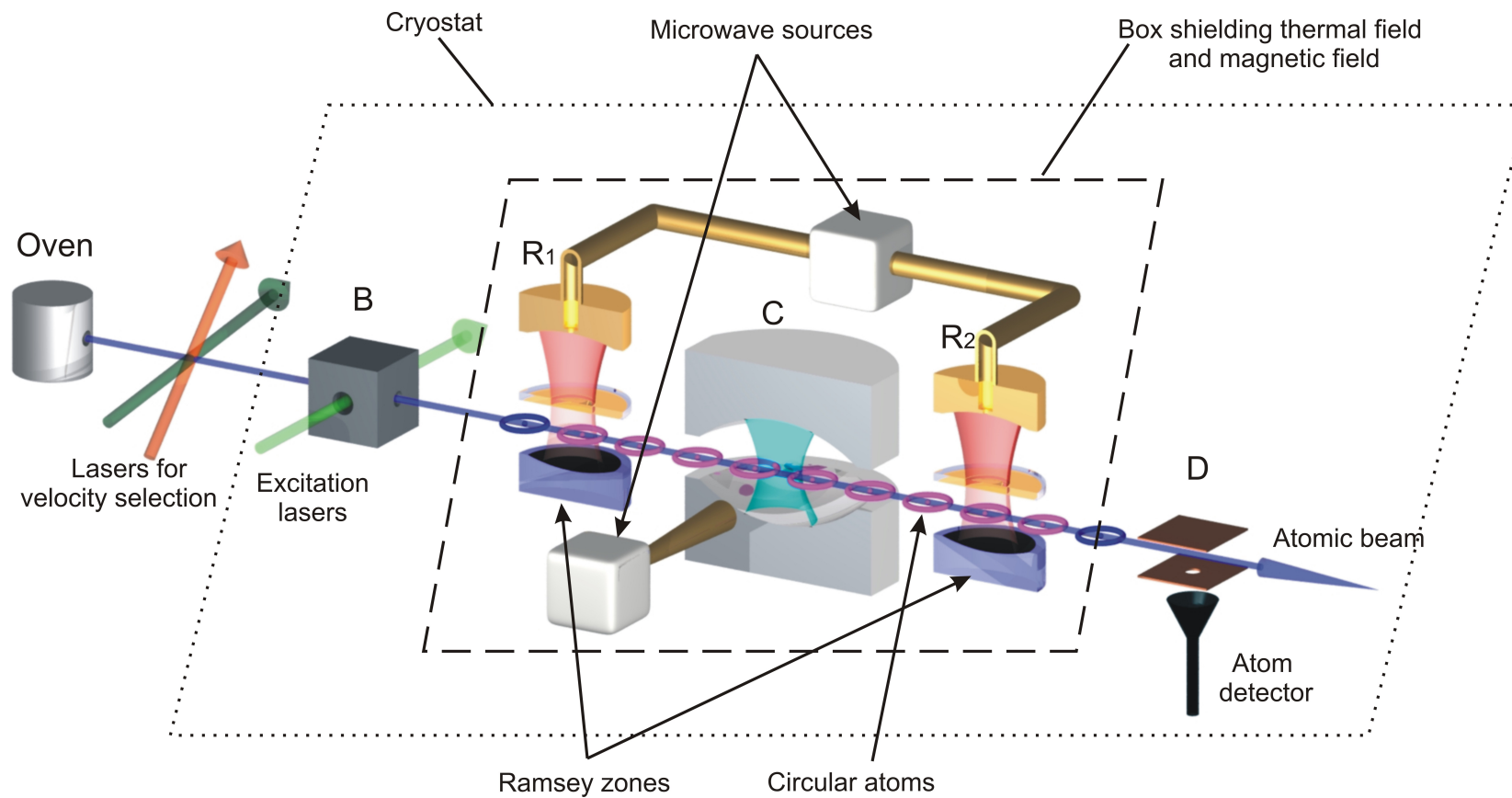


Figure I.1. The experimental scheme. The long blue arrows shows the atomic beam. The torus-shaped elements represent circular atoms.

Ramsey zones and cavities

The two Ramsey zones \mathbf{R}_1 , \mathbf{R}_2 and the high Q cavity \mathbf{C} constitute the core part of the experiment. They are shielded from thermal and magnetic fields by a metal box. The box is cooled down to 0.8 K, by combining a Nitrogen cryostat, a ^4He cryostat and a ^3He refrigerator. The almost completely closed structure of the box suppresses the leakage of thermal photons into it, thus guarantees a well thermally equilibrated environment at 0.8 K for the cavity field. The two Ramsey zones are fed by the same microwave synthesizer through holes on one of their mirrors. The cavity is fed by another microwave synthesizer from one side. This design avoids damaging the mirror surface with a coupling hole and helps to obtain a high finesse cavity.

Detector

We apply an electric field between the two electrodes of \mathbf{D} . The atom is then ionized, leaving a free electron focused by electric lens and detected by an electron multiplier.

I.1 Two-level atoms

I.1.1 Circular Rydberg atoms

The atom with an electron excited to energy levels with very high principal quantum numbers n is called a Rydberg atom. It is further designated as a “circular” Rydberg atom if that electron is excited to the level with maximal orbital and magnetic quantum numbers, i.e. $l = m = n - 1$, because in this situation the electron has a circular orbit in the classical limit. Let us use $|nc\rangle$ to denote such circular states. In our experiment we use the two circular levels $|50c\rangle$ and $|51c\rangle$ of ^{85}Rb , which are also denoted as $|g\rangle$ and $|e\rangle$, respectively. Figure I.2 shows these levels and their energy difference. Their properties, preparation and detection will be described in the following.

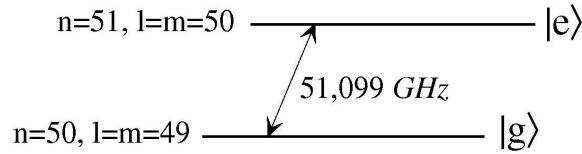


Figure I.2. Energy levels of the circular Rydberg states used in our experiments.

I.1.1.a Properties

Hydrogen-like energy levels

In the circular states $|g\rangle$ and $|e\rangle$, the valence electron is far away from the nucleus (the distance is much larger than the Bohr radius), the Rb atom thus has a hydrogen-like structure, in which the nucleus and all inner core electrons serve as a “heavier proton”. Within a very good approximation, the energy levels of this system can be written as

$$E_n = -\frac{R_y}{n^2},$$

where R_y is the slightly modified Rydberg constant that takes into account the mass of the “heavier proton” [39].

Under the condition $n \gg 1$, the transition frequency between two neighboring circular levels reads

$$\omega_n = \frac{R_y}{\hbar} \left(\frac{1}{(n-1)^2} - \frac{1}{n^2} \right) \simeq \frac{R_y}{\hbar} \cdot \frac{2}{n^3}.$$

For states with $n \sim 50$, the transition frequency 51.099 GHz falls in the microwave regime, a regime where there exist high quality field resonators, facilitating the search for high Q cavities.

Large electric dipole

The $|nc\rangle \longleftrightarrow |(n-1)c\rangle$ transition is σ^+ -circularly polarized. Its dipole matrix element is given by [40, p. 254]

$$d_n = n^2 \frac{|q|a_0}{\sqrt{2}}, \quad (\text{I.1})$$

with q being the electron charge and $a_0 = 0.53 \text{ \AA}$ the Bohr radius.

Note that this value is proportional to n^2 , since the radius of a Rydberg atom is proportional to n^2 in a hydrogen-like approximation. For the transition $|50c\rangle \longleftrightarrow |51c\rangle$, we have $d_{51} = 1776|q|a_0$, which is a large number on the atomic scale.

Long lifetime

Among all states with a given principal quantum number, the circular states have the longest radiative lifetime [41]. In fact, the circular Rydberg state can only decay to the first lower circular level by spontaneous emission, i.e. $|nc\rangle \longrightarrow |(n-1)c\rangle$, according to the selection rules. This transition occurs at a frequency $\omega_n \propto n^{-3}$, with $d_n \propto n^2$. So the lifetime of the circular level reads:

$$T_{\text{at}} = \gamma_{\text{at}}^{-1} = \left(\frac{\omega_n^3 d_n^2}{3\pi\epsilon_0 \hbar c} \right)^{-1} \propto n^5. \quad (\text{I.2})$$

We see that T_{at} is proportional to n^5 . Particularly, the circular levels $|50c\rangle$ and $|51c\rangle$ have lifetimes 28.5 ms and 31.5 ms, respectively.

Quadratic Stark effect

Circular Rydberg atoms have long lifetimes and strong coupling to microwave field, which enable them to be good candidates as two-level systems. However, they are also very fragile in the sense that they can mix with other levels which have the same principal quantum number n , the so-called ‘‘elliptical’’ levels, because all these levels are degenerate in the absence of external electric or magnetic fields. These elliptical and circular states form the hydrogenic *multiplicity* of principal quantum number n .

The application of an external electric field F lifts this degeneracy. In this situation, l is no longer a good quantum number, since F breaks the spherical symmetry. But m , related to the symmetry around the z axis, remains as a good quantum number. The new eigenstates of the Hamiltonian can be denoted as $|n; n_1; m\rangle$, with n_1 being the parabolic quantum number and satisfying $0 \leq n_1 \leq (n - |m| - 1)$. Circular states have $n_1 = 0$. It can be shown [42] that with a development up to the second order in F , the energy levels in the multiplicity of n can

be expressed as $E = E^{(0)} + E^{(1)} + E^{(2)}$, with the three terms given by

$$E^{(0)} = -\frac{1}{2n^2} \quad (\text{I.3})$$

$$E^{(1)} = \frac{3}{2}knF \quad (\text{I.4})$$

$$E^{(2)} = -\frac{1}{16}(17n^2 - 3k^2 - 9m^2 + 19)n^4F^2, \quad (\text{I.5})$$

with $k = 2n_1 - n + |m| + 1$. The energy and field amplitude are expressed in the atomic units. States $|e\rangle$ and $|g\rangle$ together with the related elliptical levels are shown in Fig. I.3.

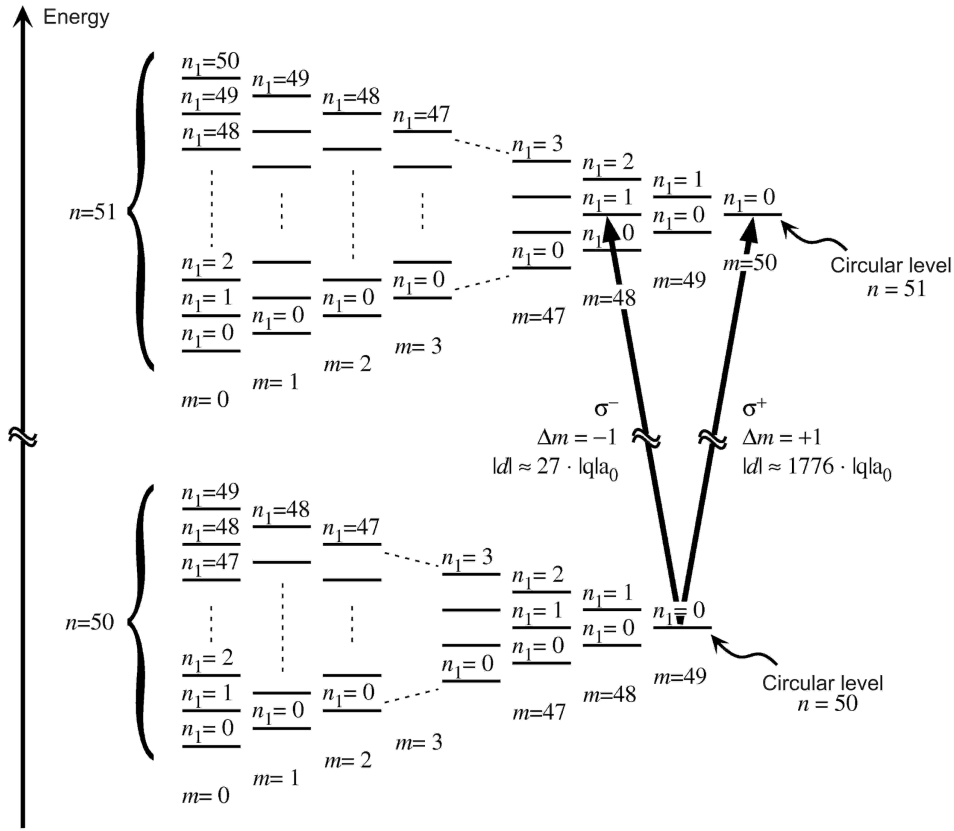


Figure I.3. Energy levels of the multiplicity of $n = 50$ and $n = 51$ in the presence of an external electric field.

Note that the linear Stark effect lifts the degeneracy between the circular level ($m = n - 1$) and the levels with $m = n - 2$ in the same multiplicity by $\pm 100 \text{ MHz}/(\text{V}/\text{cm})$. Thus in the presence of even a relatively weak electric field, the transitions starting from $|(n - 1)c\rangle$ to $|nc\rangle$ ($\Delta m = +1$) or to elliptical levels $|n; n_1; m = n - 2\rangle$ ($\Delta m = 0$) can be well distinguished. The σ^- transition as depicted in Fig. I.3 has a frequency very close to that between the two circular levels. However, the matrix element of its electric dipole $|d|_{\sigma^-} = 27|q|a_0$ is much smaller than that of the circular levels $|d|_{\sigma^+} = 1776|q|a_0$, making it negligible. To summarize, by applying an external electric field, we obtain a system with two levels well separated from other levels. This electric field, known as a *guiding electric field*, should have non zero values

along the whole path of the circular Rydberg atoms in order to avoid mixing between the circular and elliptical levels. But its amplitude and direction can vary smoothly.

Also note that the linear Stark effect is zero for a circular level, but a quadratic term remains and shifts the frequency of $|g\rangle \longleftrightarrow |e\rangle$ transition by $-255 \text{ kHz}/(\text{V}/\text{cm})^2$. This effect is quite useful for tuning the atomic frequency in experiments. For instance, the atoms can be tuned to be on or off resonance with the cavity field by adjusting the static electric field between the cavity mirrors.

I.1.1.b Preparation

The preparation of circular atoms is a complex process, in which we need to transfer a lot of energy and angular momentum to the atoms being initially in their ground state. The whole process, involving the participation of several lasers, RF field and varying electric field, etc., is shown in Fig. I.4. Since detailed explanation can be found in the thesis of Tristan Meunier [43], here we only outline the main procedures.

Circularization of Rubidium atoms

The excitation of atoms to the circular levels is performed in the presence of a magnetic field of 18 G. The atoms are first excited from the fundamental level $|5S_{1/2}, F = 3, m_F = +3\rangle$ to the Rydberg level $|52f, m = 2\rangle$ by three lasers at the wavelengths 780 nm, 776 nm and 1.26 μm . The laser at 780 nm also plays a role of *optical pumping*, which brings atoms at other sub-levels of $|5S_{1/2}, F = 3\rangle$ to $|5S_{1/2}, F = 3, m_F = +3\rangle$. This laser is also pulsed with a typical duration of 2 μs , which defines a time origin for all following pulses.

The laser excitation process is performed in the absence of electric field. Then the electric field is gradually switched on and lifts the degeneracy of the multiplicity of $n = 52$. Atoms are then transferred to the level $|n = 52, n_1 = 1, m = 2\rangle$. The electric field is then swept and a RF field is turned on at the same time, transferring atoms to the circular level $|52c\rangle$ through a rapid adiabatic passage during which 49 photons at 255 MHz are absorbed. In this process, the degeneracy of σ^+ and σ^- transitions are lifted by the magnetic field at 18 G. This field, however, needs to be shielded in order not to perturb, by the Zeeman effect, the circular levels going into the cavity. In the setup, we use a cylinder container made of superconducting Niobium to shield the magnetic field. It is in this container, also called the *circularization box*, that the circular levels are prepared.

Nevertheless, the prepared circular states are not pure, because some atoms may end up in one of the elliptical states during the adiabatic passage. So after the preparation of state $|52c\rangle$, a purification microwave is switched on, which brings atoms to $|51c\rangle$ by one-photon transition at 48.2 GHz, or $|50c\rangle$ by two-photon transition at 49.6 GHz. Eventually, the atoms staying on the levels of $n = 52$, no matter circular or elliptical, are ionized by a strong electric field at the exit of the circularization box. At the end, we can obtain pure circular levels $|e\rangle$ or $|g\rangle$. In all experiments discussed in this manuscript, the atoms are prepared in the state $|g\rangle$ in this process.

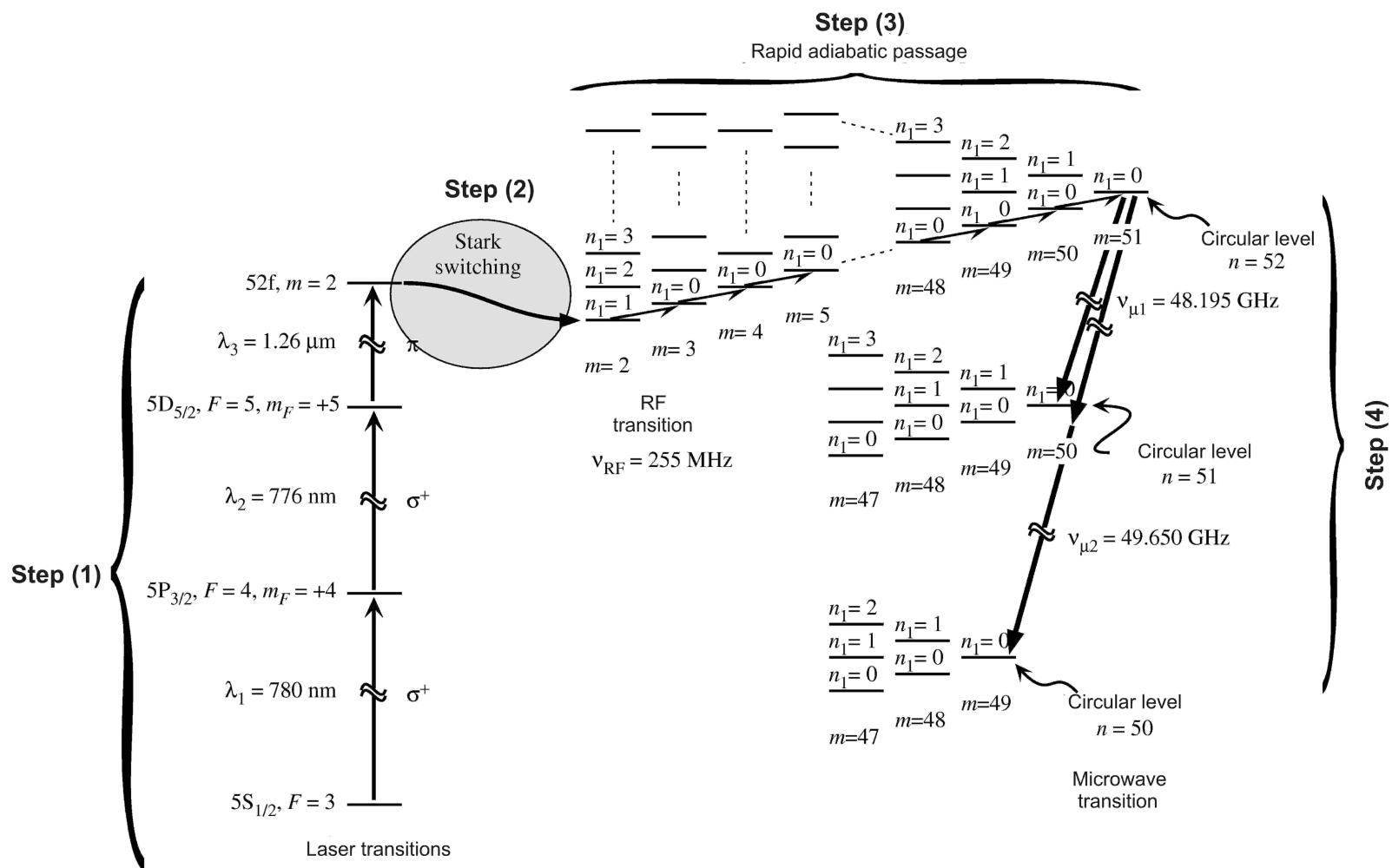


Figure I.4. Preparation of circular Rydberg states.

Controlling atomic position and velocity

Controlling the transverse profile of the atomic beam is necessary in order to reduce the effect of inhomogeneous static electric field and to let the atoms pass through the center of the cavity, such that strongest coupling to the cavity field is achieved. A quasi unidimensional atomic beam is selected by the exit hole of the oven and the entrance hole of the circularization box. The Rubidium atoms contained in the oven are heated up to about 185 °C. They diffuse out of the oven at their thermal velocities through a 0.7 mm hole and need to pass through another 0.7 mm hole at the entrance of the circularization box before entering the cavity. The two holes, separated by 550 mm, thus select an atomic beam with a transverse diameter of about 0.7 mm.

Thermal velocities of the atoms satisfy a Maxwell-Boltzmann distribution, which has a width of about 270 m/s. In experiments, we need to know the position of atoms at a given time, in other words, the velocity of atoms should be well selected and controlled. This is done by two techniques: the first is velocity selection using *Doppler effect* and the second is *flight time selection*. The principle of the first technique is shown in Fig. I.5.

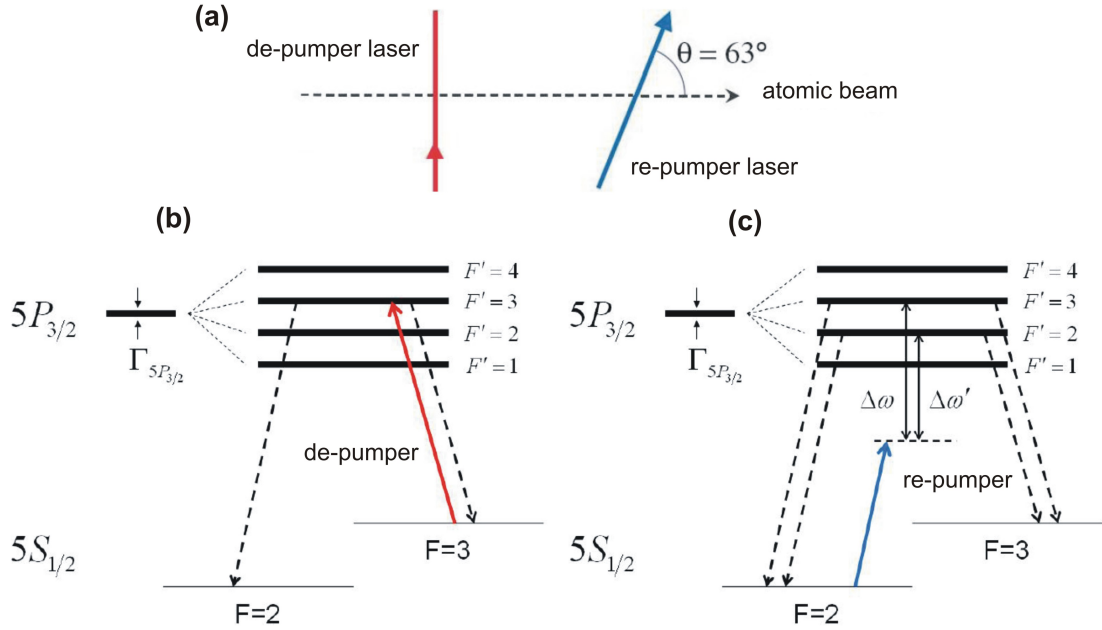


Figure I.5. Velocity selection using Doppler effect. (a) Directions of the de-pumper and re-pumper lasers relative to the atomic beam. (b) Hyperfine structure of the atomic levels. The de-pumper laser depopulates the level $|F = 3\rangle$ by pumping atoms to $|F = 2\rangle$ via $|F' = 3\rangle$. (c) The re-pumper laser brings atoms with velocity $v = \Delta\omega\lambda_{\text{rep}}/2\pi \cos\theta$ from $|F = 2\rangle$ to $|F = 3\rangle$ via $|F' = 3\rangle$. Another velocity class $v' = \Delta\omega'\lambda_{\text{rep}}/2\pi \cos\theta$ is also selected via $|F' = 2\rangle$.

The de-pumper laser, resonant with the transition $|5S_{1/2}, F = 3\rangle \longleftrightarrow |5P_{3/2}, F' = 3\rangle$, is always on. It depopulates the level $|5S_{1/2}, F = 3\rangle$ by pumping all atoms to the lower hyperfine level $|5S_{1/2}, F = 2\rangle$. The re-pumper laser, at an angle $\theta \approx 63^\circ$ to the atomic beam, is detuned by $\Delta\omega$ with respect to the transition $|5S_{1/2}, F = 2\rangle \longleftrightarrow |5P_{3/2}, F' = 3\rangle$. Due to Doppler effect, only the atoms with velocity $v = \Delta\omega\lambda_{\text{rep}}/2\pi \cos\theta$ see a laser frequency shift which compensates $\Delta\omega$. They are thus pumped to the level $|F = 3\rangle$ via $|F' = 3\rangle$. Beside this

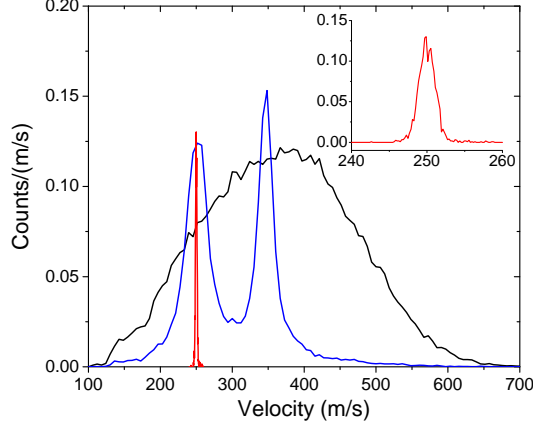


Figure I.6. Velocity distributions of the atoms. Black broad: Maxwell-Boltzmann distribution of the thermal velocity; blue double peaked: selection using Doppler effect with re-pumper laser always on; red thin (see inset): with re-pumper laser pulsed with a duration of $4 \mu\text{s}$.

velocity class, another class $v' = \Delta\omega' \lambda_{\text{rep}} / 2\pi \cos \theta$ can also be selected via $F' = 2$. The double peaked curve in Fig. I.6 shows the selected velocity classes.

The full width at half maximum (FWHM) of the velocity distribution after selection by the Doppler effect is about $\Delta v = 30 \text{ m/s}$. It leads to a longitudinal dispersion of about 3 cm at the position of the detector, which is much larger than the 6 mm hole on the detector. So we use flight time selection to further reduce the velocity dispersion. As mentioned before, the excitation laser at 780 nm is pulsed, with a typical duration of $2 \mu\text{s}$. Since the re-pumper laser is separated from this laser by about 340 mm , we can also make the re-pumper laser pulsed, with its timing adjusted such that only atoms with the selected velocity can arrive in B when the excitation process starts. The velocity distribution thus obtained around 250 m/s is shown in the inset of Fig. I.6. As an example, using a $4 \mu\text{s}$ pulse for re-pumper laser, we can obtain a velocity class of $(250 \pm 2) \text{ m/s}$, resulting in a longitudinal length of about 4 mm , which is smaller than the hole on the detector.

Atom number per sample

The preparation process of the circular states is not deterministic, i.e. the prepared atom number is not fixed. We use the term *atomic sample* to describe the atom ensemble obtained by a preparation process. The atom numbers in an atomic sample satisfies a Poisson distribution:

$$P_n = e^{-\bar{n}_{\text{at}}} \frac{\bar{n}_{\text{at}}^n}{n!}, \quad (\text{I.6})$$

with P_n denoting the probability for containing n atoms, and \bar{n}_{at} representing the average atom number in the sample.

The standard deviation of this distribution is $\sqrt{\bar{n}_{\text{at}}}$, which means that the more atoms the sample contains the broader the atom number distribution is. We usually choose a relatively weak \bar{n}_{at} , such that the probability for an atomic sample to contain more than two atoms can be neglected. The value of \bar{n}_{at} can be tuned by varying pulse duration of the re-pumper laser.

For instance, pulses with durations of $2\ \mu\text{s}$ or $4\ \mu\text{s}$ lead to $\bar{n}_{\text{at}} = 0.4$ or 0.6 with dispersions in velocity of about $2\ \text{m/s}$ or $4\ \text{m/s}$.

I.1.1.c Detection

Experimental measurements are performed by state resolved detections of the atoms. Since the Rydberg atom has a valence electron far away from the nucleus, it can be easily ionized. For instance, a static electric field on the order of $100\ \text{V/cm}$ is sufficient to ionize atoms with $n \sim 50$. Moreover, this ionization field is state dependent [44]. Detailed information concerning the detection process can be found in the thesis of Alexia Auffèves-Garnier [45]. Here we only explain briefly the operation principle of the detector.

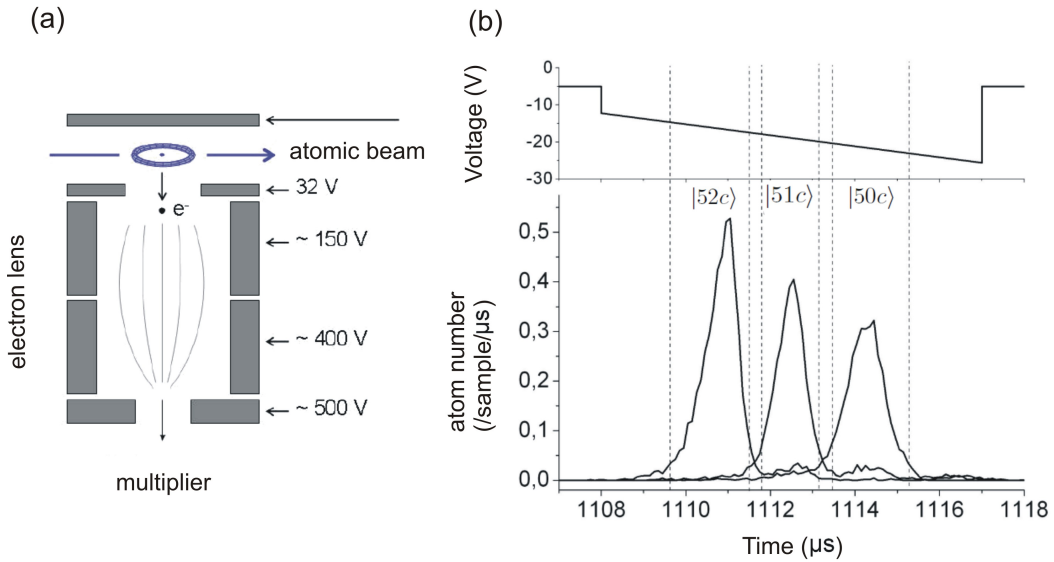


Figure I.7. State resolved detection of atoms. (a) Operation principle of the detector. A variable potential applied on one of the cathode ionizes the atoms above the hole. The free electron is then focused by the electron lens and detected by the electron multiplier. (b) Ionization signal resolving atomic states. By applying a potential ramp, the atoms with different n are ionized at different times. The three well separated circular levels are $|52c\rangle$, $|51c\rangle$, and $|50c\rangle$.

The structure of the detector and detected signals are shown in Fig. I.7. The ionization part of the detector consists of a plane cathode and an anode containing a $6\ \text{mm}$ hole. When the atom is just above the hole, a potential ramp, also known as *ionization ramp*, is applied on the cathode while the anode stays at a constant potential. The atom is then ionized, and the free electron is guided by the electron lens and eventually detected by the electron multiplier. Since the ionization electric field is state dependent, the three circular levels with $n = 50, 51, 52$ are well separated into different time windows. Summation of the atom counts in each time window defined by the dotted lines in Fig. I.7 gives us the total count of each state.

I.1.2 Theory of two-level systems

This section presents the theoretical description of a two-level system. We use the ground and excited states of the circular Rydberg atoms to denote the two levels:

$$|g\rangle \equiv |-\rangle_z \qquad |e\rangle \equiv |+\rangle_z. \quad (\text{I.7})$$

They are the eigenstates of the Hamiltonian

$$H_{\text{at}} = \frac{\hbar\omega_{\text{at}}}{2}\sigma_z, \quad (\text{I.8})$$

where ω_{at} is the angular frequency of the transition $|g\rangle \longleftrightarrow |e\rangle$ and σ_z is one of the three Pauli operators, which can be written in the matrix forms as:

$$\sigma_x = \begin{pmatrix} 0 & 1 \\ 1 & 0 \end{pmatrix} \qquad \sigma_y = \begin{pmatrix} 0 & -i \\ i & 0 \end{pmatrix} \qquad \sigma_z = \begin{pmatrix} 1 & 0 \\ 0 & -1 \end{pmatrix}. \quad (\text{I.9})$$

The three Pauli operators plus the unity operator \hat{I}_{at} constitute a basis in the operator space for two-level systems.

I.1.2.a Atomic pseudo spin and Bloch sphere

By analogy to electron spins, we can define a *atomic pseudo spin* $\mathbf{S} = \hbar\boldsymbol{\sigma}/2$, where $\boldsymbol{\sigma} = (\sigma_x, \sigma_y, \sigma_z)$, is the vector formed by Pauli matrices. This definition paves the way for depicting the quantum state of a two-level system in a geometrical representation. Consider the arbitrary pure state

$$|\psi_a\rangle = \cos\frac{\theta}{2}|e\rangle + e^{i\varphi}\sin\frac{\theta}{2}|g\rangle, \quad (\text{I.10})$$

with the two angles constrained by $0 \leq \theta \leq \pi$ and $0 \leq \varphi < 2\pi$.

As shown in Fig. I.8, $|\psi_a\rangle$ can be denoted by $|+\rangle_{\mathbf{n}}$, since the expectation value $\langle\psi_a|\boldsymbol{\sigma}|\psi_a\rangle$ is a unitary vector \mathbf{n} with (θ, ϕ) being its spherical coordinates. If the parameters θ and φ vary, the ending points of this unitary vector form a spherical surface, known as *Bloch sphere*. The unitary vector \mathbf{n} is called a *Bloch vector*. The state with the parameters $(\pi - \theta, \pi + \phi)$ is orthogonal to $|\psi_a\rangle$ and can be represented by $|-\rangle_{\mathbf{n}}$. The state pairs $|\pm\rangle_{\mathbf{n}}$ also constitute a vector basis of the Hilbert space.

Now let us consider the evolution of state $|\psi_a\rangle$ under the Hamiltonian (I.8). After simple calculations we obtain the evolving state:

$$|\psi_a(t)\rangle = e^{-i\omega_{\text{at}}t/2} \left(\cos\frac{\theta}{2}|e\rangle + e^{i(\varphi+\omega_{\text{at}}t)}\sin\frac{\theta}{2}|g\rangle \right). \quad (\text{I.11})$$

This shows a picture of *Larmor precession* of the atomic pseudo spin around the quantization axis z .

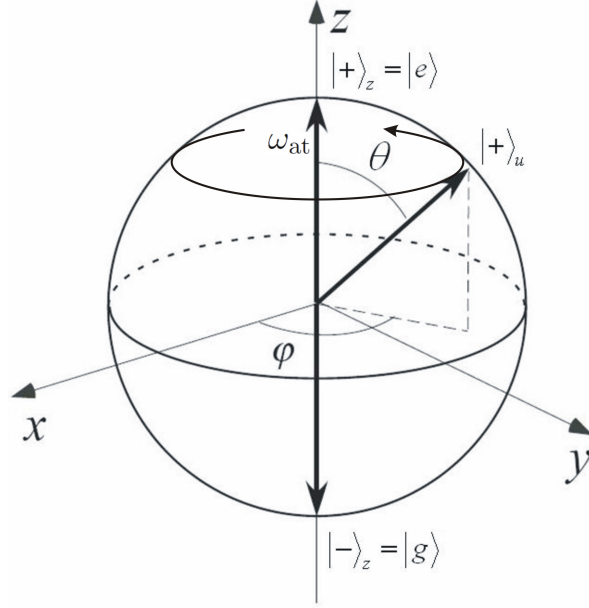


Figure I.8. Bloch sphere representation of the states of a two-level system

I.1.2.b Manipulation of atomic states

The two states $|e\rangle$ and $|g\rangle$ have opposite parities. In the Hilbert space spanned by the basis $\{|e\rangle, |g\rangle\}$, the odd parity electric dipole operator $\mathbf{D} = q\mathbf{R}$ is purely non-diagonal and can be expressed as [40]:

$$\mathbf{D} = d(\epsilon_a \sigma_- + \epsilon_a^* \sigma_+), \quad (\text{I.12})$$

with d being the *dipole matrix element* of the atomic transition (assumed to be real without loss of generality), ϵ_a being the unit vector describing the polarization of the atomic transition, and the atomic raising and lowering operators σ_{\pm} defined as:

$$\sigma_+ = |e\rangle\langle g| \quad \sigma_- = |g\rangle\langle e|. \quad (\text{I.13})$$

Let \mathbf{u}_x , \mathbf{u}_y , \mathbf{u}_z denote respectively the unitary vectors along the axes $\mathbf{O}x$, $\mathbf{O}y$ and $\mathbf{O}z$ in real space, then we have $\epsilon_a = (\mathbf{u}_x \pm i\mathbf{u}_y)/\sqrt{2}$ for a σ^{\pm} -polarized transition, and $\epsilon_a = \mathbf{u}_z$ for a π -polarized transition.

The interaction Hamiltonian of the dipole with a classical electric field \mathbf{E}_r is given by

$$H_r = -\mathbf{D} \cdot \mathbf{E}_r(t), \quad (\text{I.14})$$

where

$$\mathbf{E}_r(t) = i\mathcal{E}_r \left(\epsilon_r e^{-i(\omega_r t + \varphi_0)} + \epsilon_r^* e^{i(\omega_r t + \varphi_0)} \right), \quad (\text{I.15})$$

with \mathcal{E}_r , ω_r and ϵ_r representing respectively the amplitude, angular frequency and polarization of the electric field. By considering the problem in a reference frame rotating at ω_r , and making a secular approximation which neglects the fast rotating terms, the Hamiltonian (I.14) becomes time-independent and can be expressed as:

$$\tilde{H} = \frac{\hbar\Delta_r}{2}\sigma_z - i\frac{\hbar\Omega_r}{2} [e^{-i\varphi_0}\sigma_+ - e^{i\varphi_0}\sigma_-], \quad (\text{I.16})$$

where $\Delta_r = \omega_{\text{at}} - \omega_r$, is the atom-field frequency detuning, Ω_r is the classical Rabi frequency, which is assumed, without loss of generality, to be real and takes the form

$$\Omega_r = \frac{2d}{\hbar} \mathcal{E}_r \boldsymbol{\epsilon}_a^* \cdot \boldsymbol{\epsilon}_r. \quad (\text{I.17})$$

After substituting the expressions $\sigma_{\pm} = (\sigma_x \pm i\sigma_y) / \sqrt{2}$ into the Hamiltonian (I.16), we can show that it reads:

$$\tilde{H} = \frac{\hbar\Omega'_r}{2} \boldsymbol{\sigma} \cdot \mathbf{n}. \quad (\text{I.18})$$

By analogy with the Hamiltonian (I.8), we can identify Ω'_r as an effective precession frequency and \mathbf{n} as a unitary vector on the Bloch sphere along the axis of precession. They are given by

$$\Omega'_r = \sqrt{\Omega_r^2 + \Delta_r^2}, \quad \mathbf{n} = \frac{1}{\Omega'_r} [\Delta_r \mathbf{e}_z + \Omega_r (-\sin \varphi_0 \mathbf{e}_x + \cos \varphi_0 \mathbf{e}_y)]. \quad (\text{I.19})$$

Note that:

- if $\Omega_r = 0$, then $\mathbf{n} = \mathbf{e}_z$,
- if $\Delta_r = 0$, then \mathbf{n} is in the equatorial plane of the Bloch sphere, and $\Omega'_r = \Omega_r$.

In the second case, it is the phase of electric field φ_0 that determines the precession axis \mathbf{n} . An example of this precession with $\varphi_0 = 0$ is given in Fig. I.9.

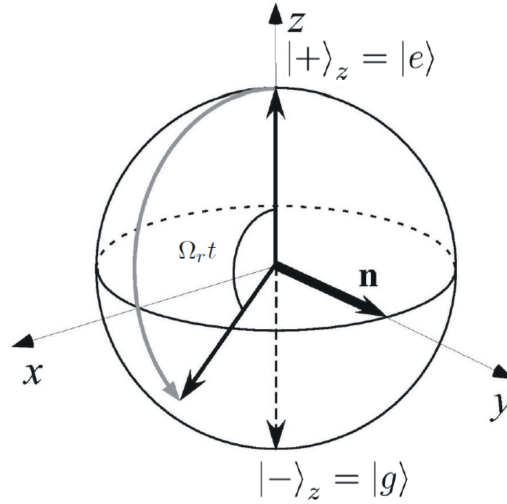


Figure I.9. Manipulation of atomic states. In the presence of a resonant oscillating electric field, the atomic state can be rotated continuously from $|e\rangle$ to a superposition state $(|e\rangle + e^{i\varphi_0}|g\rangle) / \sqrt{2}$, then to $|g\rangle$. The phase φ_0 determines the rotation axis \mathbf{n} . The rotation “speed” is the classical Rabi frequency Ω_r .

Consider that an atom initially in state $|e\rangle$ or $|g\rangle$ interacts with a resonant oscillating electric field during a time t which satisfies the condition

$$\Omega_r t = \pi/2. \quad (\text{I.20})$$

Then the Bloch vector is rotated to the equatorial plane, and the corresponding state is a superposition of $|e\rangle$ and $|g\rangle$ with equal probabilities:

$$|e\rangle \longrightarrow \frac{1}{\sqrt{2}} (|e\rangle + e^{i\varphi_0}|g\rangle) \quad |g\rangle \longrightarrow \frac{1}{\sqrt{2}} (-e^{-i\varphi_0}|e\rangle + |g\rangle). \quad (\text{I.21})$$

In the following, this elementary manipulation of atomic states is called as $\pi/2$ pulse. Similarly, the interaction with time $2t$ realizing the following transformations:

$$|e\rangle \longrightarrow e^{i\varphi_0}|g\rangle \quad |g\rangle \longrightarrow -e^{-i\varphi_0}|e\rangle, \quad (\text{I.22})$$

is called a π pulse.

I.1.2.c Ramsey interferometer

The scheme of a Ramsey interferometer is shown in Fig. I.10, with R_1 and R_2 denoting the two Ramsey zones where $\pi/2$ pulses are applied.

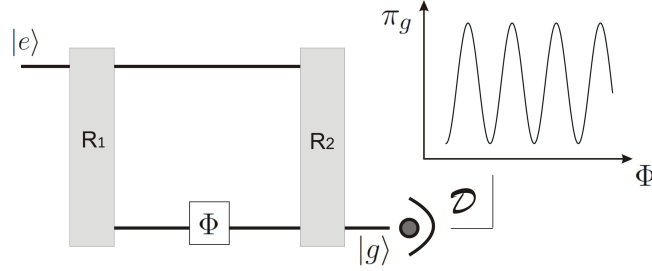


Figure I.10. Scheme of the Ramsey interferometer. R_1 and R_2 denote the two Ramsey zones where $\pi/2$ pulses are applied. \mathcal{D} is a state resolved detector. The oscillating signal shows the probability for detecting state $|g\rangle$ as a function of the phase shift Φ .

The first $\pi/2$ pulse in R_1 transfers the atom from state $|e\rangle$ to a superposition state

$$|e\rangle \longrightarrow \frac{1}{\sqrt{2}} (|e\rangle + |g\rangle). \quad (\text{I.23})$$

On the path to R_2 , a phase shift element changes the atomic state to

$$\frac{1}{\sqrt{2}} (|e\rangle + e^{i\Phi}|g\rangle). \quad (\text{I.24})$$

Another $\pi/2$ pulse in R_2 at a phase ϕ_r relative to that of the first one transforms the atomic state to

$$\frac{1}{2} \left[\left(1 - e^{i(\phi_r - \Phi)}\right) |e\rangle + e^{i\Phi} \left(1 + e^{i(\phi_r - \Phi)}\right) |g\rangle \right]. \quad (\text{I.25})$$

The probabilities for detecting $|e\rangle$ or $|g\rangle$ are then given by

$$\pi_g(\Phi, \phi_r) = \frac{1}{2} + \frac{1}{2} \cos(\phi_r - \Phi) \quad \pi_e(\Phi, \phi_r) = \frac{1}{2} - \frac{1}{2} \cos(\phi_r - \Phi). \quad (\text{I.26})$$

First, consider the case with $\phi_r = 0$, in which the probabilities for π_g and π_e are oscillating functions depending only on Φ . These oscillations can be seen as an atomic interference

process, since there are two indistinguishable quantum paths leading the atom from the initial to the final state. As an example, for the detected state $|g\rangle$, the atom may be transferred to the state $|g\rangle$ either in R_1 or in R_2 . To obtain the final probability we must sum the two corresponding amplitudes. The Ramsey fringes appear as a result of the interference between these two amplitudes.

Secondly, consider the situation with $\Phi = 0$. The expressions (I.25) then lead to oscillating functions of ϕ_r . In this situation, the oscillating probabilities for observing the atomic states are obtained by varying the *observation axis* defined by ϕ_r . Varying ϕ_r can be achieved by using two microwave sources for R_1 and R_2 with well controlled tunable phase differences. But this is not convenient in practice. In fact, in experiments we use the same microwave source for R_1 and R_2 and scan its frequency. This technique is effectively equivalent to varying ϕ_r , as explained in the following.

Suppose that the microwave at frequency ω_r is on resonance with the atom. It implements a $\pi/2$ pulse in R_1 and prepares a superposition state according to the transformation (I.23). Once the microwave field is switched off, the atomic state evolves under the Hamiltonian (I.8) and stays still in the reference frame rotating at ω_r , since $\omega_{\text{at}} = \omega_r$. Nevertheless, if ω_r is slightly changed such that $\Delta_r = \omega_{\text{at}} - \omega_r \neq 0$, but the resonant condition is still satisfied, i.e.:

$$|\Delta_r| \ll \Omega_r, \quad (\text{I.27})$$

the atomic state then rotates at the angular frequency Δ_r . After a flight time T_f , the atom arrives at R_2 , and the phase of the microwave source has accumulated a difference $\phi_r = -\Delta_r T_f$ with respect to that of the atomic coherence. Hence, the second $\pi/2$ pulse is effectively applied with a different phase from that of the first one.

This method is constrained by the condition (I.27), which guarantees the implementation of the two $\pi/2$ pulses. In fact, this requirement can be easily fulfilled in our experiments. The two Ramsey zones R_1 and R_2 are separated by 9 cm, which leads to a flight time $T_f = 360 \mu\text{s}$ for atoms with a velocity 250 m/s. A detuning $\Delta_r = 2.8 \text{ kHz}$ is sufficient for accumulating a phase of 2π . By contrast, the classical Rabi frequency Ω_r is about 125 kHz. Thus the condition in (I.27) can be easily satisfied.

I.2 Photons in cavity

A cavity confining several quanta of an electromagnetic field is an experimental realization of the ‘‘photon box’’ used in the *gedanken* experiments for illustrating the fundamental principles of quantum mechanics in its early days. Nowadays, very high Q cavities which can confine microwave field by up to 0.1 s already exist [46] and have been used to study the quantum nature of light. In this section, we first give some detailed information about the cavity we use, then present the theoretical descriptions of a quantized field and its coupling to the environment.

I.2.1 The high finesse Fabry-Pérot cavity

We use a cavity in the Fabry-Pérot configuration to isolate a mode of electromagnetic field in the microwave range. The mode should have a frequency close to that of the two-level atoms and a lifetime long enough for reaching the strong coupling regime. To achieve these, the geometry, material and fabrication method of mirrors need to be carefully optimized.

Geometrical parameters

The geometrical structure of the cavity and individual mirrors are shown in Fig. I.11. In the paraxial approximation, the modes of a spherical Fabry-Pérot cavity can be calculated. Particulary, the mode TEM_{q00} , which has q antinodes between the two mirrors and a Gaussian transverse profile has a frequency

$$\nu_q = \frac{c}{2d} \left(q + \frac{1}{\pi} \arccos \left(1 - \frac{d}{R} \right) \right), \quad (\text{I.28})$$

with c , d , and R being the speed of light in vacuum, distance between the two mirror centers and the radius of curvature of the mirror surface, respectively.

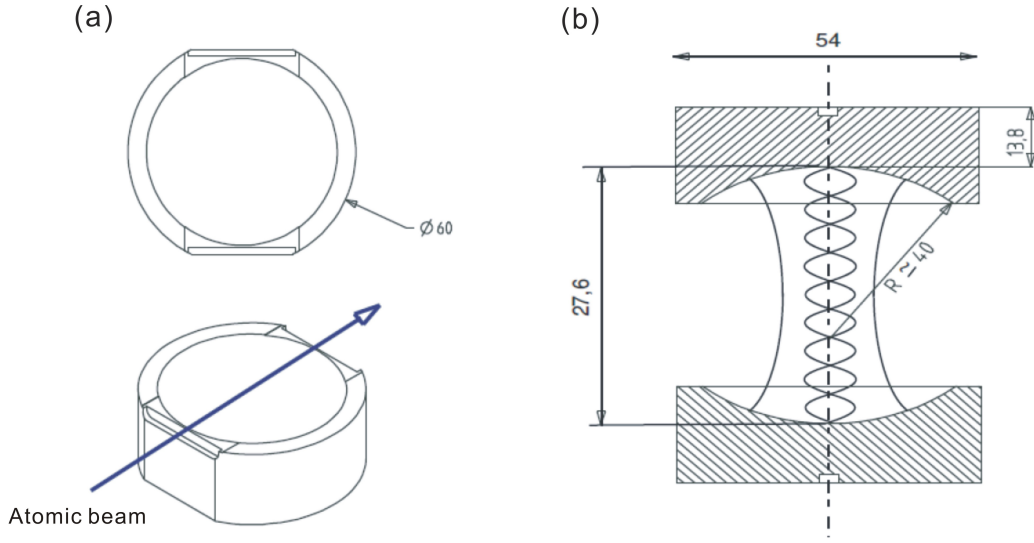


Figure I.11. Geometrical parameters of the cavity and mirrors. (a) Top and side view of a mirror. (b) Cavity scheme and the TEM_{900} mode of the microwave field. The values in the figure are in unit of millimeter.

The mode that we use has $q = 9$, which corresponds to a frequency of 51.1 GHz. The electric field of this mode has a cylindrical symmetry with respect to the cavity axis z , and is given by

$$\mathcal{E}_0(\mathbf{r}) = \mathcal{E}_0(r, z) \equiv \mathcal{E}_0 f(r, z), \quad (\text{I.29})$$

with $f(r, z)$ being the *spatial profile of the mode*, which can be expressed in the cylindrical coordinates as

$$f(r, z) = \frac{w_0}{w(z)} \cos \left(kz - \arctan \left(\frac{\lambda z}{\pi w_0^2} \right) + \frac{r^2 k}{2R(z)} \right) e^{-\frac{r^2}{w(z)^2}}, \quad (\text{I.30})$$

where $\lambda = c/\nu = 5.87$ mm is the wavelength, and $k = 2\pi/\lambda$ is the wavenumber. The waist of the mode is given by

$$w_0 = \left(\frac{\lambda}{2\pi} \sqrt{d(2R - d)} \right)^{1/2} \approx 5.96 \text{ mm}. \quad (\text{I.31})$$

The radius of curvature and mode width vary as position changes. This dependence is given by

$$R(z) = z \left[1 + \left(\frac{\pi w_0^2}{\lambda z} \right)^2 \right] \quad w(z) = w_0 \sqrt{1 + \left(\frac{\lambda z}{\pi w_0} \right)^2}. \quad (\text{I.32})$$

We can also deduce the volume of the mode:

$$\mathcal{V} = \int |f(\mathbf{r})|^2 d^3\mathbf{r} = \frac{\pi w_0^2 d}{4} \simeq 769 \text{ mm}^3, \quad (\text{I.33})$$

and the amplitude of electric field associated to one photon:

$$\mathcal{E}_0 = \sqrt{\frac{\hbar \omega_c}{2\epsilon_0 \mathcal{V}}} \simeq 1.5 \cdot 10^{-3} \text{ V/m}. \quad (\text{I.34})$$

We see that strong confinement of the field results in a large electric field even for a single photon.

The theoretical analysis above is based on spherical mirrors, whose cylindrical symmetry about the axis z results in the frequency degeneracy of two linear polarization modes being perpendicular to each other and labeled as x and y . However, in practice, machining of the mirror surface can hardly achieve a perfect spherical geometry. In this situation, the two modes x and y have slightly different frequencies, which can both couple to the atoms. In order to avoid the simultaneous coupling of atoms to two cavity modes, it is better to purposely break the frequency degeneracy of the two modes and make them far away from each other (much farther than the cavity-atom coupling strength). Based on this argument, the mirrors used for our cavity actually have two slightly different radii of curvature along the axis x and y , such that the two modes are separated by about 1.26 MHz.

High finesse

The mirror substrate is made from copper, which can be machined to have a very smooth surface. On its surface, a 12 μm thick Niobium layer is deposited by cathode sputtering [47]. Niobium becomes superconducting below 9 K, such that the surface loss of the mode is eventually reduced.

The cavity used in current experiments has a lifetime of $T_{\text{cav}} = 65 \text{ ms}$ for the TEM_{900} mode. This value is linked to the spectral width $\delta\nu$ by [48]

$$2\pi\delta\nu T_{\text{cav}} = 1. \quad (\text{I.35})$$

So the width of the cavity spectrum is about $\delta\nu = 2.5 \text{ Hz}$ as shown Fig. I.12. Correspondingly the Q factor and finesse of the cavity are:

$$Q = \nu/\delta\nu = 2.1 \cdot 10^{10} \quad \mathcal{F} = Q/q = 2.3 \cdot 10^9. \quad (\text{I.36})$$

Control of cavity frequency

In experiments, the frequency of the cavity mode needs to be finely tuned and precisely controlled. This is achieved by four piezoelectric transducer (PZT) tubes mounted at the corners of the cavity block, as shown in panel (a) of Fig. I.13. By applying a voltage difference on the PZT tubes, we slightly change the distance between the two mirrors, and thus the frequency of the cavity mode. As displayed in panel (b) of Fig. I.13, the voltage-frequency conversion is about 2.4 kHz/V. With a high voltage source that goes up to 2000 V, we can tune the cavity frequency by about $\pm 5 \text{ MHz}$ with a precision of 2.4 kHz.

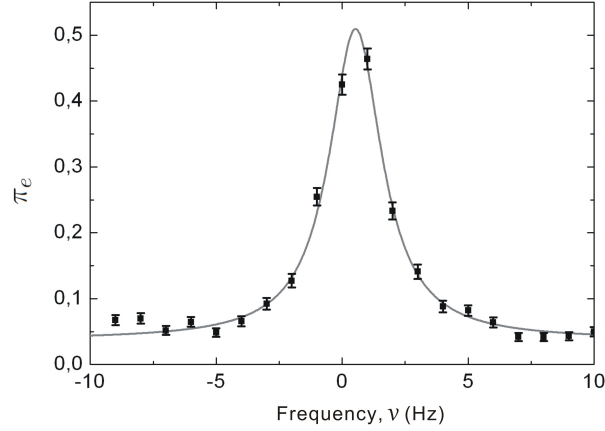


Figure I.12. Spectrum of the cavity mode (a value $\nu_0 \simeq 51.1$ GHz is taken as the frequency origin in the figure). The cavity is fed by a microwave field at the frequency ν . The atoms prepared in state $|g\rangle$ pass through the cavity and interact resonantly with the microwave field. The probability for transferring to state $|e\rangle$ is plotted (solid squares) and fitted using a Lorentz distribution. The FWHM $\delta\nu$ is about 2.5 Hz.

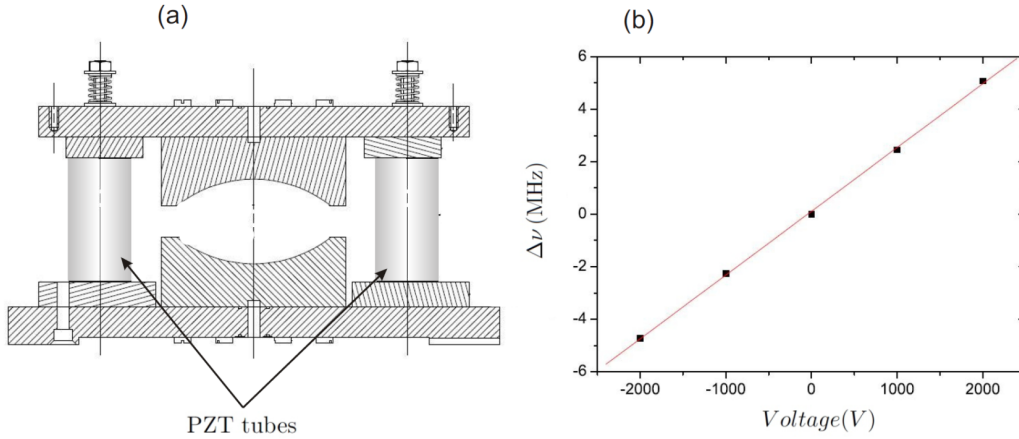


Figure I.13. Mounts of PZT tubes and adjustment of cavity frequency. (a) PZT tubes are mounted between the two plates holding the mirrors. (b) Variation of cavity frequency as a function of the voltage difference on the PZT tubes.

I.2.2 Theoretical description

I.2.2.a A quantized field

The high Q cavity confines a mode of the electromagnetic field at frequency ω_c . This quantized field can be described by the Hamiltonian of a harmonic oscillator [49]:

$$H_c = \hbar\omega_c \left(a^\dagger a + \frac{1}{2} \right) \equiv \hbar\omega_c \left(\hat{N} + \frac{1}{2} \right). \quad (\text{I.37})$$

Here we have introduced the *annihilation* and *creation* operators, a and a^\dagger , being the Hermitian conjugates of each other. $\hat{N} = a^\dagger a$ is the *photon number operator*, whose eigenstates are

the *photon number states* $|n\rangle$, also known as *Fock states*. These states are also the eigenstates of the Hamiltonian (I.37). The operators introduced above have the following properties:

$$a|n\rangle = \sqrt{n}|n-1\rangle \quad a^\dagger|n\rangle = \sqrt{n+1}|n+1\rangle \quad \hat{N}|n\rangle = n|n\rangle. \quad (\text{I.38})$$

Let us also introduce the eigenstate of the annihilation operator a , denoted as $|\alpha\rangle$ [50], which satisfies the relationship

$$a|\alpha\rangle = \alpha|\alpha\rangle. \quad (\text{I.39})$$

The state $|\alpha\rangle$ describes a *coherent* field and can be expressed as

$$|\alpha\rangle = e^{-\frac{|\alpha|^2}{2}} \sum_{n \geq 0} \frac{\alpha^n}{\sqrt{n!}} |n\rangle, \quad (\text{I.40})$$

with the average photon number given by

$$\langle \hat{N} \rangle = \langle \alpha | \hat{N} | \alpha \rangle = |\alpha|^2. \quad (\text{I.41})$$

The photon number distribution $P(n)$ in a coherent field $|\alpha\rangle$ obeys the Poisson distribution:

$$P(n) = |\langle n | \alpha \rangle|^2 = e^{-|\alpha|^2} \frac{|\alpha|^{2n}}{n!}. \quad (\text{I.42})$$

Let us also introduce the electric field operator

$$\hat{\mathbf{E}}(\mathbf{r}) = \mathcal{E}_0(\mathbf{r}) (\boldsymbol{\epsilon} a + \boldsymbol{\epsilon}^* a^\dagger), \quad (\text{I.43})$$

with $\boldsymbol{\epsilon}$ denoting its polarization and $\mathcal{E}_0(\mathbf{r}) = \mathcal{E}_0 f(\mathbf{r})$ being its amplitude.

The evolution of a coherent field in the Hamiltonian (I.37) leads to

$$|\alpha(t)\rangle = e^{-i\frac{\omega_c t}{2}} |\alpha e^{-i\omega_c t}\rangle. \quad (\text{I.44})$$

We see that the state remains coherent, but the complex amplitude rotates at the frequency of the field. The average electromagnetic field in this state evolves exactly in the same way as its classical counterpart. This can be easily verified by evaluating $\hat{\mathbf{E}}(\mathbf{r})$ in $|\alpha(t)\rangle$.

I.2.2.b Coupling to the environment

The electromagnetic field confined in the cavity is not an isolated system. The surrounding environment at 0.8 K serves as a big reservoir, which can exchange energy with the cavity field. Due to this effect, a field in the cavity relaxes and eventually reaches a thermal equilibrium state.

In an equilibrium thermal field at temperature T , the mode at frequency ω_c has a photon number distribution given by the Bose-Einstein statistics:

$$P_{\text{th}}(n) = \frac{1}{e^{n\hbar\omega_c/k_B T} - 1}, \quad (\text{I.45})$$

with k_B being the Boltzmann constant and \hbar being the reduced Planck constant. The average photon number is

$$n_{\text{th}} = \frac{1}{e^{\hbar\omega_c/k_B T} - 1}. \quad (\text{I.46})$$

At the frequency of the cavity mode $\omega_c = 2\pi \times 51.1$ GHz, $n_{\text{th}} \simeq 0.05$ at $T = 0.8$ K.

The *master equation* governing the evolution of the field can be expressed in the Lindblad form [40]:

$$\frac{d\rho}{dt} = -\frac{i}{\hbar} [H, \rho] + \mathbf{L}\rho, \quad (\text{I.47})$$

$$\mathbf{L}\rho = \sum_{\mu=\{+,-\}} \left(L_{\mu}\rho L_{\mu}^{\dagger} - \frac{1}{2}L_{\mu}^{\dagger}L_{\mu}\rho - \frac{1}{2}\rho L_{\mu}^{\dagger}L_{\mu} \right), \quad (\text{I.48})$$

with the jump operators describing the gain or loss of one photon defined as

$$L_{+} = \sqrt{\kappa_{+}}a^{\dagger} \quad L_{-} = \sqrt{\kappa_{-}}a. \quad (\text{I.49})$$

The first term in (I.47), corresponding to the unitary evolution under the Hamiltonian H , can be removed by switching to an interaction representation with respect to H . In this representation, the relaxation term remains unchanged. The evolution of the field from time t to $t + dt$ can be expressed as

$$\rho(t + dt) = (\mathbb{1} + dt\mathbf{L})\rho(t). \quad (\text{I.50})$$

The probabilities per unit time for a quantum jump to occur are given by

$$\begin{aligned} p_{+} &= \text{Tr} \left(L_{+}^{\dagger}L_{+}\rho \right) = \kappa_{+}\text{Tr} \left(aa^{\dagger}\rho \right) = \kappa_{+}(1 + \langle \hat{N} \rangle) \\ p_{-} &= \text{Tr} \left(L_{-}^{\dagger}L_{-}\rho \right) = \kappa_{-}\text{Tr} \left(a^{\dagger}a\rho \right) = \kappa_{-}\langle \hat{N} \rangle. \end{aligned} \quad (\text{I.51})$$

At thermal equilibrium, these two probabilities should be equal, leading to:

$$\frac{\kappa_{+}}{\kappa_{-}} = \frac{n_{\text{th}}}{n_{\text{th}} + 1} \simeq 0.05, \quad (\text{I.52})$$

which tells that the field has a probability for losing one photon about 20 times larger than that of gaining one photon. Furthermore, we can introduce the notation κ for *relaxation rate*, and express the rate for gaining or losing one photon as

$$\kappa_{+} = n_{\text{th}}\kappa \quad \kappa_{-} = (1 + n_{\text{th}})\kappa. \quad (\text{I.53})$$

Substituting (I.53) into (I.48) and (I.50), we can evaluate the effect of field relaxation on $P(n)$ and obtain the rate equation:

$$\begin{aligned} \frac{dP(n)}{dt} &= \kappa(1 + n_{\text{th}})(n + 1)P(n + 1) \\ &\quad - [\kappa(1 + n_{\text{th}})n + \kappa n_{\text{th}}(n + 1)]P(n) \\ &\quad + \kappa n_{\text{th}}nP(n - 1). \end{aligned} \quad (\text{I.54})$$

After simple calculations, we also obtain the evolution of the average photon number $\langle \hat{N} \rangle = \sum_{n \geq 0} nP(n)$:

$$\frac{d\langle \hat{N} \rangle}{dt} = -\kappa \left(\langle \hat{N} \rangle - n_{\text{th}} \right). \quad (\text{I.55})$$

Consider the situation with $T = 0$, which leads to $n_{\text{th}} = 0$. The equation (I.55) tells that the average photon number decays exponentially with a rate κ , which is related to the lifetime of the cavity mode by $T_{\text{cav}} = 1/\kappa$. From the equation (I.54), we see that the decay rate of a Fock state $|n\rangle$ is $n\kappa$, giving rise to a lifetime T_{cav}/n .

I.3 Coupling the two systems

In the previous sections, we presented separately the circular Rydberg atoms as two-level systems and the photon field confined in a high Q cavity as a harmonic oscillator. Now let us combine the two systems and consider their interactions. We first introduce the Jaynes-Cummings model, then discuss the resonant and dispersive interactions. Afterwards, we explain the principle of the *rapid adiabatic passage*, which is used in experiments.

Jaynes-Cummings model

The Hamiltonian describing the coupled atom-field system includes three terms:

$$H = H_{\text{cav}} + H_{\text{at}} + H_{\text{int}}, \quad (\text{I.56})$$

with H_{cav} and H_{at} being the free uncoupled Hamiltonians of the field and the atoms. The interaction term can be written as

$$\begin{aligned} H_{\text{int}} &= -\mathbf{D} \cdot \hat{\mathbf{E}}(\mathbf{r}) \\ &= -d\mathcal{E}_0(\mathbf{r}) (\epsilon_a \sigma_- + \epsilon_a^* \sigma_+) \cdot (\epsilon a + \epsilon^* a^\dagger) \\ &= -d\mathcal{E}_0(\mathbf{r}) \left(\epsilon_a \epsilon^* \sigma_- a^\dagger + \epsilon_a^* \epsilon \sigma_+ a + \epsilon_a \epsilon \sigma_- a + \epsilon_a^* \epsilon^* \sigma_+ a^\dagger \right). \end{aligned} \quad (\text{I.57})$$

We see that H_{int} includes four possible processes, with the first two being atomic level moving down by emitting and moving up by absorbing one photon. In the situation $\omega_{\text{at}} \sim \omega_c$, these two terms dominate over the other two, which can thus be neglected. This is essentially equivalent to making a rotating wave approximation in the case of a classical field [40], as mentioned in paragraph I.1.2.b. After making this approximation, H_{int} can be written as

$$H_{\text{int}} = \frac{\hbar \Omega_0(\mathbf{r})}{2} (\sigma_+ a + \sigma_- a^\dagger), \quad (\text{I.58})$$

with

$$\Omega_0(\mathbf{r}) = -\frac{2d\mathcal{E}_0 \epsilon_a \cdot \epsilon}{\hbar} f(\mathbf{r}) \equiv \Omega_0 f(\mathbf{r}), \quad (\text{I.59})$$

where $f(\mathbf{r})$ denotes the profile of the cavity field amplitude, and Ω_0 is the frequency of *vacuum Rabi oscillations* characterizing the coupling strength of the two systems.

The total Hamiltonian (I.56) can then be expressed in the Jaynes-Cummings form:

$$H_{\text{JC}} = \frac{\hbar \omega_{\text{at}}}{2} \sigma_z + \hbar \omega_c \left(a^\dagger a + \frac{1}{2} \right) + \frac{\hbar \Omega_0}{2} (\sigma_+ a + \sigma_- a^\dagger) f(\mathbf{r}). \quad (\text{I.60})$$

This Hamiltonian couples the states $|e, n\rangle$ with $|g, n+1\rangle$ ($n \geq 0$), and the subspace $\mathcal{S}_n = \{|e, n\rangle, |g, n+1\rangle\}$ remains closed¹. In the subspace \mathcal{S}_n , H_{JC} can be expressed in the matrix form:

$$H_n = \hbar \begin{pmatrix} \omega_c(n+1) + \delta/2 & \Omega_n f(\mathbf{r})/2 \\ \Omega_n f(\mathbf{r})/2 & \omega_c(n+1) - \delta/2 \end{pmatrix}, \quad (\text{I.61})$$

¹The state $|g, 0\rangle$ does not couple to any other states.

with $\delta = \omega_{\text{at}} - \omega_c$ being the atom-field frequency detuning, and

$$\Omega_n = \Omega_0 \sqrt{n+1} \quad (\text{I.62})$$

being the Rabi frequency of the oscillation $|e, n\rangle \longleftrightarrow |g, n+1\rangle$.

At the center of the cavity mode, $f(\mathbf{r}) = 1$, and the eigenstates of H_n can then be expressed as:

$$|+, n\rangle = \cos \frac{\Theta_n}{2} |e, n\rangle + \sin \frac{\Theta_n}{2} |g, n+1\rangle \quad (\text{I.63})$$

$$|-, n\rangle = \sin \frac{\Theta_n}{2} |e, n\rangle - \cos \frac{\Theta_n}{2} |g, n+1\rangle. \quad (\text{I.64})$$

with the angle Θ_n defined by

$$\tan \Theta_n = \frac{\Omega_n}{\delta}, \quad (\text{I.65})$$

and constrained by $0 \leq \Theta_n < \pi$. These states are called the *dressed states* of the atom-field system, and their corresponding eigenenergies are

$$E_{\pm, n} = \hbar\omega_c(n+1) \pm \frac{\hbar}{2} \sqrt{\Omega_n^2 + \delta^2}. \quad (\text{I.66})$$

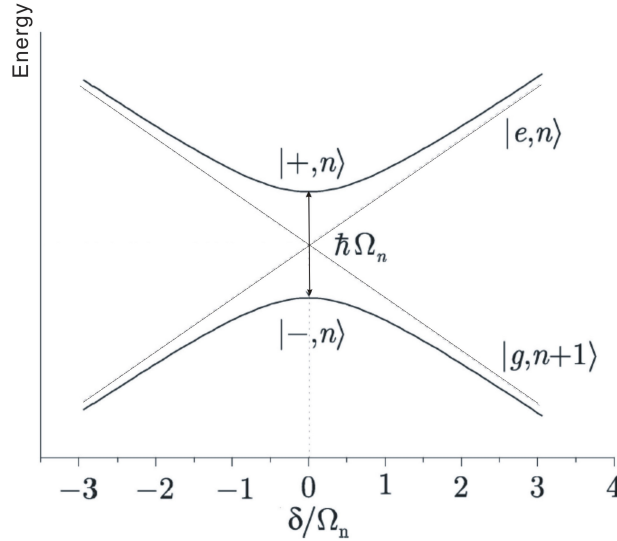


Figure I.14. Energies of dressed states as functions of the ratio between detuning and Rabi frequency

Figure I.14 shows $E_{\pm, n}$ as functions of the ratio between detuning and Rabi frequency. From the energy spectrum, we can identify two regimes of the atom-field interaction. One is the *dispersive regime*² with $|\delta| \gg \Omega_n$, in which the uncoupled bare states remain good approximations of the dressed states. The other is the *resonant regime* with $\delta = 0$, in which the degeneracy of the bare states is lifted by the coupling Hamiltonian, resulting in an energy gap given by the Rabi frequency Ω_n between the two dressed states. We discuss in more detail these two regimes in the following paragraphs.

²More precisely, the far detuned dispersive regime.

I.3.1 Resonant regime

In the resonant regime, $\delta = 0$, then the Hamiltonian (I.61) reduces to

$$H_n = \hbar\omega_c(n+1) + \frac{\hbar\Omega_n}{2} \begin{pmatrix} 0 & 1 \\ 1 & 0 \end{pmatrix}. \quad (\text{I.67})$$

This Hamiltonian is effectively the same as that given by (I.18) after setting $\mathbf{n} = \mathbf{e}_x$, $\Omega'_r = \Omega_n$ and making the following analogy:

$$|e\rangle \longrightarrow |e, n\rangle \quad (\text{I.68})$$

$$|g\rangle \longrightarrow |g, n+1\rangle. \quad (\text{I.69})$$

We can thus conclude that H_n describes a quantum Rabi oscillation between $|e, n\rangle$ and $|g, n+1\rangle$ with the frequency Ω_n . Consider the evolution of the coupled state $|e, n\rangle$. After omitting a global phase factor, the state at time t can be written as

$$|\psi_{ac}(t)\rangle = \cos\left(\frac{\Omega_n t}{2}\right) |e, n\rangle - i \sin\left(\frac{\Omega_n t}{2}\right) |g, n+1\rangle, \quad (\text{I.70})$$

leading to the probability for detecting the atomic state $|g\rangle$:

$$\pi_g(t) = \frac{1}{2} [1 - \cos(\Omega_n t)]. \quad (\text{I.71})$$

Figure I.15 shows these oscillations in different photon number states, using $\Omega_0/2\pi = 46$ kHz which is close to the measured value in our setup.

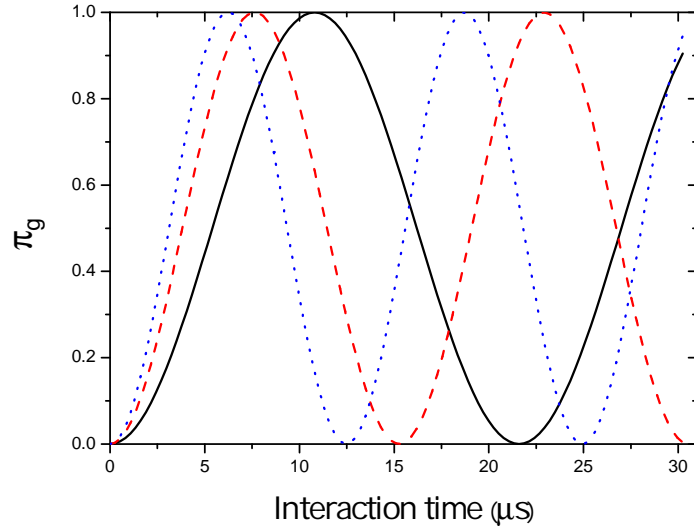


Figure I.15. Quantum Rabi oscillations in different photon number states $|n\rangle$. The photon numbers are $n = 0$ (black solid), 1 (red dashed), and 2 (blue dotted). The atom is prepared in the state $|e\rangle$ before entering the cavity.

I.3.2 Dispersive regime

In the far detuned dispersive regime, $|\delta| \gg \Omega_n$, the interaction term H_{int} can be treated in a perturbative way. The bare states remain good approximations³ of the dressed states:

$$|+, n\rangle \simeq |e, n\rangle \quad \text{and} \quad |-, n\rangle \simeq |g, n+1\rangle \quad \text{if } \delta > 0 \quad (\text{I.72})$$

$$|+, n\rangle \simeq |g, n+1\rangle \quad \text{and} \quad |-, n\rangle \simeq |e, n\rangle \quad \text{if } \delta < 0, \quad (\text{I.73})$$

but the corresponding energies are modified:

$$\begin{aligned} E_{e,n} &= E_{e,n}^0 + \frac{\hbar\Omega_0^2}{4\delta}(n+1) \\ E_{g,n+1} &= E_{g,n+1}^0 - \frac{\hbar\Omega_0^2}{4\delta}(n+1), \end{aligned} \quad (\text{I.74})$$

where the notations with the superscript “0” correspond to the energies of the unperturbed bare states. The energy shift with respect to that of the unperturbed bare state is called a *light shift*.

In fact, the energy shift can be described by an effective Hamiltonian⁴ with the bare states as eigenstates:

$$H_{\text{JC}}^{\text{disp}} = H_{\text{cav}} + \frac{\hbar}{2} \left[\omega_{\text{at}} + \frac{\Omega_0^2}{2\delta} \left(a^\dagger a + \frac{1}{2} \right) \right] \sigma_z. \quad (\text{I.75})$$

The second term in $H_{\text{JC}}^{\text{disp}}$ can be considered as an energy shift either to the field state or to the atomic state. If we consider it as an energy shift to the atomic state, then the atomic frequency ω_{at} is shifted by

$$\Delta\omega_{\text{at}}(n) = \frac{\Omega_0^2}{2\delta} \left(n + \frac{1}{2} \right), \quad (\text{I.76})$$

with n denoting the photon number of the field, and the term $1/2$ describing the light shift due to the vacuum field, i.e. the *Lamb shift*.

Due to these light shifts, the interaction with the photon state $|n\rangle$ during time t_{int} leads to a phase shift on the atomic coherence:

$$\Delta\omega_{\text{at}}(n)t_{\text{int}} = \phi_0 \left(n + \frac{1}{2} \right) \equiv \phi(n) + \frac{\phi_0}{2}, \quad (\text{I.77})$$

with

$$\phi_0 = \frac{\Omega_0^2 t_{\text{int}}}{2\delta} \quad (\text{I.78})$$

being the *phase shift per photon*. It can be tuned in experiments by adjusting the atom-field frequency detuning δ or the interaction time t_{int} . The phase shift $\phi_0/2$, due to the Lamb shift,

³The modification of wave functions is on the order of Ω_n/δ , which results in a modification to the state probability on the order of $(\Omega_n/\delta)^2$.

⁴In this Hamiltonian, a constant term $\frac{\hbar\Omega_0^2}{8\delta}$ has been omitted, since it can be compensated by redefining the energy origin.

is independent of the photon number, and can be compensated by redefining a phase origin for the atomic coherence. It is thus omitted in the following analysis.

The phase shift $\phi(n)$ tells that an atom prepared in $(|e\rangle + |g\rangle)/\sqrt{2}$ ends up in a state⁵

$$|+\rangle_n \equiv \frac{1}{\sqrt{2}} \left(|e\rangle + e^{i\phi(n)} |g\rangle \right), \quad (\text{I.79})$$

after interacting with the cavity field during time t_{int} . In the Bloch sphere representation, the Bloch vectors of $|+\rangle_n$, as shown in Fig. I.16, point to different directions in the equatorial plane depending on photon numbers.

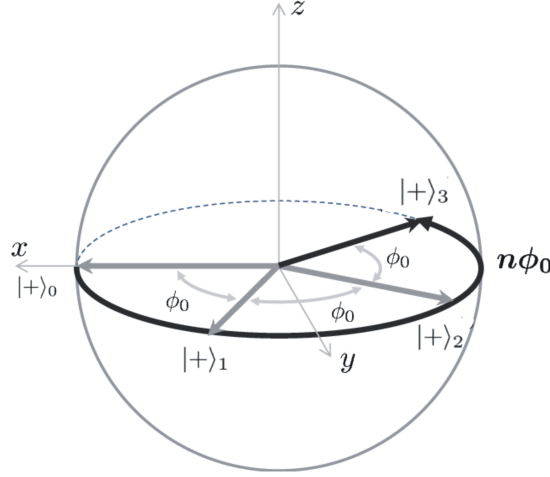


Figure I.16. Evolution of the Bloch vector after interacting dispersively with a Fock state $|n\rangle$. The global phase shift $\phi_0/2$ is not shown and the phase shift per photon is assumed to be a constant ϕ_0 .

Non linear phase shift

So far, we have assumed the far detuning condition $|\delta| \gg \Omega_n$. This condition is necessary for obtaining the expressions (I.74), which lead to a constant phase shift per photon ϕ_0 .

However, since $\Omega_n \propto \sqrt{n+1}$, the condition $|\delta| \gg \Omega_n$ may not hold for higher photon numbers. In this situation, we need to use the exact formula (I.66) and deduce the modification terms [51]:

$$\Delta E_{e,n} = \frac{\hbar}{2} \left(\sqrt{\Omega_n^2 + \delta^2} - |\delta| \right) \quad (\text{I.80})$$

$$\Delta E_{g,n} = -\frac{\hbar}{2} \left(\sqrt{\Omega_{n-1}^2 + \delta^2} - |\delta| \right). \quad (\text{I.81})$$

We can then define the phase shifts as:

$$\phi(n) = \frac{1}{\hbar} (\Delta E_{e,n} - \Delta E_{g,n}) t_{\text{int}}. \quad (\text{I.82})$$

We can further define a phase shift operator $\phi(\hat{N})$, such that

$$\langle n | \phi(\hat{N}) | n \rangle = \phi(n). \quad (\text{I.83})$$

⁵A global phase factor has been omitted.

I.3.3 Rapid adiabatic passage

In previous sections, we considered the interactions between the atom and cavity field with a fixed frequency detuning. In the current section, we discuss the rapid adiabatic passage (RAP), in which the atom-field frequency detuning is swept. This technique leads to an efficient photon transfer between the cavity field and atom. In our experiments, it is used for absorbing residual photons in order to prepare the cavity field in its vacuum state.

The principle of the RAP is shown in panel (a) of Fig. I.17. For sweeping the atom-field detuning, we keep the field frequency fixed and tune the atomic frequency through the quadratic Stark effect. The latter is achieved by varying the potential applied on one of the cavity mirrors. The applied potential and the corresponding detuning are displayed in the panel (b).

Initially, the coupled state is $|g, n+1\rangle$, and the detuning has a positive large value, i.e. $\delta_0 \gg \Omega_0$. Then the amplitude of the static electric field increases, and the atomic frequency is tuned down. The detuning passes through 0 and stops at a large negative value. The coupled state is then transformed from $|g, n+1\rangle$ to $|e, n\rangle$. Hence, one photon is transferred from the cavity field to the atom.

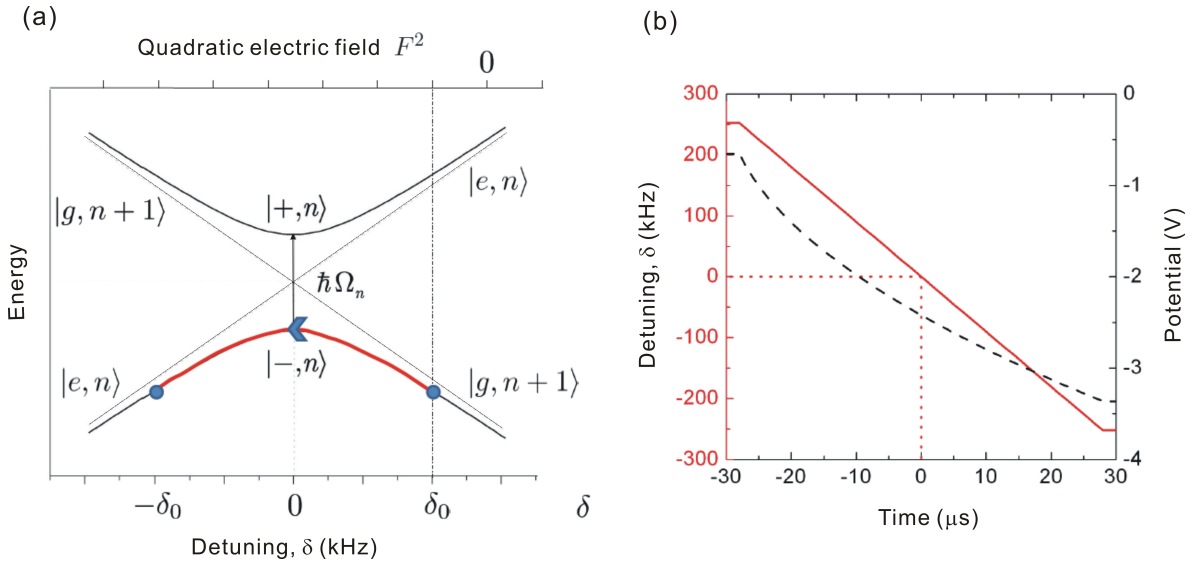


Figure I.17. Rapid adiabatic passage. (a) the principle of the RAP. (b) the applied potential (black dashed) and corresponding detuning δ (red solid).

I.4 Measurement of field state

In this section, we discuss the measurement of the field state. We first recall the postulates on measurement in quantum mechanics, then explain the principle of the QND measurement of the photon number and its backactions. We also explain the methods for state reconstruction and measurement of the phase shift per photon.

I.4.1 General measurement theory

Projective measurement

Consider a system S in a pure state represented by a vector $|\Psi\rangle$ in the Hilbert space \mathcal{H} . The measured observable is described by a Hermitian operator \hat{O} in \mathcal{H} with eigenvalues o_i , which are the only possible results of the measurement. The observable \hat{O} can be expressed as

$$\hat{O} = \sum_i o_i \hat{P}_i,$$

with \hat{P}_i being the projective operator onto the eigenspace with eigenvalue o_i , and satisfies

$$\hat{P}_i^\dagger = \hat{P}_i = \hat{P}_i^2 \qquad \sum_i \hat{P}_i = \hat{I}.$$

The postulates in quantum mechanics tell that

1. The measurement results o_i come out randomly, with probabilities given by

$$\pi_i = \langle \Psi | \hat{P}_i | \Psi \rangle.$$

2. After obtaining the result o_i , the state is projected onto the corresponding sub-space

$$|\Psi\rangle \mapsto \frac{\hat{P}_i |\Psi\rangle}{\sqrt{\pi_i}}.$$

More generally, suppose that the system S is in a statistical mixture represented by the density matrix ρ . Those postulates can then be generalized to:

1. The measurement results o_i come out randomly, with the probability given by

$$\pi_i = \text{Tr}(\rho \hat{P}_i). \tag{I.84}$$

2. After obtaining the result o_i , the state becomes

$$\rho \mapsto \rho_i = \frac{\hat{P}_i \rho \hat{P}_i}{\pi_i}. \tag{I.85}$$

Remark:

- If the observable \hat{O} commutes with the Hamiltonian of the system S , the projective measurement is repeatable, i.e. once obtaining the result o_i , the following measurement of the same observable always leads to the same result o_i .
- If the measurement is unread, the density matrix becomes

$$\rho \mapsto \sum_i \pi_i \rho_i = \sum_i \hat{P}_i \rho \hat{P}_i.$$

We see that only the diagonal elements (in the basis spanned by the eigenvectors of the observable \hat{O}) of the density matrix are preserved. The off diagonal elements related to coherence are suppressed.

Now let us apply these postulates in an experimental situation [40]. Consider a meter system A which performs a measurement on the system S by being entangled to it with a proper unitary operator \hat{U}_M . Suppose that \hat{O}_A is an observable of A with eigenvalues o_i^A and corresponding eigenvectors $|u_i^A\rangle$, which form an orthonormal basis. The operator \hat{U}_M transforms A from its initial state $|0^A\rangle$ to the state $|u_i^A\rangle$ while making a transformation described by an operator \hat{M}_i on the state of S , i.e.:

$$\begin{aligned}\hat{U}_M|\Psi^S\rangle \otimes |0^A\rangle &= \sum_i \langle u_i^A | \hat{U}_M | 0^A \rangle |\Psi^S\rangle \otimes |u_i^A\rangle \\ &\equiv \sum_i \hat{M}_i |\Psi^S\rangle \otimes |u_i^A\rangle.\end{aligned}\quad (\text{I.86})$$

If we now perform a projective measurement on the meter system A and obtain the outcome o_i^A , A is then projected onto the state $|u_i^A\rangle$. Correspondingly, the state of S is transformed according to

$$|\Psi^S\rangle \mapsto \frac{\hat{M}_i |\Psi^S\rangle}{\sqrt{\pi_i}}, \quad (\text{I.87})$$

with

$$\pi_i = \langle \Psi^S | \hat{M}_i^\dagger \hat{M}_i | \Psi^S \rangle \quad (\text{I.88})$$

being the probability for obtaining the result o_i^A .

More generally, if S is in a statistical mixture $\rho^S = \sum_i p_i |\Psi_i^S\rangle \langle \Psi_i^S|$, with each $|\Psi_i^S\rangle$ being linearly transformed according to (I.87), then the operator \hat{U}_M transforms the coupled state according to

$$\hat{U}_M (\rho^S \otimes |0^A\rangle \langle 0^A|) \hat{U}_M^\dagger = \sum_{i,j} \hat{M}_i \rho^S \hat{M}_j^\dagger \otimes |u_i^A\rangle \langle u_j^A|. \quad (\text{I.89})$$

Again the projective measurement of \hat{O}_A is performed on A , and we assume that the result o_i^A shows up. Then the state of S is transformed according to

$$\rho^S \mapsto \frac{\hat{M}_i \rho^S \hat{M}_i^\dagger}{\pi_i}, \quad (\text{I.90})$$

with

$$\pi_i = \text{Tr} \left(\rho^S \hat{M}_i^\dagger \hat{M}_i \right) \quad (\text{I.91})$$

being the probability for obtaining o_i^A .

By analogy with the postulates given in (I.84) and (I.85), we see that the ensemble of operators \hat{M}_i also describes a type of measurement, which is known as *generalized measurement*.

Generalized measurement

In this type of measurement, the operators \hat{M}_i are not required to be Hermitian, but since the probabilities of all possible measurement outcomes sum to one regardless of ρ^S , i.e.:

$$\sum_i \text{Tr} \left(\rho^S \hat{M}_i^\dagger \hat{M}_i \right) = 1 \quad \forall \rho^S, \quad (\text{I.92})$$

they should satisfy

$$\sum_i \hat{M}_i^\dagger \hat{M}_i = \hat{I}. \quad (\text{I.93})$$

In the example above, if the projective measurement on A is unread, the density matrix of S is given by (the superscript of ρ is removed for simplicity):

$$\rho \mapsto \sum_i \hat{M}_i \rho \hat{M}_i^\dagger. \quad (\text{I.94})$$

This is a linear process for the density matrix. In general, the linear process transforming a density matrix to another is called a *quantum map*, which is described by a *superoperator*. Furthermore, quantum maps can always be expressed in the form of a *Kraus sum representation* [40]. The transformation (I.94) is already cast into this representation, with \hat{M}_i being the *Kraus operators*.

We can further define an ensemble of operators, which are positive and Hermitian:

$$\hat{E}_i = \hat{M}_i^\dagger \hat{M}_i \quad \sum_i \hat{E}_i = \hat{I}. \quad (\text{I.95})$$

Such an ensemble of operators constitutes a positive operator valued measure (POVM). The probability for obtaining the result corresponding to the element \hat{E}_i of the POVM is given by

$$\pi_i = \text{Tr} \left(\rho \hat{E}_i \right)$$

In short, the generalized measurement does not involve more quantum postulate than those for the projective measurement. But it serves as a useful tool to formulate practical measurements, such as the QND measurement to be explained in the following, destructive photon counting using a photon multiplier and destructive ionization of atomic states, etc. [40].

I.4.2 Quantum nondemolition measurement of photon numbers

Using dispersive coupling between atom and photon fields, we can perform a QND measurement of photon numbers [52]. This measurement is one type of the generalized measurements, in which the probe atoms serve as meter systems.

I.4.2.a Measurement principle

Suppose that the superposition state $(|e\rangle + |g\rangle)/\sqrt{2}$ is prepared by applying a $\pi/2$ pulse in the first Ramsey zone to the state $|e\rangle$. Let us now consider its dispersive interaction with a Fock state $|n\rangle$ confined in the cavity. After interaction, the atom-field state becomes

$$|n\rangle \otimes \frac{1}{\sqrt{2}}(|e\rangle + |g\rangle) \longrightarrow \frac{1}{\sqrt{2}} \left(e^{-i(\phi(n)+\phi_0)/2} |n\rangle \otimes |e\rangle + e^{i\phi(n)/2} |n\rangle \otimes |g\rangle \right). \quad (\text{I.96})$$

A second $\pi/2$ pulse applied in the second Ramsey zone with a phase ϕ_r relative to that of the first one transforms the state into

$$\begin{aligned} & -ie^{-i(\phi_r+\phi_0/2)/2} \sin \left(\frac{\phi_0/2 + \phi(n) - \phi_r}{2} \right) |n\rangle \otimes |e\rangle \\ & + e^{i(\phi_r-\phi_0/2)/2} \cos \left(\frac{\phi_0/2 + \phi(n) - \phi_r}{2} \right) |n\rangle \otimes |g\rangle. \end{aligned} \quad (\text{I.97})$$

Note that the detection of the atomic state, no matter it is in $|g\rangle$ or $|e\rangle$, leaves $|n\rangle$ unchanged. This characteristic originates from the fact that photon number states are *pointer states* of this measurement.

Let us now consider an arbitrary field state expressed as $|\psi_c\rangle = \sum_{n \geq 0} c_n |n\rangle$. Based on the transformation (I.97), we can obtain

$$\sum_{n \geq 0} c_n |n\rangle \otimes \frac{1}{\sqrt{2}}(|e\rangle + |g\rangle) \longrightarrow \dots \quad (\text{I.98})$$

$$\longrightarrow -ie^{-i(\phi_r + \phi_0/2)/2} \sum_{n \geq 0} \sin\left(\frac{\phi_0/2 + \phi(n) - \phi_r}{2}\right) c_n |n\rangle \otimes |e\rangle \quad (\text{I.99})$$

$$+ e^{i(\phi_r - \phi_0/2)/2} \sum_{n \geq 0} \cos\left(\frac{\phi_0/2 + \phi(n) - \phi_r}{2}\right) c_n |n\rangle \otimes |g\rangle. \quad (\text{I.100})$$

By analogy with (I.86), we see that the detection of the atomic state in the basis $\{|e\rangle, |g\rangle\}$ amounts to a generalized measurement of the field state. Omitting irrelevant global phase factors, we can express the Kraus operators as

$$\hat{M}_e = \sin\left(\frac{\phi(\hat{N}) - \phi_r}{2}\right) \quad \hat{M}_g = \cos\left(\frac{\phi(\hat{N}) - \phi_r}{2}\right), \quad (\text{I.101})$$

where $\phi(\hat{N})$ is the phase operator defined in (I.83). The Lamb shift term $\phi_0/2$ is independent of photon number, and has been included in the Ramsey phase ϕ_r . The POVMs associated to these Kraus operators are given by

$$\hat{E}_e = \frac{1 - \cos(\phi_r - \phi(\hat{N}))}{2} \quad \hat{E}_g = \frac{1 + \cos(\phi_r - \phi(\hat{N}))}{2}. \quad (\text{I.102})$$

The probability for detecting the atomic state $|g\rangle$ in a Fock state $|n\rangle$ is

$$\pi(g|n) = \text{Tr}\left(|n\rangle\langle n| \hat{E}_g\right) = \frac{1}{2} + \frac{1}{2} \cos(\phi_r - \phi(n)). \quad (\text{I.103})$$

Remark: Comparing the probability $\pi(g|n)$ with that given in (I.26), we recognize that in the QND measurement the photon field serves as the phase shift element, which causes phase shifts dependent on photon numbers. By reading out these phase shifts, the Ramsey interferometer can thus extract information about the photon field.

I.4.2.b Modification of photon number distribution

Detecting the atomic state $i = \{|e\rangle, |g\rangle\}$ transforms the field state according to

$$\rho' = \frac{\hat{M}_i \rho \hat{M}_i^\dagger}{\text{Tr}\left(\rho \hat{M}_i^\dagger \hat{M}_i\right)}. \quad (\text{I.104})$$

The new photon number distribution $P(n|i)$ is then given by

$$P(n|i) = \text{Tr}\left[\frac{\hat{M}_i \rho \hat{M}_i^\dagger}{\text{Tr}\left(\rho \hat{M}_i^\dagger \hat{M}_i\right)} |n\rangle\langle n|\right]. \quad (\text{I.105})$$

Since the Kraus operators \hat{M}_i commute with $|n\rangle\langle n|$, we can express (I.105) as

$$P(n|i) = \frac{\text{Tr} \left[\hat{E}_i \rho |n\rangle\langle n| \right]}{\text{Tr} \left(\rho \hat{E}_i \right)} = \frac{\langle n | \hat{E}_i | n \rangle}{\text{Tr} \left(\rho \hat{E}_i \right)} \langle n | \rho | n \rangle, \quad (\text{I.106})$$

where the second equality is obtained from the fact that the operators \hat{E}_i are diagonal in the Fock basis.

We can easily identify the three terms: $\langle n | \rho | n \rangle = P(n)$ is the probability of state $|n\rangle$ in ρ ; $\langle n | \hat{E}_i | n \rangle = \pi(i|n)$ is the probability for detecting state i in $|n\rangle$; and $\text{Tr} \left(\rho \hat{E}_i \right) = \pi_i = \sum_{n \geq 0} P(n) \pi(i|n)$ is the probability for detecting i in ρ . The probability (I.106) can thus be written in an explicit form:

$$P(n|i) = \frac{\pi(i|n)}{\pi_i} P(n). \quad (\text{I.107})$$

This equation tells that after detecting the atomic state i , the probability of $|n\rangle$ is modified by a multiplication factor which is proportional to the probability for detecting i if the field is in $|n\rangle$. This is simply the *Bayes law* on the inversion of conditional probability [53]. This law holds because of the QND nature of this measurement, which ensures that $|n\rangle$ is not coupled to other Fock states and thus no population transfer between different photon number states occurs during the interaction.

Figure I.18 illustrates the modification of the photon number distribution $P(n)$ after one atomic detection. Here we assume an initial field with a flat bounded photon number distribution, and that the measurement is performed with a Ramsey phase $\phi_r = 0$ and a phase shift per photon $\phi_0 = \pi/4$. The histograms in panels (a), (b) and (c) correspond to the initial $P(n)$, the modified distributions $P(n|g)$ and $P(n|e)$ if the atom is detected in $|g\rangle$ or $|e\rangle$, respectively. The solid squares in panel (a) shows the probabilities $\pi(g|n)$.

If the atom is detected in $|g\rangle$, the probability of $|0\rangle$ is doubled while that for $|4\rangle$ becomes zero. This is because a field with 0 photon leads to a probability 100% of detecting $|g\rangle$. Since now we detect $|g\rangle$, the field is “more probably” in $|0\rangle$. As for the suppression of $|4\rangle$, it can be understood like this: the probability for detecting $|g\rangle$ is zero in $|4\rangle$, we now detect $|g\rangle$, so there should be no such a state in the field.

If the atom is unread, the field is transformed according to

$$\rho' = \sum_{i=\{e,g\}} \hat{M}_i \rho \hat{M}_i^\dagger. \quad (\text{I.108})$$

One can easily verify that the photon number distribution $P(n)$ is not changed, a feature related to the QND nature of this measurement.

Decimation and field collapse

The QND measurement performed by one atom is a *weak measurement*, in the sense that it does not project the field onto its pointer state. It only modifies $P(n)$ by a multiplication factor depending on the probability $\pi(i|n)$, which is also called a *decimation function*.

The probability $\pi(i|n)$ is a periodical function of n , and the period is 8 with $\phi_0 = \pi/4$. So based on this decimation function, we actually measure the photon numbers modulo 8. This

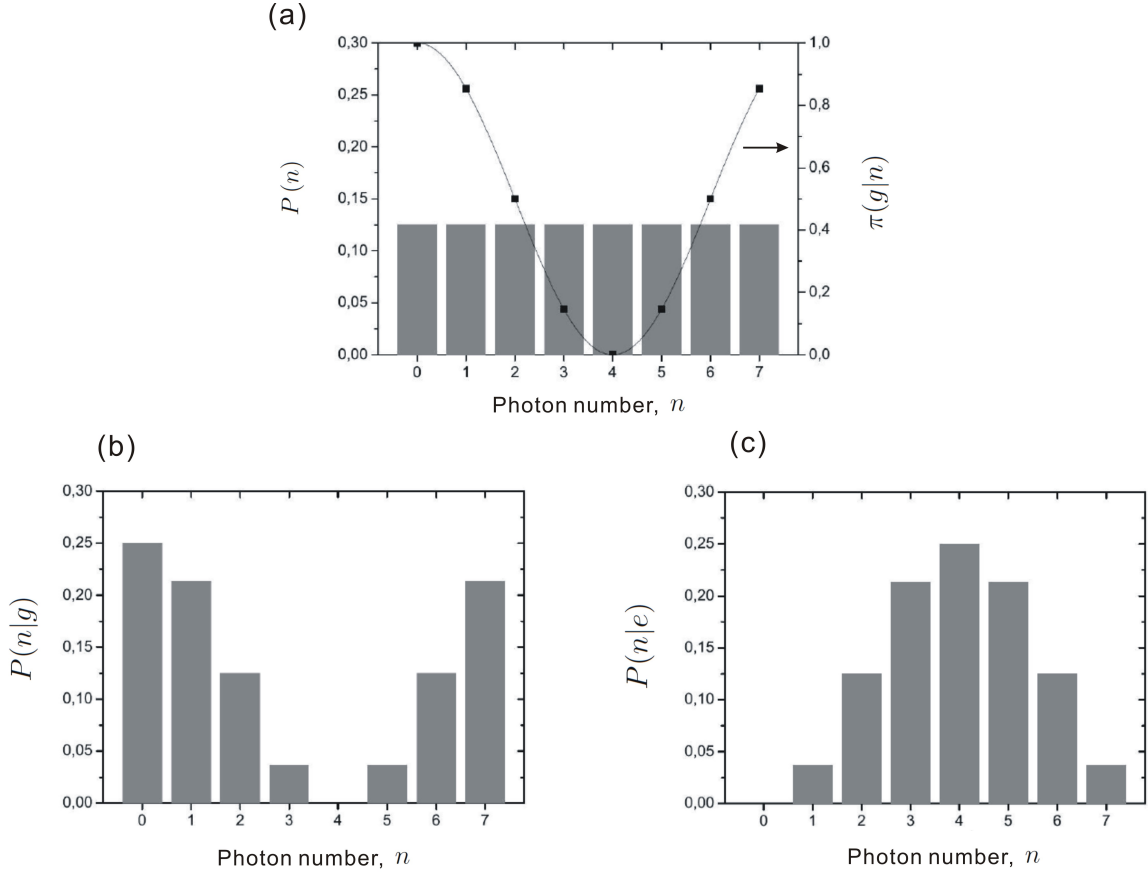


Figure I.18. Modification of $P(n)$ by one atomic detection with a Ramsey phase $\phi_r = 0$ and a phase shift per photon $\phi_0 = \pi/4$. (a) Initial photon number distribution (histogram) is assumed to be flat with up to 7 photons. The points display the conditional probability $\pi(g|n)$ of detecting $|g\rangle$ in $|n\rangle$. (b) Photon number distribution if the atom is detected in $|g\rangle$. (c) Photon number distribution if the atom is detected in $|e\rangle$.

is also why we truncate the one atom decimation process shown in Fig. I.18 at 7 photons. It is illustrating to relate this periodicity to the atomic pseudo spins. As shown in the left panel of Fig. I.19, after interacting with the field, the Bloch vectors of states $|+\rangle_n$ point to different directions in the equatorial plane, with those of $|+\rangle_{n+8}$ and $|+\rangle_n$ overlapping. The atomic detection thus cannot distinguish the two states $|n\rangle$ and $|n+8\rangle$.

Moreover, under the conditions $\phi_r = 0$ and $\phi_0 = \pi/4$, we have $\pi(i|1) = \pi(i|7)$, $\pi(i|2) = \pi(i|6)$ and $\pi(i|3) = \pi(i|5)$. The results of these equalities can be seen from panels (b) and (c) of Fig. I.18, where there are such grouped states as $|1\rangle$ and $|7\rangle$ with $P(1) = P(7)$. This feature means that we cannot distinguish these two states using only the measurement with $\phi_r = 0$. In order to distinguish them, we need to exploit another Ramsey phase, e.g. $\phi_r = \pi/2$. In fact, although 2 orthogonal ones are enough in principle, it is better to use 4 Ramsey phases to resolve the 8 photon number states from $|0\rangle$ to $|7\rangle$, as explained in the following paragraph.

From the curve of $\pi(g|n)$ shown in Fig. I.19, we see that the setting $\phi_r = 0$ is optimal for distinguishing $|2\rangle$ and $|6\rangle$ from all other states, because $\pi(g|2) = \pi(g|6) = 50\%$ differs

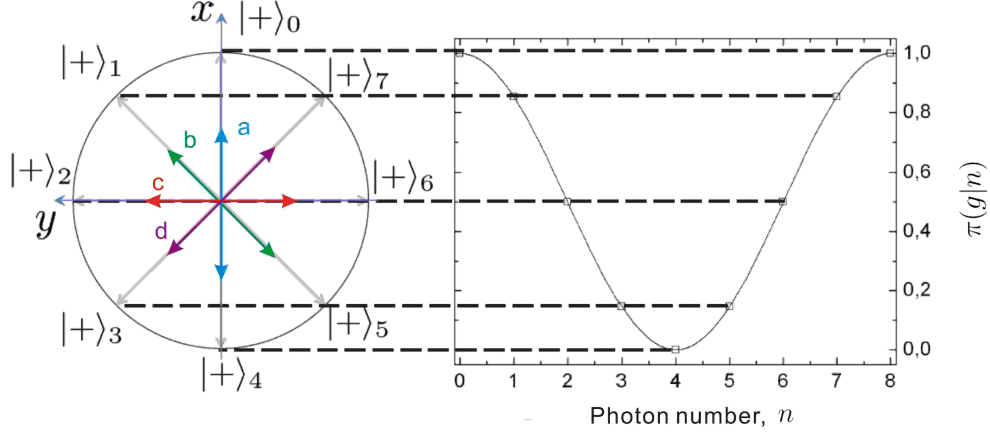


Figure I.19. Decimation process illustrated in the Bloch sphere representation. *On the left:* Equatorial plane of the Bloch sphere showing the Bloch vectors of atomic states after interacting with the states from $|0\rangle$ to $|7\rangle$, with $\phi_0 = \pi/4$. The four axes a, b, c, d are possible observation axes as explained in the text. *On the right:* Conditional probabilities $\pi(g|n)$, which are equal to the spin component S_x plus a constant term.

maximally from all other $\pi(g|n)$. The same argument also holds for the states, such as $|3\rangle$ and $|7\rangle$, $|0\rangle$ and $|4\rangle$, $|1\rangle$ and $|5\rangle$, i.e. they can also be optimally distinguished from the others by choosing a proper Ramsey phase. For example, if $\phi_r = \pi/2$, $\pi(g|0) = \pi(g|4) = 50\%$ and the two states $|0\rangle$ and $|4\rangle$ can be maximally distinguished from the others. Consequently, it is better to use 4 Ramsey phases to resolve the states from $|0\rangle$ to $|7\rangle$. A possible setting is the 4 phases labeled as a, b, c, d shown in Fig. I.19, with neighboring ones separated by $\pi/4$.

Repeating the weak measurements with alternating 4 Ramsey phases allows us to follow the progressive state collapse of an initial field [31]. Figure I.20 shows two individual quantum trajectories of such a measurement. Initially a small coherent field (to make sure that the truncation up to 7 photon is valid) is injected into the cavity. Then atomic samples with alternating phases a, b, c, d perform weak measurements. After having detected about 50 atoms, the field is randomly projected to a photon number state. So the repeated weak measurements amount to a strong measurement that projects the field into a pointer state.

I.4.2.c Reconstruction of photon number distributions

In the previous section, we discussed the collapse of an initial field into photon number states by repeated 4-phase QND measurements. In this section, we present a method which allows us to reconstruct the photon number distribution $P^{\text{real}}(n)$ of the initial field.

In this method, we also perform the 4-phase QND measurements on the initial field. As a first step, let us consider the decimation on an initial guess $P_0(n)$ performed by N_{at} atoms in an individual quantum trajectory denoted by (\mathcal{P}) . In this case, the decimation can be easily

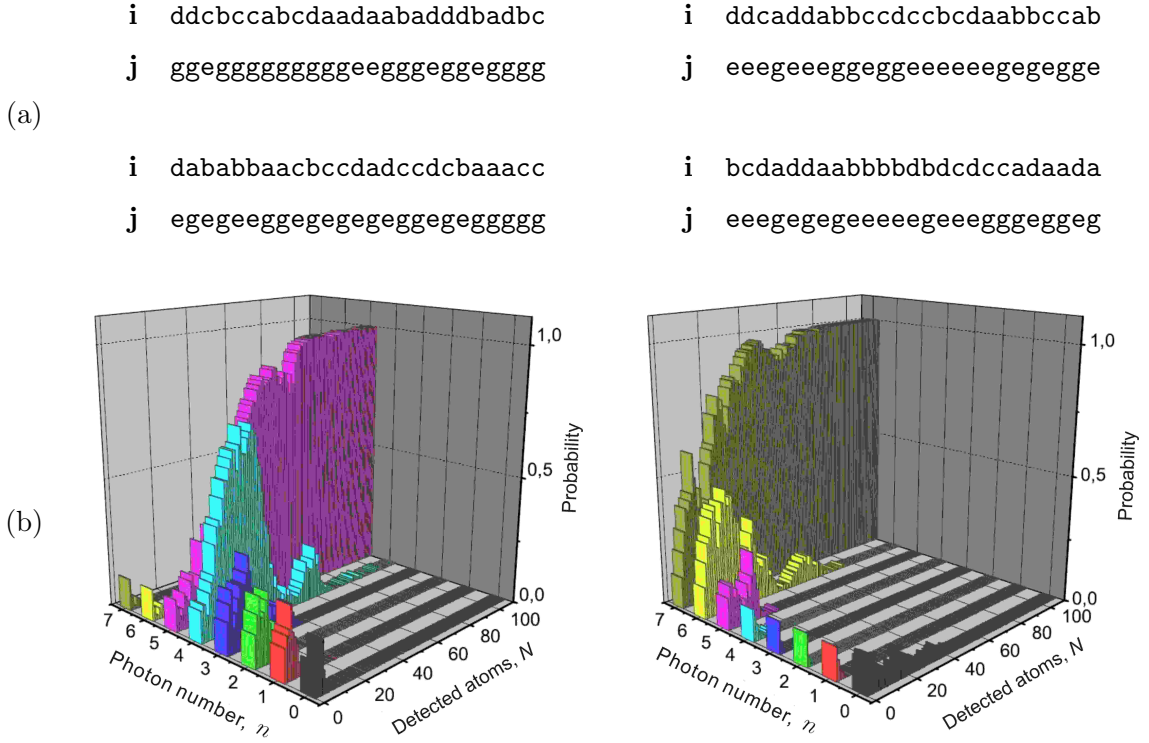


Figure I.20. Progressive decimation of photon number distribution for two individual quantum trajectories. The initial field is assumed to have a flat photon number distribution with up to 7 photons. (a) Results of the first 50 atomic detections. The Ramsey phase and the corresponding result of atomic detection is given by i and j . (b) Progressive evolution of the photon number distributions.

obtained by applying the transformation relationship (I.107) N_{at} times, i.e.

$$\begin{aligned}
 P_1^{(\mathcal{P})}(n) &= \prod_{k=1}^{N_{\text{at}}} \left[\frac{\pi(i^k | n, \phi_r^k)}{\pi_{i^k}(\phi_r^k)} \right]^{(\mathcal{P})} P_0(n) \\
 &= \frac{1}{Z^{(\mathcal{P})}} \Pi_{N_{\text{at}}}^{(\mathcal{P})}(n) P_0(n),
 \end{aligned} \tag{I.109}$$

where i^k denotes the detection result of the k th atom, ϕ_r^k denotes the Ramsey phase used for this atom. In the second line, $Z^{(\mathcal{P})}$ is a normalization constant, and the decimation function of N_{at} atoms $\Pi_{N_{\text{at}}}^{(\mathcal{P})}(n)$ is defined as

$$\Pi_{N_{\text{at}}}^{(\mathcal{P})}(n) = \prod_{k=1}^{N_{\text{at}}} \left[\pi(i^k | n, \phi_r^k) \right]^{(\mathcal{P})}. \tag{I.110}$$

For measuring the initial field, the measurement time should be short such that the field relaxation can be neglected during the measurement. In the decimation process discussed in the previous section, the field is collapsed into photon number states by the detection of 110 atoms, a measurement time of about 45 ms⁶. Considering the cavity lifetime $T_{\text{cav}} = 130$ ms,

⁶In this measurement, the average detected atom number is about 0.2/sample. So we need to use about 550 atomic samples on average.

the effect of field relaxation cannot be neglected during this time. In order to reduce the measurement time, we need to reduce the number of atoms N_{at} . However, if N_{at} is small, the weak measurements may not be able to collapse the field state into individual photon number states. In this situation, the obtained $P_1^{(\mathcal{P})}(n)$ keeps the memory of the initial guess $P_0(n)$, which, for example, is supposed to be a flat bounded distribution in the previous section. To overcome this problem, we can take an ensemble average over a large number of individual quantum trajectories (e.g. ~ 8000) and obtain a new guess of the photon number distribution:

$$P_1(n) = \overline{P_1^{(\mathcal{P})}(n)}^{(\mathcal{P})}. \quad (\text{I.111})$$

Since $P_1(n)$ contains the information from the measurement results, it is a better guess for the initial field than $P_0(n)$. We can feed this better guess into the transformation (I.109) and make the average (I.111) again. In fact, we can repeat this process many times and obtain

$$P_{m+1}(n) = \overline{\frac{1}{Z^{(\mathcal{P})}} \Pi_{N_{\text{at}}}^{(\mathcal{P})}(n) P_m(n)}^{(\mathcal{P})}. \quad (\text{I.112})$$

Suppose that at one moment we get the initial field $P^{\text{real}}(n)$ and substitute it into the transformation (I.112). Since the atoms perform QND measurements on the photon numbers, we have

$$P^{\text{real}}(n) = \overline{\frac{1}{Z^{(\mathcal{P})}} \Pi_{N_{\text{at}}}^{(\mathcal{P})}(n) P^{\text{real}}(n)}^{(\mathcal{P})}, \quad (\text{I.113})$$

which means that the real photon number distribution is a *fixed point* of the transformation (I.112). Consequently, a sufficiently large number of iterations (e.g. ~ 20) starting from an initial guess $P_0(n)$ can reach the fixed point of the transformation (I.112), which is actually $P^{\text{real}}(n)$.

In fact, the method used here is one example of the *maximum-likelihood reconstruction*, analogy to the method discussed in [54]. In this article, the authors try to find the fixed point of the following transformations:

$$\rho \mapsto R(\rho)\rho \qquad \rho \mapsto \rho R(\rho), \quad (\text{I.114})$$

with $R(\rho)$ being a matrix constructed in a similar way as the decimation function (I.110). The fixed point of these transformations is the density matrix, which maximizes the *likelihood function*, i.e. the probability for leading to the measured results.

Remark: Since the POVMs associated to the QND measurement are diagonal in the Fock basis, the reconstruction method outlined above cannot provide information about the non-diagonal elements of the density matrix. So this method enables us to reconstruct the photon number distribution of the field, but not the entire density matrix.

I.4.2.d Phase shifts in photon number states

Phase shifts $\phi(n)$ can be calculated according to the formula (I.82), and can also be measured experimentally. In this section we explain the principle and method for measuring $\phi(n)$.

Let us consider again the atomic pseudo spins shown in Fig. I.19. By relating their directions to the conditional probabilities $\pi_g(n, \phi_r) \equiv \pi(g|n, \phi_r)$ (Here and afterwards, ϕ_r is shown explicitly in the expression of π_g for clarity), we see that the detections with Ramsey phases

$\phi_r = 0$ and $\phi_r = \pi/2$ correspond respectively to measurements of the x and y components of the pseudo spins, i.e.

$$\pi_g(n, \phi_r = 0) = \cos^2\left(\frac{\phi(n)}{2}\right) = \frac{1}{2} + \frac{\langle \hat{S}_x \rangle_n}{\hbar} \quad (\text{I.115})$$

$$\pi_g(n, \phi_r = \pi/2) = \sin^2\left(\frac{\phi(n)}{2}\right) = \frac{1}{2} + \frac{\langle \hat{S}_y \rangle_n}{\hbar}. \quad (\text{I.116})$$

From the picture of atomic pseudo spins, it is clear that if we can determine precisely the x and y components of the Bloch vector associated to each state $|+\rangle_n$, the phase shifts $\phi(n)$ can then be obtained as

$$\phi(n) = \text{atan}\left(\frac{\langle \hat{S}_y \rangle_n}{\langle \hat{S}_x \rangle_n}\right). \quad (\text{I.117})$$

It is the Ramsey phase ϕ_r that chooses which spin component we measure. In order to make a full *spin tomography*, we need to use at least two Ramsey phases (ideally orthogonal to each other). But in fact, with $\phi_0 = \pi/4$, it is better to use 4 Ramsey phases with neighboring ones separated by $\pi/4$. One possible setting is the 4 phases labeled as a, b, c, d in Fig. I.19. The spin component corresponding to each phase setting is given by

$$\langle \hat{S}_i \rangle = \frac{\hbar}{2} [\pi_g(\phi_i) - \pi_e(\phi_i)], \quad i = a, b, c, d. \quad (\text{I.118})$$

If we group the phases which are quasi-orthogonal⁷, e.g. $(\phi_a, \phi_c) \rightarrow (\phi_1, \phi_2)$ or $(\phi_b, \phi_d) \rightarrow (\phi_1, \phi_2)$, we can express the x and y components of the atomic spin as

$$\langle \hat{S}_x \rangle = \frac{\langle \hat{S}_1 \rangle \sin \phi_2 - \langle \hat{S}_2 \rangle \sin \phi_1}{\sin(\phi_2 - \phi_1)} \quad \langle \hat{S}_y \rangle = \frac{-\langle \hat{S}_1 \rangle \cos \phi_2 + \langle \hat{S}_2 \rangle \cos \phi_1}{\sin(\phi_2 - \phi_1)}. \quad (\text{I.119})$$

The values obtained from (ϕ_a, ϕ_c) and (ϕ_b, ϕ_d) are then averaged to get the two components of the pseudo spin.

The measurement goes as follows: a small coherent field with roughly 4 photons is first injected into the cavity. Then atomic samples with alternating 4 phases are sent successively into the cavity. On average, about 0.2 atoms are detected in each sample. Each quantum trajectory includes 500 samples, which lead to about 100 detected atoms. In this trajectory we define a sliding “*voting*” *segment* of 60 detected atoms (i.e. from 1 to 60, 2 to 61..., etc.), which are used to calculate the spin components according to (I.118). The same measurement is then repeated 4000 times to have sufficient statistics.

The total numbers of spins in phase intervals of the size 0.02π are shown in Fig. I.21, and fitted using a sum of 7 Gaussian functions with the same width. The center of each Gaussian function corresponds to the phase shift in a photon number state. By fitting these phase shifts with a quadratic function, we obtain the phase shifts⁸ $\phi(n)$:

$$\phi(n) = (0.252 \pm 0.001) \pi n - (0.001 \pm 0.0004) \pi n^2. \quad (\text{I.120})$$

⁷In the experimental situation, the separation between neighboring phases is not precisely $\pi/4$.

⁸The phase shift due to the vacuum state is taken as the origin of these shifts.

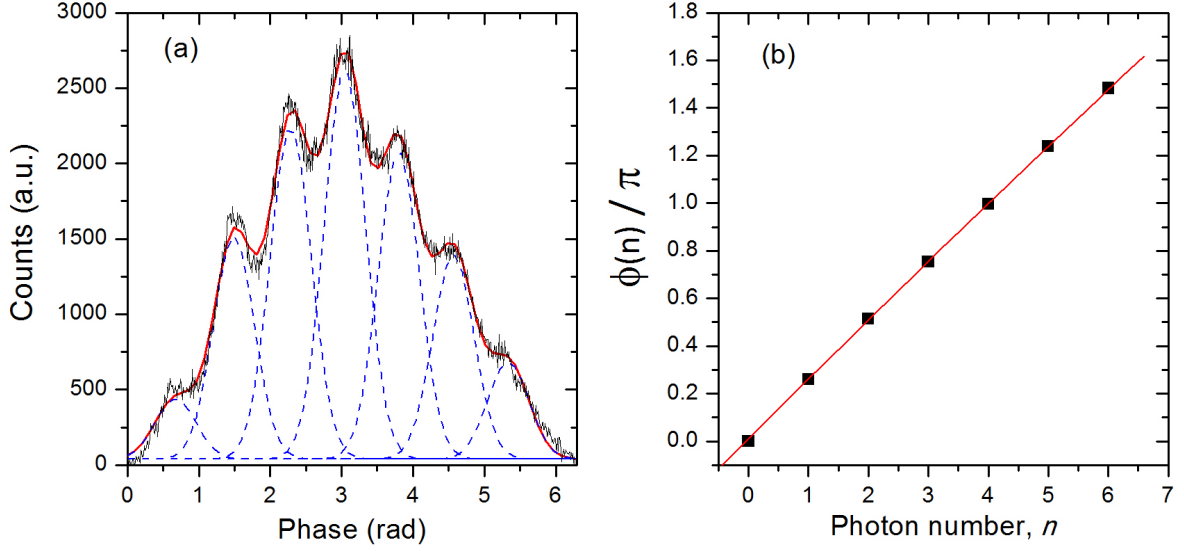


Figure I.21. Phase shifts in photon number states. (a) Numbers of atomic pseudo spins as a function of their phases. The counts are fitted using a sum of 7 Gaussian functions (blue dashed lines) with the same width. The red solid line shows the fit result. (b) The solid squares correspond to the phase shifts $\phi(n)$ in unit of π . The line is a second order polynomial fit to the measured data.

Conclusion

In this chapter, we have introduced the experimental tools: atoms and photons. We have explained the properties, preparation and detection of circular Rydberg atoms and the theoretical description of a two-level system. We have also presented the characteristics of the high Q cavity we use and the theory describing a quantized field and its coupling to the environment.

We have introduced the Jayne-Cummings model and discussed the resonant and dispersive interactions between the atoms and the cavity field. In the resonant regime, the atom and cavity exchange photons and we observe Rabi oscillations. In the dispersive regime, the coupling induces light shifts to the atomic states. Thus the dispersive interaction leads to a phase shift dependent on photon number to the atomic coherence. Reading out this shift using a Ramsey interferometer enables us to perform a QND measurement of photon numbers. We have analyzed the backactions of such a measurement performed by one atom, and discussed the collapse of a field state by repeated measurements. We have explained the method for measuring and reconstructing a field state. We have also presented the method for measuring phase shifts in photon number states and given the results.

Chapter II

Quantum feedback: state estimation

II.1 General principle

II.1.1 From classical to quantum feedback

Feedback loops are widely used in our everyday life and scientific research. For instance, in refrigerator or incubators where temperature should be stabilized, in laser systems which should operate at a well fixed frequency, etc. In these loops, as displayed in the upper panel of Fig. II.1, a signal is obtained by the *sensor* performing measurement on the system \mathcal{S} . After *signal processing*, we obtain the current state parameter S_c (e.g. temperature) of \mathcal{S} . By comparing S_c with the preset target S_t , an error signal ϵ is generated. The *controller* \mathcal{C} transforms ϵ into a feedback action c , which is then carried out by the *actuator* and stabilizes \mathcal{S} around S_t .

Quantum feedback, referring to the generalization of this feedback method to control a quantum system, must overcome a fundamental difficulty: the measurement has a *back action* on the system which needs to be controlled. The lower panel of Fig. II.1 shows the loop structure of a quantum feedback process. Comparing it with its classical counterpart, we can identify the four basic components: sensor, quantum state estimator (signal processor), controller and actuator.

The sensor performs measurements on the system \mathcal{S} . Unlike in a classical feedback loop, the backactions of the measurements need to be considered.

The quantum state estimator is an algorithm that estimates the current state ρ_k of \mathcal{S} , by taking into account all available information, such as the measured signal, the previous estimated state ρ_{k-1} stored in its memory, and the applied control action, etc. By contrast, in a classical feedback loop, the state estimate can be done based only on the measurement result.

The controller is another algorithm that chooses a feedback action in order to bring the current state ρ_k closer to the target state ρ_t . In classical feedback loops, e.g. a PID (proportional-integral-derivative) loop, the feedback action can be defined as a function of the error signal. However, in quantum feedback loops, the choice of feedback actions does not rely only on the error signal generated by the state comparison.

The actuator applies the feedback action c to \mathcal{S} .

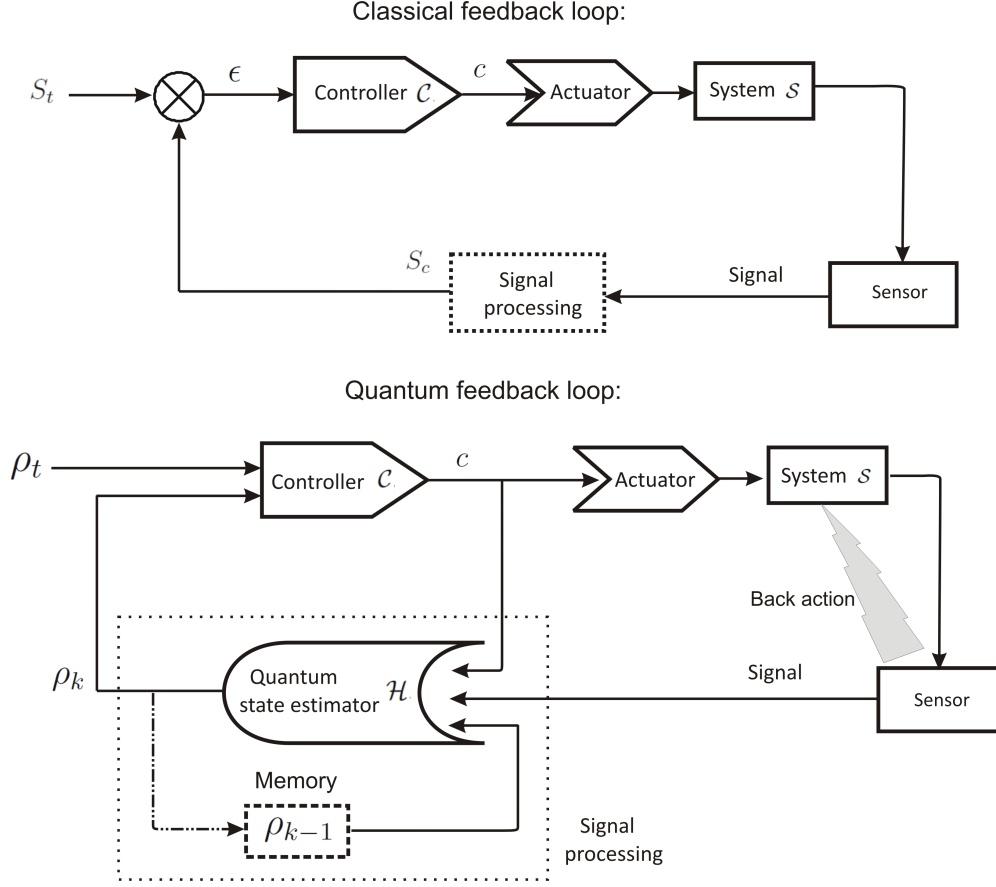


Figure II.1. Comparison of classical and quantum feedback loops. In a quantum feedback loop, the backactions of the sensor should be considered. The state estimator and controller are also different from their classical counterparts.

II.1.2 Principle of the quantum feedback experiment

The scheme of the feedback experiment is displayed in Fig. II.2. We use quantum feedback to prepare and stabilize photon number states in the high finesse cavity C. In the feedback loops, the atomic samples performing QND measurements serve as sensors and are labeled as “QND”. The samples which interact resonantly with the cavity field and exchange photons with it act as actuators. They can be prepared either in $|e\rangle$ or in $|g\rangle$ for emitting or absorbing photons, and are labeled as “RE” (resonant $|e\rangle$) or “RG” (resonant $|g\rangle$), respectively.

In order to illustrate the principle of the experiment without involving too much complication, we outline a simplified version of the feedback procedure in this chapter. Initially, the cavity field is prepared in the vacuum state. An atomic sample performs the QND measurement on the field and gets detected by the detector D. The detection result is then fed into the quantum state estimator, which estimates the current field state based on this result and all other knowledge it has, such as the initial field state, field relaxation, etc. Once a new estimated state is obtained, the controller commands a feedback action on the next atomic sample, aiming at bringing the field state closer to the target state. The “closeness” between these two states is characterized by a *distance function*, which will be carefully defined later.

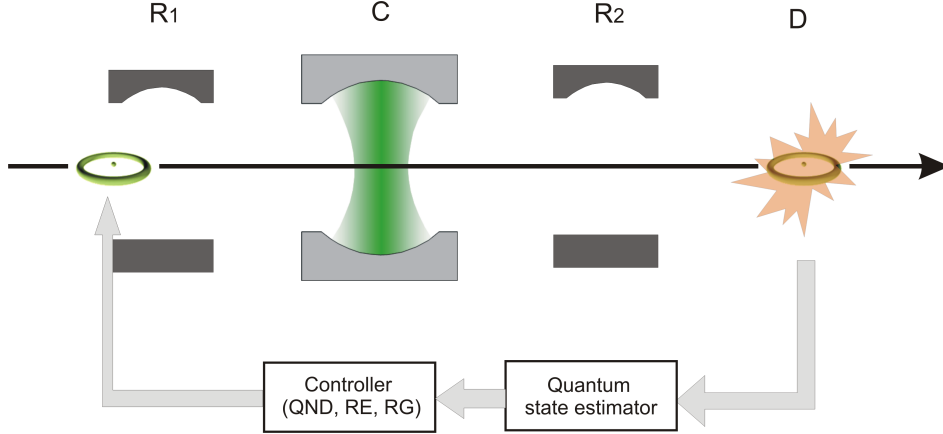


Figure II.2. The scheme of the feedback experiment. C: the cavity; D: the detector; R_1 and R_2 : the two Ramsey zones. The torus-shape elements represent the circular Rydberg atoms. The black arrow shows the atomic beam. The grey arrows display indicatively the feedback loop.

The feedback actions are: (i) an RE sample serving as a photon emitter; (ii) an RG sample serving as a photon absorber, (iii) a QND sample, if photon exchange is unnecessary. Later, the sample carrying this feedback action interacts with the cavity field and gets detected, triggering the next feedback loop. A sequence of equally spaced atomic samples passes through the cavity and get detected one by one, such that the feedback process runs continuously.

The samples of different types require different initial atomic states before entering C, which are RE: $|e\rangle$; RG: $|g\rangle$; QND: $(|e\rangle + |g\rangle)/\sqrt{2}$. The state $|g\rangle$ is prepared before the sample enters R_1 . The other atomic states are prepared by applying Ramsey pulses to $|g\rangle$ in R_1 . A π pulse is required for a RE sample and a $\pi/2$ pulse for a QND sample. So in order to prepare the corresponding atomic state, the type of the sample should be determined before it enters R_1 .

The sensor samples interact dispersively with the cavity field, whereas the actuator samples resonantly. The goal of this chapter is to discuss these two types of interactions.

The ideal QND measurement has been explained in I.4.2. However, in practice, experimental imperfections, such as the probabilistic atom number in an atomic sample, inhomogeneous static fields, preparation and detection errors of the atomic states, detector efficiency, etc. come into play. We extend the description of the ideal dispersive interaction to take into account these imperfections in section II.2.

In the feedback experiment, the detection of the actuator samples also provides information on the cavity field, and transforms the field state. The quantum maps corresponding to these transformations are presented in section II.3. Starting from discussing the ideal cases, the experimental imperfections are measured and gradually added into the ideal quantum maps.

In section II.4, we give the algorithm of the state estimation.

II.2 Sensor samples

The sensor samples interact dispersively with the cavity field and perform QND measurements. As given in (I.101), the ideal Kraus operators associated to the detection results $|e\rangle$ and $|g\rangle$

read

$$\hat{M}_e = \sin\left(\frac{\phi(\hat{N}) - \phi_r}{2}\right) \quad \hat{M}_g = \cos\left(\frac{\phi(\hat{N}) - \phi_r}{2}\right). \quad (\text{II.1})$$

In the following, we take into account the experimental imperfections and construct the quantum maps adapted to the real experiments.

Probabilistic atom number

In practice, the atomic samples interacting with the cavity field do not have a deterministic atom number, due to the probabilistic preparation process. The probabilities for different atom numbers in a sample are approximately described by a truncated Poisson distribution P_n with $n \in \{0, 1, 2\}$, i.e.

$$P_n = e^{-\bar{n}_{\text{at}}} \frac{\bar{n}_{\text{at}}^n}{n!} / \left(\sum_{m \in \{0,1,2\}} e^{-\bar{n}_{\text{at}}} \frac{\bar{n}_{\text{at}}^m}{m!} \right), \quad (\text{II.2})$$

where \bar{n}_{at} is the average atom number per sample. Considering up to 2 atoms in an atomic sample, the possible detection results by a virtual ideal detector constitute a set $S^i \equiv \{0, e, g, ee, eg, gg\}$ (the detection results “ eg ” and “ ge ” are indistinguishable and both considered as “ eg ”).

How do we describe the dispersive interaction between the cavity field and 2 atoms? In fact, if two atoms interact with the cavity field simultaneously, the interaction process is more complicated than that with only one atom. Cavity-assisted collision is possible [55], in which the two atoms may exchange their states without modifying the photon number in the cavity, i.e. $|eg, n\rangle \leftrightarrow |ge, n\rangle$. This process reduces the contrast of the Ramsey fringes. Nevertheless, we have verified with numerical simulations that, for the large atom-cavity detuning (250 kHz) used in our experiments, this process is negligible and the modification of the field state induced by 2 atoms simultaneously passing through the cavity is equivalent to that induced by 2 atoms passing through the cavity one after another. We thus consider the simultaneous dispersive interaction of the cavity field with 2 atoms as two successive interactions with 1 atom.

Consequently, the Kraus operators associated to the detection results $q \in S^i$ can be expressed as

$$\begin{aligned} \hat{S}_0 &= \sqrt{P_0} \hat{I}, \\ \hat{S}_e &= \sqrt{P_1} \hat{M}_e, \\ \hat{S}_g &= \sqrt{P_1} \hat{M}_g, \\ \hat{S}_{ee} &= \sqrt{P_2} \hat{M}_e^2, \\ \hat{S}_{eg} &= \sqrt{2P_2} \hat{M}_e \hat{M}_g, \\ \hat{S}_{gg} &= \sqrt{P_2} \hat{M}_g^2, \end{aligned} \quad (\text{II.3})$$

with \hat{I} being the identity operator. It can be easily verified that $\sum_{q \in S^i} \hat{S}_q^\dagger \hat{S}_q = \hat{I}$. In \hat{S}_{eg} , a factor $\sqrt{2}$ appears, because we consider both “ eg ” and “ ge ” as “ eg ”.

Effective detection errors

In the operators (II.3), we need also to take into account other experimental imperfections, which result in imperfect Ramsey fringes. Figure II.3 displays typical experimental Ramsey fringes. In Fig. II.3 and the following figures, while presenting the experimental data, we use e^d (g^d) to denote the event that a signal is generated in the detection channel $|e\rangle$ ($|g\rangle$). We use π_{g^d} to denote the ratio between the number of the detection events g^d over the total number of detection events N_{tot} . The errors are thus the binomial statistical errors given by $\sqrt{\pi_{g^d}(1 - \pi_{g^d})/N_{\text{tot}}}$.

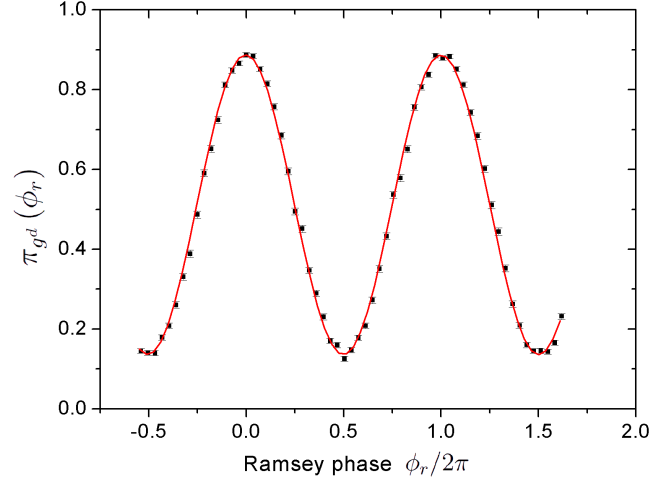


Figure II.3. Typical experimental Ramsey fringes. The probability for detecting g^d is plotted as a function of the Ramsey phases. The meaning of g^d is explained in the text.

Compared with ideal fringes, the measured fringes have a reduced contrast. This may be due to the experimental imperfections, such as imperfect Ramsey $\pi/2$ pulses, preparation and detection errors of the atomic states, and inhomogeneous static fields. In fact, it can be shown that the quantum map associated to the Ramsey interferometer in the presence of these different imperfections is effectively the same as if all of them were considered as detection errors [51]. This leads to the *effective detection errors*, which need to be determined.

Due to the effective detection errors, the detection events e^d and g^d contain contributions from both states $|e\rangle$ and $|g\rangle$. The effective detection errors can be expressed as the conditional probabilities for the atomic states to be erroneously detected:

$$\tilde{\eta}_e^d = P(g^d|e) \qquad \tilde{\eta}_g^d = P(e^d|g). \qquad (\text{II.4})$$

Let us now derive $\pi_{g^d}(\phi_r)$ from the ideal Ramsey fringes expressed as $\pi_g(\phi_r) = (1 + \cos \phi_r)/2$. Taking into account (II.4), the measured Ramsey fringes are given by:

$$\begin{aligned} \pi_{g^d}(\phi_r) &= \pi_g(\phi_r) \left(1 - \tilde{\eta}_g^d\right) + (1 - \pi_g(\phi_r)) \tilde{\eta}_e^d \\ &= \frac{1 - \tilde{\eta}_g^d + \tilde{\eta}_e^d}{2} + \frac{1 - \tilde{\eta}_g^d - \tilde{\eta}_e^d}{2} \cos \phi_r \\ &\equiv \pi_0 + \frac{C}{2} \cos \phi_r. \end{aligned} \qquad (\text{II.5})$$

By identifying the terms corresponding to the offset and the contrast, we obtain

$$\tilde{\eta}_e^d = \pi_0 - \frac{C}{2}, \quad (\text{II.6})$$

$$\tilde{\eta}_g^d = 1 - \pi_0 - \frac{C}{2}. \quad (\text{II.7})$$

The fit of the data in Fig. II.3 using the formula (II.5) gives the values $C = (75.0 \pm 0.3)\%$ and $\pi_0 = 0.510 \pm 0.001$. We then get the following values: $\tilde{\eta}_e^d = 0.140 \pm 0.002$ and $\tilde{\eta}_g^d = 0.120 \pm 0.002$.

Detector efficiency

Besides the probabilistic atom number in an atomic sample and the imperfections accounted for by the effective detection errors, another imperfection is that the atoms in a sample may not be detected. As explained in section I.1.1.c, the atoms are ionized, leaving the free electron to be guided by the electron lens and eventually detected by the electron multiplier. Since neither the electron lens nor the electron multiplier works ideally, the atoms may fail to be detected. This results in a limited detector efficiency ϵ_d , which is defined as the ratio between the number of detected atoms over the total number of atoms arriving at the detector.

An efficiency smaller than 1 causes mixing of different atom numbers in the detection results, just like a nonzero detection error causes mixing of the states $|e\rangle$ and $|g\rangle$. For instance, if $\epsilon_d < 1$, a detection result 0^d denoting no atom detected may result from three possibilities: the sample contains 0 atom, or the sample contains 1 or 2 atoms which are missed by the detector. Consequently, the quantum map associated to the detection result 0^d involves those associated to 0, 1 and 2 atoms. In order to determine this mixing, we need to measure the detector efficiency.

The method is as follows. The cavity field is first prepared in its vacuum state. An *injector* atomic sample is prepared in the state $|e\rangle$ and interacts resonantly with the cavity field. It may deposit one photon into the cavity by undergoing a Rabi π pulse. The atomic flux of the injector is weak, e.g. with an average detected atom number $\bar{n}_{\text{at}}^d \simeq 0.06$, such that the probability of containing more than 1 atom in the injector can be neglected. This condition will be checked later. The atom has a limited injection efficiency $P(1_{\text{ph}}|1_{\text{at}})$, which is essentially the conditional probability for injecting 1 photon into the cavity if it contains 1 atom. Since one photon is deposited if the prepared state $|e\rangle$ changes to $|g\rangle$, the probability $P(1_{\text{ph}}|1_{\text{at}})$ can then be measured as the ratio between the number of detection events in $|g\rangle$ for the injector sample and the atom number \bar{n}_{at}^d . We had $P(1_{\text{ph}}|1_{\text{at}}) = 0.70$ while performing the measurements¹. We then measure the number of deposited photons when no atom is detected for the injector sample, an event denoted as 0^d . Let us use $P(1_{\text{at}}|0^d)$ to denote the conditional probability for the injector to contain 1 atom while no atom is detected. Applying the Bayes' law to $P(1_{\text{at}}|0^d)$, we obtain

$$\begin{aligned} P(1_{\text{at}}|0^d) &= \frac{P(1_{\text{at}})}{P(0^d)} P(0^d|1_{\text{at}}) \\ &= \frac{\bar{n}_{\text{at}}^d / \epsilon_d}{1 - \bar{n}_{\text{at}}^d} (1 - \epsilon_d) = \frac{1/\epsilon_d - 1}{1/\bar{n}_{\text{at}}^d - 1}. \end{aligned} \quad (\text{II.8})$$

¹As will be seen later, e.g. in Fig. II.7, we can get a value for $P(1_{\text{ph}}|1_{\text{at}})$ up to 88% in a Rabi π pulse. Here, the π pulse was done in a different experimental situation (different atom-cavity detuning). We suspect that the π pulse was not optimized.

Since an empty sample cannot inject photons into the cavity, the conditional probability for depositing one photon into the cavity can then be expressed as:

$$P(1_{\text{ph}}|0^d) = P(1_{\text{ph}}|1_{\text{at}})P(1_{\text{at}}|0^d). \quad (\text{II.9})$$

Combining (II.8) and (II.9), we can express ϵ_d as

$$\epsilon_d = \left[1 + \frac{P(1_{\text{ph}}|0^d)}{P(1_{\text{ph}}|1_{\text{at}})} \frac{1 - \bar{n}_{\text{at}}^d}{\bar{n}_{\text{at}}^d} \right]^{-1}, \quad (\text{II.10})$$

where the only undetermined parameter now is $P(1_{\text{ph}}|0^d)$.

In order to measure $P(1_{\text{ph}}|0^d)$, we record Ramsey fringes $\pi_{g^d}^{0^d}(\phi_r)$ after the injector tentatively depositing one photon into the cavity but conditioned on 0^d , which are effectively a statistical mixture of the fringes in the vacuum field $\pi_{g^d}(\phi_r)$ and those in the Fock state $|1\rangle$ $\pi_{g^d}^{1_{\text{ph}}}(\phi_r)$, i.e.:

$$\begin{aligned} \pi_{g^d}^{0^d}(\phi_r) &= P(0_{\text{ph}}|0^d)\pi_{g^d}(\phi_r) + P(1_{\text{ph}}|0^d)\pi_{g^d}^{1_{\text{ph}}}(\phi_r) \\ &= \left[1 - P(1_{\text{ph}}|0^d) \right] \pi_{g^d}(\phi_r) + P(1_{\text{ph}}|0^d)\pi_{g^d}^{1_{\text{ph}}}(\phi_r). \end{aligned} \quad (\text{II.11})$$

To enhance the sensitivity of the Ramsey fringes to a single photon, we tune the phase shift per photon ϕ_0 to π . The equation (II.11) can then be expressed as

$$\begin{aligned} \pi_{g^d}^{0^d}(\phi_r) &= \left[1 - P(1_{\text{ph}}|0^d) \right] \pi_{g^d}(\phi_r) + P(1_{\text{ph}}|0^d)\pi_{g^d}(\phi_r - \pi) \\ &= \pi_0 + \frac{C}{2} \left[1 - 2P(1_{\text{ph}}|0^d) \right] \cos(\phi_r). \end{aligned} \quad (\text{II.12})$$

Then we record the fringes $\pi_{g^d}^{0^d}(\phi_r)$ and $\pi_{g^d}(\phi_r)$, as shown in Fig. II.4.

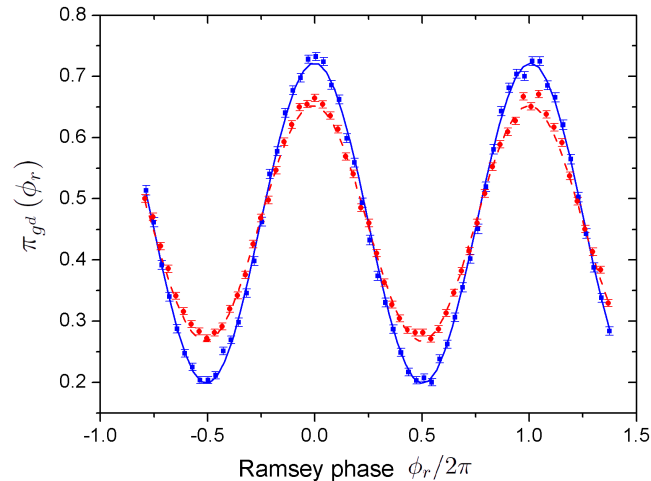


Figure II.4. Calibration of the detector efficiency. Ramsey fringes in the vacuum state $\pi_{g^d}(\phi_r)$ (larger contrast), and $\pi_{g^d}^{0^d}(\phi_r)$ (smaller contrast). The solid curves are fits to the data.

From the fits of the curves, we get $P(1_{\text{ph}}|0^d) = 0.13$. Given that $P(1_{\text{ph}}|1_{\text{at}}) = 0.70$ and $\bar{n}_{\text{at}}^d = 0.06$, we obtain

$$\epsilon_d = 0.25 \pm 0.02, \quad (\text{II.13})$$

with the error on the measured value estimated by repeating the same measurement several times. With this efficiency, the real atomic flux is given by $\bar{n}_{\text{at}} = \bar{n}_{\text{at}}^d / \epsilon_d = 0.24$, which leads to a probability of having more than 1 atom $P_{n>1} \simeq 2.5\%$. This number is negligible, supporting our approximation of neglecting events with more than 1 atom in the entire calculation.

Mixing of the Kraus operators

Knowing the detector efficiency and the effective detection errors, we are able to construct the quantum maps associated to all possible detection results. In order to distinguish the detection results from the ideal detection results listed in S^i , we add a superscript ‘ d ’ to these states, which also constitute a set S^d defined as

$$S^d \equiv \{0^d, e^d, g^d, e^d e^d, e^d g^d, g^d g^d\}. \quad (\text{II.14})$$

If a state $q \in S^i$ is detected by a virtual ideal detector, the field state is transformed, with the quantum map described by the operator \hat{S}_q . However, in the experimental situation, we do not have access to q . Instead, our detector provides the result $q^d \in S^d$, which may result from several ideal detection results. In order to obtain the corresponding quantum map, we need first to determine the contribution of all possible q to q^d , i.e. the conditional probabilities $P(q^d|q)$. They are given in Table. II.1.

| $q^d \backslash q$ | 0 | e | g | ee | eg | gg |
|--------------------|---|----------------------------------|----------------------------------|--|---|---|
| 0^d | 1 | $1-\epsilon_d$ | $1-\epsilon_d$ | $(1-\epsilon_d)^2$ | $(1-\epsilon_d)^2$ | $(1-\epsilon_d)^2$ |
| e^d | 0 | $\epsilon_d(1-\tilde{\eta}_e^d)$ | $\epsilon_d\tilde{\eta}_g^d$ | $2\epsilon_d(1-\epsilon_d)(1-\tilde{\eta}_e^d)$ | $\epsilon_d(1-\epsilon_d)(1-\tilde{\eta}_e^d + \tilde{\eta}_g^d)$ | $2\epsilon_d(1-\epsilon_d)\tilde{\eta}_g^d$ |
| g^d | 0 | $\epsilon_d\tilde{\eta}_e^d$ | $\epsilon_d(1-\tilde{\eta}_g^d)$ | $2\epsilon_d(1-\epsilon_d)\tilde{\eta}_e^d$ | $\epsilon_d(1-\epsilon_d)(1 + \tilde{\eta}_e^d - \tilde{\eta}_g^d)$ | $2\epsilon_d(1-\epsilon_d)(1-\tilde{\eta}_g^d)$ |
| $e^d e^d$ | 0 | 0 | 0 | $\epsilon_d^2(1-\tilde{\eta}_e^d)^2$ | $\epsilon_d^2\tilde{\eta}_g^d(1-\tilde{\eta}_e^d)$ | $\epsilon_d^2\tilde{\eta}_g^{d2}$ |
| $e^d g^d$ | 0 | 0 | 0 | $\epsilon_d^2\tilde{\eta}_e^d(1-\tilde{\eta}_e^d)$ | $\epsilon_d^2(\tilde{\eta}_e^d\tilde{\eta}_g^d + (1-\tilde{\eta}_e^d)(1-\tilde{\eta}_g^d))$ | $2\epsilon_d^2\tilde{\eta}_g^d(1-\tilde{\eta}_g^d)$ |
| $g^d g^d$ | 0 | 0 | 0 | $\epsilon_d^2\tilde{\eta}_e^{d2}$ | $\epsilon_d^2\tilde{\eta}_e^d(1-\tilde{\eta}_g^d)$ | $\epsilon_d^2(1-\tilde{\eta}_g^d)^2$ |

Table II.1. The conditional probability $P(q^d|q)$ related to the detector efficiency and the effective detection errors, which account for the imperfect Ramsey fringes.

Eventually, the quantum map associated to a detection result $q^d \in S^d$ is simply a statistical mixture of all quantum maps associated to the ideal detection results q which may lead to q^d , i.e.:

$$\mathbb{M}_{q^d}^{\text{QND}} \rho = \frac{\sum_{q \in S^i} P(q^d|q) \hat{S}_q \rho \hat{S}_q^\dagger}{\text{Tr} \left(\sum_{q \in S^i} P(q^d|q) \hat{S}_q \rho \hat{S}_q^\dagger \right)}. \quad (\text{II.15})$$

If the atomic state is not yet detected, the quantum map can be expressed as:

$$\mathbb{N}^{\text{QND}} \rho = \sum_{q \in S^i} \hat{S}_q \rho \hat{S}_q^\dagger. \quad (\text{II.16})$$

II.3 Actuator samples

Having completely described the interaction between sensors and the cavity field, let us now consider the actuators. Same as for the sensors, we also consider up to 2 atoms for the actuators. The cases with 1 and 2 atoms are presented following the same plan: first we explain the ideal interaction between the atom and cavity field, then we measure the experimental imperfections. At the end, we give the quantum maps associated to all possible detection results of a sample.

II.3.1 Sample with 1 atom

II.3.1.a Ideal resonant interaction

In this part, we consider the ideal resonant interaction between the cavity field and an atom prepared in $|e\rangle$ or $|g\rangle$. After interaction, the detection of the atomic states provides information on the cavity field, and transforms the field state.

Atoms in $|e\rangle$

Consider the interaction of an atom prepared in the state $|e\rangle$ with a Fock state $|n\rangle$. As in (I.70), the evolving atom-cavity state is given by

$$|\psi_{ac}(t)\rangle = \cos \theta_n |e, n\rangle - i \sin \theta_n |g, n+1\rangle, \quad (\text{II.17})$$

where we have defined

$$\theta_n = \frac{\Omega_n t}{2}. \quad (\text{II.18})$$

If the field in the cavity is initially in $|\psi_c\rangle = \sum c_n |n\rangle$ (here and afterwards, the summations are taken over all non-negative integers), its interaction with an atom prepared in $|e\rangle$ leads to

$$\sum c_n |e, n\rangle \longrightarrow \sum c_n \cos \theta_n |e, n\rangle - i \sum c_n \sin \theta_n |g, n+1\rangle. \quad (\text{II.19})$$

The projective detection of the atomic state transforms the field state, with the quantum maps described by the following Kraus operators:

$$\begin{aligned} \hat{R}_{e,e} &= \sum \cos \theta_n |n\rangle \langle n|, \\ \hat{R}_{e,g} &= \sum \sin \theta_n |n+1\rangle \langle n|, \end{aligned} \quad (\text{II.20})$$

where the irrelevant phase factor $-i$ has been omitted in the definition of $\hat{R}_{e,g}$. The operator $\hat{R}_{e,e}$ ($\hat{R}_{e,g}$) corresponds to the transformation if the state $|e\rangle$ ($|g\rangle$) is detected. As a convention in this manuscript, the subscript letters X, Y (e.g. e, e) denote atomic states with X being the prepared state and Y being the detected state.

The transformations of the field state are given by

$$\rho \mapsto \frac{\hat{R}_{e,e}\rho\hat{R}_{e,e}^\dagger}{\text{Tr}(\hat{R}_{e,e}\rho\hat{R}_{e,e}^\dagger)} \quad \rho \mapsto \frac{\hat{R}_{e,g}\rho\hat{R}_{e,g}^\dagger}{\text{Tr}(\hat{R}_{e,g}\rho\hat{R}_{e,g}^\dagger)}. \quad (\text{II.21})$$

Since these transformations do not couple the diagonal elements of ρ to the non-diagonal elements, we have the following transformations of the photon number distribution:

$$P_{e,e}(n) = \frac{P(n)\pi_{e,e}(n)}{\sum P(m)\pi_{e,e}(m)} \quad P_{e,g}(n) = \frac{P(n-1)\pi_{e,g}(n-1)}{\sum P(m-1)\pi_{e,g}(m-1)}, \quad (\text{II.22})$$

where the probabilities $\pi_{e,e}(n)$ or $\pi_{e,g}(n)$ for detecting $|e\rangle$ or $|g\rangle$ as functions of n are defined as:

$$\begin{aligned} \pi_{e,e}(n) &\equiv \cos^2 \theta_n, \\ \pi_{e,g}(n) &\equiv \sin^2 \theta_n. \end{aligned} \quad (\text{II.23})$$

Here and afterwards, we define $P(-1) = 0$.

Let us illustrate the transformations (II.22) by considering an example. Suppose that a field with a flat photon number distribution truncated at 7 photons interacts with an atom prepared in $|e\rangle$. The interaction time t is adjusted such that the interaction amounts to a 2π pulse in $|4\rangle$. The initial and modified photon number distributions are shown in Fig. II.5.

The panel (a) shows the initial $P(n)$ and the probabilities $\pi_{e,e}(n)$. From panel (b), we see that if $|e\rangle$ is detected, the probabilities for $|4\rangle$ and neighboring Fock states are enhanced, whereas those for states like $|0\rangle$ or $|7\rangle$ are reduced. This is because $P_{e,e}(n)$ is proportional to $\pi_{e,e}(n)$, so it takes a form similar to that of $\pi_{e,e}(n)$ shown in the panel (a). On the other hand, if the state $|g\rangle$ is detected, the transformed photon number distribution, as shown in the panel (c), has the following characteristics. First, the state $|5\rangle$ disappears, because $\pi_{e,g}(4) = 0$, which means that the initial field cannot be in $|4\rangle$, otherwise the atom could not have emitted a photon. As a result, the state $|5\rangle$ cannot exist in the transformed field. In fact, in this example the state $|4\rangle$ is a trapping state [33] of the field. Once the field state reaches $|4\rangle$, no more photons can be emitted into the cavity. Secondly, $P(0) = 0$, since we know that the atom has transferred energy to the cavity, so the cavity field cannot be in the vacuum state now. Thirdly, the state $|8\rangle$ beyond the truncated subspace appears in the field, because $|7\rangle$ leads to $|8\rangle$ after absorbing one photon from the atom.

If the atom is not yet detected, the field state transformation reads

$$\rho \mapsto \hat{R}_{e,e}\rho\hat{R}_{e,e}^\dagger + \hat{R}_{e,g}\rho\hat{R}_{e,g}^\dagger. \quad (\text{II.24})$$

The new photon number distribution is then given by

$$P_{e,x}(n) = P(n)\pi_{e,e}(n) + P(n-1)\pi_{e,g}(n-1), \quad (\text{II.25})$$

with the letter “ x ” in the subscript of P meaning that the atomic state is not yet detected. $P_{e,x}(n)$ contains two contributions, one depending on $P(n-1)$ and the other depending on $P(n)$. The former manifests the coupling between neighboring Fock states. In general, $P_{e,x}(n) \neq P(n)$, which means that the photon number distribution of the field is modified even if the atom is not yet detected! On the contrary, the atom performing the QND measurement

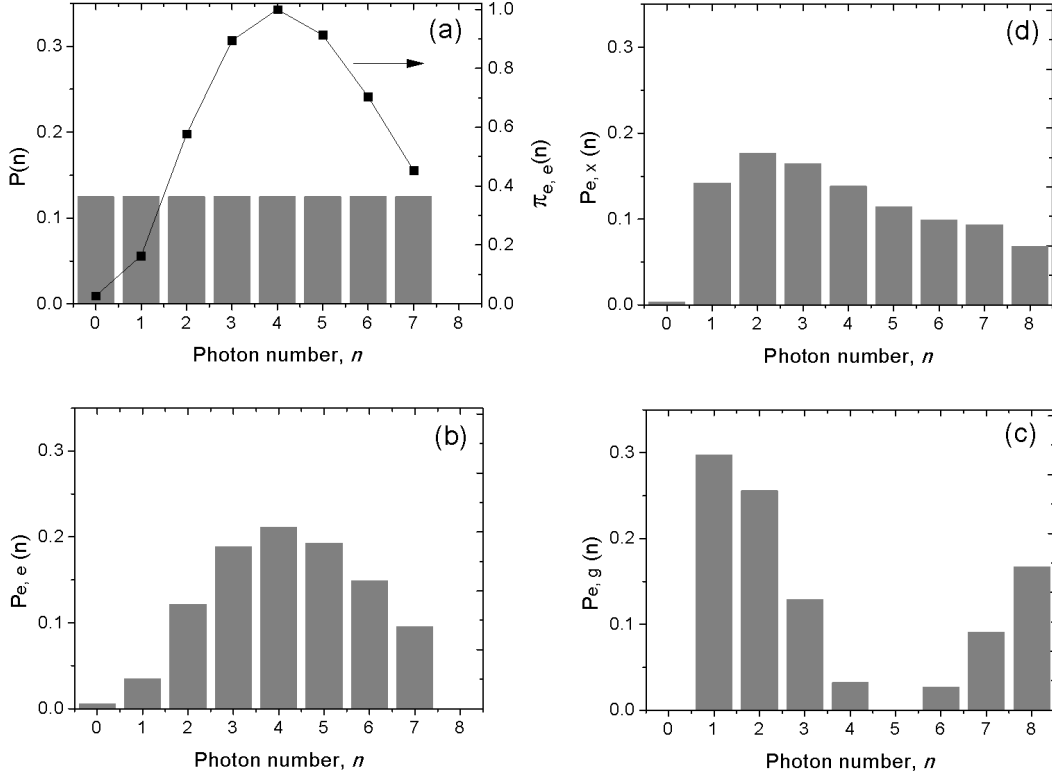


Figure II.5. Modification of the photon number distribution by the resonant interaction with an atom prepared in $|e\rangle$ and the subsequent detection of its state. The interaction time is chosen such that the interaction amounts to a 2π pulse in $|4\rangle$. The solid squares in (a) show the probabilities for detecting the state $|e\rangle$. The histograms show the photon number distributions: initial flat bounded (a); after detecting the state $|e\rangle$ (b); after detecting the state $|g\rangle$ (c); atomic state is not yet detected (d).

leaves the photon number distribution unchanged, if it is not yet detected. The panel (d) of Fig. II.5 shows $P_{e,x}(n)$, where the state $|8\rangle$ appears and $|0\rangle$ is reduced. On the average, an atom in $|e\rangle$ emits photons into the cavity.

Remark: The fact that the field state may go beyond the truncated subspace warns us that in our calculations we need to be careful when choosing the size of the truncated Hilbert space.

Atoms in $|g\rangle$

Similarly, if the atom is initially in $|g\rangle$, we have:

$$\sum c_n |n\rangle \otimes |g\rangle \longrightarrow -i \sum c_{n+1} \sin \theta_n |e, n\rangle + \sum [c_{n+1} \cos \theta_n |g, n+1\rangle + c_0 |g, 0\rangle]. \quad (\text{II.26})$$

The projective detection of the atomic state also transforms the field state, with the

quantum maps described by the following Kraus operators:

$$\begin{aligned}\hat{R}_{g,e} &= \sum \sin \theta_n |n\rangle\langle n+1|, \\ \hat{R}_{g,g} &= \sum \cos \theta_n |n+1\rangle\langle n+1| + |0\rangle\langle 0|.\end{aligned}\quad (\text{II.27})$$

The transformations of the density matrix can be obtained by substituting the operators $\hat{R}_{e,e}$ and $\hat{R}_{e,g}$ with $\hat{R}_{g,e}$ and $\hat{R}_{g,g}$ in (II.21). Here I only give the transformation of the photon number distributions:

$$P_{g,e}(n) = \frac{P(n+1) \pi_{g,e}(n+1)}{\sum P(m+1) \pi_{g,e}(m+1)} \quad P_{g,g}(n) = \frac{P(n) \pi_{g,g}(n)}{\sum P(m) \pi_{g,g}(m)}, \quad (\text{II.28})$$

where the probabilities $\pi_{g,e}(n)$ or $\pi_{g,g}(n)$ for detecting $|e\rangle$ or $|g\rangle$ as functions of n are defined as

$$\begin{aligned}\pi_{g,e}(n) &\equiv \sin^2 \theta_{n-1}, \\ \pi_{g,g}(n) &\equiv \cos^2 \theta_{n-1},\end{aligned}\quad (\text{II.29})$$

One example of these modifications of the photon number distribution is shown in Fig. II.6. The interaction time t is adjusted such that the interaction amounts to a 2π pulse in $|4\rangle$. The panel (a) shows the initial flat bounded photon number distribution and the probability $\pi_{g,g}(n)$. As with the atomic state $|e\rangle$, if the detected atomic state is the same as the prepared one, $P(n)$ is simply modified by a multiplication factor $\pi_{g,g}(n)$, leading to $P_{g,g}(n)$, as shown in the panel (b). In this case, the 2π pulse in $|4\rangle$ corresponds to a π pulse in $|1\rangle$. So if the initial cavity field was in $|1\rangle$ before the interaction, the atom would have absorbed a photon, leading to a vacuum field. Otherwise, since the atomic state is not changed, the cavity field cannot be transformed into $|1\rangle$. Consequently, we see that $P_{g,g}(1) = 0$. If the atom is detected in $|e\rangle$, the transformed photon number distribution $P_{g,e}(n)$ is shown in the panel (c). In this case, $P_{g,e}(3) = 0$, because the initial field cannot be in $|4\rangle$, otherwise the atom could not have absorbed one photon. As a result, $|3\rangle$ cannot exist in the transformed field.

If the atom is not yet detected, the photon number distribution is given by

$$P_{g,x}(n) = P(n) \pi_{g,g}(n) + P(n+1) \pi_{g,e}(n+1). \quad (\text{II.30})$$

$P_{g,x}(n)$ also includes two terms, with the latter resulting from the coupling of neighboring Fock states, and in general $P_{g,x}(n) \neq P(n)$. The panel (d) of Fig. II.6 shows $P_{g,x}(n)$. On the average, an atom in $|g\rangle$ absorbs photons from the cavity field.

II.3.1.b Imperfect Rabi oscillations

The ideal Kraus operators (II.20) and (II.27) are obtained by assuming ideal Rabi oscillations in the Fock states. However, in real experiments, this is not exactly true. Let us show the measured Rabi oscillations in vacuum and see how to modify the ideal Kraus operators.

Vacuum Rabi oscillations

The experimental procedure for recording the vacuum Rabi oscillations is as follows. About 20 atoms prepared in $|g\rangle$ absorb residual thermal photons by undergoing a rapid adiabatic passage, eventually preparing the cavity in the vacuum state. We then send an atomic sample

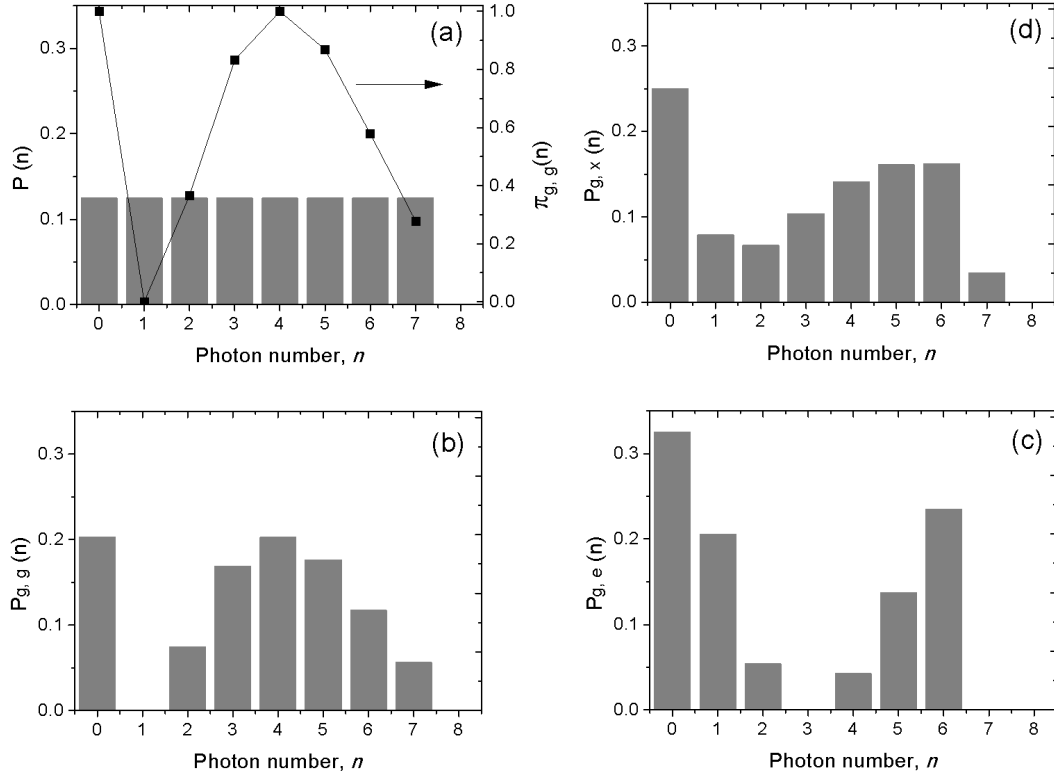


Figure II.6. Modification of the photon number distribution by the resonant interaction with an atom prepared in $|g\rangle$ and the subsequent detection of its state. The interaction time is chosen such that the interaction amounts to a 2π pulse in $|4\rangle$. The solid squares in (a) show the probabilities for detecting the state $|g\rangle$. The histograms show the photon number distributions: initial flat bounded (a); after detecting the state $|g\rangle$ (b); after detecting the state $|e\rangle$ (c); atomic state is not yet detected (d).

prepared in the state $|e\rangle$, which is tuned to be on resonance with the cavity field by applying a potential pulse on one of the cavity mirrors, with the pulse center fixed at the moment when the sample arrives at the center of the cavity. The duration T_{int} of the pulse determining the interaction time is varied. Since the field mode has a Gaussian profile along the direction of the atomic beam, the sample sees different field amplitudes and thus has different Rabi frequencies along its path. To account for the variations of the Rabi frequencies, we can define an effective interaction time T_{eff} by

$$\int_{-T_{\text{int}}/2}^{+T_{\text{int}}/2} \Omega_0 f(vt) dt \equiv \Omega_0 T_{\text{eff}}. \quad (\text{II.31})$$

where $f(vt) = e^{-\frac{(vt)^2}{w_0^2}}$ describes the amplitude profile of the microwave electric field, with v being the velocity of the sample, and w_0 being the waist of the mode.

The probability of the detection events g^d as a function of T_{eff} is shown in Fig. II.7. The

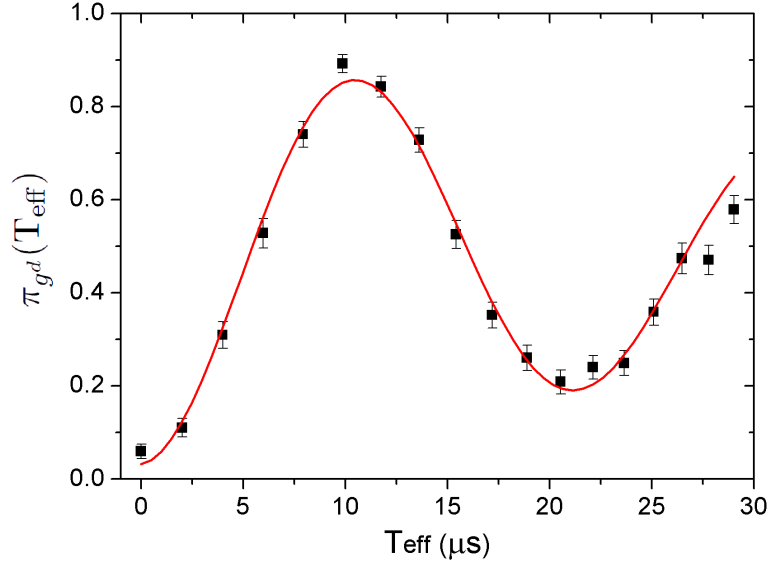


Figure II.7. Vacuum Rabi oscillations. The solid squares with error bars are the experimental data. The solid curve is a fit to the data with a formula given in the text.

solid curve is a fit to the data with a phenomenological function:

$$y(t) = y_c - \frac{A}{2} e^{-t/\tau_0} \cos(\Omega_0 t). \quad (\text{II.32})$$

The fit gives the following parameters: offset $y_c = 0.49 \pm 0.02$, contrast $A = 0.90 \pm 0.03$, vacuum Rabi frequency $\Omega_0/2\pi = 46.3 \pm 0.3$ kHz, damping time $\tau_0 = 50 \pm 8$ μs. We see that the vacuum Rabi oscillation has a contrast of 90% and damping time about twice its oscillation period. These imperfections may be due to inhomogeneous atom-cavity detuning, inhomogeneity of the vacuum Rabi frequency, preparation and detection errors of the atomic states.

Damping of the contrast

In the resonant regime, $\delta = 0$. But what if the detuning is not always 0? In fact, in order to tune the atom and the cavity field on resonance, we apply a potential ~ -2.5 V on one of the cavity mirrors while the other remains at 0 V. The potential difference generates a static electric field ~ 0.9 V/cm. Since the mirror surface is curved and since the atomic beam has a transverse diameter of about 0.7 mm, the atoms actually see different amplitudes of the static electric field while interacting with the cavity field. Due to the quadratic Stark effect, these different field amplitudes result in nonuniform values of δ . According to our estimation, the variation of δ during the interaction time is about 5 kHz. Given that $\Omega_0/2\pi = 46.3$ kHz, this inhomogeneity shifts the offset of the vacuum Rabi oscillations by about 1% and reduces the contrast by about 2%. So this imperfection cannot account alone for the reduced contrast of the Rabi oscillations shown in Fig. II.7.

Another possible inhomogeneity can occur on the vacuum Rabi frequency Ω_0 , because the amplitude of the cavity field varies along the axis of the cavity. The profile of the field amplitude as a function of the vertical position z can be approximately expressed as:

$$\mathcal{E}(z) = \mathcal{E}_0 \left| \cos \left(\frac{2\pi}{\lambda} z \right) \right|, \quad (\text{II.33})$$

with $\lambda = 5.87$ mm.

Since the spread of the atomic beam along the z axis is about 0.7 mm, the microwave field amplitude can have a variation of up to about 10%, which leads to a variation of Ω_0 of about $\Delta = 5$ kHz. But in fact, we suspect that the atomic beam is also displaced with respect to the center of the cavity, because we now have a vacuum Rabi frequency of 46.3 kHz instead of 49 kHz measured several years ago. The current position of the atomic beam was chosen by maximizing the detected atom number. It could be that at this position the beam does not pass through the center of the cavity. We estimate that a displacement of 0.3 mm is enough to reduce the Rabi frequency from 49 kHz to 46.3 kHz. In this case, within the spread of the atomic beam, the Rabi frequency varies by up to 15 kHz, which contributes to the damping of the contrast.

Besides a displacement of the atomic beam, there might be other unknown imperfections which deteriorate the vacuum Rabi oscillation. For the time being, we do not search for all those imperfections. But instead, we introduce an effective inhomogeneity denoted as ζ to Ω_0 in order to account for the observed exponential damping of the contrast. The value of ζ has an unknown probability density function $p(\zeta)$. Based on the fact that (II.32) fits well the data, we can write down:

$$\int p(\zeta) \cos [(\Omega_0 + \zeta) t] d\zeta \simeq e^{-t/\tau_0} \cos (\Omega_0 t). \quad (\text{II.34})$$

Here, I have assumed implicitly that the integration is taken within a proper range of ζ , and that the integral exists. For the state $|e, n\rangle$, we have

$$\int p(\zeta) \cos [\sqrt{n+1} (\Omega_0 + \zeta) t] d\zeta \simeq e^{-t\sqrt{n+1}/\tau_0} \cos (\Omega_0 t \sqrt{n+1}) \equiv e^{-t/\tau_n} \cos (\Omega_n t). \quad (\text{II.35})$$

We find that the damping rate $1/\tau_n$ is also proportional to $\sqrt{n+1}$, i.e.:

$$1/\tau_n = \sqrt{n+1}/\tau_0. \quad (\text{II.36})$$

Since the vacuum Rabi oscillations are damped, the ideal Kraus operators (II.20) and (II.27) need to be modified. After this modification, the Kraus operators can be expressed as:

$$\begin{aligned} \hat{\mathcal{R}}_{e,e} &= \sum \sqrt{\frac{1 + e^{-t/\tau_n} \cos (\Omega_n t)}{2}} |n\rangle \langle n| \\ \hat{\mathcal{R}}_{e,g} &= \sum \sqrt{\frac{1 - e^{-t/\tau_n} \cos (\Omega_n t)}{2}} |n+1\rangle \langle n| \end{aligned} \quad (\text{II.37})$$

and

$$\begin{aligned} \hat{\mathcal{R}}_{g,e} &= \sum \sqrt{\frac{1 - e^{-t/\tau_n} \cos (\Omega_n t)}{2}} |n\rangle \langle n+1| \\ \hat{\mathcal{R}}_{g,g} &= \sum \sqrt{\frac{1 + e^{-t/\tau_n} \cos (\Omega_n t)}{2}} |n+1\rangle \langle n+1| + |0\rangle \langle 0|, \end{aligned} \quad (\text{II.38})$$

where Ω_n and $1/\tau_n$ denote the Rabi frequency and damping rate of the oscillations $|e, n\rangle \longleftrightarrow |g, n+1\rangle$.

Let us consider the Rabi oscillations in the Fock state $|n\rangle$. Suppose that the atoms in the states $|e\rangle$ and $|g\rangle$ interact ideally with the field. The interaction during time t leads to the probabilities (II.23) and (II.29). But as discussed before, in order to account for the damping of the contrast, we need to introduce exponentially damping terms into the oscillating functions. After this modification, those probabilities can be expressed as:

$$\begin{aligned}\tilde{\pi}_{e,g}(n,t) &= \frac{1}{2} \left(1 - e^{-t/\tau_n} \cos(\Omega_n t) \right) \\ \tilde{\pi}_{g,g}(n,t) &= \frac{1}{2} \left(1 + e^{-t/\tau_{n-1}} \cos(\Omega_{n-1} t) \right),\end{aligned}\quad (\text{II.39})$$

Reduction of the contrast and shift of the offset

So far, we have discussed the damping of the contrast of the Rabi oscillations. Besides this imperfection, we also notice that $\pi_{g^d}(t=0) \neq 0$ on the curve in Fig. II.7. The value $\pi_{g^d}(0)$ is only related to the preparation and detection of the atomic states. Its nonzero value means that either the initial atomic state is not pure or that the state $|e\rangle$ is erroneously detected as $|g\rangle$ or both. These imperfections are characterized by the preparation and detection errors.

The detection errors η_g^d or η_e^d are defined as the probabilities that the atomic states $|g\rangle$ or $|e\rangle$ are erroneously detected:

$$\eta_e^d = P(g^d|e) \qquad \eta_g^d = P(e^d|g), \quad (\text{II.40})$$

where g^d and e^d , as introduced in section II.2, denote the events that a signal is generated in the detection channel $|g\rangle$ and $|e\rangle$, respectively. It is worth to emphasize that the detection errors defined here are only related to the imperfections of the detector itself, instead of being parameters that account for several experimental imperfections as those in (II.4).

The preparation errors are defined as:

$$\eta_g^p = P(e|g^p) \qquad \eta_e^p = P(g|e^p), \quad (\text{II.41})$$

where e^p and g^p denote the prepared states of an atom. In real experimental situation, we prepare a RE (RG) sample, which may contain 0, 1 or 2 atoms. If the sample contains 1 atom, it is denoted as e^p (g^p). If the sample contains 2 atoms, it is denoted as $e^p e^p$ ($g^p g^p$) in the following. Since the current section is devoted to the ‘‘one-atom’’ event, we only consider the samples with 1 atom. In fact, e^p and g^p are statistical mixtures of $|e\rangle$ and $|g\rangle$. They are described by the following density matrices:

$$\rho_{e^p} = (1 - \eta_e^p) |e\rangle\langle e| + \eta_e^p |g\rangle\langle g| \quad (\text{II.42})$$

$$\rho_{g^p} = \eta_g^p |e\rangle\langle e| + (1 - \eta_g^p) |g\rangle\langle g|. \quad (\text{II.43})$$

Let us consider the Rabi oscillations starting from the mixture e^p in $|n\rangle$ or g^p in $|n\rangle$. By exploiting the expressions (II.39), the probabilities for detecting $|g\rangle$ (by a virtual ideal detector) can be expressed as

$$\begin{aligned}\tilde{\pi}_{e^p,g}(n,t) &= (1 - \eta_e^p) \tilde{\pi}_{e,g}(n,t) + \eta_e^p \tilde{\pi}_{g,g}(n,t) \\ \tilde{\pi}_{g^p,g}(n,t) &= \eta_g^p \tilde{\pi}_{e,g}(n,t) + (1 - \eta_g^p) \tilde{\pi}_{g,g}(n,t).\end{aligned}\quad (\text{II.44})$$

Due to the detection errors, the atomic states $|e\rangle$ and $|g\rangle$ can both be detected as g^d or e^d . The detection of atomic states then leads to the following probabilities for obtaining g^d :

$$\begin{aligned}\tilde{\pi}_{e^p, g^d}(n, t) &= \left(1 - \eta_g^d\right) \tilde{\pi}_{e^p, g}(n, t) + \eta_e^d \left(1 - \tilde{\pi}_{e^p, g}(n, t)\right), \\ \tilde{\pi}_{g^p, g^d}(n, t) &= \left(1 - \eta_g^d\right) \tilde{\pi}_{g^p, g}(n, t) + \eta_e^d \left(1 - \tilde{\pi}_{g^p, g}(n, t)\right).\end{aligned}\quad (\text{II.45})$$

Combining equations (II.39), (II.44) and (II.45), we obtain the following expressions:

$$\begin{aligned}\tilde{\pi}_{e^p, g^d}(n, t) &= \frac{1 + \eta_e^d - \eta_g^d}{2} + \frac{1 - \eta_g^d - \eta_e^d}{2} \left[\eta_e^p e^{-t/\tau_{n-1}} \cos(\Omega_{n-1}t) - (1 - \eta_e^p) e^{-t/\tau_n} \cos(\Omega_n t) \right] \\ \tilde{\pi}_{g^p, g^d}(n, t) &= \frac{1 + \eta_e^d - \eta_g^d}{2} + \frac{1 - \eta_g^d - \eta_e^d}{2} \left[(1 - \eta_g^p) e^{-t/\tau_{n-1}} \cos(\Omega_{n-1}t) - \eta_g^p e^{-t/\tau_n} \cos(\Omega_n t) \right].\end{aligned}\quad (\text{II.46})$$

Particularly, the vacuum Rabi oscillations starting from e^p in $|0\rangle$ or g^p in $|1\rangle$ are given by

$$\tilde{\pi}_{e^p, g^d}(0, t) = \frac{1 + \eta_e^d - \eta_g^d}{2} - \frac{1 - \eta_g^d - \eta_e^d}{2} (1 - \eta_e^p) e^{-t/\tau_0} \cos(\Omega_0 t) \quad (\text{II.47})$$

$$\tilde{\pi}_{g^p, g^d}(1, t) = \frac{1 + \eta_e^d - \eta_g^d}{2} + \frac{1 - \eta_g^d - \eta_e^d}{2} \left[(1 - \eta_g^p) e^{-t/\tau_0} \cos(\Omega_0 t) - \eta_g^p e^{-t/\tau_1} \cos(\Omega_1 t) \right]. \quad (\text{II.48})$$

By comparing (II.47) with (II.32), we see that the preparation and detection errors can shift the offset and reduce the contrast of the vacuum Rabi oscillations. In order to determine these errors, we record oscillations starting from e^p in $|0\rangle$ and g^p in the prepared ‘‘photon number state’’ ρ_{1^p} , with the results shown in Fig. II.8. Here and afterwards, we use ρ_{n^p} to denote a prepared state with n^p photons, which is actually a statistical mixture of several photon number states. The state ρ_{1^p} is prepared by the QND decimation process. Initially a coherent field is injected into the cavity. Repeated 4-phase QND measurements performed by ~ 100 successive atoms project the field into photon number states randomly, among which those states with $P(1) \geq 90\%$ are post-selected. In this way, we obtain a photon number distribution with $P(1) = 93.4\%$, $P(0) = 4.5\%$, $P(2) = 2.1\%$, and sum of the others smaller than 0.1%.

Note that the data in the panel (a) are not the same as those in Fig. II.7, although their parameters, such as contrast, offset, frequency and damping time are essentially identical within error bars. Here, I use the data in the panel (a), because they are taken under the same experimental conditions as those of the data in the panel (b).

From (II.47) and (II.48), we obtain

$$\tilde{\pi}_{e^p, g^d}(0, t=0) = \eta_e^d + \eta_e^p, \quad (\text{II.49})$$

$$\tilde{\pi}_{g^p, g^d}(1, t=0) = \eta_g^d + \eta_g^p, \quad (\text{II.50})$$

where since $(\eta_e^d, \eta_e^p, \eta_g^d, \eta_g^p) \ll 1$, the second order terms have been neglected. From the measured values of $\pi_{g^d}(0)$, we get

$$\begin{aligned}\eta_g^d + \eta_g^p &= 0.03 \pm 0.01 \\ \eta_e^d + \eta_e^p &= 0.07 \pm 0.01\end{aligned}\quad (\text{II.51})$$

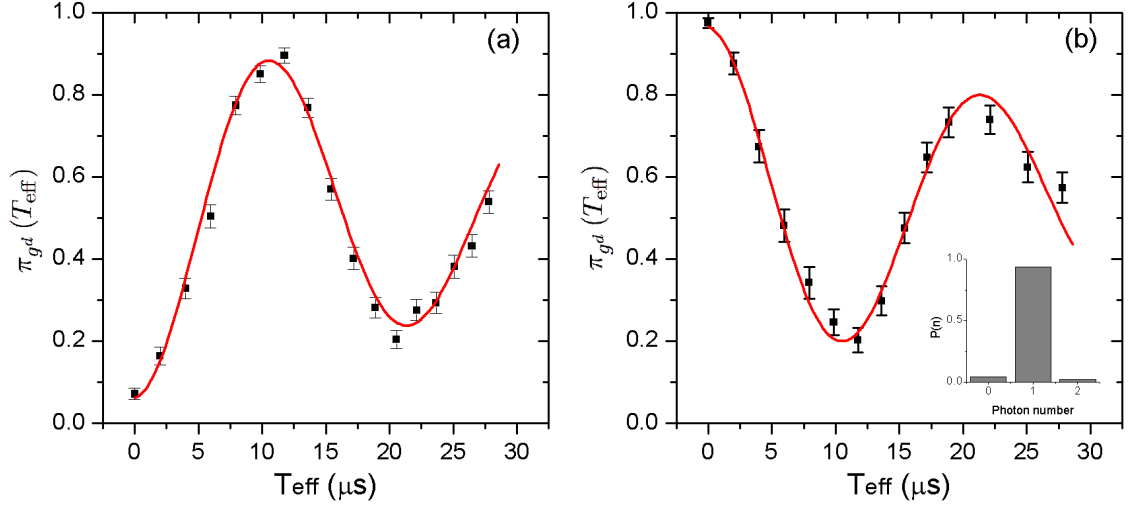


Figure II.8. Vacuum Rabi oscillations starting from e^p in $|0\rangle$ (a) or g^p in ρ_{1^p} (b). The inset of (b) shows the $P(n)$ of the prepared state ρ_{1^p} . The curves are fits to the data with a method explained in the text.

Let us first discuss η_g^p and η_g^d . As explained in section I.1.1.b, the state $|g\rangle$ is prepared by a two-photon transition from the circular level [52c], during which the transition to $|e\rangle$ is negligible, because it is far off resonance. So the prepared state should be pure, i.e. $\eta_g^p = 0$. Hence, we consider that $\eta_g^d = 0.03 \pm 0.01$.

Since the errors η_e^d and η_e^p are linked by (II.51), the Rabi oscillations can be fitted with the three parameters: Ω_0 , τ_0 and η_e^p . It is worth to mention that since the prepared state ρ_{1^p} is not pure, we need also to take into account the effect of other Fock states in the fit process. The main contamination is the neighboring states, i.e. $|2\rangle$ and $|0\rangle$. The measured histogram of $P(n)$ is shown in the inset of the panel (b). In the fit, the frequency and damping rate of the Rabi oscillations starting from $|g, 2\rangle$ are set as $\sqrt{2}\Omega_0$ and $\sqrt{2}/\tau_0$ as has been assumed in (II.36).

We fit the data in the panels (a), (b) together and obtain the following parameters:

$$\Omega_0/2\pi = 46.0 \pm 0.3 \text{ kHz} \quad 1/\tau_0 = 0.022 \pm 0.006 \mu\text{s}^{-1}, \quad (\text{II.52})$$

and the values for preparation and detection errors as given in Table. II.2. Substituting these values into (II.47), we obtain an offset of 0.50 ± 0.01 and a contrast of 0.91 ± 0.01 for the vacuum Rabi oscillations, which agree well with the fit using (II.32).

| η_e^p | η_g^p | η_e^d | η_g^d |
|-----------------|------------|-----------------|-----------------|
| 0.04 ± 0.01 | 0 | 0.03 ± 0.01 | 0.03 ± 0.01 |

Table II.2. Preparation and detection errors of the atomic states.

II.3.1.c Rabi oscillations in the Fock states

In order to explain the damping of the contrast of the vacuum Rabi oscillations, we introduced an effective inhomogeneity to Ω_0 , which leads to the expression (II.36). In this section, we

check this expression experimentally by recording Rabi oscillations in the prepared photon number states with up to 6 photons.

The photon states are prepared by the QND decimation process on a coherent field. Repeated 4-phase QND measurements performed by ~ 100 successive atoms project the field into photon number states randomly. An atom prepared in state e^p or g^p interacts resonantly with the cavity field during a variable interaction time T_{int} , which is converted into T_{eff} according to (II.31). A state is declared to be prepared in the state ρ_{n^p} , with $1 \leq n^p \leq 6$, once the probability of having n^p is larger than a certain threshold, i.e. $P(n^p) \geq F(n^p)$. We choose $F(n^p)$ to be 90%, 85%, 80%, 75%, 70% and 60% for n^p from 1 to 6, respectively. Their interactions with the atoms lead to the probabilities $\pi_{g^d}(T_{\text{eff}})$ displayed in Fig. II.9 and Fig. II.10.

From the measured data, we can already see oscillating signals. But they are not directly the Rabi oscillations in Fock states, because the preparation and detection errors of atomic states come into play, and because that the prepared states are not pure Fock states. So in order to extract the parameters for the Rabi oscillations of a pure atomic state in a Fock state, we perform a fit to the data.

The main contaminations to the prepared states ρ_{n^p} come from the neighboring states $|n^p \pm 1\rangle$ (see the inset of each panel, the probabilities of these three states sum to more than 98%). In the fit process, we only consider the three states $|n^p\rangle$ and $|n^p \pm 1\rangle$ for each prepared state ρ_{n^p} , with their contributions weighed by their probabilities $P(n)$.

The preparation and detection errors have already been determined. Since their values are only related to the atomic preparation and detection processes, they should remain the same regardless of the cavity field with which the atom interacts. Thus these parameters are fixed at values given in Table II.2 in the fit.

The Rabi frequency Ω_n and damping time τ_n for the Rabi oscillations starting from a pure atomic state in a Fock state are then set as free parameters, i.e.:

- Ω_n^e, τ_n^e : for oscillations starting from $|e, n\rangle$, with $0 \leq n \leq 7$
- Ω_n^g, τ_n^g : for oscillations starting from $|g, n+1\rangle$, with $0 \leq n \leq 6$

Inserting the photon number distributions of the states ρ_{n^p} , all fixed and free parameters mentioned above into the expressions (II.46), the ensemble of data in Fig. II.9 and Fig. II.10 are thus fitted. The solid curves show the results of the fit.

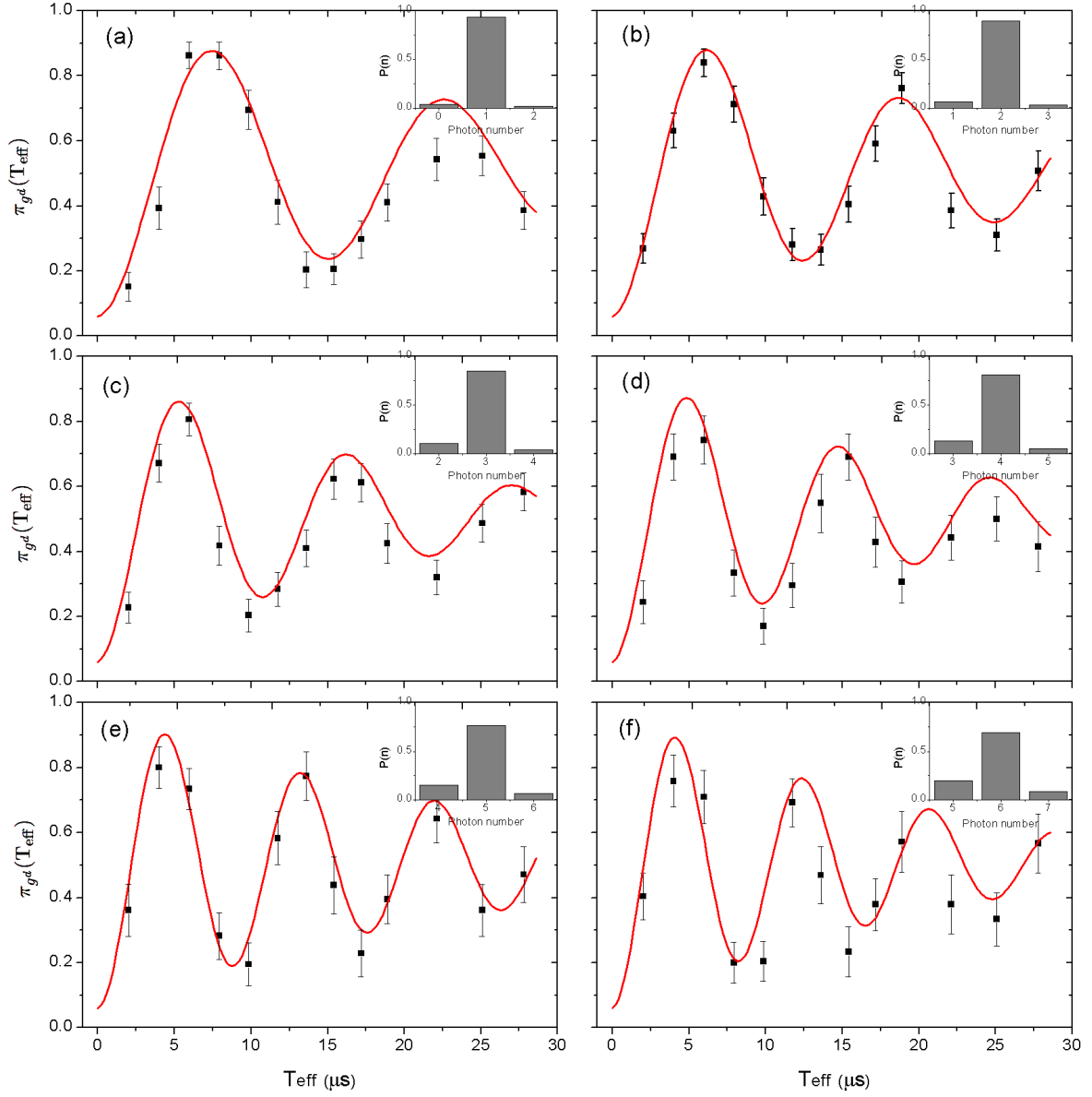


Figure II.9. Rabi oscillations in prepared photon number states with atoms prepared in the state e^p . From (a) to (f): prepared photon number states ρ_{n^p} with $n^p = 1$ to 6. The insets show $P(n)$ for each prepared states. The error bars for the data are calculated using the binomial statistical error model. The solid curves are fits of the data with a method described in the text.

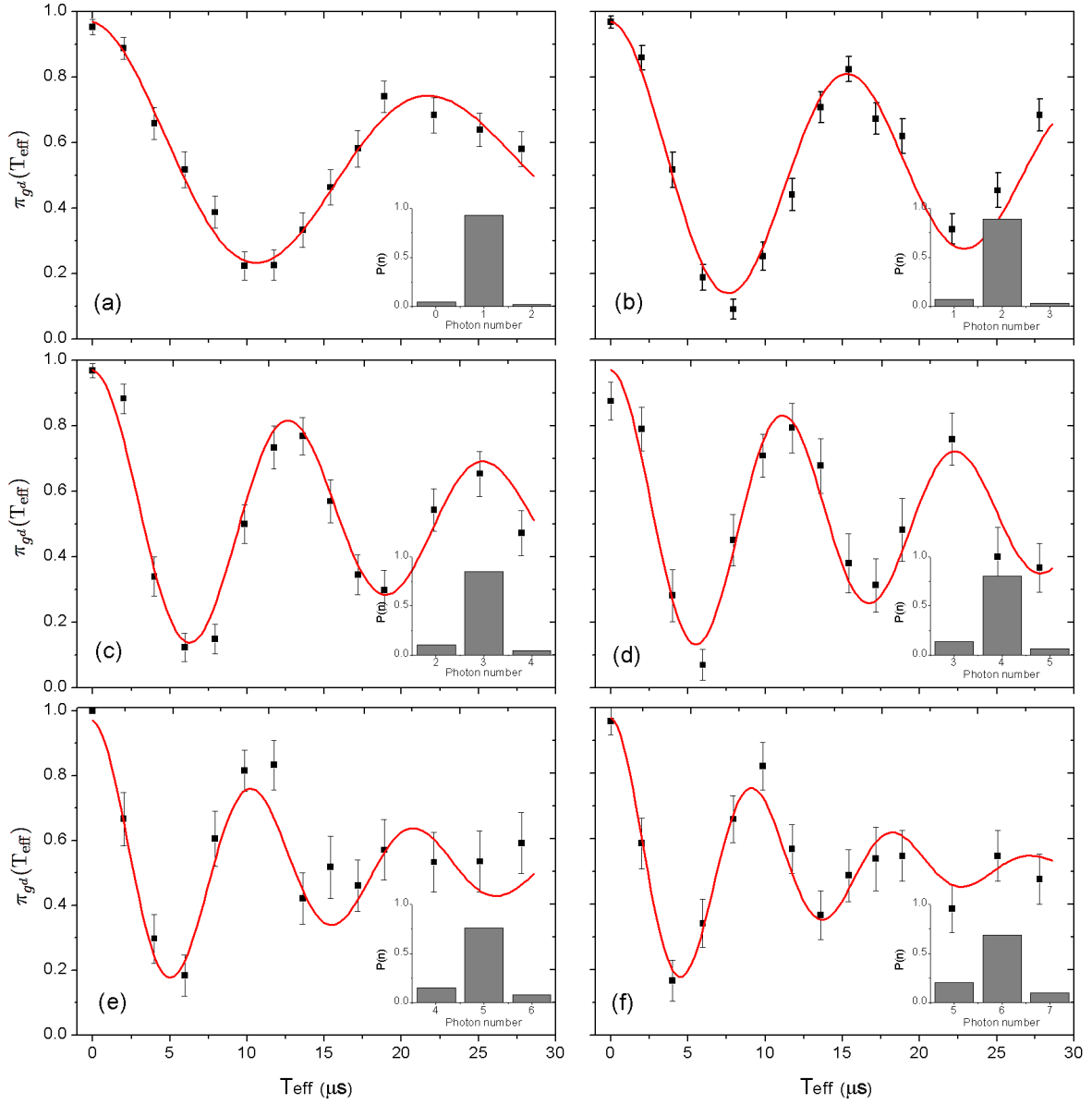


Figure II.10. Rabi oscillations in prepared photon number states with the atoms prepared in state g^p . From (a) to (f): prepared photon number states ρ_{n^p} with $n^p = 1$ to 6. The insets show $P(n)$ for each prepared states. The error bars for the data are calculated using the binomial statistical error model. The solid curves are fits of the data with a fit method described in the text.

In the fit process, the Rabi oscillations starting from $|e, n\rangle$ or $|g, n+1\rangle$ are considered separately, and we use two sets of free parameters for $\{\Omega_n, \tau_n\}$. The obtained two sets of $\{\Omega_n, \tau_n\}$ are displayed in Fig. II.11 as functions of $\sqrt{n+1}$.

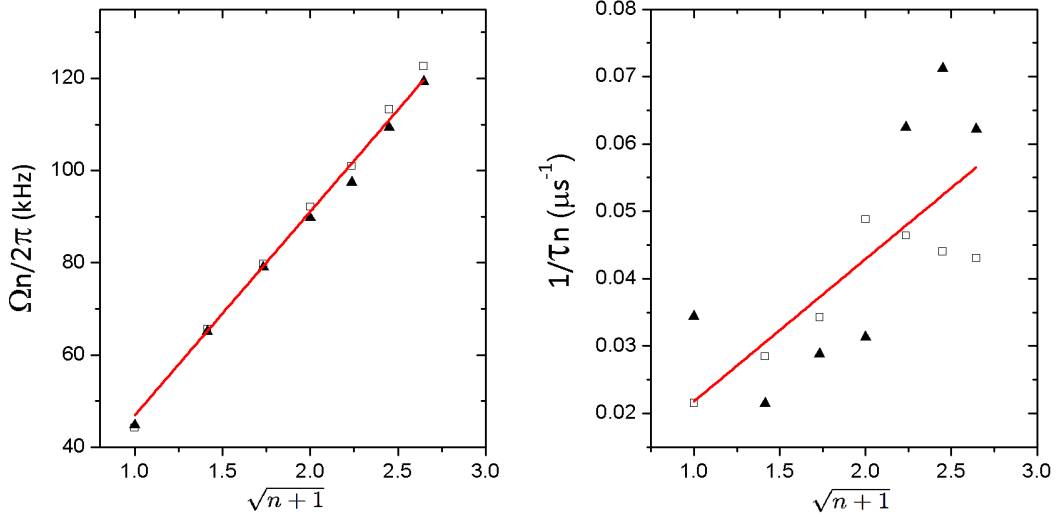


Figure II.11. Frequencies and damping rates of the Rabi oscillations in the Fock states. The squares correspond to the data $\{\Omega_n^e, 1/\tau_n^e\}$. The triangles correspond to the data $\{\Omega_n^g, 1/\tau_n^g\}$. In both panels, the two sets of data are fitted together, with the lines showing the results of the fits.

In fact, since the underlying dynamics of the Rabi oscillations starting from $|e, n\rangle$ or $|g, n+1\rangle$ are the same, the two sets of values $\{\Omega_n^e, \tau_n^e\}$ and $\{\Omega_n^g, \tau_n^g\}$ are parameters of the same process. Thus they are fitted together using the functions $\Omega_n/2\pi = \alpha\sqrt{n+1}$ and $1/\tau_n = \beta\sqrt{n+1}$. We obtain $\{\alpha = 46.0 \pm 0.5 \text{ kHz}, \beta = 0.020 \pm 0.009 \mu\text{s}^{-1}\}$. We see that these results agree with the values given in (II.52). But we also notice that the relative error of the Rabi frequency is only about 1%, whereas that of the damping rate is about 45%.

In summary, we can conclude that $\Omega_n = \Omega_0\sqrt{n+1}$ holds in our setup, whereas $1/\tau_n = \sqrt{n+1}/\tau_0$ only holds qualitatively. The latter may be due to unknown experimental imperfections that cannot be considered as inhomogeneities on the vacuum Rabi frequency.

II.3.1.d Mixing of the Kraus operators

Having determined the preparation and detection errors of the atomic states and checked the expression (II.36), we now construct the quantum maps associated to the resonant interaction between a single atom and the cavity field.

The Kraus operators $\hat{\mathcal{R}}_{i,q}$ given in (II.37) and (II.38) describe the field transformation induced by an atom which is initially in the state $i \in S^i$ and gets detected in the state $q \in S^i$ after interacting with the cavity field, where S^i denotes the set of ideal detection results²:

$$S^i \equiv \{e, g\}. \quad (\text{II.53})$$

Nevertheless, in real experiments, we do not have access to i or q . Instead, what we know is the prepared state $i^p \in S^p \equiv \{e^p, g^p\}$ and the detection result $q^d \in S^d \equiv \{0^d, e^d, g^d\}$. Due

²Different from its definition before, here S^i is defined to contain only the states of an atom.

to the preparation errors, i^p is a statistical mixture of $i \in S^i$. Similarly, due to the detection errors, q^d also contains the contributions of many pure states $q \in S^i$. So in order to determine the quantum map associated to the transition $i^p \rightarrow q^d$, we need to determine the mixing of i^p and i , as well as q and q^d .

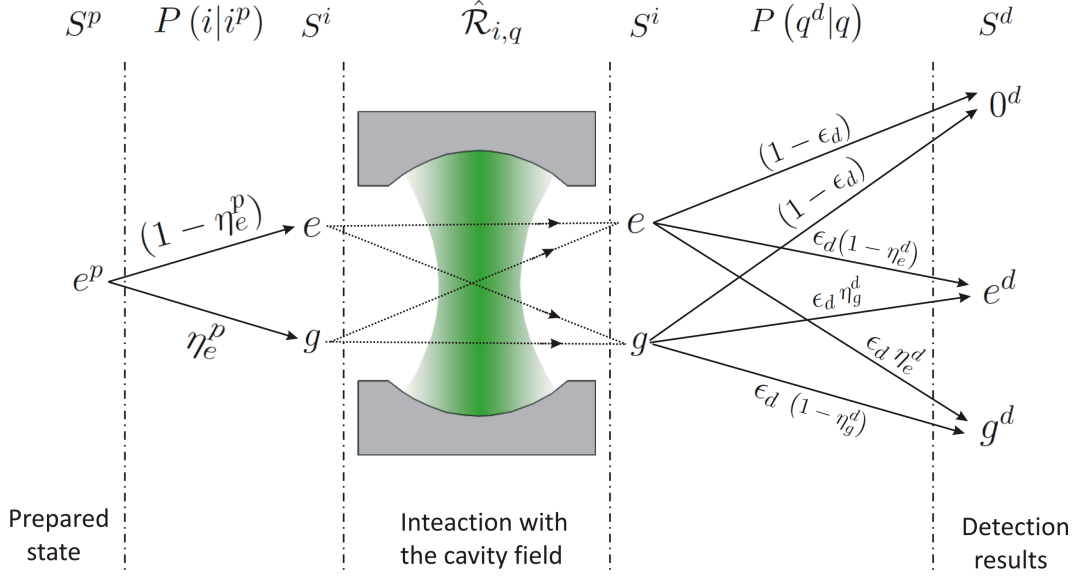


Figure II.12. Scheme showing the atomic states from a prepared state to possible detection results. The prepared state e^p is actually a mixture of $|e\rangle$ and $|g\rangle$, due to preparation errors. After interacting with the cavity field, the atomic states may lead to three possible detection results 0^d , e^d and g^d with the weights also shown in the figure.

Let us take the prepared state e^p as an example. Figure II.12 represents the atomic states at different stages in a real experimental situation. The state e^p is actually a mixture of states $|e\rangle$ and $|g\rangle$, with weights $(1 - \eta_e^p)$ and η_e^p , respectively. The atoms in these two states interact with the cavity field and end up in states $|e\rangle$ or $|g\rangle$ (detection results by a virtual ideal detector), transforming the field state with the quantum maps described by the Kraus operators (II.37) and (II.38). Once the atoms are detected, the true atomic states $|e\rangle$ and $|g\rangle$ can lead to the detection results 0^d , e^d or g^d , with the weights also shown in Fig. II.12.

The question is: how is the field state transformed if the prepared state $i^p \in S^p$ leads to the detection result $q^d \in S^d$? To answer this question, we follow the arrows in Fig. II.12 and analyze the atomic states step by step.

First, the probabilities for having the states i in the prepared states i^p , i.e. $P(i|i^p)$ are given in Table II.3. Secondly, the atomic state transition $i \rightarrow q$ transforms the field state with a quantum map described by the Kraus operator $\hat{\mathcal{R}}_{i,q}$. Finally, the conditional probability $P(q^d|q)$ for detecting the state $q^d \in S^d$ while the atomic state is in q are given in Table II.4.

In summary, the quantum map associated to the $i^p \rightarrow q^d$ transition can be expressed as

| | | | |
|-------------|----------------|----------------|-------|
| i | i^p | e^p | g^p |
| $ e\rangle$ | $1 - \eta_e^p$ | η_g^p | |
| $ g\rangle$ | η_e^p | $1 - \eta_g^p$ | |

Table II.3. The conditional probability $P(i|i^p)$ related to the preparation errors.

| | | | |
|-------|-----|----------------------------|----------------------------|
| q^d | q | $ e\rangle$ | $ g\rangle$ |
| 0^d | | $1 - \epsilon_d$ | $1 - \epsilon_d$ |
| e^d | | $\epsilon_d(1 - \eta_e^d)$ | $\epsilon_d \eta_g^d$ |
| g^d | | $\epsilon_d \eta_e^d$ | $\epsilon_d(1 - \eta_g^d)$ |

Table II.4. The conditional probability $P(q^d|q)$, related to the detector efficiency and the detection errors.

a statistical mixture of the maps associated to all transitions $i \rightarrow q$ that lead to $i^p \rightarrow q^d$:

$$\mathbb{M}_{q^d}^{i^p} \rho = \frac{\sum_{q \in S^i} \sum_{i \in S^i} P(q^d|q) \hat{\mathcal{R}}_{i,q} \rho \hat{\mathcal{R}}_{i,q}^\dagger P(i|i^p)}{\text{Tr} \left(\sum_{q \in S^i} \sum_{i \in S^i} P(q^d|q) \hat{\mathcal{R}}_{i,q} \rho \hat{\mathcal{R}}_{i,q}^\dagger P(i|i^p) \right)}. \quad (\text{II.54})$$

If the atom is not yet detected, the quantum map is then given by

$$\mathbb{N}^{i^p} \rho = \sum_{q \in S^i} \sum_{i \in S^i} \hat{\mathcal{R}}_{i,q} \rho \hat{\mathcal{R}}_{i,q}^\dagger P(i|i^p). \quad (\text{II.55})$$

II.3.2 Sample with 2 atoms

In the previous section, we have discussed the resonant interaction between a single atom and the cavity field. But in practice, we also need to consider the simultaneous interaction of two atoms with the cavity field. In fact, for the RE or RG samples, we use an atomic flux $\bar{n}_{\text{at}}^d \simeq 0.1$, which leads to a negligible probability of about 0.4% for detecting two atoms simultaneously. However, the real atomic flux is $\bar{n}_{\text{at}} = \bar{n}_{\text{at}}^d / \epsilon_d \simeq 0.4$, leading to $P_2 \simeq 5\%$, which is not negligible. As explained in section II.3.1.a, after the resonant interaction with an atom, the photon number distribution of the field is modified even if the atomic state is unread. So although we rarely detect events with two atoms, their presence and interaction with the cavity field should still be considered. This is the topic of the current section.

II.3.2.a Ideal resonant interaction

Suppose that \mathcal{N} independent two-level atoms, which are not interacting with each other, couple to the cavity field identically. The Hamiltonian of the system can be written as [40]

$$H = \hbar \omega_{\text{at}} J_z + \hbar \omega_c \left(\hat{a}^\dagger \hat{a} + \frac{1}{2} \right) + \frac{\hbar \Omega_0}{2} \left(J_+ \hat{a} + J_- \hat{a}^\dagger \right), \quad (\text{II.56})$$

where the operators J_z and J_{\pm} are defined as the sum of corresponding individual pseudo spins:

$$J_z = \frac{1}{2} \sum_j \sigma_{z,j} \quad J_{\pm} = \sum_j \sigma_{\pm,j},$$

with $\sigma_{z,j}$, $\sigma_{+,j}$, and $\sigma_{-,j}$ being the z component of the Pauli matrices, the atomic raising and lowering operators associated to the j th atom.

The Hamiltonian (II.56) conserves the total angular momentum of the \mathcal{N} atoms. In the case of $\mathcal{N} = 2$, the basis $\{|ee, n-1\rangle, |(eg+ge)/\sqrt{2}, n\rangle, |gg, n+1\rangle\}$ with $n \geq 1$ forms a closed subspace of the Hilbert space. In this subspace, the Hamiltonian can be expressed in the matrix form:

$$H_n = \hbar \begin{pmatrix} \omega_c(n+1/2) & \sqrt{2n}\Omega_0/2 & 0 \\ \sqrt{2n}\Omega_0/2 & \omega_c(n+1/2) & \sqrt{2(n+1)}\Omega_0/2 \\ 0 & \sqrt{2(n+1)}\Omega_0/2 & \omega_c(n+1/2) \end{pmatrix}$$

By diagonalizing it, we obtain the eigenenergies:

$$\begin{aligned} \xi_0 &= 0 \\ \pm\xi(n) &= \pm\hbar\frac{\Omega_0}{2}\sqrt{2(2n+1)}. \end{aligned}$$

Here, without loss of generality, a common term $\hbar\omega_c(n+1/2)$ in ξ_0 and $\xi(n)$ has been removed by redefining the energy origin.

The corresponding eigenstates and the evolution of the system are given in Appendix A. Based on these results we can define the Kraus operators with interaction time t :

$$\begin{aligned} \hat{R}_{ee,ee} &= \sum \left[1 + \frac{n+1}{2n+3} \left(\cos \frac{\xi(n+1)t}{\hbar} - 1 \right) \right] |n\rangle\langle n|, \\ \hat{R}_{ee,eg} &= \sum \sqrt{\frac{n+1}{2n+3}} \sin \frac{\xi(n+1)t}{\hbar} |n+1\rangle\langle n|, \\ \hat{R}_{ee,gg} &= \sum \frac{\sqrt{(n+1)(n+2)}}{2n+3} \left(\cos \frac{\xi(n+1)t}{\hbar} - 1 \right) |n+2\rangle\langle n|. \end{aligned} \quad (\text{II.57})$$

$$\begin{aligned} \hat{R}_{eg,ee} &= \sum \sqrt{\frac{n+1}{2n+3}} \sin \frac{\xi(n+1)t}{\hbar} |n\rangle\langle n+1|, \\ \hat{R}_{eg,eg} &= \sum \cos \frac{\xi(n)t}{\hbar} |n\rangle\langle n|, \\ \hat{R}_{eg,gg} &= \sum \sqrt{\frac{n+1}{2n+1}} \sin \frac{\xi(n)t}{\hbar} |n+1\rangle\langle n|. \end{aligned} \quad (\text{II.58})$$

$$\begin{aligned} \hat{R}_{gg,ee} &= \sum \frac{\sqrt{(n+1)(n+2)}}{2n+3} \left(\cos \frac{\xi(n+1)t}{\hbar} - 1 \right) |n\rangle\langle n+2|, \\ \hat{R}_{gg,eg} &= \sum \sqrt{\frac{n+1}{2n+1}} \sin \frac{\xi(n)t}{\hbar} |n\rangle\langle n+1|, \\ \hat{R}_{gg,gg} &= \sum \left[1 + \frac{n}{2n-1} \left(\cos \frac{\xi(n-1)t}{\hbar} - 1 \right) \right] |n\rangle\langle n|. \end{aligned} \quad (\text{II.59})$$

where $\xi(-1)$ is defined to be zero.

II.3.2.b Vacuum Rabi oscillations of two atoms

In order to check the theoretical model leading to the ideal Kraus operators (II.57), (II.58) and (II.59), we record vacuum Rabi oscillations of two atoms both prepared in e^p . The theoretical vacuum Rabi oscillations of two atoms both in $|e\rangle$ and coupled to the field can be easily obtained by setting $n = 1$ in (A.2). The probabilities for detecting the three states of the atomic pair are then given by

$$\begin{aligned}\pi_{ee,ee}^{(2)}(t) &= \frac{1}{2} + \frac{1}{18} \cos(\sqrt{6}\Omega_0 t) + \frac{4}{9} \cos\left(\frac{\sqrt{6}\Omega_0 t}{2}\right), \\ \pi_{ee,gg}^{(2)}(t) &= \frac{1}{3} + \frac{1}{9} \cos(\sqrt{6}\Omega_0 t) - \frac{4}{9} \cos\left(\frac{\sqrt{6}\Omega_0 t}{2}\right), \\ \pi_{ee,eg}^{(2)}(t) &= \frac{1}{6} - \frac{1}{6} \cos(\sqrt{6}\Omega_0 t).\end{aligned}\quad (\text{II.60})$$

Figure II.13 shows the measured vacuum Rabi oscillations. The atomic flux is chosen such that the average detected atom number is $\bar{n}_{\text{at}}^d = 0.06$. Only the events with two atoms detected are selected for calculating the probabilities shown in Fig. II.13. But due to the limited detector efficiency, the samples containing more than 2 atoms may also contribute.

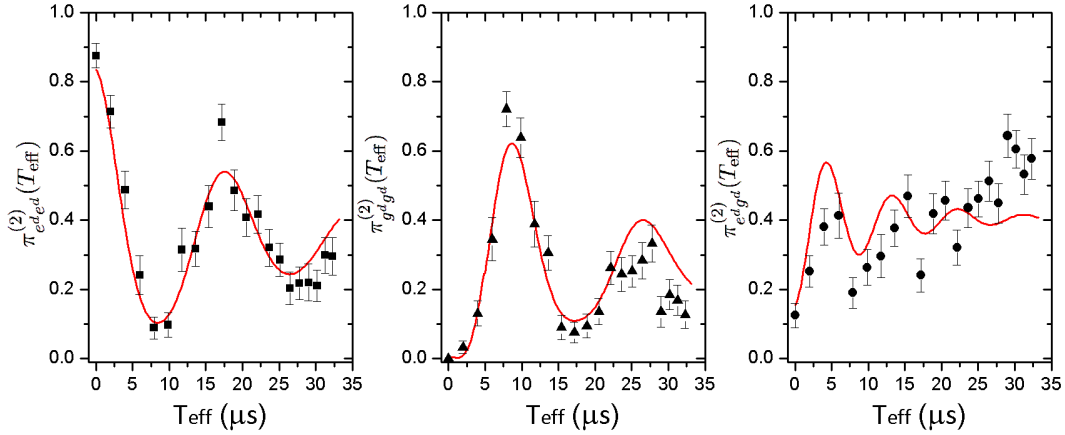


Figure II.13. Vacuum Rabi oscillations of two atoms both prepared in e^p and coupled to the cavity field. The points are the measured data and the lines are fits to the data. Here $e^d e^d$, $e^d g^d$ and $g^d g^d$ represent the three detected states of the atomic pair.

In order to analyze the data using the formulae (II.60), we need first to introduce phenomenological damping terms into the cosine functions. Based on the same argument leading to (II.36), we can introduce a damping time $\tau_n^{(2)}$ into the oscillations with the frequency $2\xi(n)/\hbar$, according to

$$\tau_n^{(2)} = \frac{\Omega_0 \tau_0}{2\xi(n)/\hbar}. \quad (\text{II.61})$$

We then use the following functions to fit the data:

$$\begin{aligned}
\tilde{\pi}_{ee,ee}^{(2)}(t) &= a_1 + b_1 e^{-\sqrt{6}t/\tau_0} \cos(\sqrt{6}\Omega_0 t) + c_1 e^{-\sqrt{6}t/2\tau_0} \cos\left(\frac{\sqrt{6}\Omega_0 t}{2}\right) \\
\tilde{\pi}_{ee,gg}^{(2)}(t) &= a_2 + b_2 e^{-\sqrt{6}t/\tau_0} \cos(\sqrt{6}\Omega_0 t) - c_1 e^{-\sqrt{6}t/2\tau_0} \cos\left(\frac{\sqrt{6}\Omega_0 t}{2}\right) \\
\tilde{\pi}_{ee,eg}^{(2)}(t) &= (1 - a_1 - a_2) - (1 - b_1 - b_2) e^{-\sqrt{6}t/\tau_0} \cos(\sqrt{6}\Omega_0 t),
\end{aligned} \tag{II.62}$$

with Ω_0 , τ_0 , a_1 , b_1 , c_1 , a_2 and b_2 chosen as free parameters. The preparation and detection errors of the atomic states are not included in the fit explicitly. But they are already incorporated into the parameters for the oscillation amplitudes and offsets, such as a_1 , b_1 , c_1 , etc. From the fits, we obtain the parameters shown in Table II.5. As a comparison, the theoretical values of these parameters according to (II.60) are also shown in the table.

| | $\Omega_0/2\pi$ | τ_0 | a_1 | b_1 | c_1 | a_2 | b_2 |
|--------|-----------------|------------|-------|-------|-------|-------|-------|
| fit | 45.7 kHz | 35 μ s | 0.43 | 0.08 | 0.42 | 0.27 | 0.15 |
| theory | - | - | 0.50 | 0.06 | 0.44 | 0.33 | 0.11 |

Table II.5. Theoretical and fitted parameters of the vacuum Rabi oscillations of two atoms both coupled to the cavity field.

The fit results qualitatively agree with the theoretical values. This means that the theoretical model seems to be a reasonably good approximation for describing the simultaneous resonant interaction of two atoms with the cavity field. But at the same time, we also notice the relatively large discrepancy between the measured data and the fit for $\pi_{e^d g^d}^{(2)}(T_{\text{eff}})$. This reflects the limitation of our theoretical model. But given the relatively low probability for a two-atom event to occur in real experiments (about 4 times lower than that of an one-atom event), we expect that this small deviation in the theoretical model may have very limited effect on the overall performance of the model including both 1 and 2 atom events.

Similar to the situation of the one-atom event, the damping terms introduced in (II.61) should also be included in the ideal Kraus operators (II.57), (II.58) and (II.59). Here I omit the explicit expressions for the modified Kraus operators, but simply give their notations:

$$\hat{\mathcal{R}}_{i,q} \quad i, q \in \{ee, eg, gg\} \tag{II.63}$$

The preparation and detection errors of the atomic states result in mixing of these operators, which is presented in the following section.

II.3.3 Quantum maps

So far, we have obtained the Kraus operators associated to 1 and 2 atoms in the presence of the experimental imperfections. But in the experimental situation, we deal with atomic samples which contain nondeterministic atom numbers. The detection of an atomic sample involves mixing of different atom numbers, since the detector has a limited efficiency. In the current section, we discuss how to express the quantum map associated to an atomic sample.

We tentatively prepare an atomic sample in $|e\rangle$ ($|g\rangle$) for an actuator sample with the RE (RG) type. Since the atom number in the sample is probabilistic, we need first to determine the probabilities of having 0, 1 and 2 atoms in a sample $p \in \{\text{RE}, \text{RG}\}$. These conditional probabilities $P(i^p|p)$ related to the Poisson distribution of the atom number per sample are given in Table II.6. We also need to enlarge the set S^p in order to include the two-atom and 0 atom events:

$$S^p \equiv \{0^p, g^p, g^p g^p, e^p, e^p e^p\} \quad (\text{II.64})$$

| $i^p \backslash p$ | RE | RG |
|--------------------|-------|-------|
| 0^p | P_0 | P_0 |
| e^p | P_1 | 0 |
| $e^p e^p$ | P_2 | 0 |
| g^p | 0 | P_1 |
| $g^p g^p$ | 0 | P_2 |

Table II.6. The conditional probability $P(i^p|p)$, with P_n , $n \in \{0, 1, 2\}$, as defined in (II.2).

Once we know the prepared state i^p , the following steps are similar to those outlined for the one-atom event. Before proceeding, we need first to enlarge the sets S^i and S^d to include the two-atom and 0 atom events:

$$S^i \equiv \{0, e, g, ee, eg, gg\} \quad (\text{II.65})$$

and

$$S^d \equiv \{0^d, e^d, g^d, e^d e^d, e^d g^d, g^d g^d\}. \quad (\text{II.66})$$

Next we enlarge the Tables II.3 and II.4 and get new values for $P(i|i^p)$ and $P(q|q^d)$, as given in Tables II.7 and II.8.

Exploiting the same methodology as that in deriving (II.54), we can express the quantum map corresponding to a detection result $q^d \in S^d$ of a sample $p \in \{\text{RE}, \text{RG}\}$ as:

$$\mathbb{M}_{q^d}^p \rho = \frac{\sum_{q \in S^r} \sum_{i \in S^r} \sum_{i^p \in S^p} P(q^d|q) \hat{\mathcal{R}}_{i,q} \rho \hat{\mathcal{R}}_{i,q}^\dagger P(i|i^p) P(i^p|p)}{\text{Tr} \left(\sum_{q \in S^r} \sum_{i \in S^r} \sum_{i^p \in S^p} P(q^d|q) \hat{\mathcal{R}}_{i,q} \rho \hat{\mathcal{R}}_{i,q}^\dagger P(i|i^p) P(i^p|p) \right)}. \quad (\text{II.67})$$

If the atomic sample is not yet detected, the quantum map is given by

$$\mathbb{N}^p \rho = \sum_{q \in S^i} \sum_{i \in S^i} \sum_{i^p \in S^p} \hat{\mathcal{R}}_{i,q} \rho \hat{\mathcal{R}}_{i,q}^\dagger P(i|i^p) P(i^p|p). \quad (\text{II.68})$$

| $i \backslash i^p$ | 0^p | e^p | g^p | $e^p e^p$ | $g^p g^p$ |
|--------------------|-------|----------------|----------------|---------------------------|---------------------------|
| 0 | 1 | 0 | 0 | 0 | 0 |
| $ e\rangle$ | 0 | $1 - \eta_e^p$ | η_g^p | 0 | 0 |
| $ g\rangle$ | 0 | η_e^p | $1 - \eta_g^p$ | 0 | 0 |
| ee | 0 | 0 | 0 | $(1 - \eta_e^p)^2$ | η_g^{p2} |
| eg | 0 | 0 | 0 | $2(1 - \eta_e^p)\eta_e^p$ | $2(1 - \eta_g^p)\eta_g^p$ |
| gg | 0 | 0 | 0 | η_e^{p2} | $(1 - \eta_g^p)^2$ |

Table II.7. The conditional probability $P(i|i^p)$ related to the preparation errors.

| $q^d \backslash q$ | 0 | e | g | ee | eg | gg |
|--------------------|---|----------------------------|----------------------------|---|--|---|
| 0^d | 1 | $1 - \epsilon_d$ | $1 - \epsilon_d$ | $(1 - \epsilon_d)^2$ | $(1 - \epsilon_d)^2$ | $(1 - \epsilon_d)^2$ |
| e^d | 0 | $\epsilon_d(1 - \eta_e^d)$ | $\epsilon_d \eta_g^d$ | $2\epsilon_d(1 - \epsilon_d)(1 - \eta_e^d)$ | $\epsilon_d(1 - \epsilon_d)(1 - \eta_e^d + \eta_g^d)$ | $2\epsilon_d(1 - \epsilon_d)\eta_g^d$ |
| g^d | 0 | $\epsilon_d \eta_e^d$ | $\epsilon_d(1 - \eta_g^d)$ | $2\epsilon_d(1 - \epsilon_d)\eta_e^d$ | $\epsilon_d(1 - \epsilon_d)(1 + \eta_e^d - \eta_g^d)$ | $2\epsilon_d(1 - \epsilon_d)(1 - \eta_g^d)$ |
| $e^d e^d$ | 0 | 0 | 0 | $\epsilon_d^2(1 - \eta_e^d)^2$ | $\epsilon_d^2 \eta_g^d(1 - \eta_e^d)$ | $\epsilon_d^2 \eta_g^{d2}$ |
| $e^d g^d$ | 0 | 0 | 0 | $\epsilon_d^2 \eta_e^d(1 - \eta_e^d)$ | $\epsilon_d^2(\eta_e^d \eta_g^d + (1 - \eta_e^d)(1 - \eta_g^d))$ | $2\epsilon_d^2 \eta_g^d(1 - \eta_g^d)$ |
| $g^d g^d$ | 0 | 0 | 0 | $\epsilon_d^2 \eta_e^{d2}$ | $\epsilon_d^2 \eta_e^d(1 - \eta_g^d)$ | $\epsilon_d^2(1 - \eta_g^d)^2$ |

Table II.8. The conditional probability $P(q^d|q)$ related to the detector efficiency and the detection errors.

II.4 State estimation

In the feedback loop, atomic samples of 3 different types interact with the cavity field. We have derived the quantum maps associated to the detection results of these samples. Now let us discuss in more detail how the quantum state estimator operates.

Suppose that the initial field state is ρ_0 . A sequence of equally spaced atomic samples, separated in time by T_a , pass through the cavity and get detected one by one. Suppose that the k th sample with the type $\mu_k \in \{\text{QND, RE, RG}\}$, leads to the detection result $q_k^d \in S^d$. If we use ρ_k to denote the estimated state in the k th loop, we can then write down the transformation:

$$\rho_k = \mathbb{T}M_{q_k^d}^{\mu_k} \rho_{k-1}, \quad (\text{II.69})$$

where $M_{q_k^d}^{\mu_k}$ denotes the quantum map associated to the detection of the k th sample and \mathbb{T} describes the field relaxation during T_a . It is defined as:

$$\mathbb{T}\rho \equiv (\mathbb{1} + T_a \mathbf{L}) \rho, \quad (\text{II.70})$$

where the approximation in the first order of T_a/T_{cav} has been used, and the operator \mathbf{L} is given in (I.48). Starting from the initial field state ρ_0 , the current estimated state ρ_k can be expressed as

$$\rho_k = \prod_{j=1}^k \left(\text{TM}_{q_j^d}^{\mu_j} \right) \rho_0. \quad (\text{II.71})$$

Conclusion

This chapter is mainly devoted to the descriptions of the dispersive and resonant interactions in the presence of experimental imperfections. Starting by presenting the principle and procedure of the feedback experiment, we have discussed the quantum maps associated to the sensor and actuator samples.

For the sensor samples, we have first recalled the Kraus operators associated to an ideal QND measurement, then gradually taken into account the experimental imperfections, such as the probabilistic atom number in an atomic sample, reduced contrast and shifted offset of the Ramsey fringes and the detector efficiency. The imperfections of the Ramsey fringes are accounted for by the effective detection errors. Finally, we gave the quantum maps adapted to real experimental situations.

For the actuator samples, we have discussed the samples containing one or two atoms. In both cases, we first presented the ideal Kraus operators associated to their interactions with the cavity field, then gradually took into account the experimental imperfections. These imperfections include the damped contrast of the vacuum Rabi oscillations, the preparation and detection errors of atomic states, etc. To measure them, we recorded Rabi oscillations in the Fock states with up to 6 photons, and the Rabi oscillations of two atoms simultaneously coupled to the field. At the end, we obtained the quantum maps associated to an actuator sample, and presented a general formula for state estimation.

Chapter III

Quantum feedback: algorithms and optimizations

In the previous chapter, we have presented the quantum maps associated to the sensors and actuators. Based on these maps, we have expressed the estimated state after the detection of each atomic sample. In practice, the sample cannot be detected immediately once it exits the cavity, since the cavity and detector are spatially separated. In fact, at the moment when the k th sample is detected, several others after it have already interacted with the cavity field. They need to be taken into account in the state estimation, leading to a modified algorithm for the quantum state estimator.

Besides modifying the algorithm for the state estimation, we also discuss the algorithm of the controller in this chapter. We first present the spatial configuration of the atomic samples when we choose the feedback actions and explain how to implement different sample types, in section III.1. These are necessary for understanding the algorithms of the quantum state estimator and controller, which are then presented in the two subsequent sections III.2 and III.3. Knowing the algorithms, we perform numerical simulations and present the results in section III.4. Based on these simulations, we optimize several parameters of the feedback process.

III.1 Complete timing of the feedback experiment

Spatial configuration of the atomic samples

In our experiments, we use a sequence of atomic samples separated by $T_a = 82 \mu\text{s}$. So if we take a snapshot of the experiment at the moment when the k th sample is detected, the spatial configuration of the samples is shown in panel (a) of Fig. III.1.

The detection result of the k th sample is fed into the quantum state estimator, which carries out calculations and provides an estimate on the current field state. During this process, the samples have moved. When the controller chooses a feedback action, their spatial configuration is as that shown in panel (b) of Fig. III.1. At this moment, the samples from $k+1$ to $k+5$ have interacted with the cavity field and remain in an entangled state with the field. The algorithm of the state estimation in which those not-yet-detected samples are taken into account will be presented in section III.2.

The sample $k+8$ has just entered R_1 and can be chosen as RE or RG to emit or absorb photons, or as QND to perform a measurement. The samples $k+6$ and $k+7$ have not entered

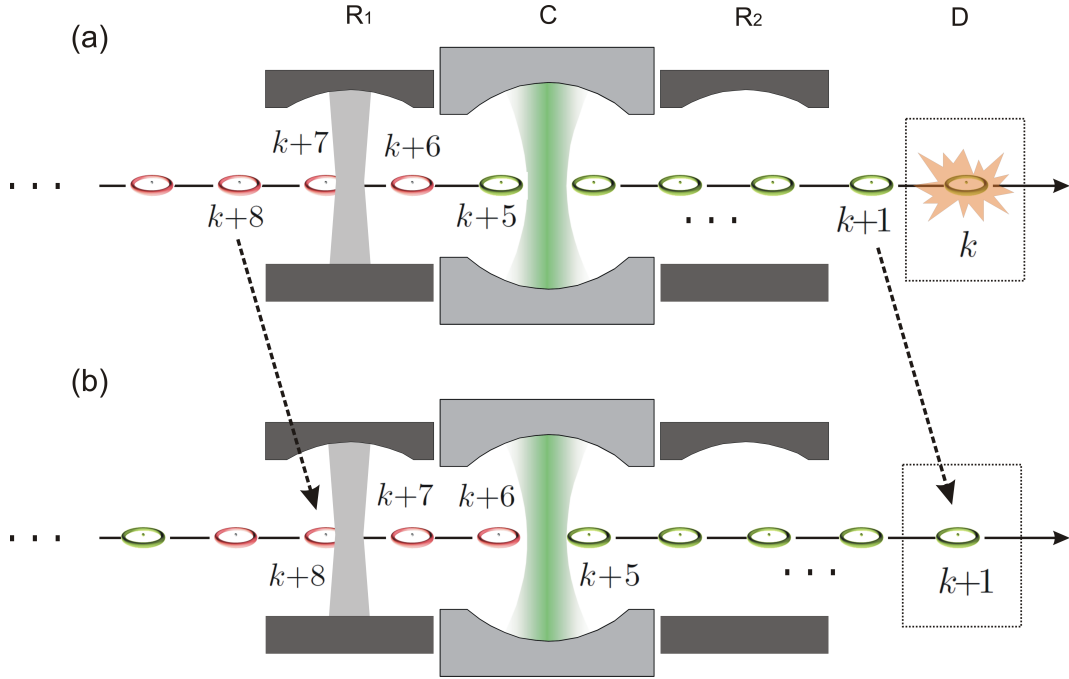


Figure III.1. Spatial configurations of the atomic samples when the sample k is detected (a) and when the controller chooses a feedback action (b). C: the cavity; R_1 and R_2 : the first and second Ramsey zones; D: the detector. The torus-shape elements represent the atomic samples: sensor samples (green) and control samples (red). The black solid arrow shows the atomic beam. The black dashed arrows link the same samples at the two moments. Several samples are labeled with their corresponding numbers.

the cavity and their interactions with the cavity field may still be changed. So we use these 3 samples to carry out feedback actions. Nevertheless, for the samples $k+6$, $k+7$, we have fewer options, since they have passed R_1 and their atomic states cannot be modified. In practice, for the types RE or RG, we need to apply potential pulses across C in order to tune the field and sample on resonance by the Stark effect. This provides us a means of controlling the interaction of a sample with the cavity field without modifying its atomic state. For example, if the samples $k+6$ or $k+7$ have resonant types (RE or RG), we can decide not to apply the potential pulses associated to them. As a result, we change the resonant interaction to a dispersive one and avoid emitting or absorbing photons. In this case, the sample is effectively discarded and labeled as DS (discarded sample). It does not modify the field state, and can be completely neglected in the feedback process. The algorithm of the controller in which we use multiple samples to carry out feedback actions will be presented in section III.3.

In our experiments, a feedback action is to add or subtract a photon. Ideally, this process requires an atom. On the contrary, for gaining information about the field, we need many sensors, since each of them provides one bit information (binary detection results for the atomic state). So in the sequence of atomic samples, we introduce a partition of *sensor* and *control* samples. We first define a structure consisting of a segment of N_s sensor samples and another segment of N_c control samples. The typical values¹ are $N_s = 12$ and $N_c = 4$. Then

¹These values are chosen for optimizing the performance of the feedback process. Later in this chapter, we will come back to discuss this choice.

a sequence of atomic samples is simply many repetitions of this structure. While the sensor samples have fixed QND type and perform the QND measurements, the control samples can be chosen to be RE, RG or QND by the controller. As shown in Fig. III.1, the red (green) atomic samples correspond to the control (sensor) samples.

Implementation of different sample types

The atomic samples in a sequence have different types. In the following paragraphs, we discuss, on the level of hardware, the requirements of these different types. This is necessary for understanding the algorithm of the controller presented later.

In the feedback experiment, there are essentially two types of interactions between the atomic samples and the cavity field: dispersive and resonant. The atomic and field frequencies are tuned to be off resonance while the potential on one of the cavity mirrors is at -0.62 V (a default value). They are tuned on resonance by applying potential pulses on that mirror, which can go up to -2.5 V. To implement different sample types, we need to control these potential pulses. Moreover, different types also require different manipulations on their atomic states. So we also need to control the microwave pulses in R_1 and R_2 . In summary, the pulses corresponding to different types are shown in Fig. III.2, with their functions explained in the following text.

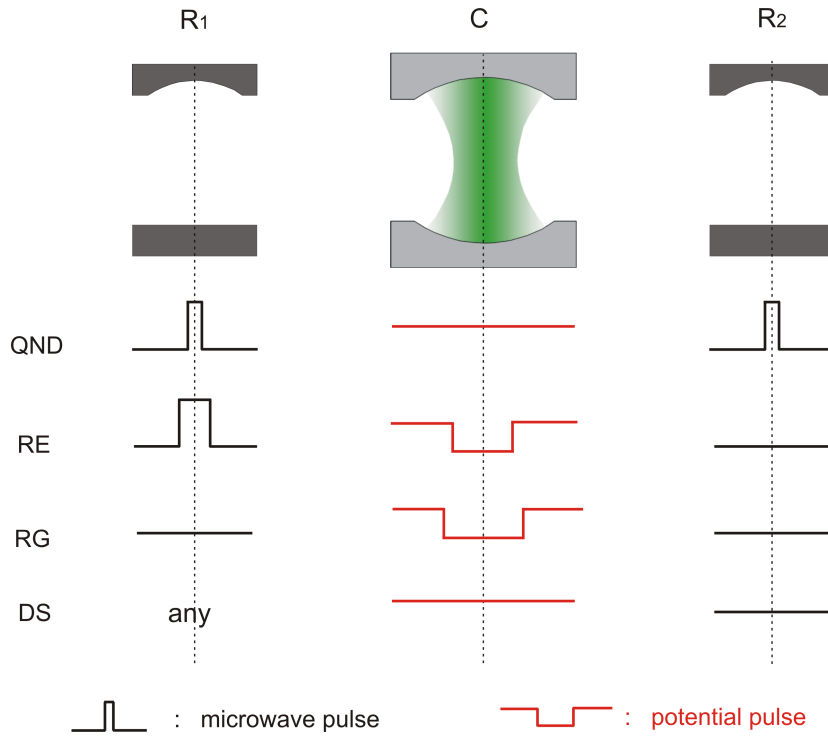


Figure III.2. Microwave pulses and potential pulses for implementing different sample types. A QND sample requires microwave pulses in both R_1 and R_2 , while the potential in C remains at the default value. A RE sample requires a microwave pulse in R_1 and a potential pulse in C . A RG sample only requires a potential pulse in C . The RE or RG samples are effectively changed to the DS type, if we do not apply the potential pulses associated to them.

- QND : the microwave pulse in R_1 is a $\pi/2$ pulse, which transforms the atomic state from $|g\rangle$ to a superposition state $(|e\rangle + |g\rangle)/\sqrt{2}$. The potential on the cavity mirror remains at its default value such that the atomic sample and the cavity field interact dispersively. The microwave pulse in R_2 is another $\pi/2$ pulse.
- RE : the microwave pulse in R_1 is a π pulse, which transforms the atomic state from $|g\rangle$ to $|e\rangle$. A potential pulse applied across C tunes the sample to be on resonance with the cavity field. After interaction, the atomic state is no more manipulated in R_2 .
- RG : no microwave pulse in either R_1 or R_2 . The sample enters the cavity in the state $|g\rangle$ and is tuned to be on resonance with the cavity field by a potential pulse across C.
- DS : default potential value in C and no microwave pulse in R_2 , despite the microwave pulses in R_1

Remark: The resonant samples (RE or RG) require potential pulses across C, which can go up to -2.5 V. The potential difference between the two mirrors of the cavity generates an extra inhomogeneous static electric field. Due to the Stark effect, this inhomogeneous static field results in inhomogeneity in the atomic frequencies of their neighboring QND samples. These samples accumulate different phases between the two $\pi/2$ pulses applied in R_1 and R_2 , and lead to suppressed Ramsey fringes. In this situation, the measurements performed by the QND samples can no longer extract information about the field state. So they are omitted while estimating the field state.

III.2 Quantum state estimator

Photon number distribution versus density matrix

In the whole feedback process, all involved quantum maps, such as those associated to the dispersive or resonant interactions and that associated to the field relaxation, do not couple the diagonal elements of the density matrix ρ to the non-diagonal elements. Hence, all calculations in the state estimation and the controller can be based on the diagonal elements of ρ , i.e. the photon number distribution $P(n)$. Moreover, since in our experiments the field is initially in its vacuum state, the non-diagonal elements of the density matrix are actually zero during the whole feedback process. So we only need to follow the evolution of $P(n)$.

Following the evolution of $P(n)$ instead of ρ enables us to carry out calculations based on $N^{\mathcal{H}}$ -dimensional vectors, rather than a $N^{\mathcal{H}} \times N^{\mathcal{H}}$ -dimensional matrices, with $N^{\mathcal{H}}$ denoting the size of a truncated Hilbert space. This saves calculation time for the quantum state estimator and controller. Furthermore, since not-yet-detected QND samples do not modify $P(n)$, all calculations involving such samples can be simplified.

Although in experiments and simulations, all calculations are based on $P(n)$, I use the density matrix more often in this manuscript for simplicity and clarity of expressions. While reading these expressions, the readers just need to bear in mind that all these density matrices are actually diagonal.

Algorithm of the state estimation

In section II.4, we have given the state estimation (II.71). Nevertheless, in practice, this state estimation should be modified in order to take into account the 5 samples from $k+1$ to $k+5$,

which have already interacted with the cavity field at the moment when we choose a feedback action.

Suppose that the initial state of the cavity field is ρ_0 . We now consider the estimated state given in (II.71) as an auxiliary state, which would be the field state after the detection of the k th sample, if the 5 samples did not exist.

$$\rho'_k = \prod_{j=1}^k (\mathbb{T}\mathbb{M}_{q_j}^{\mu_j}) \rho_0. \quad (\text{III.1})$$

The state ρ'_k satisfies the following recursive relationship:

$$\rho'_k = \mathbb{T}\mathbb{M}_{q_k}^{\mu_k} \rho'_{k-1}. \quad (\text{III.2})$$

Since those 5 samples are not yet detected, we can only consider them as unread measurements. Consequently the estimated state of the cavity field reads

$$\rho_k = \prod_{l=k+1}^{k+5} (\mathbb{T}\mathbb{N}^{\mu_l}) \rho'_k. \quad (\text{III.3})$$

where \mathbb{N}^{μ_l} denotes the quantum map associated to a not-yet-detected sample introduced in (II.16) and (II.55).

In practice, since ρ'_k can be obtained based solely on the detection result of the k th sample and ρ'_{k-1} , we can store it in the memory of the quantum state estimator and use it for the next loop. So in experiments, we combine the expressions (III.2) and (III.3) to calculate the estimated state of the cavity field.

III.3 Controller

After obtaining the estimated state ρ_k , the controller chooses a feedback action to bring the state closer to the target Fock state $\rho_t = |n_t\rangle\langle n_t|$. Before presenting the algorithm of the controller, let us first explain how to measure the ‘‘closeness’’ of an arbitrary state ρ to our target state.

III.3.1 Measure of distance

We can use the *fidelity* \mathcal{F} [56] between two quantum states to measure their ‘‘closeness’’. For two pure states $|\psi_1\rangle$ and $|\psi_2\rangle$, the natural choice for \mathcal{F} would be their *overlap*:

$$\mathcal{F}_p(|\psi_1\rangle, |\psi_2\rangle) = |\langle\psi_1|\psi_2\rangle|^2. \quad (\text{III.4})$$

This definition, however, cannot be easily generalized to describe statistical mixtures. A widely used generalization takes the form [57]:

$$\mathcal{F}_m(\rho_1, \rho_2) = \left[\text{Tr} \left(\sqrt{\sqrt{\rho_1} \rho_2 \sqrt{\rho_1}} \right) \right]^2. \quad (\text{III.5})$$

Particularly, since $\rho_t = |n_t\rangle\langle n_t|$, the fidelity between ρ_t and an arbitrary state ρ can be expressed as:

$$\mathcal{F}_m(\rho_t, \rho) = P_\rho(n_t), \quad (\text{III.6})$$

with $P_\rho(n_t)$ denoting the probability to have n_t photons in the state ρ . We see that $\mathcal{F}_m(\rho_t, |n_t\rangle\langle n_t|) = 1$ and $\mathcal{F}_m(\rho_t, |n\rangle\langle n|) = 0, \forall n \neq n_t$.

Let us consider $1 - \mathcal{F}_m(\rho_t, \rho)$ as a *fidelity-defined distance* between ρ_t and ρ . We see that this distance only reduces to zero once the target state is reached, i.e. $\rho = \rho_t$. For all other Fock states it has the same maximum value of 1. Thus using this distance, the controller cannot tell the difference between the state with $n \gg n_t$ (or $n \ll n_t$) and those with $n = n_t \pm 1$ representing the results of quantum jumps by one photon.

In order to reflect that the states $|n\rangle$ with $n \gg n_t$ are ‘‘farther’’ from $|n_t\rangle$ than $|n_t \pm 1\rangle$, we define the distance between a state with the photon number distribution $P(n)$ and the target state $|n_t\rangle$ as

$$\begin{aligned} d(P(n), n_t) &= \sum_m P(m) (m - n_t)^2 \\ &= (\bar{n} - n_t)^2 + \Delta n^2, \end{aligned} \quad (\text{III.7})$$

with Δn^2 and \bar{n} denoting the photon number variance and mean value, respectively. The minimization of $d(P(n), n_t)$ can then be interpreted as pushing the average photon number towards n_t and narrowing the photon number distribution.

We can also write (III.7) in the following form:

$$d(\rho, \rho_t) = \text{Tr} \left(\rho \hat{D}_{n_t} \right), \quad (\text{III.8})$$

in which the distance operator \hat{D}_{n_t} is defined as

$$\hat{D}_{n_t} \equiv \sum_n d_{n_t}(n) |n\rangle\langle n|, \quad (\text{III.9})$$

with

$$d_{n_t}(n) = (n - n_t)^2. \quad (\text{III.10})$$

III.3.2 Decision making

As mentioned briefly in section III.1, the controller uses the samples $k+6$, $k+7$ and $k+8$ to carry out feedback actions. For the sample $k+8$, we can choose its type to be RE, RG or QND. For the samples $k+6$, $k+7$, their interactions with the cavity field may be modified, only if they have the types RE or RG in the first place. For instance, we can set them to the DS type by not applying the potential pulses associated to them. Or we may change our mind again and reinstall the potential pulses associated to them. Since the atomic states of the samples are not modified, the samples are recovered to their original types (RE or RG).

Let us use $\{\nu_{k+8}, \nu_{k+7}, \nu_{k+6}\}$ to denote one possible choice for the types of the 3 samples. The controller estimates the average field state resulting from the pending interaction of the cavity field with these samples, by considering them performing unread measurements. Then we can calculate the distance between the resulted state and the target state:

$$d^{\{\nu_{k+8}, \nu_{k+7}, \nu_{k+6}\}} = \text{Tr} \left[(\text{TN}^{\nu_{k+8}} \text{TN}^{\nu_{k+7}} \text{TN}^{\nu_{k+6}} \rho_k) \hat{D}_{n_t} \right]. \quad (\text{III.11})$$

Among all possible choices, we find the one $\{\nu'_{k+8}, \nu'_{k+7}, \nu'_{k+6}\}$ which minimizes the distance. These types are then assigned to the corresponding samples correspondingly, i.e.:

$$\begin{aligned}\mu_{k+6} &= \nu'_{k+6}, \\ \mu_{k+7} &= \nu'_{k+7}, \\ \mu_{k+8} &= \nu'_{k+8}.\end{aligned}\tag{III.12}$$

The chosen types for the samples $k+7$ and $k+8$ may still be modified in subsequent loops.

III.4 Simulations and optimization of parameters

So far, we have explained the algorithms of the quantum state estimator and the controller. The current section is then devoted to numerical simulations of the feedback experiment and optimizations of certain parameters.

The experiment is simulated using the quantum Monte Carlo method [58, 59], in which each quantum trajectory is generated by dice tossing for the probabilistic events, such as the atom number in a sample, the prepared atomic states, the result of a virtual ideal detection and the nature of a quantum jump. The field state obtained in this way is denoted by $P^R(n)$, which is only known by a virtual observer. In the mean time, we perform state estimation on $P^R(n)$ using the algorithm present in section III.2 and obtain an estimated state denoted by $P(n)$. Based on $P(n)$, the controller chooses feedback actions according to the algorithm given in section III.3. A detailed procedure for the simulation process can be found in Appendix B. In the following, we summarize the parameters for the simulations and present the results.

III.4.1 Parameters for the simulations

In the simulations, we use the measured experimental parameters, such as the cavity lifetime, the detector efficiency, the preparation and detection errors, etc. These parameters have been given before. The other not-yet determined parameters are as follows.

We use a partition for the sensor and control samples $N_s = 12$ and $N_c = 4$, except for the results presented in III.4.3.a, where we vary this parameter in order to check its effect on the performance on the feedback process.

We use the distance defined in (III.7), except for the results presented in III.4.3.b, where we use different definitions for the distance in order to check its effect on the performance on the feedback process.

The settings for the sensors and actuators are discussed in the following paragraphs.

The sensors

As explained in section I.4.2, in order to distinguish the states from $|0\rangle$ to $|7\rangle$, we have chosen a phase shift per photon $\phi_0 \simeq \pi/4$. In the feedback loops, the sensitivity of the sensor samples to deviations from the target Fock states is determined by the Ramsey phase ϕ_r . As given in (I.102), the ideal POVMs associated to the dispersive interaction plus detection of the atomic state read

$$\hat{E}_e = \frac{1 - \cos(\phi_r - \phi(\hat{N}))}{2} \quad \hat{E}_g = \frac{1 + \cos(\phi_r - \phi(\hat{N}))}{2}.\tag{III.13}$$

For a target state $|n_t\rangle$, a straightforward choice for the Ramsey phase would be

$$\phi_r = \phi(n_t) + \frac{\pi}{2}, \quad (\text{III.14})$$

such that the probability of detecting $|e\rangle$ or $|g\rangle$ is 50%, and that the sensitivity to photon number deviation around n_t is maximized. To illustrate the setting (III.14), we show the probabilities for detecting the state $|g\rangle$ as a function of n in Fig. III.3, with $n_t = 3$ or 5.

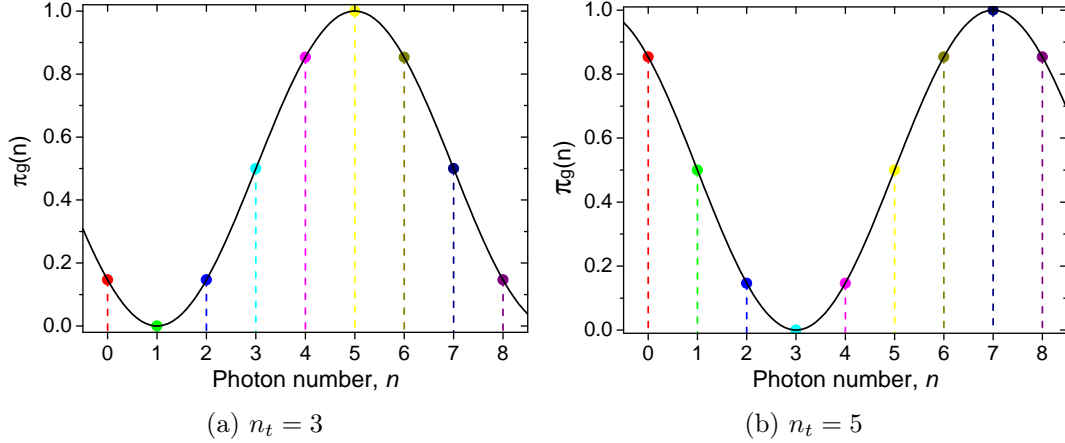


Figure III.3. Probabilities for detecting the atomic state $|g\rangle$ in different Fock states for a sensor atom. The Ramsey phases are set such that $\pi_g(n_t) = 0.5$.

From Fig. III.3a, we see that the states with $n < 3$, e.g. $|0\rangle$, $|1\rangle$ and $|2\rangle$, as well as those with $n > 3$, e.g. $|4\rangle$, $|5\rangle$ and $|6\rangle$ can be well distinguished from $|3\rangle$. Consequently, the state estimator can efficiently estimate if there are fewer or more photons than 3 in the cavity field, and the controller can then react correspondingly. Nevertheless, $\pi_g(3) = \pi_g(7)$, which means that $|7\rangle$ cannot be distinguished from $|3\rangle$ straightforwardly. But field relaxation can help to remove this ambiguity rapidly². Once $|7\rangle$ decays to $|6\rangle$, the controller can then realize that the field contains more photons than wanted (since $\pi_g(6) > \pi_g(3)$), and send photon absorbers to further reduce the photon number. So the state $|7\rangle$ is actually an unstable state while the feedback process is running.

This instability originates from the fact that the function $\pi_g(n)$ has opposite slopes for the states $|3\rangle$ and $|7\rangle$. So correspondingly, if $n_t = 7$, the state $|3\rangle$ is then an unstable state in the feedback process. In our experiments, there exist other such state pairs, such as $|1\rangle$ and $|5\rangle$, $|2\rangle$ and $|6\rangle$. Figure III.3b shows the setting of the Ramsey phase for $n_t = 5$. With this setting, the state $|1\rangle$ is an unstable state while the feedback process is running. The field can eventually be stabilized around $|5\rangle$.

The actuators

The actuators interact resonantly with the cavity field during a certain time interval, denoted by $t_e(n_t)$ for the RE samples, and $t_g(n_t)$ for the RG samples. A possible choice for these interaction time is given by the conditions of a *trapping state* [33]: making a Rabi 2π pulse in the target state for both RE and RG samples. The corresponding interacting time are denoted by $t_e^{2\pi}(n_t)$ and $t_g^{2\pi}(n_t)$, respectively. Under these conditions, if the field is in $|n_t\rangle$, it

²The time needed for this process can be roughly estimated as the lifetime of $|7\rangle$, which is $T_{\text{cav}}/7 \simeq 9\text{ms}$.

is left unchanged (assuming ideal Rabi oscillations). Whereas, if it is in other photon number states, it may gain or lose photons and move towards $|n_t\rangle$. For the following simulations, we use these interaction time, except in section III.4.3.c, where we adjust the interaction time in order to optimize the performance of the feedback process.

III.4.2 Results of the simulations

Individual quantum trajectory

A typical individual quantum trajectory with the target state $|n_t = 3\rangle$ is shown in Fig. III.4.

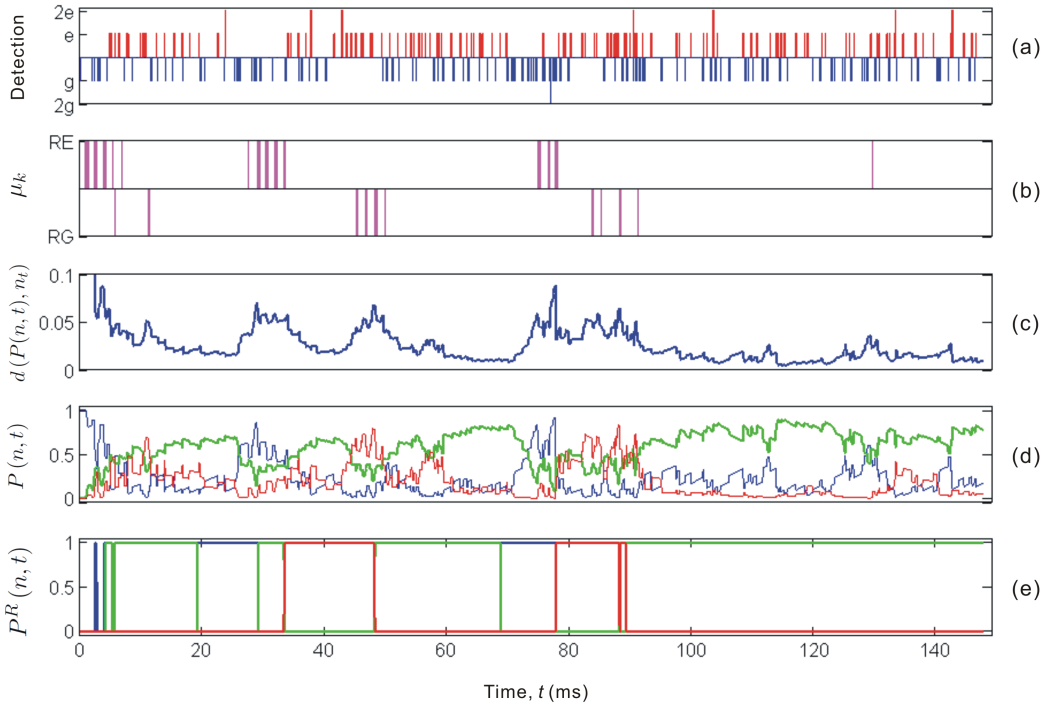


Figure III.4. Individual quantum trajectory with $n_t = 3$. (a) detected results of the sensor samples, with e or g denoting that 1 atom is detected in the states $|e\rangle$ or $|g\rangle$, and $2e$ or $2g$ denoting that 2 atoms are detected in the states $|e\rangle$ or $|g\rangle$; (b) the samples chosen as actuators (the samples chosen as QND type are not shown in this figure); (c) distance between the current and the target states; (d) estimated photon number distribution, with $P(3)$ (green), $P(n > 3)$ (red), $P(n < 3)$ (blue); (e) the photon number distribution of the real field, with $P^R(3)$ (green), $P^R(4)$ (red), $P^R(2)$ (blue) and others not shown here.

Panel (a) showing the detection results of the sensor samples. The field is initially in the vacuum state. Once the feedback process is started, the controller commands many RE samples in order to inject photons, as we can see in panel (b). Then the distance between the current and the target state decreases as shown in panel (c). The estimated field state are given in panel (d). We see that the probability of $|3\rangle$ (green curve in (d)) in the estimated state gradually increases until about $t = 26$ ms when the quantum state estimator realizes the occurrence of a quantum jump to $|2\rangle$. This jump actually occurred at about $t = 20$ ms in the real field, as shown in panel (e). Comparing the results in (d) and (e), we see that

the evolution of the estimated state lags behind the real state of the field. Whenever there is a sudden quantum jump, the estimator needs some time to realize it, e.g. ~ 6 ms for the case mentioned above. Nevertheless, if the real field remains at a specific state for a relatively long time, e.g. the period between about 48 ms to 65 ms and from 90 ms till the end of the trajectory, the quantum state estimator reaches a relatively close estimate of the real state, thanks to the measurements performed by many sensor samples during these periods.

The stationary regime

Instead of looking at an individual trajectory, we can also take an ensemble average of many of them. Figure III.5 shows the average $P(n, t)$ of 2000 individual quantum trajectories. In fact, the average $P(n, t)$ is identical to the average $P^R(n, t)$ (not shown here), meaning that the field state is correctly estimated from an ensemble point of view [60]. We see that once the feedback process is started, $P(0)$ quickly drops and $P(1)$, $P(2)$ and probabilities of other higher photon number states grow. In about 20 ms, the distribution $P(n, t)$ reaches a stationary regime, in which $P(n, t)$ remain generally stable but with small visible variations. These small variations, related to the periodical structure of the partition (N_c, N_s) in the sample sequence, will be discussed in more detail while analyzing the experimental results in section IV.3.

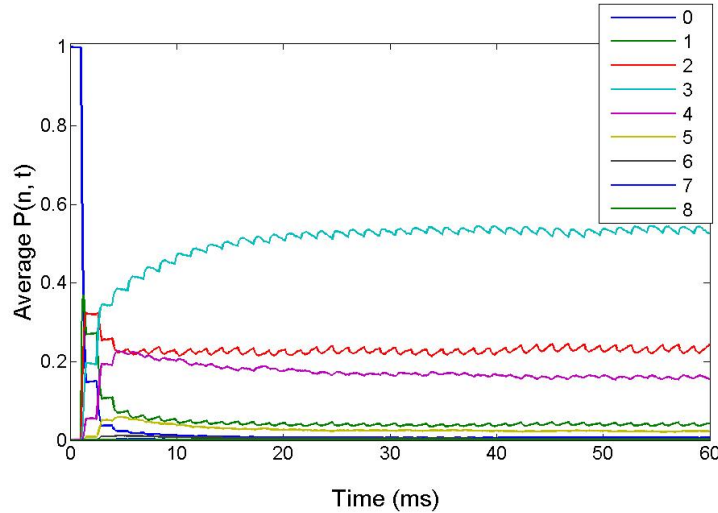


Figure III.5. Evolution of the $P(n, t)$ averaged over 2000 individual quantum trajectories, with $n_t = 3$.

In the stationary regime, we can average the photon number distribution over the period $N_c + N_s$ to smooth out the small variations and obtain the $P(n)$ shown in Fig. III.6. Here, the field reaches a fidelity of about 53%, called a *steady state fidelity* in the following.

Convergence speed

On the individual trajectories, we see that $P(n_t, t)$ can reach fidelities higher than the steady state fidelity. So instead of looking at the steady state $P(n)$, which is equivalent to terminating the feedback process at a random time in the stationary regime, we can terminate the feedback process once the estimated fidelity of the target state reaches a certain value, say, 80%. In this case, we would ask: how fast can the individual trajectories reach that fidelity?

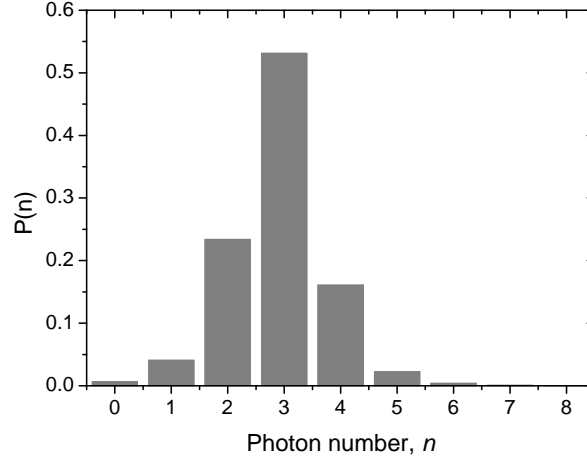


Figure III.6. Photon number distribution $P(n)$ of the steady state, with $n_t = 3$.

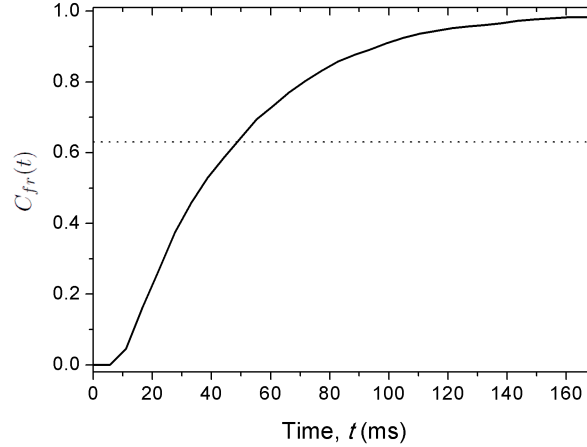


Figure III.7. Converged fraction as a function of time. The dotted line shows the 63% level.

The results of 2000 individual trajectories are shown in Fig. III.7. In this simulation, an individual trajectory is declared to be *converged*, once the fidelity of the target state reaches 80% in 3 successive feedback loops. The fraction of the converged trajectories $C_{fr}(t)$ as a function of time, defined as the ratio between the number of trajectories converged before t and the total number of trajectories, is thus obtained. We can further define a convergence time t_{conv} , which is the time needed for $1 - e^{-1} = 63\%$ of the trajectories to reach the convergence criterion. The level of 63% is highlighted by the dotted line in Fig. III.7. In the current simulation, $t_{\text{conv}} \simeq 50$ ms.

III.4.3 Optimizations

Now we know the steady state fidelity and the speed of convergence. We can then finely tune the parameters of the feedback process to optimize its performance on both aspects.

III.4.3.a The partition of samples

In section III.1, we have explained the structure of the sample sequence, in which we define a partition of the sensor and control samples. We then use numerical simulations to search for the optimal partition (N_c, N_s) .

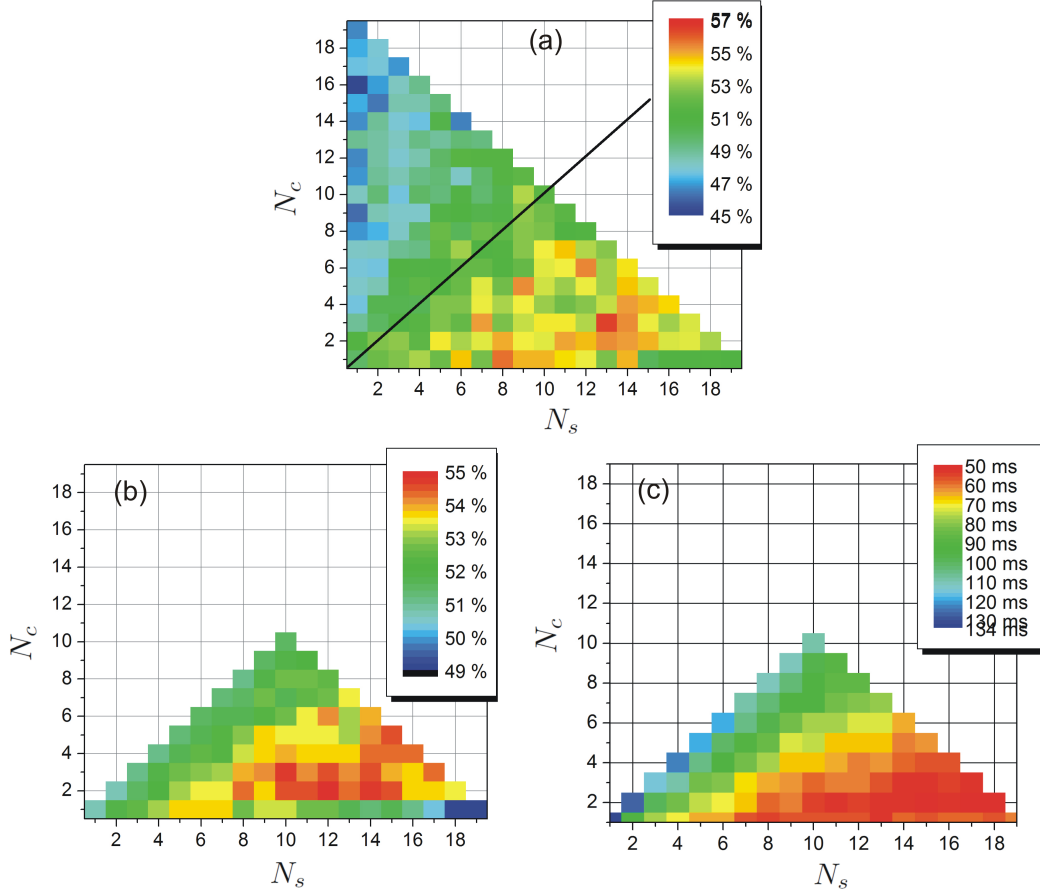


Figure III.8. Steady state fidelity of the target state and convergence time as functions of different partitions (N_s, N_c) , with $n_t = 3$. (a) Steady state fidelity as a function of (N_s, N_c) . The relatively high fidelity is obtained below the solid line. (b) Same simulations as in panel (a), but with 10 times more trajectories and thus smaller statistical errors. (c) Convergence time for different partitions, based on the same data as in (b).

With $|3\rangle$ being the target state, Fig. III.8 displays the simulation results on the steady state fidelity and the convergence time as functions of N_s and N_c . In panel (a), both N_s and N_c are varied from 1 to 19 with the total number limited by 20. For each partition, 200 individual quantum trajectories are averaged. Note that the pairs (N_c, N_s) leading to relatively high fidelities concentrate within the region below the solid line, in which we have $N_s > N_c$. On the contrary, if we have very few QND samples (on the left-most region), the fidelity is generally low. The panel (b) shows the simulation results in the region with $N_s \geq N_c$. Each point is obtained by averaging over 2000 quantum trajectories, such that the statistical error is below 0.5%. The panel (c) shows the convergence time, based on the same

data as those in panel (b). The fastest convergence also occurs in the right bottom corner. The partition (2, 14) seems to be an optimal setting, because it leads to not only the highest fidelity, but also one of the shortest convergence time.

We performed experiments with the partition $(N_c, N_s) = (2, 14)$, and several other partitions with different ratios between N_c and N_s , while keeping their sum constant. We found that the partition $(N_c, N_s) = (4, 12)$ led to a steady state fidelity about 5% higher than that obtained by the partition (2, 14), although the convergence time for both was almost the same. This small discrepancy between simulations and experiments may originate from certain experimental conditions not fully taken into account in the models used in the simulations. In the end, we kept the partition $(N_c, N_s) = (4, 12)$ in experiments.

III.4.3.b Distance functions

In section III.3.1, we define a distance to the target state by (III.7). Compared with the fidelity-defined distance, it can tell the relative ‘‘closeness’’ of different Fock states to the target state $|n_t\rangle$. In fact, for the purpose of revealing the relative ‘‘closeness’’ of different Fock states to $|n_t\rangle$, we can define many other functions, such as $d_{n_t}(n) = |n - n_t|^\Lambda$, with different values for Λ . Does the performance of the feedback process depend on the distance function? To answer this question, we perform simulations with several values for Λ .

The results are summarized in Fig. III.9. The panel (a) shows the fidelity-defined distance function and the functions $d_{n_t}(n)$ with $\Lambda = 0.5, 1, 1.5, 2$. These functions are normalized to have a maximum value of 1. The panel (b) shows the obtained steady state photon number distributions.

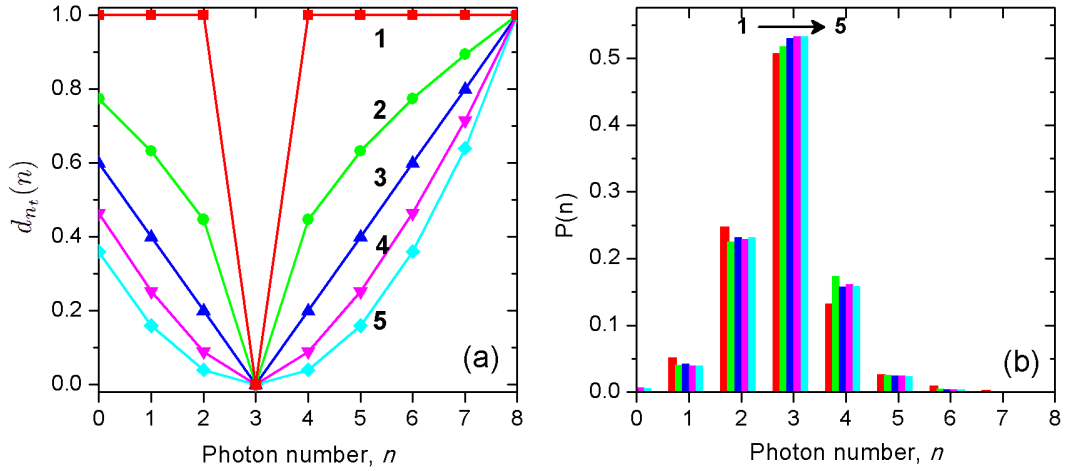


Figure III.9. Different distance functions (a) and the corresponding steady state photon number distributions $P(n)$ (b). The distance functions $d_{n_t}(n)$ are labeled with number 1 to 5. The $P(n)$ are arranged such that from left to right they correspond to the $d_{n_t}(n)$ from 1 to 5. They are also linked to each other by the same color.

We see that the fidelity-defined distance leads to a steady state fidelity about 6% lower than that obtained by using the distance function with $\Lambda = 2$. The corresponding convergence time (not shown here) is also longer by about 20%. However, the performances using the distance functions 3 to 5 are almost the same. This means that the feedback process is not very

sensitive to the form of the distance function. Eventually, we choose the function with $\Lambda = 2$, which leads to the distance defined in (III.7).

III.4.3.c The interaction time for actuators

So far, we use the interaction time $t_e^{2\pi}(n_t)$ and $t_g^{2\pi}(n_t)$ in simulations, which would leave the target state unchanged if the Rabi oscillations were ideal. Nevertheless, in practice the Rabi oscillations have a limited contrast. As a result, these interaction time does not suppress photon exchange even if the field is in the target state. For instance, in experiments, with interacting time $t_e^{2\pi}(3)$ or $t_g^{2\pi}(3)$, the probability for photon exchange, although minimal, is still about 20% in $|3\rangle$. So in this situation, are the conditions of the “trapping state” still an optimal choice? To answer this question, we perform simulations with different interaction times.

The steady state fidelities of the target states $|2\rangle$ and $|3\rangle$ as functions of the interaction time $t_e(n_t)$ and $t_g(n_t)$ are shown in Fig. III.10. The coordinates of the solid circles in the figure show the interaction times used in the simulations, while all other parameters remain the same. The figures are generated by interpolation within the measured values.

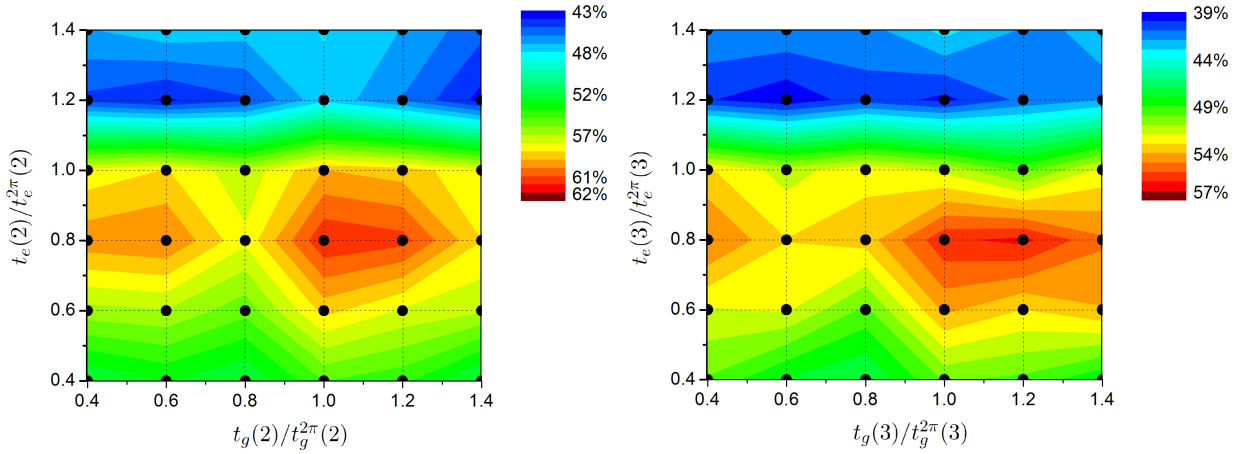


Figure III.10. Steady state fidelities of the target states $|2\rangle$ (left) and $|3\rangle$ (right) obtained with different settings for $t_e(n_t)$ and $t_g(n_t)$. The coordinates of the solid circles show the parameters for different runs of the simulations.

We see that the highest fidelity is obtained using the setting close to $t_e(n_t) = 0.8t_e^{2\pi}(n_t)$ and $t_g(n_t) = 1.2t_g^{2\pi}(n_t)$. Compared with the results using the conditions of the “trapping states”, the fidelity is increased from about 53% to 57% for $|3\rangle$ and from about 58% to 62% for $|2\rangle$. The convergence time (not shown here) is also slightly optimized.

Discussion

The actuator samples exchange photons with the cavity field. In order to stabilize the field state around $|n_t\rangle$, this exchange process should be constrained by several requirements. First, it should be avoided in $|n_t\rangle$ (ideally). Secondly, the RE sample should emit a photon efficiently for the states with $n < n_t$ and inefficiently for those with $n > n_t$. Thirdly, the RG type should absorb a photon efficiently in states with $n > n_t$ and inefficiently in the states with $n < n_t$.

In practice, the photon exchange process is achieved by switching on the resonant interaction during a certain time interval. In simulations, we see that the performance of the feedback process is optimized, if we reduce (by $\sim 20\%$) the interaction time for a RE sample and increase (by $\sim 20\%$) the interaction time for the RG sample. This phenomenon essentially originates from a trade-off between minimizing the perturbation to the target state and enhancing the efficiency for absorbing (RG) or emitting (RE) photons while the field state deviates from the target state.

To illustrate this point, we make a comparison of the interactions with different interaction time. Based on the non ideal Kraus operators in (II.37) and (II.38), the triangles in Fig. III.11 display the probabilities for emitting $P_{\text{emi}}(n)$ or absorbing $P_{\text{abs}}(n)$ a photon in different Fock states with interaction time $t_e^{2\pi}(n_t)$ and $t_g^{2\pi}(n_t)$ for $n_t = 3$. We see that the probability for photon exchanges in $|3\rangle$ is minimized, but still has a value of about 20%.

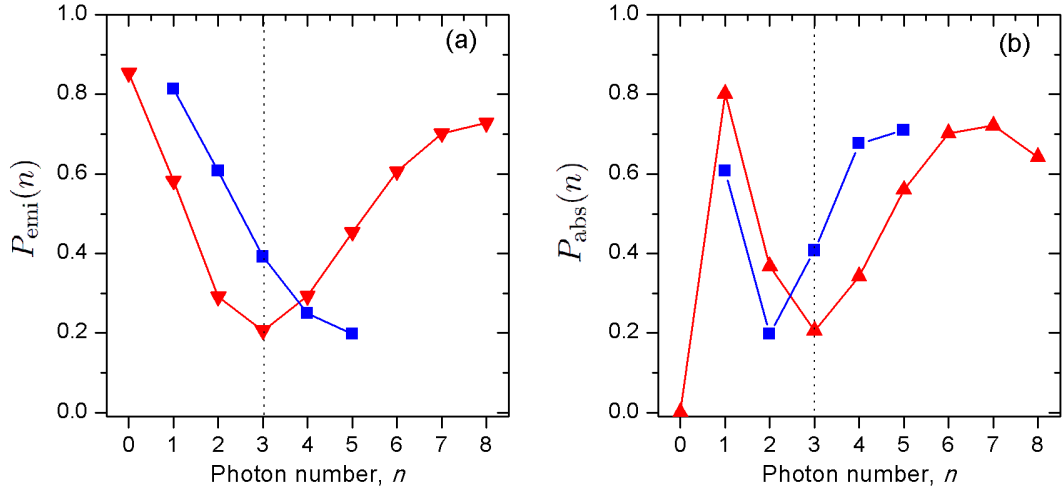


Figure III.11. Probability for photon exchanges in different photon number states with $n_t = 3$. (a) Probabilities for emitting one photon by an atom in $|e\rangle$. The triangles correspond to the probabilities with the interaction time $t_e^{2\pi}(3)$. The squares correspond to those with $0.8t_e^{2\pi}(3)$. (b) Probabilities for absorbing one photon by an atom in $|g\rangle$. The triangles correspond to the probabilities with $t_g^{2\pi}(3)$. The squares correspond to those with $1.2t_g^{2\pi}(3)$.

As a comparison, the squares in Fig. III.11 show the probabilities of photon exchanges for the interaction time $t_e(n_t) = 0.8t_e^{2\pi}(n_t)$ (panel (a)) and $t_g(n_t) = 1.2t_g^{2\pi}(n_t)$ (panel (b)). Here only the photon numbers satisfying $|n - n_t| \leq 2$ are shown, because these states are actually the most relevant ones in a feedback experiment with the target state $|n_t\rangle$. The probabilities for photon exchanges in $|3\rangle$ are enhanced from 20% to about 40%. However, the probabilities in other Fock states are modified in a desirable way. For instance, the probability $P_{\text{emi}}(n)$ is enhanced for the states with $n < 3$ and reduced for states with $n > 3$. So we can expect that a RE sample works more efficiently as a photon emitter. Similarly, the probability $P_{\text{abs}}(n)$ becomes larger in states with $n > 3$ and smaller in states with $n < 3$. So we may also expect that the RG sample work more efficiently as a photon absorber.

In summary, balancing the effects of the actuators to the target and other states, a compromise is found with the following interacting time $t_e(n_t) = 0.8t_e^{2\pi}(n_t)$ and $t_g(n_t) = 1.2t_g^{2\pi}(n_t)$, which are used in our experiments.

Conclusion

In the very beginning of this chapter, we present the sequence of atomic samples. Their spatial configuration at the moment when we choose a feedback action and their implementation in experiments are necessary information for understanding the algorithms of the quantum state estimator and the controller. We then present the algorithms for the state estimator and the controller, which are used in the simulations. Based on the simulation results, we optimize certain parameters of the feedback process. For instance, we have chosen a partition³ for sensor and control samples $(N_c, N_s) = (4, 12)$. We have also checked our choice for the distance function (III.7), which does lead to a better performance than a distance merely relying on fidelity. We have also chosen the interaction time for the actuator samples: $t_e(n_t) = 0.8t_e^{2\pi}(n_t)$ and $t_g(n_t) = 1.2t_g^{2\pi}(n_t)$ and discussed why this setting is better than the conditions of the “trapping state”.

³This partition is inspired by simulations, and then chosen according to experimental performances.

Chapter IV

Experimental implementation

In this chapter, we present the experimental implementation of the feedback process. We first explain the control systems in section IV.1, and the experimental sequence in section IV.2. We then present the results in section IV.3. These results include individual quantum trajectories showing how the feedback procedure operates and the photon number distributions averaged over many individual trajectories. We also study how the controller makes decisions.

IV.1 Control systems

An experimental control system usually consists of two parts: software and hardware. In the software, we program a sequence of experimental events, which is essentially a series of digital (TTL) pulses and analog waveforms. These signals are then output by the hardware. In former experiments, we used a control software developed by Stefan Kuhr, in which we first programmed a complete sequence of events and uploaded it to various output boards. Using this system, we cannot modify the sequence while running experiments. Thus we call it a “Passive system” in the following.

In the feedback experiment, we need to modify the control events in real time according to calculation results of the quantum state estimator and the controller. So we need to have a control system which can both carry out calculations and output digital and analog signals. We thus introduced an additional control system: “ADwin Pro-II” developed by Jäger Messtechnik and adapted to our experiments by Igor Dotsenko. This new system is designated as “Active system”. In the following paragraphs, we explain its role in the feedback experiment and the functions of its modules.

IV.1.1 Organization of the control systems

The Passive and Active systems fulfil different tasks, with the main ones displayed in Fig. IV.1. The Active system controls the digital and analog signals which need to be modified in real time. All the other signals, as well as experimental parameters which do not need to be modified in real time are still controlled by the Passive system.

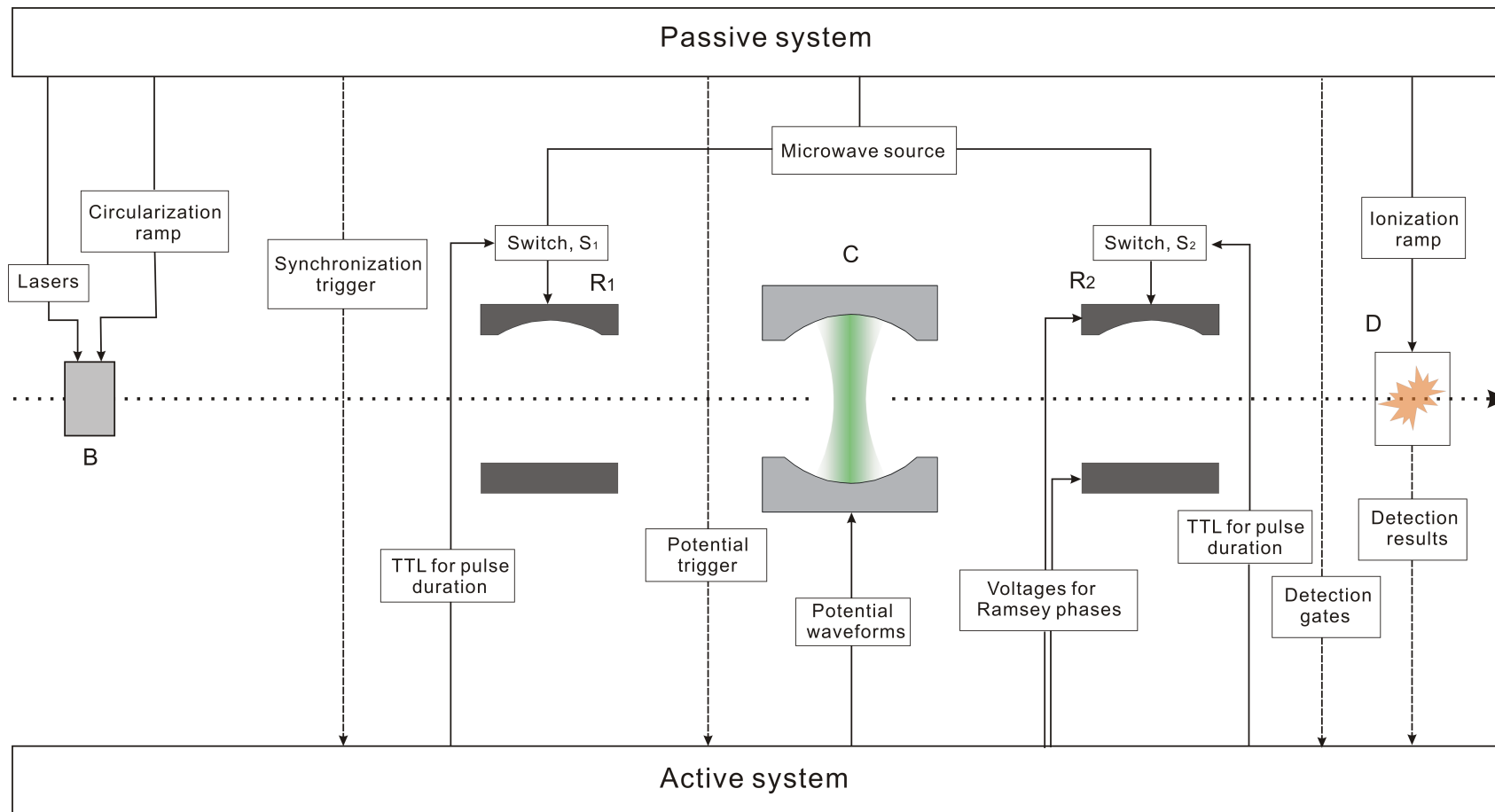


Figure IV.1. Organization of the control systems. Basic components of the experimental setup: the circularization box B, two Ramsey zones R_1 and R_2 , the cavity C and the detector D. The dotted line shows the atomic beam. The tasks fulfilled by the Passive and Active systems are displayed by the solid and dashed lines. The dashed lines also indicate the input signals for the Active system

The specific tasks fulfilled by the two systems are as follows:

Passive system

- Control pulses for the excitation lasers, circularization ramps, etc. in B for preparing circular Rydberg atoms
- Frequency and power of the microwave sources coupled to the Ramsey zones
- Ionization ramp in D for detecting the atomic samples
- Synchronization trigger sent to the Active system, which triggers the execution of a feedback loop and serves as a common time reference for the two systems
- Potential trigger sent to the Active system for outputting the potential waveform associated to an atomic sample
- Detection gates sent to the Active system, which define the time windows for detecting states $|e\rangle$ and $|g\rangle$

Besides the tasks listed above, the Passive system also controls such experimental parameters as the period of the atomic samples, the number of samples in a sequence, and the number of repetitions of the sequence, etc.

Active system

- Calculations of quantum state estimator and controller (not shown in the figure)
- Duration of microwave pulses in R_1 and R_2 by controlling switches S_1 and S_2 , respectively.
- Potential waveforms on C for changing the interaction regimes: dispersive or resonant.
- Voltages on the two mirrors of R_2 for setting a phase for the Ramsey interferometer
- Registration of detection results received as TTL pulses

IV.1.2 Main components of the Active system

Figure IV.2 displays the front panel of the Active system, on which the individual modules are highlighted. In the following paragraphs, we explain briefly their functions.

The CPU carries out the calculations for state estimation and choosing feedback actions. It has an operating frequency of 300 MHz and a very stable timing. Its response to the synchronization trigger received through the port “Event IN” is rapid and precise (about 300 ± 30 ns). These features are important for the synchronization between the Passive and Active systems, as well as for controlling precisely the timings of subsequent pulses.

The CPU has an internal memory of 250 kB, which can be accessed rapidly and is mainly used for carrying out calculations in real time. It also has an external memory of 250 MB, which has a longer and relatively less stable access time. It provides ample space for storing matrices, arrays, and other parameters used in the calculations.

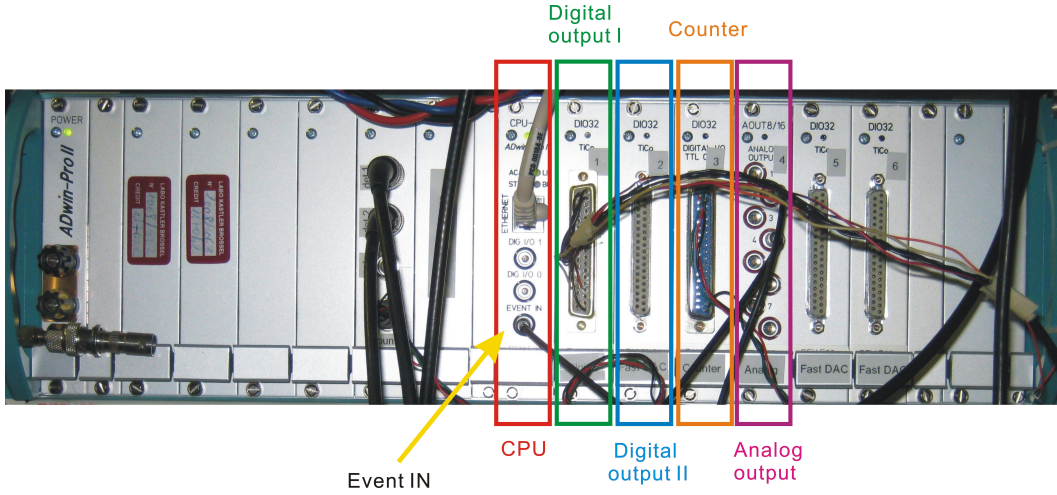


Figure IV.2. Front panel of the ADwin Pro-II system showing the following modules: CPU, Digital output I and II, Counter, and Analog output. Their functions are explained in the text. The arrow shows the input port of the synchronization trigger.

The Digital output I (DIO32 board) uses two digital output channels to control the durations of the microwave pulses in R_1 and R_2 . It outputs signals through a FIFO stack (first in, first out), which is filled by the CPU.

The Digital output II (DIO32 board with a processor) is used for applying voltage waveforms on the cavity. It uses 16 bits to encode a voltage in a binary format and outputs it every 100 ns. The digital signal is converted to an analog signal by a home-made external digital-to-analog convertor (DAC) (not shown in Fig. IV.2).

The counter (DIO32 board) is used to register the detection results of the atomic states. The board receives two sets of TTL signals, one being the detection gates which define the beginning and ending of the time windows corresponding to the atomic states $|e\rangle$ and $|g\rangle$, the other being the detection clicks corresponding to detected atoms.

The analog output is used to control the voltages on the mirrors of R_2 . It has 8 channels in total (2 of them are used in our experiments). All of them have a time resolution of about $2\ \mu\text{s}$, and are controlled by the CPU.

IV.2 Sequence

An experimental sequence consists of many equally spaced atomic samples, which can be divided into three groups. The first one includes 50 atomic samples. It prepares the cavity field in the vacuum state and is called an *initialization sequence*. The principle of this process has been explained in section I.3.3. The second group is used for the feedback process and is called a *feedback sequence*. The third group performs an independent 4-phase QND measurement as introduced in section I.4.2.b and is called a *measurement sequence*. In the following paragraphs, we explain the main experimental events associated to one sample, then discuss the feedback and measurement sequences in more detail.

IV.2.1 Experimental events for one sample

For each atomic sample, the pulsed laser at 780 nm defines a time origin for all subsequent events. A space-time diagram of one sample is given in Fig. IV.3. Several main experimental events associated to this sample are shown in the figure and explained in the following text.

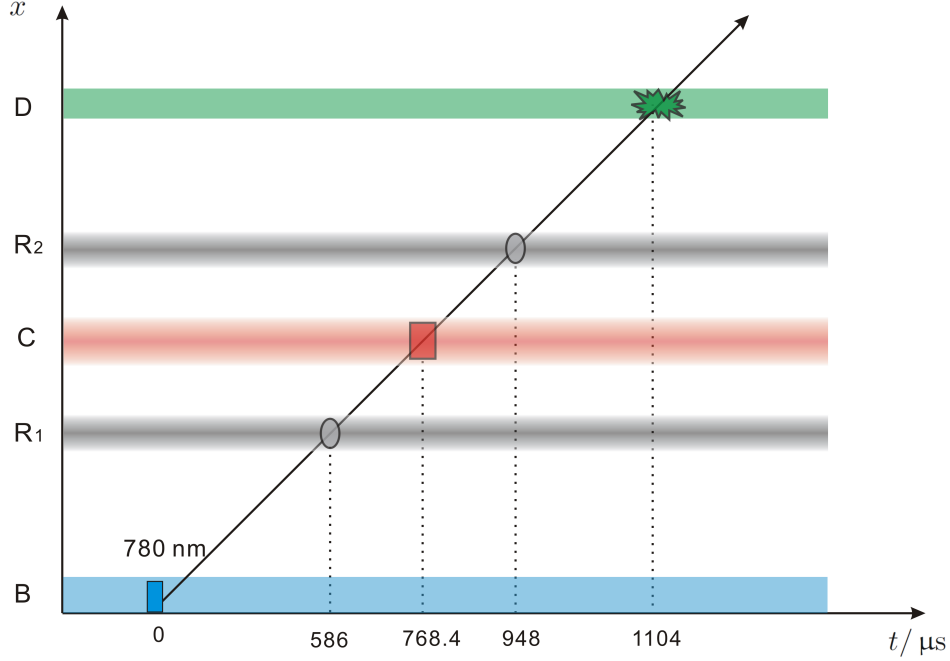


Figure IV.3. Space-time diagram of one atomic sample (not to scale). The horizontal bars show the following components: the circularization box B, the field modes of two Ramsey zones R_1 , R_2 and the cavity C, and the detector D. The timings of the pulsed laser at 780 nm, the Ramsey pulse in R_1 , the potential waveform, the Ramsey pulse in R_2 and the detection of the sample are $0 \mu\text{s}$, $586 \mu\text{s}$, $768.4 \mu\text{s}$, $948 \mu\text{s}$, $1104 \mu\text{s}$, respectively.

- At $t = 0$, the atomic sample is excited to the state $|g\rangle$ in B.
- At $t = 586 \mu\text{s}$, the sample arrives at the center of R_1 , in which a $\pi/2$ pulse, π pulse, or no pulse may be applied, depending on the type of this sample.
- At $t = 768.4 \mu\text{s}$, the sample arrives at the center of C. By default, the sample and the cavity field interact dispersively. The resonant interaction is achieved by applying a potential waveform.
- At $t = 948 \mu\text{s}$, the sample arrives at the center of R_2 , where it may experience a $\pi/2$ pulse or not, depending on its type.
- At $t = 1104 \mu\text{s}$, an ionization ramp is triggered, and the sample is detected in D.

IV.2.2 The feedback sequence

At the beginning of each sequence, 8 samples are set as sensors. They are then followed by the structure of $N_c = 4$ control samples and $N_s = 12$ sensor samples. This structure is typically

repeated 110 times. So in total we have 1768 atomic samples in the feedback sequence. Given the period of the samples $T_a = 82 \mu\text{s}$, the total duration of this sequence is $144 \text{ ms} \simeq 2.2T_{\text{cav}}$.

We associate a synchronization trigger to each atomic sample. It is sent at $t = 556 \mu\text{s}$ (with respect to the time origin of the sample), which is chosen such that the k th sample has just been detected when the trigger associated to the sample $k+7$ is sent to the Active system. Figure IV.4 shows the space-time diagram, in which the timing of the pulsed laser of the sample $k+7$ is chosen as the time origin. After receiving the synchronization trigger, the Active system executes a predefined program, in which it retrieves from its counter the detection result of the sample k , estimates the field state and chooses a feedback action using the algorithms presented in sections III.2 and III.3. Besides these, it also outputs signals to the corresponding hardware for the following $82 \mu\text{s}$. This time interval is highlighted by the two vertical lines in the upper panel and zoomed in in the lower panel of Fig. IV.4.

As shown in Fig. IV.4, the samples $k+7$, $k+5$ and $k+3$ will reach the center of R_1 , C and R_2 at $t = 586 \mu\text{s}$, $604.4 \mu\text{s}$ and $620 \mu\text{s}$, respectively. The Active system first identifies their types, then outputs the corresponding signals shown in Fig. III.2.

The digital signals to R_1 and R_2 are directly applied from the module ‘‘Digital output I’’. The constant potentials corresponding to the Ramsey phase of sample $k+3$ are applied on the two mirrors of R_2 directly from the module ‘‘Analog output’’¹. The potential waveforms on C are applied as follows. We predefine several potential waveforms in digital format and store them in the memory of the board ‘‘Digital output II’’. The application of the waveform is then divided into two steps. First, the Active system identifies the potential waveform that the sample $k+5$ requires and sets it as the next one to output. Second, the board outputs the waveform after receiving the potential trigger associated to the sample $k+5$. The waveform, in a digital format, is then converted into an analogy signal by the DAC and applied on C.

IV.2.3 The measurement sequence

During the feedback process, the quantum state estimator provides an estimated field state by incorporating a lot of *a priori* information about the field, including the field relaxation, the backactions of the sensor and actuator samples. The theoretical models describing the field relaxation and the backactions of the sensor samples were checked while performing the feedback experiments presented in [61], and agreed well with the 4-phase QND measurement. The theoretical description of the resonant interaction between the actuators and the field is a new element of the current experiment. In order to check this description, and to evaluate the performance of the feedback process, we perform an independent 4-phase QND measurement on the field state.

The method of the 4-phase QND measurement and state reconstruction have been introduced in section I.4.2.b. With a phase shift per photon $\phi_0 \simeq \pi/4$, it can distinguish 8 consecutive Fock states, e.g., from $n = 0$ to 7, 1 to 8, 2 to 9, etc. To perform the measurement, the feedback sequence is followed by 10 atomic samples with 4 alternating Ramsey phases. Given an average detected atom number 0.33/sample, we actually use 3 detected atoms on average to perform the measurement, with a duration $T_{\text{mes}} = 820 \mu\text{s}$.

The lifetime of the Fock state $|n\rangle$ is T_{cav}/n . Field relaxation during the QND measurement may not be negligible for high photon number n . On average, the field decays by $T_{\text{mes}}/2$ during the measurement. The probability for a Fock state $|n\rangle$ to lose one photon is $P_{\text{loss}}(n) =$

¹This signal is not shown in Fig. IV.4

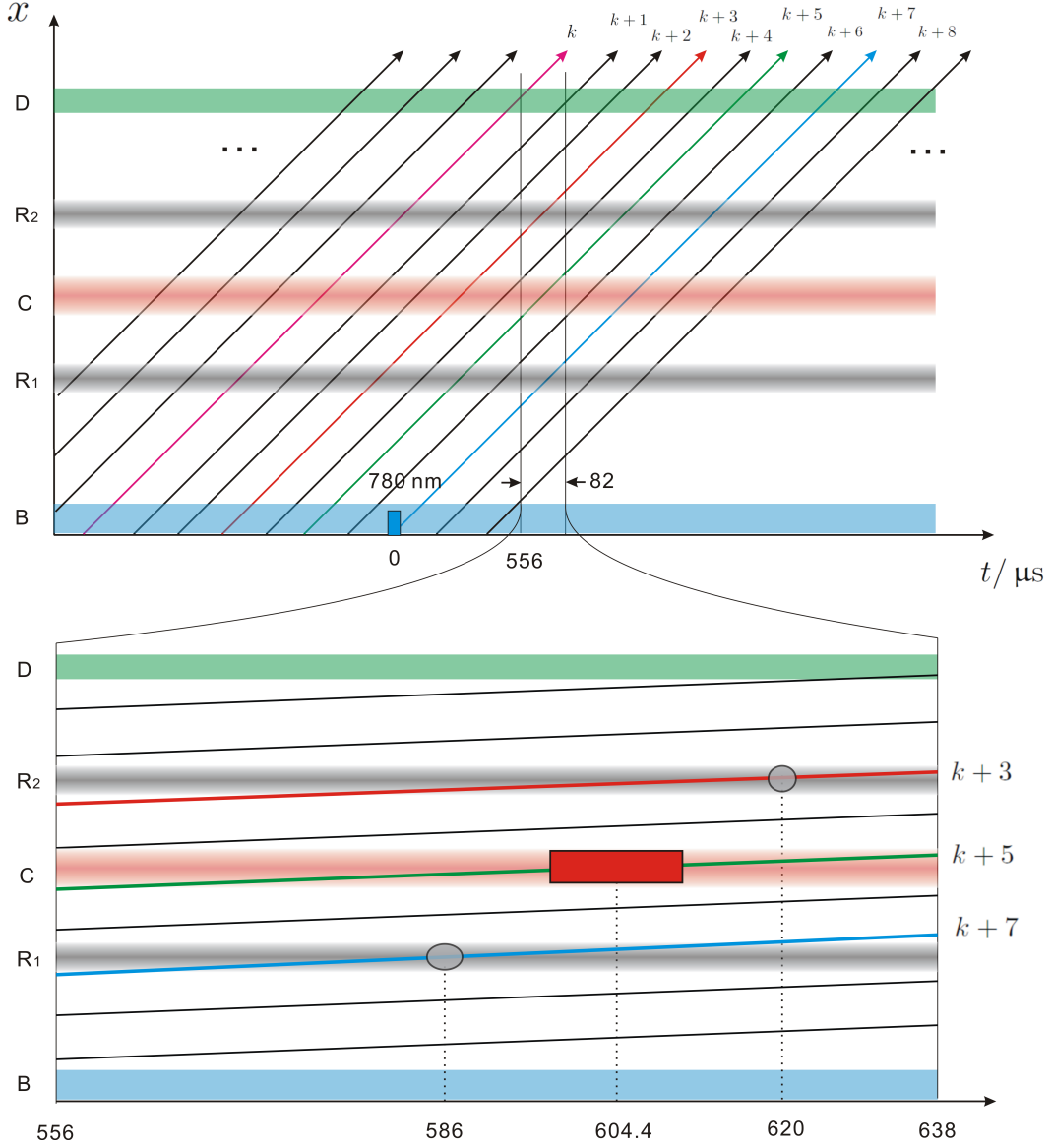


Figure IV.4. Space-time diagram of the feedback sequence (not to scale). The components of the experimental setup are the same as those given in Fig. IV.3. The upper panel shows a whole view of the samples. The sample $k+7$ sends a synchronization trigger to the Active system at $t = 556 \mu\text{s}$. In the following $82 \mu\text{s}$, the Active system needs to retrieve the detection result of sample k (purple) and output signals to the hardware for the samples $k+3$ (red), $k+5$ (green) and $k+7$ (blue). These signals are shown in the lower panel, which is a zoom in of the region between the two vertical lines.

$\exp[-n(1+n_{\text{th}})T_{\text{mes}}/2T_{\text{cav}}]$. Given that $n_{\text{th}} = 0.05$ and $T_{\text{cav}} = 65 \text{ ms}$, we get $P_{\text{loss}}(n) \simeq 0.6\%$, $\simeq 1.3\%$, $\simeq 2.0\%$, $\simeq 2.6\%$, $\simeq 3.3\%$, $\simeq 3.9\%$ and $\simeq 4.5\%$ corresponding to $n = 1$ to 7 . Since these probabilities are small, we may neglect the effect of field relaxation during the QND measurement.

IV.3 Results

We now present the experimental results. In order to illustrate how the feedback procedure operates, we first show several individual quantum trajectories. Then we present the results of the QND measurement on thousands of trajectories. We also study the chosen types for the control samples and analyze the behavior of the controller.

IV.3.1 Individual trajectories

Typical individual quantum trajectories with target states from $n_t = 1$ to 7 are shown in Figs. IV.5 to IV.11. In these figures, panel (a) shows the detection results of sensor samples. Panel (b) shows the types μ_k of the control samples which are used as actuators. Panel (c) displays the distance $d(\rho_t, \rho_k)$ between the current and the target states. Panel (d) shows the estimated photon number distribution $P(n, t)$, with $P(n_t, t)$ (green), $P(n > n_t, t)$ (red), and $P(n < n_t, t)$ (blue). For the trajectories with $n_t = 1$ to 4, certain events, such as initial convergence, quantum jumps and recoveries, are also indicated in the figures.

Initially, the cavity is prepared in its vacuum state. We see that at the beginning of each trajectory, many control samples are set as RE types in order to inject photons into the cavity. The field state gradually converges to the target state and reaches a relatively high fidelity, a process referred to as *initial convergence* in the following.

Once the target state reaches a high fidelity, the controller finds that photon emission or absorption is unnecessary and sets all the control samples to the QND type. Suddenly a quantum jump occurs, which can be either a jump down or up. In either case, the state estimator reveals that the field state deviates from the target state, and thus the distance increases. The controller then chooses the RE or RG samples to reduce the distance, i.e. to correct this jump. Finally, the target state is recovered and the following control samples are again set to the QND type. Within the trajectory, we can see many such jumps, especially for higher photon numbers, because the lifetime of a Fock state $|n\rangle$ is T_{cav}/n , thus the higher the photon number is, the more frequent quantum jumps occur. So the controller needs to command corrections more frequently for stabilizing a state with higher n_t . We can also see that the quantum jumps towards lower n are more frequent than those towards higher n , since photon losses induced by cavity decay dominates over photon gains induced by thermal excitation.

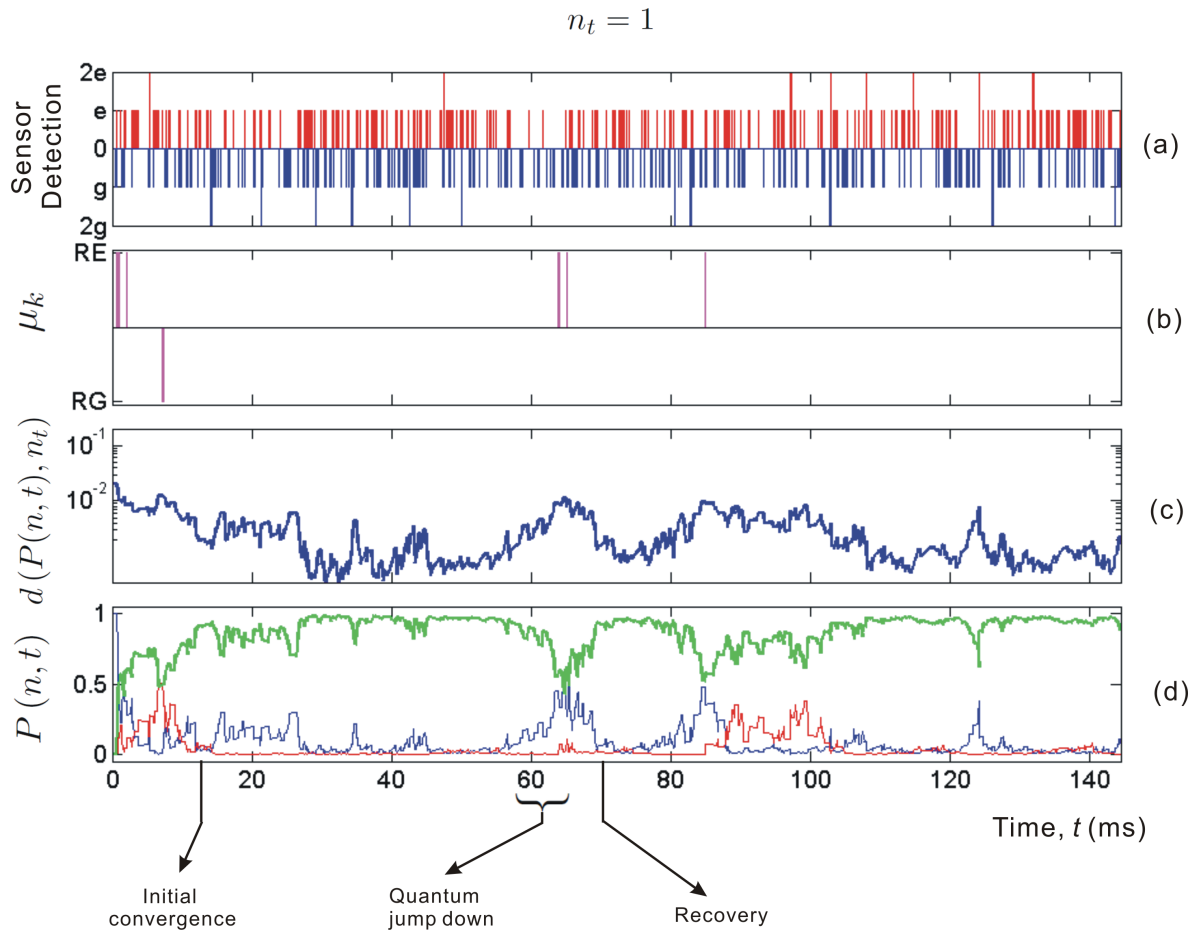


Figure IV.5. Individual quantum trajectory with $n_t = 1$. (a) Detection results of the sensor samples, with e or g denoting that 1 atom is detected in the states $|e\rangle$ or $|g\rangle$, and $2e$ or $2g$ referring to events with two atoms detected in $|e\rangle$ or $|g\rangle$. (b) the types μ_k of the control samples chosen as actuators. (c) the distance between the current and the target states. (d) the photon number distributions: $P(n_t, t)$ (green), $P(n > n_t, t)$ (red) and $P(n < n_t, t)$ (blue). The events, such as initial convergence to the target state, quantum jumps and recovery are indicated by the arrows.

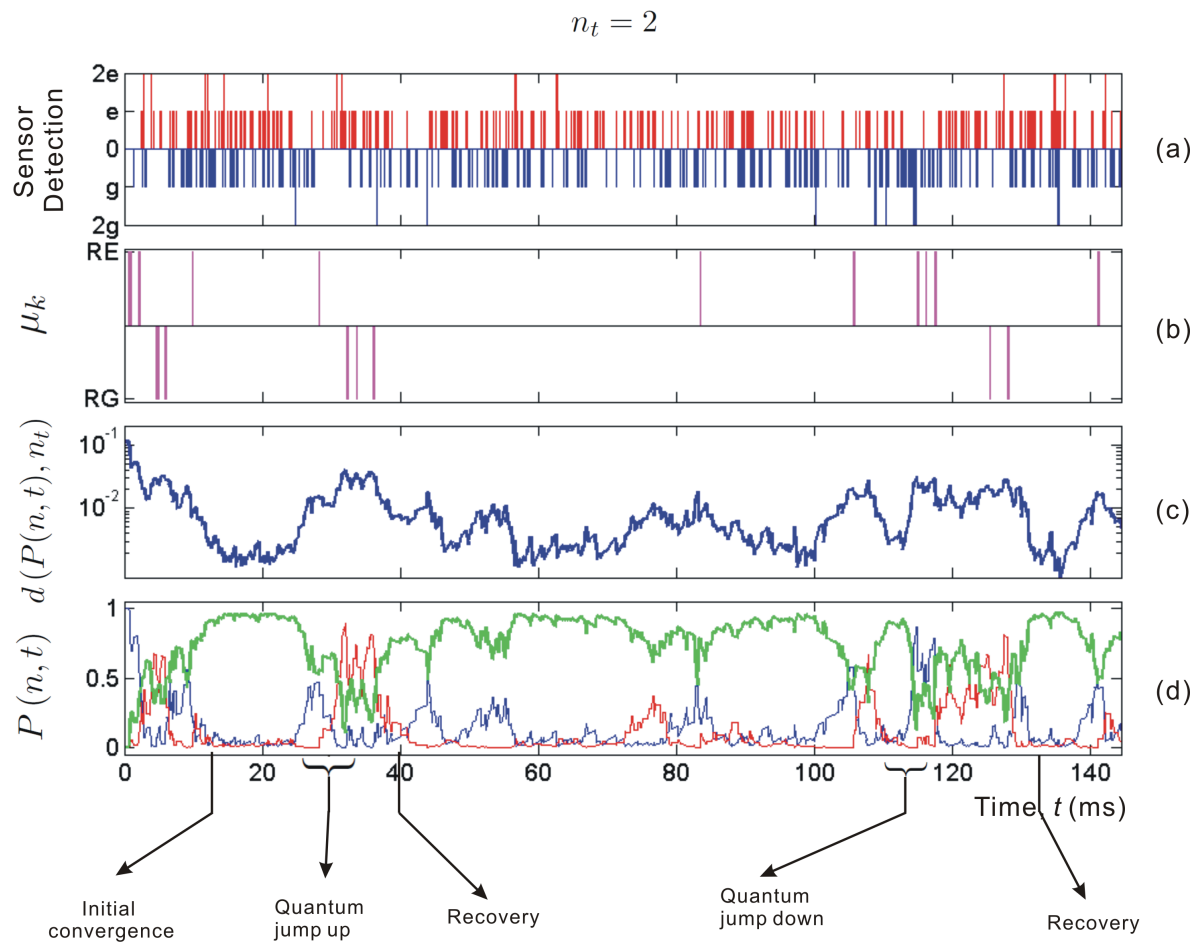


Figure IV.6. Individual quantum trajectory with $n_t = 2$. See the caption of Fig. IV.5 for explanations.

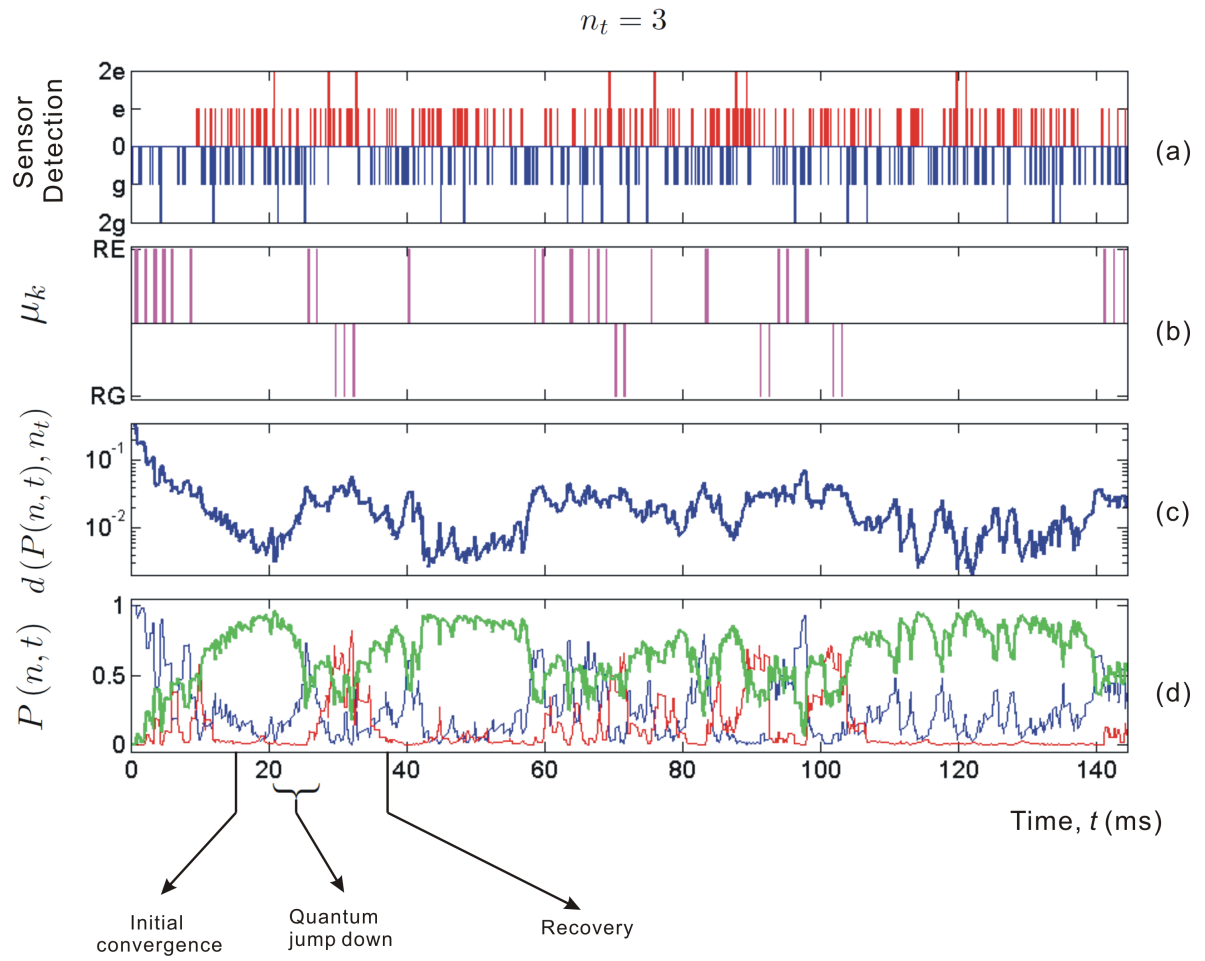


Figure IV.7. Individual quantum trajectory with $n_t = 3$. See the caption of Fig. IV.5 for explanations.

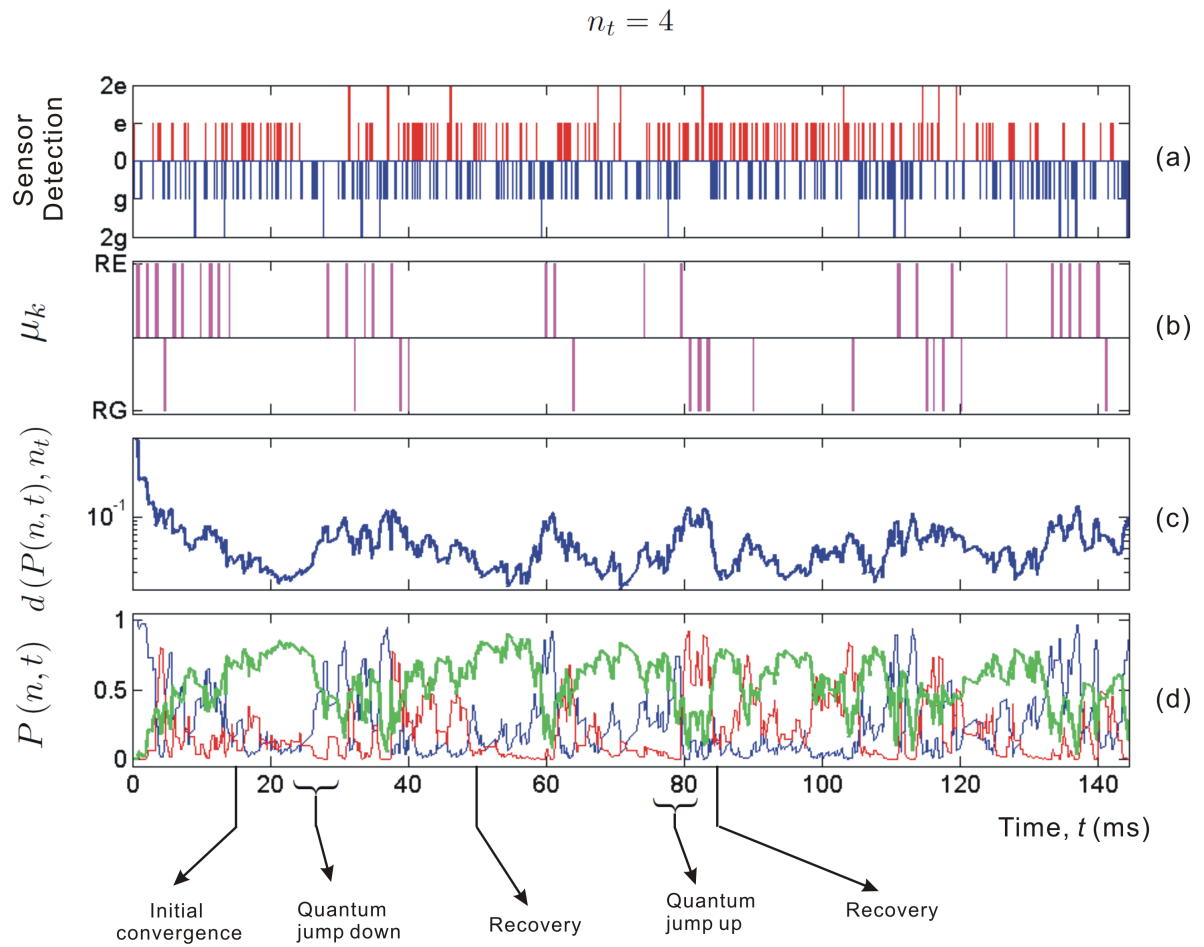


Figure IV.8. Individual quantum trajectory with $n_t = 4$. See the caption of Fig. IV.5 for explanations.

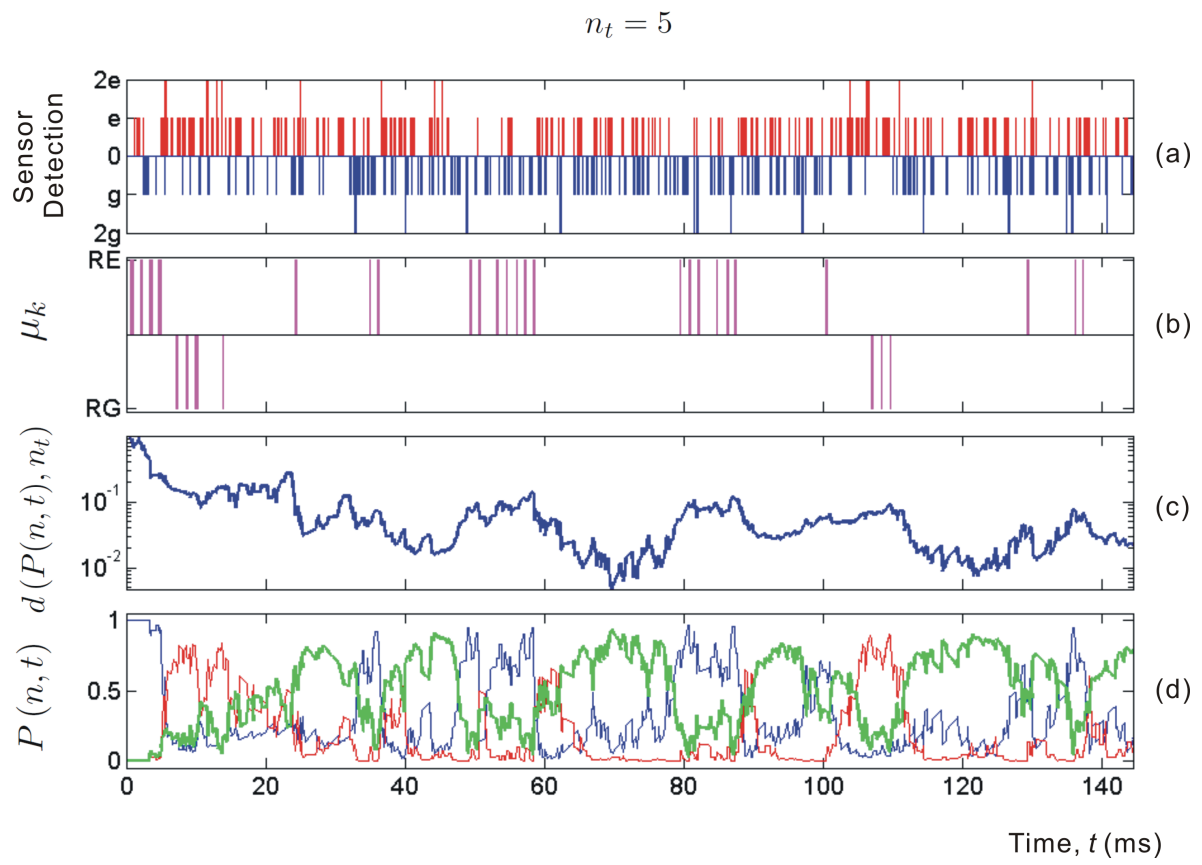


Figure IV.9. Individual quantum trajectory with $n_t = 5$. See the caption of Fig. IV.5 for explanations.

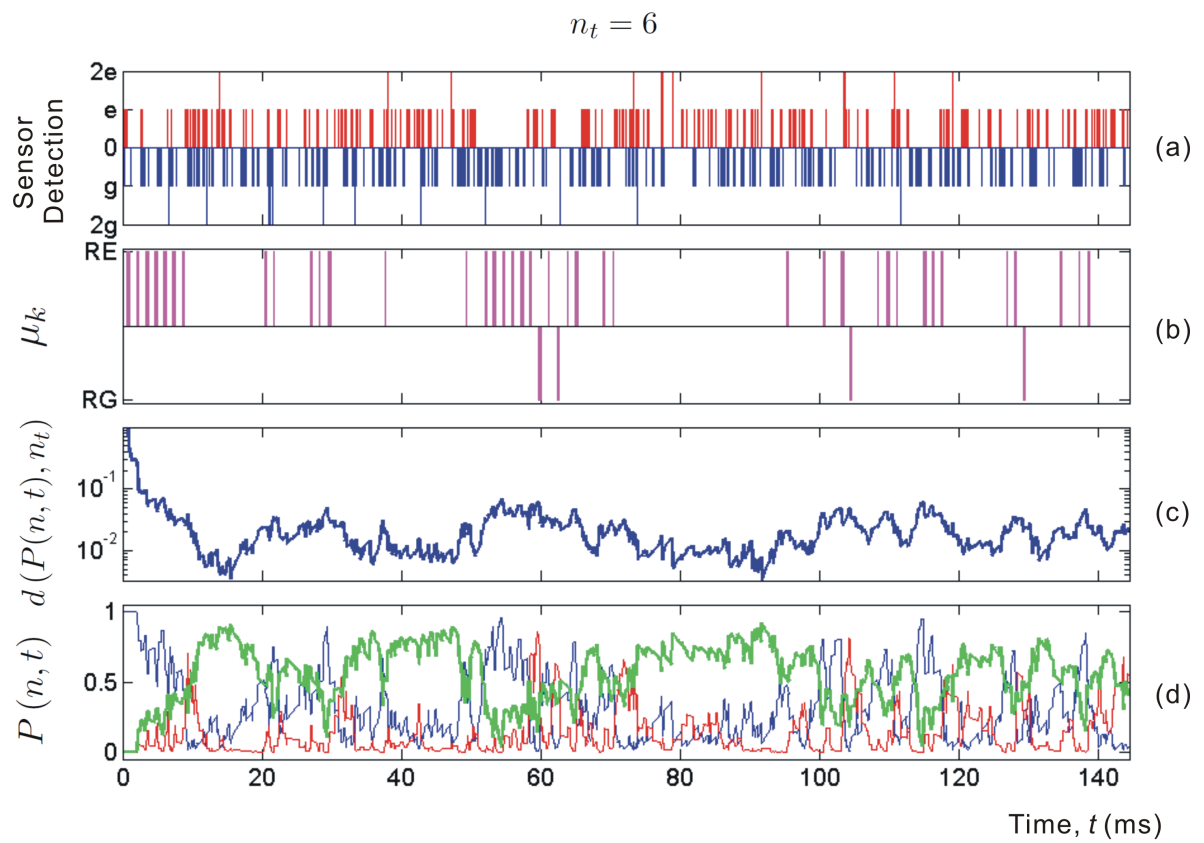


Figure IV.10. Individual quantum trajectory with $n_t = 6$. See the caption of Fig. IV.5 for explanations.

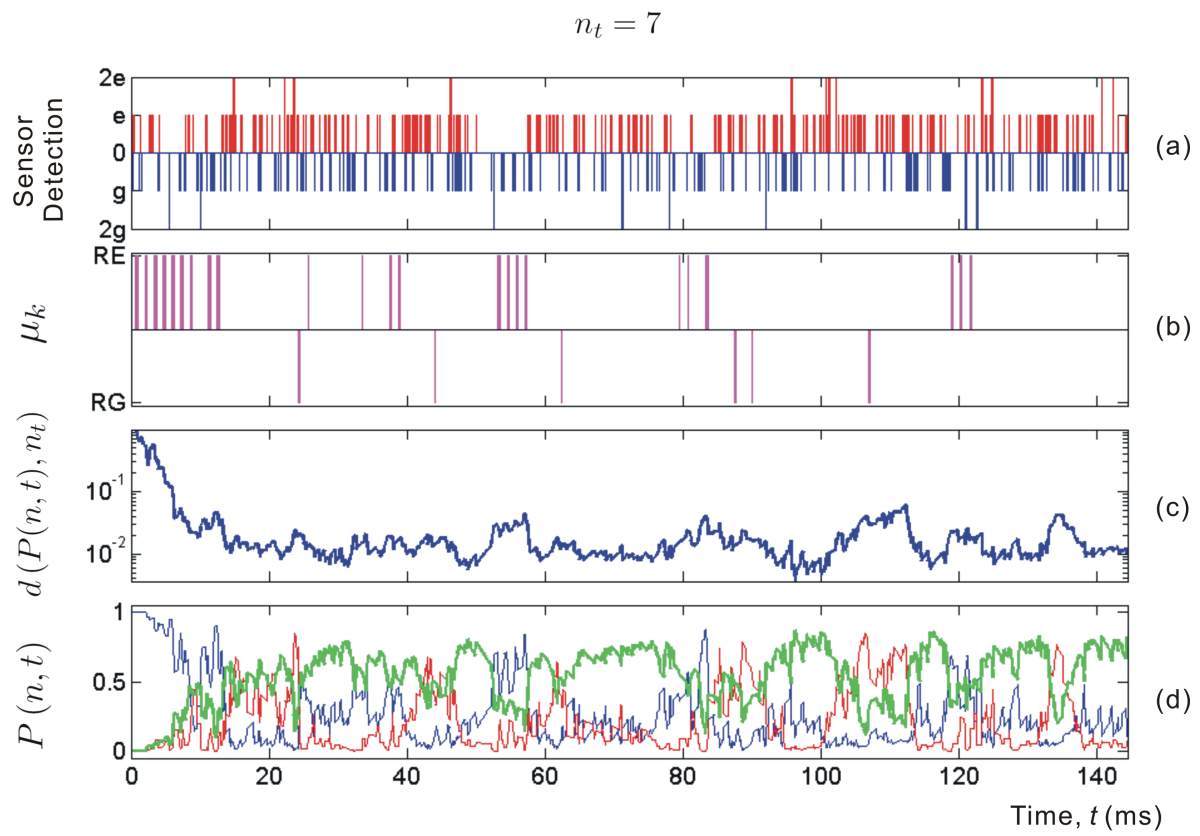


Figure IV.11. Individual quantum trajectory with $n_t = 7$. See the caption of Fig. IV.5 for explanations.

Sequential preparation

Besides preparing a single target state, the feedback process can also prepare a series of pre-programmed states. In this experiment, called *sequential preparation*, the controller switches from one n_t to the next one, once $P(n_t)$ reaches 80% in 3 successive feedback loops. Then the setting of the Ramsey phase is changed, such that $\phi_r = \phi(n_t) + \pi/2$ is guaranteed. The parameters for the quantum maps associated to the sensors and actuators are also changed correspondingly in the quantum state estimator and controller.

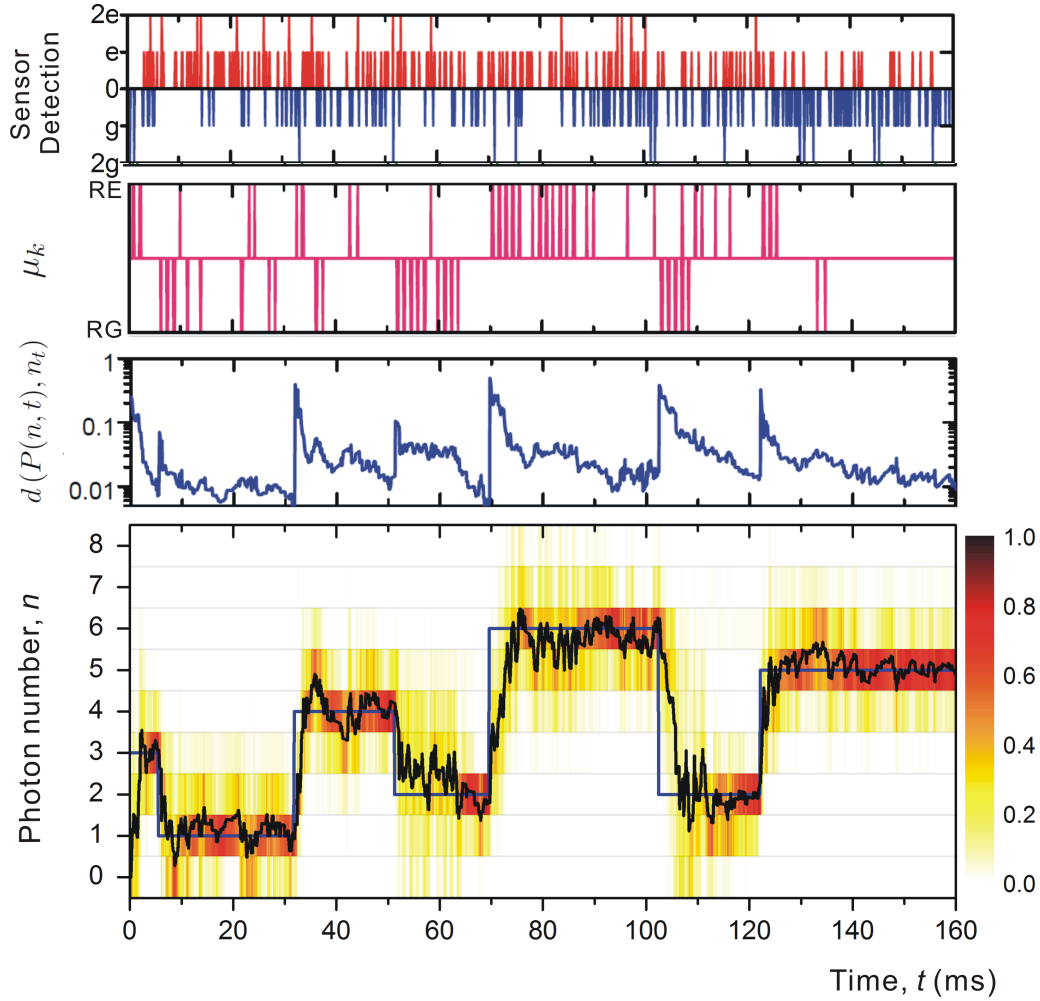


Figure IV.12. Individual quantum trajectory of a sequential preparation experiment. See the caption of Fig. IV.5 for the explanations of the three upper panels. The lowest panel shows the photon number distribution $P(n, t)$ (color scale), the mean photon number $\bar{n}(t)$ (thick black line) and the sequence of target states (thin blue line).

Figure IV.12 shows an individual trajectory for the sequential preparation experiment, in which the target states $\{3, 1, 4, 2, 6, 2, 5\}$ are prepared successively. The lowest panel shows the photon number distribution $P(n, t)$ (color scale), the mean photon number $\bar{n}(t)$ (thick black line) and the sequence of target states (thin blue line). We see that whenever the target

state is changed, the distance increases suddenly and the controller reacts correspondingly by commanding many actuator samples. The field then converges towards the new target state as clearly shown in the lowest panel. The ability of steering the field state towards different target states reflects the flexibility of the feedback process.

IV.3.2 Photon number distributions

The feedback process is flexible for preparing different photon number states. But we also notice that it becomes more difficult to stabilize the states with higher n . In order to evaluate the efficiency for stabilizing different photon number states, we repeat the feedback process many times and study its performance from an ensemble point of view.

We repeat the feedback process and obtain 4000 individual quantum trajectories for each n_t . Each trajectory is terminated according to a predefined criterion, and followed by the 4-phase QND measurements. Bases on these measurements, the field states are reconstructed.

We may terminate the feedback process in two ways. In one way, we terminate it at a fixed time within the stationary regime. The QND measurement thus reconstructs the photon number distribution in the stationary regime. In the other way, we terminate the feedback process by setting a threshold on the fidelity of the target state. Both cases are studied in our experiments, and the results are presented in the following.

IV.3.2.a Stationary regime

The feedback process is terminated at $t = 145$ ms, which is well within the stationary regime. The 4-phase QND measurement leads to a reconstructed photon number distribution denoted by $P_{\text{QND}}(n)$, shown as histograms in Fig. IV.13. In each panel, the solid bars correspond to $P_{\text{QND}}(n)$ obtained using the ‘‘atomic actuator’’ feedback process, and the patterned bars correspond to those of the ‘‘coherent actuator’’ feedback. The step lines show the theoretical Poisson distributions of $P(n)$ in a coherent field $|\alpha\rangle$, with $\alpha = \sqrt{n_t}$. The hollow circles show the estimated photon number distribution $P(n)$ when the feedback process is terminated. Compared with coherent fields, $P_{\text{QND}}(n)$ obtained using both feedback processes become narrower around the target states. The fidelities of the target states are about 2 times the maximum possible values in coherent fields.

In the panels (a) to (d), we compare $P_{\text{QND}}(n)$ of the ‘‘atomic actuator’’ and ‘‘coherent actuator’’ feedback processes. For all 4 target states, the ‘‘atomic actuator’’ feedback process leads to fidelities higher by more than 10% than those obtained by its ‘‘coherent actuator’’ counterpart. Moreover, the photon number distributions are also narrower around the target states. In order to make a quantitative comparison of this ‘‘narrowness’’, we calculate the relative dispersion σ defined as

$$\sigma = \sqrt{\frac{\langle \hat{N}^2 \rangle - \langle \hat{N} \rangle^2}{\langle \hat{N} \rangle}},$$

which has the value 1 for a coherent field. The fidelities of the target states and values of σ for $P_{\text{QND}}(n)$ are given in Table IV.1. The fact $\sigma < 1$ means that the field state has a sub-Poisson distribution. Smaller values for σ are obtained in the ‘‘atomic actuator’’ feedback process. In summary, compared with its ‘‘coherent actuator’’ counterpart, the ‘‘atomic actuator’’ feedback process leads to not only higher fidelities for the target states, but also narrower photon number distributions.

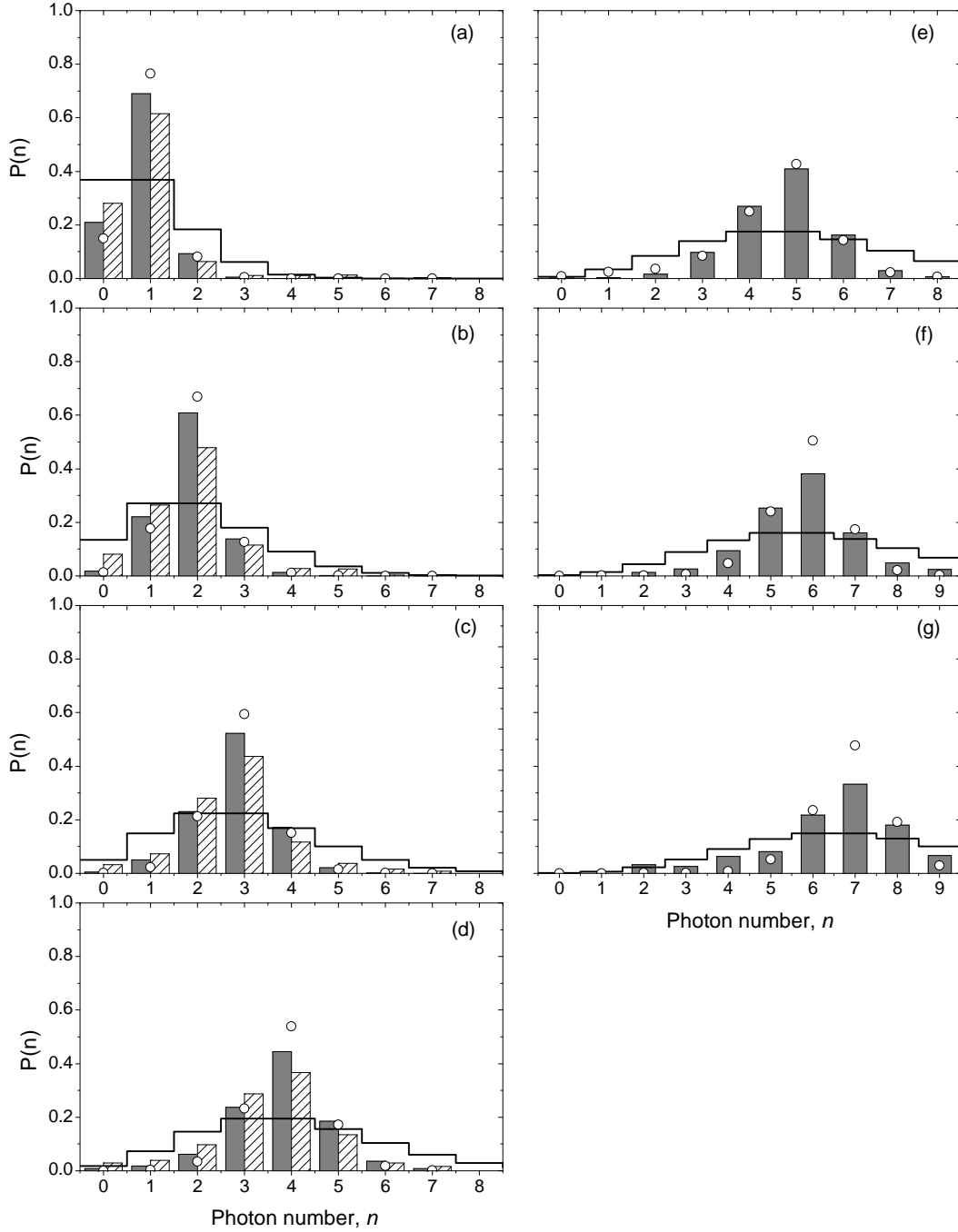


Figure IV.13. Photon number distributions in the stationary regime. From (a) to (g), $n_t = 1$ to 7. The step lines show the theoretical Poisson distribution $P(n)$ of a coherent field $|\alpha\rangle$, with $\alpha = \sqrt{n_t}$. The hollow circles represent the estimated state when the feedback process is terminated. The histograms show the reconstruction results $P_{\text{QND}}(n)$ by the 4-phase QND measurement, with the solid bars corresponding to the “atomic actuator” feedback process and the patterned bars corresponding to the “coherent actuator” feedback process (only from (a) to (d)).

| | | $ 1\rangle$ | $ 2\rangle$ | $ 3\rangle$ | $ 4\rangle$ | $ 5\rangle$ | $ 6\rangle$ | $ 7\rangle$ |
|-----------------------|----------|-------------|-------------|-------------|-------------|-------------|-------------|-------------|
| $P_{\text{QND}}(n_t)$ | atomic | 69% | 61% | 52% | 45% | 43% | 38% | 33% |
| | coherent | 61% | 49% | 44% | 37% | - | - | - |
| σ | atomic | 0.70 | 0.51 | 0.50 | 0.55 | 0.52 | 0.52 | 0.62 |
| | coherent | 0.95 | 0.79 | 0.69 | 0.69 | - | - | - |

Table IV.1. Fidelities of the target states and relative dispersions of the reconstructed photon number distributions. Both the results using the “atomic actuator” and “coherent actuator” feedback processes are shown.

It is not surprising to see that the “atomic actuator” feedback process outperforms the “coherent actuator” feedback process. In the latter, the injection of a small coherent field simply broadens the photon number distribution for most of the time. It is the sensor samples which pin down the field towards the target state. This mismatch between the classical nature of the actuators and the quantumness of the target states limits the speed of correcting quantum jumps, thus limits the ability of stabilizing higher photon number states (e.g $|5\rangle$, $|6\rangle$ and $|7\rangle$). On the contrary, the quantum actuator used in the “atomic actuator” feedback emits or absorbs one photon at a time². This is thus particularly suitable for reversing photon jumps.

We also notice the discrepancy between $P_{\text{QND}}(n)$ and the estimated state $P(n)$. The estimator seems more optimistic than the QND measurement. This may be due to the following reasons.

- The resonant interaction between the actuators and the cavity field is not perfectly described. As we can see in section II.3.1.c, the damping rates of the Rabi oscillations in the Fock states only satisfy the relationship $1/\tau_n = \sqrt{n+1}/\tau_0$ qualitatively. As a result, the Kraus operators based on (II.36) may not describe accurately the interaction between the actuator samples and the cavity field. Moreover, the resonant interaction of 2 atoms coupled to the cavity field is not perfectly described either. As can be seen from section II.3.2, the theoretical model only agrees with the measured data qualitatively.
- Fluctuation of the atom number. The actuator sample has an flux of about 0.5/sample on average (averaged over the 4000 trajectories), which is used to calculate the probabilities for different atom numbers in a sample. However, in practice, the average atom number per sample (over an individual trajectory) fluctuates by about $\pm 50\%$ among different quantum trajectories. These fluctuations result in different probabilities for the atom numbers 0, 1 and 2 from the preset values in our model. This may also lead to inaccurate description of the resonant interaction.

²In fact, the atom number in an atomic sample is probabilistic and the samples have an atomic flux of about 0.5/sample. The probability for photon exchanges is about 50% on average. So more precisely, we should say that an actuator sample has a 25% probability for exchanging one photon with the cavity field.

IV.3.2.b Termination by a threshold on fidelity

Terminating all trajectories at a fixed time is essentially equivalent to terminating the individual trajectories at a random time within the stationary regime. So in this case, we actually neglect the knowledge of the quantum state estimator. In this section, we discuss the results obtained by terminating the quantum trajectories relying on real-time information about the field.

The feedback process is terminated once the fidelity of the target state reaches 80% in 3 successive feedback loops, and the trajectory is declared to be converged. In practice, a trajectory can be terminated at the position of either a sensor or a control sample. In either case, we use the next segment of N_s sensor samples to perform the QND measurement³. The reconstruction results based on about 4000 individual trajectories are shown in Fig. IV.14. From the panels (a) to (g), the target states are from $n_t = 1$ to 7. The histograms show the reconstructed photon number distributions $P_{\text{QND}}(n)$: lighter bars corresponding to the stationary regime and darker bars corresponding to the converged trajectories. The hollow circles show the estimated states $P(n)$ when the feedback process is terminated. The solid lines show the theoretical Poisson distributions as those in Fig. IV.13.

As expected, we obtain better results by relying on the knowledge of the state estimator, in which the fidelities of the target states are higher and the distributions are narrower. For the feedback processes with $n_t = 1$ or $n_t = 2$, we also see good agreement between the estimated states and those reconstructed by the QND measurement. Nevertheless, the discrepancy between them becomes larger as n_t increases. We think there are two reasons for this discrepancy. First, since quantum jumps become more frequent for the Fock states with larger n , there is less time for the sensor samples to perform measurements between two jumps. As a result, the state estimator fails to detect these jumps and provides an estimate different from the real field. Second, once the trajectory is terminated, the QND measurement cannot be started immediately, since we need to wait till the next N_s sensor samples. On average, the waiting time is about 1 ms, which leads to a probability of about 10% for losing one photon for the state $|7\rangle$. So field relaxation also contributes to the observed discrepancy.

³Within these 12 samples, we only use the detection results of the first 10 samples.

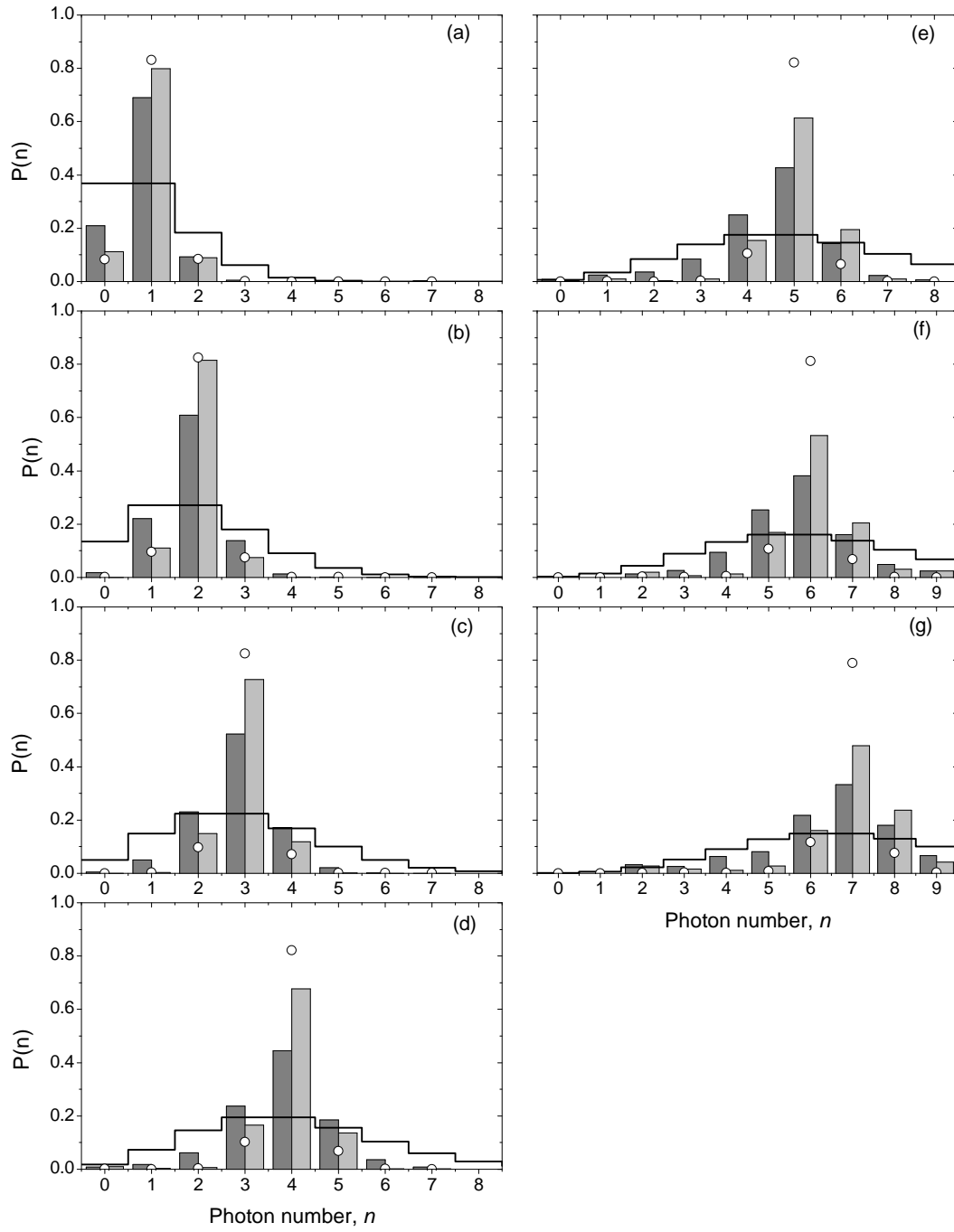


Figure IV.14. Photon number distributions of the converged trajectories. From (a) to (g), $n_t = 1$ to 7. The step lines show the theoretical Poisson distribution $P(n)$ of a coherent field $|\alpha\rangle$, with $\alpha = \sqrt{n_t}$. The hollow circles correspond to the estimated state when the feedback process is terminated. The histograms show the reconstructed results $P_{\text{QND}}(n)$, with the lighter bars corresponding to the converged trajectories and the darker bars corresponding to the stationary regime.

Convergence speed

Having obtained the photon number distributions, we want to check how fast the trajectories reach the predefined criterion. As defined in section III.4.2, the function $C_{fr}(t)$ represents the probability for the trajectories to reach the termination criterion before time t . The functions corresponding to different n_t are shown in Fig. IV.15.

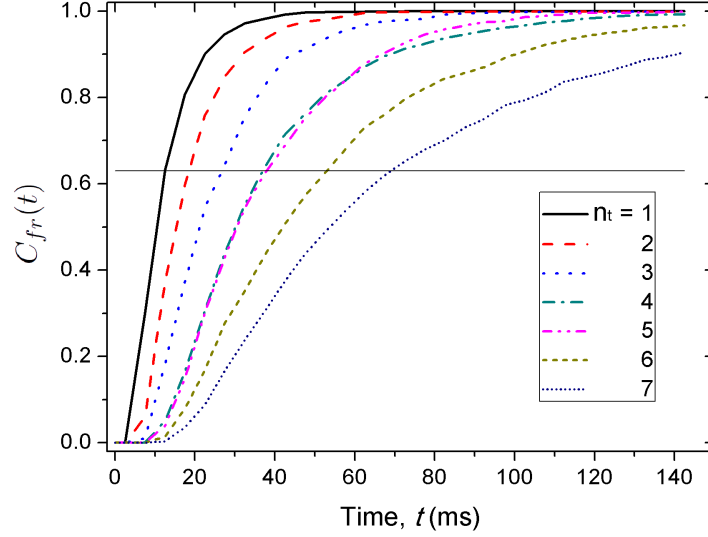


Figure IV.15. Probabilities for individual trajectories to reach the termination criterion as functions of time. The target states are $n_t = 1$ to 7. The horizontal line shows the 63% level.

On each curve $C_{fr}(t)$, we see an initial time interval within which no trajectory is converged. This time interval depends on n_t and varies from ~ 2 ms to ~ 12 ms for $n_t = 1$ to 7. This is the time needed for pumping photons into the cavity and for acquiring enough information about the field state through the sensors. The convergence time t_{conv} , which is defined as the time needed for $1 - e^{-1} = 63\%$ of the trajectories to reach the predefined criterion, for different target states are given in Table IV.2. As a comparison, we also show the convergence time for $n_t = 1$ to 4 of the “coherent actuator” feedback process. Roughly speaking, the convergence speed in the “atomic actuator” feedback process is about twice as fast as those achieved by the “coherent actuator” process.

| | $ 1\rangle$ | $ 2\rangle$ | $ 3\rangle$ | $ 4\rangle$ | $ 5\rangle$ | $ 6\rangle$ | $ 7\rangle$ |
|----------|-------------|-------------|-------------|-------------|-------------|-------------|-------------|
| atomic | 12 ms | 19 ms | 27 ms | 37 ms | 38 ms | 53 ms | 69 ms |
| coherent | 26 ms | 31 ms | 49 ms | 58 ms | - | - | - |

Table IV.2. Convergence time in different feedback processes.

IV.3.3 Behavior of the controller

On the individual trajectories, we see that once a quantum jump down (up) occurs, the controller commands several RE (RG) samples to reverse this jump. In order to look into the way by which the controller makes choices, we analyze the chosen types for the control samples. We first analyze how the controller chooses sample types at different time in the stationary regime, then analyze its choice dependent on the mean photon number of the estimated field state.

IV.3.3.a Sample types in the stationary regime

The average photon number distribution $\bar{P}(n, t)$ is obtained by making an ensemble average of $P(n, t)$ over 4000 individual trajectories. Figure IV.16 shows the distribution with $n_t = 3$. We see small oscillations of $\bar{P}(n)$: $\bar{P}(3)$ increases while $\bar{P}(n < 3)$ decreases⁴. A zoom in of $\bar{P}(3)$ is shown in the lower panel. The fidelity of $|3\rangle$ oscillates between 61% and 58% with a period $(N_s + N_c)T_a$.

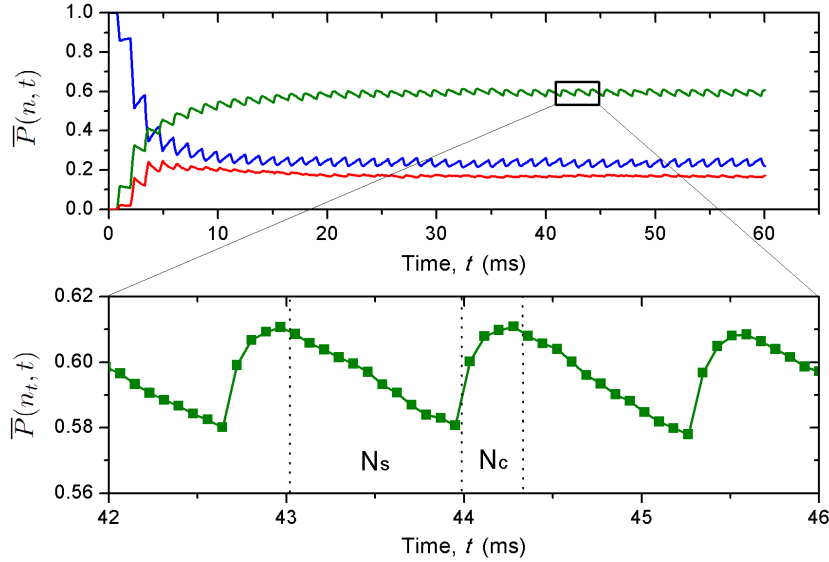


Figure IV.16. Evolution of the average photon number distribution with $n_t = 3$. The upper panel shows the evolutions of $\bar{P}(n_t, t)$ (green), $\bar{P}(n > n_t, t)$ (red) and $\bar{P}(n < n_t, t)$ (blue). The lower panel is a zoom in of $\bar{P}(n_t, t)$ in the selected region. The numbers of the samples are $N_s = 12$ and $N_c = 4$.

Although the oscillation amplitude is small, it is worth to emphasize that the fidelity decreases within the segments of the sensor samples and increases within the segments of the control samples. Since the sensor samples cannot inject photons into the cavity, photon losses induced by the cavity decay cannot be corrected. As a result, the probability $\bar{P}(3)$ decreases while $\bar{P}(n < 3)$ increases. Nevertheless, within the segments of the control samples, photon losses can be corrected by the feedback actions, eventually recovering the fidelity of the target

⁴Due to overshoots of the feedback actions, $\bar{P}(n > 3)$ also oscillates following the same trend as that of $\bar{P}(3)$, but on a much smaller scale. So the major interplay is between $\bar{P}(3)$ and $\bar{P}(n < 3)$.

state. Consequently, we see that the fidelity of the target state increases within each control segment and saturates at the maximum value at the end.

Now let us check how the controller makes decisions in this situation. Figure IV.17 shows the probabilities $\Pi_p(t)$ for choosing different types for the control samples as functions of time. The subscript p refers to the types QND, RE or RG.

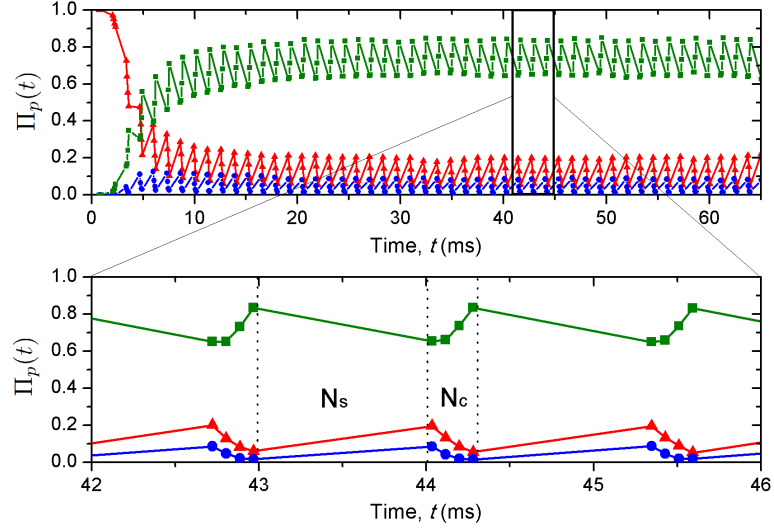


Figure IV.17. Probabilities of commanding control sample types $\Pi_p(t)$, with $p = \text{QND}$ (green squares), RE (red triangles), or RG (blue circles). The lower panel is a zoom in of the selected region in the upper panel.

As shown in the upper panel, within the stationary regime, about 70% of the control samples are set as sensors. From the lower panel, we see that the first sample in the control segment has a probability of about 20% for being an RE type. The probability then decreases and reaches a value of about 5% for the last sample in the same segment. In the meantime, the probabilities for the RG type has the same behavior, but with a value about 3 times smaller. This behavior reflects the fact that at the beginning the controller tries to correct the deviation of the field state from the target, then it quiets down as it finds that any more action could lead the field state farther to the target.

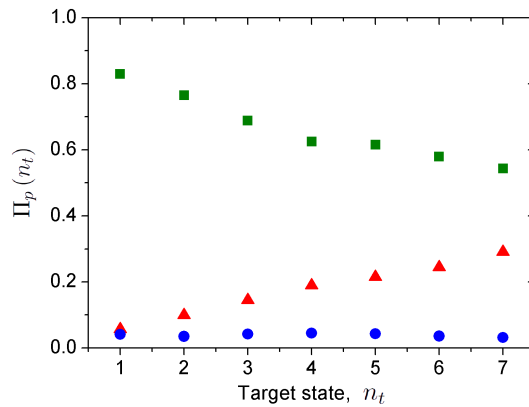


Figure IV.18. Probabilities of different sample types as functions of n_t . The type $p = \text{QND}$ (green squares), RE (red triangles), or RG (blue circles).

In fact, for the feedback processes with other target states, we see qualitatively the same behavior for the control samples. Here, we do not show the graphs for all n_t . But instead, we average the probabilities $\Pi_p(t)$ over t within the stationary regime and obtain the probabilities $\Pi_p(n_t)$ for different target states, which are shown in Fig. IV.18. As expected, for all the target states, the controller commands more RE than RG samples, reflecting that photon losses dominates over photon gains. Furthermore, for higher n_t , the controller commands more RE samples, since photon losses become more frequent.

IV.3.3.b Sample types dependent on the mean photon number

In order to have an intuitive understanding about how the controller chooses different sample types, we also study the choices of the controller dependent on the average photon number \bar{n} estimated at a given time. The results for $n_t = 1$ to 7 are given in Fig. IV.19.

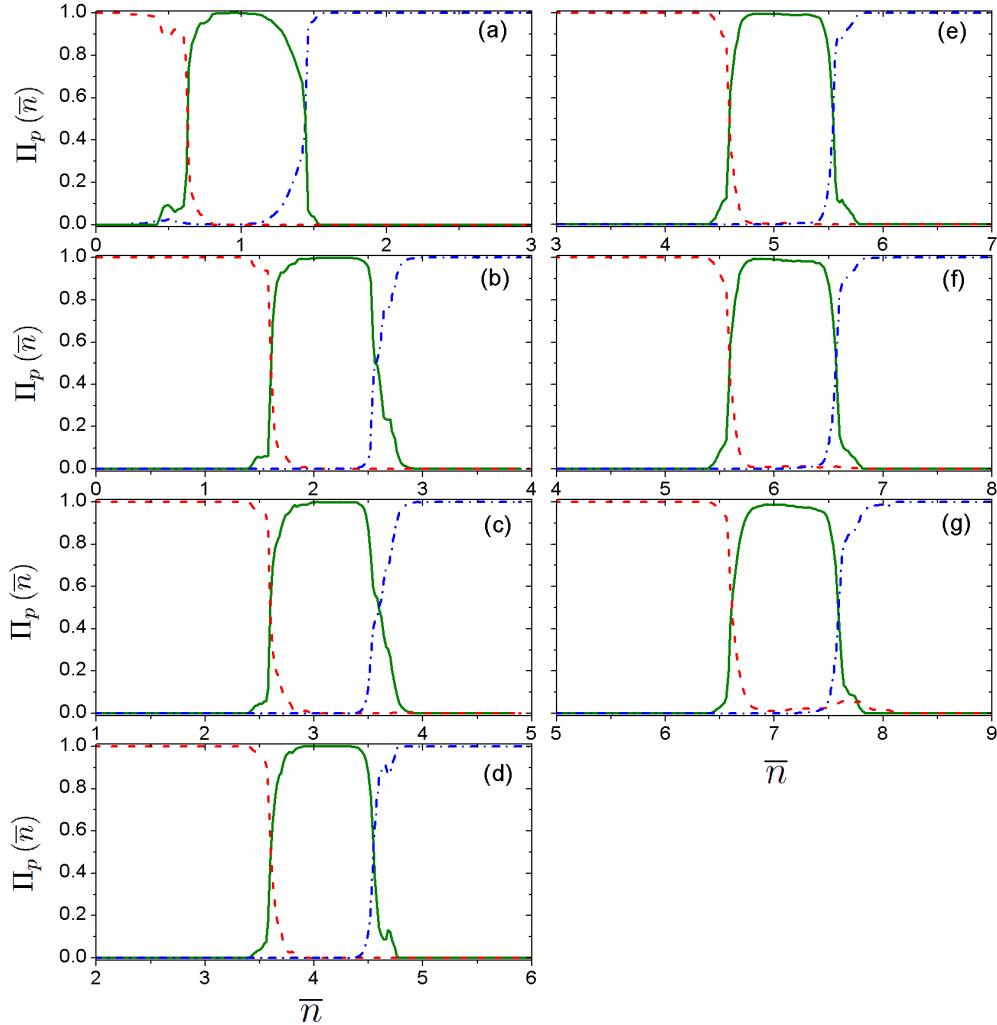


Figure IV.19. Probabilities $\Pi_p(\bar{n})$ of the types chosen for the control samples as functions of the average photon number \bar{n} of the estimated field. The types are $p = \text{QND}$ (green solid line), RE (red dashed line), or RG (blue dash-dot line). The panels from (a) to (g) correspond to the target states with $n_t = 1$ to 7.

The inspection of these results reveals that the controller effectively works under a simple rule: when $\bar{n} < n_t - 0.4$, it commands RE samples; when $\bar{n} > n_t + 0.6$, it commands RG samples; and in between it commands QND samples. The domain of \bar{n} within which the QND type is chosen has a width $\delta n \simeq 1$, and is centered at a value slightly larger than n_t , reflecting that field relaxation alone reduces \bar{n} .

Based on these results, we may think of a simpler algorithm than the one presented in section III.3 for the controller. In this simpler algorithm, the controller only needs to calculate \bar{n} at a moment, and compare it with n_t . Depending on whether there are “fewer” or “more” photons than wanted, the controller simply commands a photon emitter or absorber correspondingly. We have performed numerical simulations using this simpler algorithm while all the other settings remain the same. The results are, however, worse than the current results. The fidelity of the target state is about 10% smaller. This may be because of the difference between the two algorithms at the boundary domains ($\bar{n} \simeq n_t + 0.6$ and $\bar{n} \simeq n_t - 0.4$). In these domains, the fractions of the actuator and sensor samples change sharply in the simpler algorithm, whereas in the other algorithm they have small overlaps. Although the algorithm used in our experiments involves more complex calculations, it justifies its value by leading to better performance for the feedback process.

Conclusion

In this manuscript, we present quantum feedback experiments which prepare and stabilize photon number states with up to 7 photons. Circular Rydberg atoms are used either as sensors performing QND measurements or as actuators exchanging photons with the cavity field. The quantum nature of the actuators is matched to that of the single-photon quantum jumps induced by the field relaxation. Consequently, we achieve better performance than that using the “coherent actuator” feedback process, as presented in [61].

To perform the feedback experiments, we need to know the backactions of the sensors and actuators on the field. The theoretical description of the QND measurement was first presented. The experimental imperfections were then measured and taken into account in this description, leading to the quantum maps associated to the sensors in the experimental situation. Similarly, for the actuators, we first provided an ideal theoretical description on their interactions with the cavity field, then gradually took into account experimental imperfections and obtained the quantum maps in real experiments.

Having fully described the interactions of cavity field with the sensors and actuators, we gave the algorithms of the quantum state estimator and controller. Based on these algorithms, we performed numerical simulations to check whether the feedback process works or not, and to optimize certain feedback parameters. Through optimization, we gained in both the steady state fidelity of the target state and the convergence speed. The optimized parameters were then used in the experiments.

In order to perform real-time state estimation and feedback control, we introduced the ADwin Pro-II system. After briefly explaining its operation and the structure of an experimental sequence, we presented the experimental results, which demonstrated our ability to prepare and stabilize photon number states with up to 7 photons. In the first place, we showed the individual quantum trajectories, which gave us an intuitive picture about how the feedback process operated. Afterwards, we presented the results averaged over 4000 trajectories. We terminated the feedback process either at a fixed time or once the fidelity of the target state reached a predefined value. In both cases, we performed independent QND measurements and reconstructed the photon field. We then compared these results with those obtained using the “coherent actuator” feedback process. Thanks to the quantum nature of the actuators, the “atomic actuator” feedback process outperformed its “coherent actuator” counterpart in several aspects. It led to higher fidelities for the target states and narrower photon number distributions. It also made the field converge to the target state faster. In the end, we analyzed the behavior of the controller and revealed that its algorithm actually made intuitively simple choices.

Perspectives

The feedback process may be optimized in two aspects: the sensors and the actuators. First, instead of using fixed Ramsey phase ϕ_r and phase shift per photon ϕ_0 for the sensors, we can use adaptive ones. The field starts in its vacuum state and gradually climbs the ladders of Fock states till the target state. We may use different ϕ_r and ϕ_0 at different stages, such that the sensors are most sensitive to any variations of the current field state. The sensitivity of the sensors to the cavity field is thus maximized during the whole feedback process. Second, for the actuators, we may use several interaction times for both the RE and RG types. In this way, we expect to enhance the efficiency of photon exchange, thus ameliorate the corrections of quantum jumps.

Using adaptive ϕ_r and ϕ_0 also enables us to improve the QND measurement of photon numbers. So far, in our measurements, we keep a constant ϕ_0 and choose randomly the Ramsey phases of the atomic samples among 4 possible options. Nevertheless, this method is not optimal as far as the measurement speed concerned. An optimal method for distinguishing different photon numbers was proposed in [40, 62]. In this method, after the detection of each atom, ϕ_0 is divided by 2 and a proper Ramsey phase depending on the previous detection result is chosen for the next atom. The method only needs $\log_2(N)$ atoms for distinguishing N photon number states in an ideal situation. We have incorporated the experimental imperfections and performed numerical simulations. Using 3 velocity classes for the atomic samples, corresponding to $\phi_0 = \pi, \pi/2$ and $\pi/4$, we can distinguish photon number states from $|0\rangle$ to $|7\rangle$ by detecting 13 atoms. To make a comparison, in the experiments presented in [31], we used 110 atoms to distinguish those 8 Fock states. So we expect that performing the QND measurement in this adaptive way would reduce dramatically the measurement time.

Another perspective is to exploit the feedback procedure to prepare and protect Schrödinger's cat states. To this end, we choose $\phi_0 = \pi$. The measurement of photon numbers thus reduces to the measurement of parity. The parity operator is defined as:

$$\begin{aligned}\hat{P}|n\rangle &= +|n\rangle \quad \text{if } n \text{ is even,} \\ &= -|n\rangle \quad \text{if } n \text{ is odd.}\end{aligned}$$

A single parity measurement on the coherent field $|\alpha\rangle$ transforms it into the Schrödinger's cat states. The "even" and "odd" cat states are:

$$|\psi_e\rangle = \frac{1}{\sqrt{2}} (|\alpha\rangle + |-\alpha\rangle) \quad |\psi_o\rangle = \frac{1}{\sqrt{2}} (|\alpha\rangle - |-\alpha\rangle),$$

which are eigenstates of the parity operator and satisfy the following relationship:

$$\hat{P}|\psi_e\rangle = |\psi_e\rangle \quad \hat{P}|\psi_o\rangle = -|\psi_o\rangle.$$

The state $|\psi_e\rangle$ only contains the Fock states with even photon numbers, whereas the state $|\psi_o\rangle$ only those with odd photon numbers.

Consider that we have prepared the even cat state $|\psi_e\rangle$. If decoherence induces the loss of a photon, the field is then projected into the odd cat state $|\psi_o\rangle$. The sensor atoms performing parity measurement can reveal this quantum jump. The feedback process then commands the injection of a photon to recover the original field state. In this way, we can stabilize the Schrödinger's cat states [63, 64].

We see that the current feedback scheme can be easily adapted to this experiment, since the resonant atoms can emit or absorb a photon at a time. Nevertheless, in practice, the actuator is the atomic sample, which contains a nondeterministic atom number. The probabilistic nature of the atom number in a sample stands as an obstacle for this experiment, since an atomic sample may be empty or contains more than 1 atom, we cannot be sure that one photon is deposited at a time. Moreover, the limited detector efficiency is also a concern, since an atom may deposit a photon and be missed by the detector. In this case, the controller fails to realize that the jump has been corrected. But these obstacles may be overcome by adopting the strategy used in the current feedback experiment, i.e. introduce a partition of sensor and control samples. Then we do not rely on the detection of the actuator samples but the subsequent sensor samples to judge if one photon is successfully deposited or not. This protocol can be checked and optimized in numerical simulations.

Appendix A

Two-atom Rabi oscillations

The basis $\{|ee, n-1\rangle, |(eg+ge)/\sqrt{2}, n\rangle, |gg, n+1\rangle\}$ with $n \geq 1$ forms a closed subspace of the Hilbert space. The atomic states constitute a spin triplet state with $M_J = 0, \pm 1$. To simplify the notation, we make the following substitutions:

$$|M_J^1\rangle \equiv |ee, n-1\rangle \quad |M_J^0\rangle \equiv |(eg+ge)/\sqrt{2}, n\rangle \quad |M_J^{-1}\rangle \equiv |gg, n+1\rangle \quad (\text{A.1})$$

The eigenstates corresponding to the eigenenergies ξ_0 and $\pm\xi(n)$ are:

$$\begin{aligned} |\psi_0\rangle &= \frac{1}{\sqrt{2n+1}} (\sqrt{n+1}|M_J^1\rangle - \sqrt{n}|M_J^{-1}\rangle) \\ |\psi_{\pm}\rangle &= \frac{1}{\sqrt{2(2n+1)}} (\pm\sqrt{n}|M_J^1\rangle + \sqrt{2n+1}|M_J^0\rangle \pm \sqrt{n+1}|M_J^{-1}\rangle). \end{aligned}$$

The coupled states in (A.1) can then be expressed in terms of these eigenstates:

$$\begin{aligned} |M_J^1\rangle &= \frac{1}{\sqrt{2n+1}} \left(\sqrt{\frac{n}{2}} (|\psi_+\rangle - |\psi_-\rangle) + \sqrt{n+1} |\psi_0\rangle \right) \\ |M_J^0\rangle &= \frac{1}{\sqrt{2}} (|\psi_+\rangle + |\psi_-\rangle) \\ |M_J^{-1}\rangle &= \frac{1}{\sqrt{2n+1}} \left(\sqrt{\frac{n+1}{2}} (|\psi_+\rangle - |\psi_-\rangle) - \sqrt{n} |\psi_0\rangle \right). \end{aligned}$$

After time t , these states evolve to:

$$\begin{aligned} |M_J^1\rangle(t) &= \left[1 + \frac{n}{2n+1} \left(\cos \frac{\xi(n)t}{\hbar} - 1 \right) \right] |1\rangle \\ &\quad - i\sqrt{\frac{n}{2n+1}} \sin \frac{\xi(n)t}{\hbar} |0\rangle \\ &\quad + \frac{\sqrt{n(n+1)}}{2n+1} \left(\cos \frac{\xi(n)t}{\hbar} - 1 \right) |-1\rangle, \end{aligned} \quad (\text{A.2})$$

$$\begin{aligned}
|M_J^0\rangle(t) &= -i\sqrt{\frac{n}{2n+1}}\sin\frac{\xi(n)t}{\hbar}|1\rangle \\
&\quad + \cos\frac{\xi(n)t}{\hbar}|0\rangle \\
&\quad - i\sqrt{\frac{n+1}{2n+1}}\sin\frac{\xi(n)t}{\hbar}|-1\rangle,
\end{aligned} \tag{A.3}$$

$$\begin{aligned}
|M_J^{-1}\rangle(t) &= \frac{\sqrt{n(n+1)}}{2n+1}\left(\cos\frac{\xi(n)t}{\hbar}-1\right)|1\rangle \\
&\quad - i\sqrt{\frac{n+1}{2n+1}}\sin\frac{\xi(n)t}{\hbar}|0\rangle \\
&\quad + \left[1 + \frac{n+1}{2n+1}\left(\cos\frac{\xi(n)t}{\hbar}-1\right)\right] |-1\rangle,
\end{aligned} \tag{A.4}$$

with $\xi(n)$ defined as

$$\xi(n) \equiv \hbar\frac{\Omega_0}{2}\sqrt{2(2n+1)}. \tag{A.5}$$

Appendix B

Simulation procedure

While simulating the evolution of ρ^R , we exploit the following properties.

- The atom number and atomic state of each sample are known.
- Virtual ideal detection of the atomic state: 100% detector efficiency and no detection errors.
- The field relaxation in a small time period $T_a \ll T_{\text{cav}}$ is considered as quantum jumps.

In the following, we consider the quantum maps induced on ρ_k^R by the virtual ideal detection of the atomic state and the field relaxation separately. We thus introduce the notations given in Fig. B.1. The detection of the atomic sample k transforms the field state ρ_{k-1}^R to $\rho_{k-\frac{1}{2}}^R$, which is transformed to the state ρ_k^R by the field relaxation.

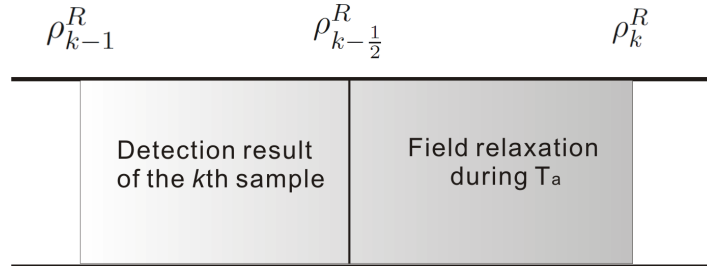


Figure B.1. Notations of the transformed states.

Simulating the evolution of the cavity field

1. The cavity field is initially prepared in the vacuum state:

$$\rho_0^R = |0\rangle\langle 0|. \quad (\text{B.1})$$

2. The atomic sample k interacts with the cavity field. The virtual ideal detection of its atomic state transforms the field state ρ_{k-1}^R . To express these transformations, we need to determine its atom number, atomic state and the results of the detection.

Atom number

The Poisson distribution of the atom number in a sample is simulated by generating a random number $0 \leq \chi < 1$ and determining the atom number according to

- 0, if $\chi \leq P_0$,
- 1, if $\chi \leq P_0 + P_1$,
- 2, otherwise,

where P_0 and P_1 denote the probabilities given by the truncated Poisson distribution (II.2). In our simulations, we consider up to 2 atoms for each atomic sample. But here for simplicity of expressions, I only consider up to 1 atom. The cases with 2 atoms can be analyzed similarly.

If the sample k contains 0 atom, the transformation leaves ρ_{k-1}^R unchanged. In the following we consider the case of 1 atom.

Atomic state

Due to the preparation errors of atomic states, the sample of type RE or RG may be either in state $|e\rangle$ or $|g\rangle$. So we need first to determine the true atomic state.

We draw a random number $0 \leq \chi_1 < 1$ and determine the atomic states as follows.

- Type RE
 - If $\chi_1 \leq \eta_e^p$, the state is $|g\rangle$.
 - Otherwise, the state is $|e\rangle$.
- Type RG
 - If $\chi_1 \leq \eta_g^p$, the state is $|e\rangle$.
 - Otherwise, the state is $|g\rangle$.

Virtual ideal detection

After detection of the atomic state, the field state is transformed. The quantum maps are described by the Kraus operators \hat{K}_e , and \hat{K}_g , corresponding to the detection results $|e\rangle$ or $|g\rangle$, respectively. These operators are as follows.

- For the sample with the type QND: $\hat{K}_e = \hat{M}_e$ and $\hat{K}_g = \hat{M}_g$.
- For the sample with the type RE or RG:
 - If the atomic state is $|e\rangle$, $\hat{K}_e = \hat{\mathcal{R}}_{e,e}$ and $\hat{K}_g = \hat{\mathcal{R}}_{e,g}$.
 - If the atomic state is $|g\rangle$, $\hat{K}_e = \hat{\mathcal{R}}_{g,e}$ and $\hat{K}_g = \hat{\mathcal{R}}_{g,g}$.

The probabilities for detecting the states $|e\rangle$ for $|g\rangle$ are

$$\pi_e = \text{Tr}\left(\hat{K}_e \rho_{k-1}^R \hat{K}_e^\dagger\right) \quad \pi_g = 1 - \pi_e. \quad (\text{B.2})$$

We draw a random number $0 \leq \chi_2 < 1$ to determine the outcome of the virtual ideal detection:

- If $\chi_2 \leq \pi_e$, the atom is detected in $|e\rangle$, and ρ_{k-1}^R is transformed to

$$\rho_{k-\frac{1}{2}}^R = \frac{\hat{K}_e \rho_{k-1}^R \hat{K}_e^\dagger}{\pi_e}. \quad (\text{B.3})$$

- If $\chi_2 > \pi_e$, the atom is detected in $|g\rangle$, and ρ_{k-1}^R is transformed to

$$\rho_{k-\frac{1}{2}}^R = \frac{\hat{K}_g \rho_{k-1}^R \hat{K}_g^\dagger}{\pi_g}. \quad (\text{B.4})$$

Result of the realistic detection

If the sample k contains 0 atom, the result of the realistic detection is 0^d .

For the case of 1 atom, in order to obtain the result of the realistic detection, we need first to determine whether the atom misses detection, then to determine in which detection channel it is detected.

We draw a random number $0 \leq \chi_3 < 1$ and determine the realistic detection result as follows.

- If $\chi_3 > \epsilon_d$, the atom misses detection, leading to a detection result 0^d .
- If $\chi_3 \leq \epsilon_d$, the atom generates a detection click. We need further to determine whether it leads to e^d or g^d . Suppose the result of the virtual ideal detection is $j \in \{e, g\}$. We draw a random number $0 \leq \chi_4 < 1$ and determine the detection result as:¹
 - If $\chi_4 > \eta_j^d$, the atom is correctly detected, leading to the result j^d
 - Otherwise, the atom is erroneously detected, leading to the result other than j^d .

3. Take into account the field relaxation during T_a .

Recall the jump operators associated to the field relaxation:

$$\hat{L}_+ = \sqrt{\kappa_+} a^\dagger \quad \hat{L}_- = \sqrt{\kappa_-} a. \quad (\text{B.5})$$

The probabilities of quantum jumps within time T_a are given by:

$$p_+ = \kappa_+ T_a \text{Tr} \left(a a^\dagger \rho_{k-\frac{1}{2}}^R \right) \quad p_- = \kappa_- T_a \text{Tr} \left(a^\dagger a \rho_{k-\frac{1}{2}}^R \right). \quad (\text{B.6})$$

We draw a random number $0 \leq \chi_5 < 1$ to determine whether a quantum jump occurs.

- if $\chi_5 \leq p_+$, a jump up occurs and the state is transformed to

$$\rho_k^R = \frac{\left(a^\dagger \rho_{k-\frac{1}{2}}^R a \right)}{\text{Tr} \left(a a^\dagger \rho_{k-\frac{1}{2}}^R \right)}. \quad (\text{B.7})$$

¹For the QND sample, the detection errors should be substituted by the effective detection errors.

- if $p_+ < \chi_5 \leq p_+ + p_-$, a jump down occurs and the state is transformed to

$$\rho_k^R = \frac{\left(a \rho_{k-\frac{1}{2}}^R a^\dagger \right)}{\text{Tr} \left(a^\dagger a \rho_{k-\frac{1}{2}}^R \right)}. \quad (\text{B.8})$$

- if $p_+ + p_- < \chi_5$, no jump occurs and the state is transformed to

$$\rho_k^R = \frac{1}{p_0} \left[(\mathbb{1} - T_a \hat{J}) \rho_{k-\frac{1}{2}}^R (\mathbb{1} - T_a \hat{J}) \right], \quad (\text{B.9})$$

with the operator \hat{J} defined as

$$\hat{J} = \frac{1}{2} \left(\hat{L}_+^\dagger \hat{L}_+ + \hat{L}_-^\dagger \hat{L}_- \right) = \frac{1}{2} \left(\kappa_+ a a^\dagger + \kappa_- a^\dagger a \right). \quad (\text{B.10})$$

Performing the feedback experiment

1. Decide whether we close the feedback loop or not.

If the 3 samples $k+6$, $k+7$ and $k+8$ belong to the predefined sensor segment in the sample sequence, we do not close the feedback loop.

Otherwise, we close the feedback loop by executing the procedure listed in the following box.

2. Estimate the state based on which we choose the feedback action using the algorithm given in section III.2.
3. Choose a feedback action using the algorithm given in section III.3.

Bibliography

- [1] A. TONOMURA, J. ENDO, T. MATSUDA, T. KAWASAKI, and H. EZAWA. “Demonstration of single-electron buildup of an interference pattern”. *American Journal of Physics*, **57**, n° 2, 117 (1989). Journal article, URL <http://dx.doi.org/doi/10.1119/1.16104>.
- [2] M. BRUNE, E. HAGLEY, J. DREYER, X. MAÎTRE, A. MAALI, C. WUNDERLICH, J. M. RAIMOND, and S. HAROCHE. “Observing the progressive decoherence of the “meter” in a quantum measurement”. *Phys. Rev. Lett.*, **77**, n° 24, 4887 (Sep 1996).
- [3] A. ASPECT, P. GRANGIER, and G. ROGER. “Experimental tests of realistic local theories via bell’s theorem”. *Phys. Rev. Lett.*, **47**, n° 7, 460 (Aug 1981).
- [4] A. ASPECT, P. GRANGIER, and G. ROGER. “Experimental realization of Einstein-Podolsky-Rosen-Bohm gedankenexperiment: A new violation of bell’s inequalities”. *Phys. Rev. Lett.*, **49**, n° 2, 91 (Jul 1982).
- [5] A. ASPECT, J. DALIBARD, and G. ROGER. “Experimental test of bell’s inequalities using time-varying analyzers”. *Phys. Rev. Lett.*, **49**, n° 25, 1804 (Dec 1982).
- [6] J. VON NEUMANN. *Mathematical Foundations of Quantum Mechanics*. Princeton University Press (1955).
- [7] V. B. BRAGINSKII and Y. I. VORONTSOV. “Quantum-mechanical limitations in macroscopic experiments and modern experimental technique”. *Soviet Physics Uspekhi*, **17**, n° 5, 644 (1975). URL <http://stacks.iop.org/0038-5670/17/i=5/a=R02>.
- [8] V. B. BRAGINSKY, Y. I. VORONTSOV, and K. S. THORNE. “Quantum nondemolition measurements”. *Science*, **209**, n° 4456, 547 (1980). URL <http://www.sciencemag.org/content/209/4456/547.abstract>.
- [9] C. M. CAVES, K. S. THORNE, R. W. P. DREVER, V. D. SANDBERG, and M. ZIMMERMANN. “On the measurement of a weak classical force coupled to a quantum-mechanical oscillator. i. issues of principle”. *Rev. Mod. Phys.*, **52**, n° 2, 341 (Apr 1980).
- [10] K. S. THORNE, R. W. P. DREVER, C. M. CAVES, M. ZIMMERMANN, and V. D. SANDBERG. “Quantum nondemolition measurements of harmonic oscillators”. *Phys. Rev. Lett.*, **40**, n° 11, 667 (Mar 1978).
- [11] C. H. BENNETT and G. BRASSARD. “Quantum cryptography: Public-key distribution and coin tossing”. *Proceedings of IEEE International Conference on Computers, Systems and Signal Processing, Bangalore, India* (1984).

- [12] C. H. BENNETT, G. BRASSARD, C. CRÉPEAU, R. JOZSA, A. PERES, and W. K. WOOTTERS. “Teleporting an unknown quantum state via dual classical and einstein-podolsky-rosen channels”. *Phys. Rev. Lett.*, **70**, n° 13, 1895 (March 1993).
- [13] D. BOUWMEESTER, J.-W. PAN, K. MATTLE, M. EIBL, H. WEINFURTER, and A. ZEILINGER. “Experimental quantum teleportation”. *Nature*, **390**, 575 (December 1997).
- [14] D. P. DIVINCENZO. “Two-bit gates are universal for quantum computation”. *Phys. Rev. A*, **51**, n° 2, 1015 (Feb 1995).
- [15] P. W. SHOR. “Algorithms for quantum computation: discrete logarithms and factoring”. Dans *Proceedings of the 35th Annual Symposium on Foundations of Computer Science*, p. 124–134. IEEE Computer Society, Washington, DC, USA (1994). URL <http://portal.acm.org/citation.cfm?id=1398518.1399018>.
- [16] L. M. K. VANDERSYPEN, M. STEFFEN, G. BREYTA, C. S. YANNONI, M. H. SHERWOOD, and I. L. CHUANG. “Experimental realization of shor’s quantum factoring algorithm using nuclear magnetic resonance”. *Nature*, **414**, n° 2, 883 (December 2001).
- [17] S. GULDE, M. RIEBE, G. P. T. LANCASTER, C. BECHER, J. ESCHNER, H. HAFFNER, F. SCHMIDT-KALER, I. L. CHUANG, and R. BLATT. “Implementation of the deutsch jozsa algorithm on an ion-trap quantum computer”. *Nature*, **421**, n° 2, 48 (January 2003).
- [18] K. STANNIGEL, P. RABL, A. S. SORENSEN, P. ZOLLER, and M. D. LUKIN. “Optomechanical transducers for long-distance quantum communication”. *Phys. Rev. Lett.*, **105**, n° 22, 220501 (Nov. 2010).
- [19] A. M. STEANE. “Error correcting codes in quantum theory”. *Phys. Rev. Lett.*, **77**, n° 5, 793 (Jul 1996).
- [20] D. A. LIDAR and K. B. WHALEY. “Decoherence-free subspaces and subsystems”. Dans F. BENATTI and R. FLOREANINI (éditeurs), *Irreversible Quantum Dynamics*, tome 622 de *Springer Lecture Notes in Physics*, p. 83–120 (2003). ArXiv:quant-ph/0301032, URL <http://www.citebase.org/abstract?id=oai:arXiv.org:quant-ph/0301032>.
- [21] R. VAN HANDEL, J. K. STOCKTON, and H. MABUCHI. “Modelling and feedback control design for quantum state preparation”. *Journal of Optics B: Quantum and Semiclassical Optics*, **7**, n° 10, S179 (2005). URL <http://stacks.iop.org/1464-4266/7/i=10/a=001>.
- [22] W. P. SMITH, J. E. REINER, L. A. OROZCO, S. KUHR, and H. M. WISEMAN. “Capture and release of a conditional state of a cavity qed system by quantum feedback”. *Phys. Rev. Lett.*, **89**, n° 13, 133601 (Sep 2002).
- [23] R. L. COOK, P. J. MARTIN, and J. M. GEREMIA. “Optical coherent state discrimination using a closed-loop quantum measurement”. *Nature*, **446**, n° 7137, 774 (avril 2007). URL <http://dx.doi.org/10.1038/nature05655>.
- [24] G. G. GILLETT, R. B. DALTON, B. P. LANYON, M. P. ALMEIDA, M. BARBIERI, G. J. PRYDE, J. L. O’BRIEN, K. J. RESCH, S. D. BARTLETT, and A. G. WHITE.

- “Experimental feedback control of quantum systems using weak measurements”. *Phys. Rev. Lett.*, **104**, n° 8, 080503 (Feb 2010).
- [25] J. GEREMIA, J. K. STOCKTON, and H. MABUCHI. “Real-time quantum feedback control of atomic spin-squeezing”. *Science*, **304**, n° 5668, 270 (2004). URL <http://www.sciencemag.org/content/304/5668/270.abstract>.
- [26] P. GOY, J. M. RAIMOND, M. GROSS, and S. HAROCHE. “Observation of cavity-enhanced single-atom spontaneous emission”. *Phys. Rev. Lett.*, **50**, n° 24, 1903 (June 1983).
- [27] E. M. PURCELL, H. C. TORREY, and R. V. POUND. “Resonance absorption by nuclear magnetic moments in a solid”. *Phys. Rev.*, **69**, 37 (Jan 1946). URL <http://link.aps.org/doi/10.1103/PhysRev.69.37>.
- [28] M. BRUNE, F. SCHMIDT-KALER, A. MAALI, J. DREYER, E. HAGLEY, J. M. RAIMOND, and S. HAROCHE. “Quantum rabi oscillation: A direct test of field quantization in a cavity”. *Phys. Rev. Lett.*, **76**, n° 11, 1800 (Mar 1996).
- [29] G. NOGUES, A. RAUSCHENBEUTEL, S. OSNAGHI, M. BRUNE, J. M. RAIMOND, and S. HAROCHE. “Seeing a single photon without destroying it”. *Nature*, **400**, n° 6741, 239 (juillet 1999). URL <http://dx.doi.org/10.1038/22275>.
- [30] S. GLEYZES, S. KUHR, C. GUERLIN, J. BERNU, S. DELÉGLISE, U. B. HOFF, M. BRUNE, J.-M. RAIMOND, and S. HAROCHE. “Quantum jumps of light recording the birth and death of a photon in a cavity”. *Nature*, **446**, n° 7133, 297 (Mars 2007).
- [31] C. GUERLIN, J. BERNU, S. DELÉGLISE, C. SAYRIN, S. GLEYZES, S. KUHR, M. BRUNE, J.-M. RAIMOND, and S. HAROCHE. “Progressive field-state collapse and quantum non-demolition photon counting”. *Nature*, **448**, n° 23, 889 (August 2007).
- [32] S. DELÉGLISE, I. DOTSENKO, C. SAYRIN, J. BERNU, M. BRUNE, J.-M. RAIMOND, and S. HAROCHE. “Reconstruction of non-classical cavity field states with snapshots of their decoherence”. *Nature*, **455**, n° 7212, 510 (septembre 2008). URL <http://dx.doi.org/10.1038/nature07288>.
- [33] B. T. H. VARCOE, S. BRATKE, M. WEIDINGER, and H. WALTHER. “Preparing pure photon number states of the radiation field”. *Nature*, **403**, n° 6771, 743 (Feb. 2000). URL <http://dx.doi.org/10.1038/35001526>.
- [34] M. BRUNE, J. BERNU, C. GUERLIN, S. DELÉGLISE, C. SAYRIN, S. GLEYZES, S. KUHR, I. DOTSENKO, J. M. RAIMOND, and S. HAROCHE. “Process tomography of field damping and measurement of fock state lifetimes by quantum nondemolition photon counting in a cavity”. *Phys. Rev. Lett.*, **101**, n° 24, 240402 (Dec 2008).
- [35] H. WANG, M. HOFHEINZ, M. ANSMANN, R. C. BIALCZAK, E. LUCERO, M. NEELEY, A. D. O’CONNELL, D. SANK, J. WENNER, A. N. CLELAND, and J. M. MARTINIS. “Measurement of the decay of fock states in a superconducting quantum circuit”. *Phys. Rev. Lett.*, **101**, n° 24, 240401 (Dec 2008).
- [36] J. GEREMIA. “Deterministic and nondestructively verifiable preparation of photon number states”. *Phys. Rev. Lett.*, **97**, n° 7, 073601 (Aug 2006).

- [37] I. DOTSENKO, M. MIRRAHIMI, M. BRUNE, S. HAROCHE, J.-M. RAIMOND, and P. ROUCHON. “Quantum feedback by discrete quantum nondemolition measurements: Towards on-demand generation of photon-number states”. *Phys. Rev. A*, **80**, n° 1, 013805 (Jul 2009).
- [38] C. SAYRIN, I. DOTSENKO, X. ZHOU, B. PEAUDECERF, T. RYBARCZYK, S. GLEYZES, P. ROUCHON, M. MIRRAHIMI, H. AMINI, M. BRUNE, J. RAIMOND, and S. HAROCHE. “Real-time quantum feedback prepares and stabilizes photon number states” (2011). Accepted in *Nature*.
- [39] S. GLEYZES. *Vers la préparation de cohérences quantiques mésoscopiques: réalisation d'un montage à deux cavités supraconductrices*. Thèse de doctorat, Université Paris VI (2006).
- [40] S. HAROCHE and J. M. RAIMOND. *Exploring the quantum*. Oxford Graduate Texts (2006).
- [41] R. G. HULET and D. KLEPPNER. “Rydberg atoms in "circular" states”. *Phys. Rev. Lett.*, **51**, n° 16, 1430 (Oct 1983).
- [42] J. HARE. *Étude théorique et expérimentale des atomes de Rydberg circulaires : vers une mesure directe de la constante de Rydberg en unités de fréquence*. Thèse de doctorat, Université Paris 6 (1991).
- [43] T. MEUNIER. *Oscillations de Rabi induites par renversement du temps : un test de la cohérence d'une superposition quantique mésoscopique*. Thèse de doctorat, Université Paris 6 (2004).
- [44] T. F. GALLAGHER. *Rydberg Atoms*. Cambridge Monographs on Atomic, Molecular and Chemical Physics. Cambridge University Press (1994).
- [45] A. AUFFÈVES-GARNIER. *Oscillation de Rabi à la frontière classique-quantique. Génération de Chats de Schrödinger*. Thèse de doctorat, Université Paris 6 (2004).
- [46] S. KUHR, S. GLEYZES, C. GUERLIN, J. BERNU, U. B. HOFF, S. DELÉGLISE, S. OSNAGHI, M. BRUNE, J.-M. RAIMOND, and S. HAROCHE. “An ultrahigh finesse Fabry-Perot superconducting resonator as photon box for cavity-QED experiments”. *APL*, **90**, 164101 (2007).
- [47] P. BOSLAND, A. ASPART, E. JACQUES, and M. RIBEAUDEAU. “Preparation and rf tests of l-band superconducting niobium-coated copper cavities”. Dans *1998 Applied Superconductivity Conference*, tome 9, p. 896–899. Ieee-Inst Electrical Electronics Engineers Inc, Palm Desert, California (1998). 13 NEW YORK 2 Part 1 225LY.
- [48] J. JACKSON. *Classical Electrodynamics*. Wiley, New York (1975).
- [49] C. COHEN-TANNOUDJI, J. DUPONT-ROC, and G. GRYNBERG. *An Introduction to Quantum Electrodynamics*. Wiley (1992).
- [50] R. J. GLAUBER. “Coherent and incoherent states of the radiation field”. *Phys. Rev.*, **131**, n° 6, 2766 (Sep 1963).

- [51] S. DELÉGLISE. *Reconstruction complète d'états non-classiques du champ en électrodynamique quantique en cavité*. Thèse de doctorat, Université Paris 6 (2009).
- [52] M. BRUNE, S. HAROCHE, J. M. RAIMOND, L. DAVIDOVICH, and N. ZAGURY. "Manipulation of photons in a cavity by dispersive atom-field coupling: Quantum-nondemolition measurements and generation of "schrödinger cat" states". *Phys. Rev. A*, **45**, n° 7, 5193 (Apr 1992).
- [53] M. BAYES and M. PRICE. "An essay towards solving a problem in the doctrine of chances. by the late rev. mr. bayes, f. r. s. communicated by mr. price, in a letter to john canton, a. m. f. r. s." *Philosophical Transactions*, **53**, 370 (1763). URL <http://rstl.royalsocietypublishing.org/content/53/370.short>.
- [54] A. I. LVOVSKY. "Iterative maximum-likelihood reconstruction in quantum homodyne tomography". *Journal of Optics B: Quantum and Semiclassical Optics*, **6**, n° 6, S556 (2004). URL <http://stacks.iop.org/1464-4266/6/S556>.
- [55] S. OSNAGHI, P. BERTET, A. AUFFEVES, P. MAIOLI, M. BRUNE, J. M. RAIMOND, and S. HAROCHE. "Coherent control of an atomic collision in a cavity". *Phys. Rev. Lett.*, **87**, n° 3, 037902 (Jun 2001).
- [56] C. FUCHS and J. VAN DE GRAAF. "Cryptographic distinguishability measures for quantum-mechanical states". *IEEE Transactions on Information Theory*, **45**, n° 4, 1216 (1999).
- [57] R. JOZSA. "Fidelity for mixed quantum states". *Journal of Modern Optics*, **41**, n° 12, 2315 (1994). URL <http://www.informaworld.com/10.1080/09500349414552171>.
- [58] J. DALIBARD, Y. CASTIN, and K. MØLMER. "Wave-function approach to dissipative processes in quantum optics". *Phys. Rev. Lett.*, **68**, n° 5, 580 (Feb 1992).
- [59] M. B. PLENIO and P. L. KNIGHT. "The quantum-jump approach to dissipative dynamics in quantum optics". *Rev. Mod. Phys.*, **70**, n° 1, 101 (Jan 1998).
- [60] H. AMINI, M. MIRRAHIMI, and P. ROUCHON. "On stability of continuous-time quantum-filters". *ArXiv e-prints* (2011).
- [61] C. SAYRIN. *Préparation et stabilisation d'un champ non classique en cavité par rétroaction quantique*. Thèse de doctorat, Université PARIS 6 (Septembre 2011).
- [62] S. HAROCHE, M. BRUNE, and J. RAIMOND. "Measuring photon numbers in a cavity by atomic interferometry: optimizing the convergence procedure". *J. Phys. II France*, **2**, n° 4, 659 (1992). URL <http://dx.doi.org/10.1051/jp2:1992157>.
- [63] D. VITALI, P. TOMBESI, and G. J. MILBURN. "Controlling the decoherence of a "meter" via stroboscopic feedback". *Phys. Rev. Lett.*, **79**, n° 13, 2442 (Sep 1997).
- [64] D. VITALI, S. ZIPPILLI, P. TOMBESI, and J.-M. RAIMOND. "Decoherence control with fully quantum feedback schemes". *Journal of Modern Optics*, **51**, n° 6-7, 799 (2004). URL <http://www.tandfonline.com/doi/abs/10.1080/09500340408233597>.